Negative Thermal Expansion in Substituted ZrW_2O_8 and its Ceramic Composites

Klaartje De Buysser

Promotor: prof. dr. S. Hoste
Co-Promotor: prof. dr. I. Van Driessche
Thesis submitted to the Faculty of Sciences in fulfillment of the requirements for the degree of Doctor of Sciences: Chemistry

Department of Inorganic and Physical Chemistry
Faculty of Sciences

October 2007

UNIVERSITEIT GENT

I am among those who think that science has great beauty. A scientist in his laboratory is not only a technician: he is also a child placed before natural phenomena which impress him like a fairy tale.

Marie Curie (1867-1934)

Ziezo, hier is het dan.

Het resultaat van 6 jaar omzwervingen om uiteindelijk tot dit resultaat te komen. Op mijn reis ben ik heel wat mensen tegengekomen die me een tijdje of zelfs volledig tot de eindbestemming vergezeld hebben. Ik wil hen hier en nu bedanken. Ik wil ook mijn oprechte excuses aanbieden aan diegene die ik ongetwijfeld vergeet te vermelden in dit dankwoord.

Vooraleerst Prof. Serge Hoste die me de volledige tocht begeleid heeft: Bedankt voor het vertrouwen die u in mij stelde. Ik hoop dat we onze samenwerking op die basis kunnen verder zetten.

Prof. Isabel Van Driessche draag ik een warm hart toe. Uw enthousiasme is ongekend. Bedankt voor de aangename momenten en de schouderklopjes.

Ik wil ook de leden van de lees – en examencommissie bedanken voor het nalezen en becommentariëren van dit werk. A warm thank you to Prof. Vincze. I want to thank Prof Evans not only for reading this work but also for his help along the way.

Thank you Wim Bras and Serge Nikitenko for your help during my stay in Grenoble at the Dubble EXAFS station. It was a learnful experience.

Bedankt collega's van S1 en S12.
Philippe, jij zorgde goed voor mijn "sopjes" en Olivier, jij hebt talloze XRD'tjes opgenomen. Bedankt voor de leuke SEM babbels. Ik wil ook Geert Silversmit bedanken voor de snelcursus EXAFS.

Bedankt collega's binnenshuis.
Gedurende deze 6 jaar in S3 heb ik heel wat mensen weten vertrekken en heel wat nieuwe gezichten leren kennen. Jullie zijn stuk voor stuk leuke collega's en fijne mensen.

Bedankt collega-doctorandi
Nu ligt hier mijn doctoraat. Er zijn me al velen voorafgegaan en jullie volgen nog. Ik wil jullie veel succes wensen bij het vervolledigen van jullie onderzoek.
Ook de thesisstudenten met in het bijzonder Bart, wil ik bedanken voor hun bijdrage tot dit werk.

Dan is er nog de vaste-stof ploeg
Greet, Christy, Thang en Kim, al zijn jullie reeds weggevaren, ik wil jullie toch nog eens bedanken.
Petra, ook jij hebt je koers gewijzigd maar jouw bijdrage in dit doctoraat werd erg geapprecieerd. See you in Ename! Dank je, Els, voor de wetenschappelijke en niet-wetenschappelijke babbels.
Onze youngsters: Thuy, Pieter, Nigel, Frederik en Jonas wens ik veel succes en een goede wind in de zeilen.
Bart en Veerle, met jullie heb ik leuke momenten beleefd in ons bureautje. Jullie zijn fijne mensen. Bedankt en veel geluk…

Dichter bij huis kon ik op de vriendschap en ontspanning rekenen dankzij Steven en Patsy, Gunther en Caroline, Jeroen en Inge, Yves en Annelies en de kleine meisjes. Ik wil mijn nichtje Maya speciaal bedanken voor haar glimlachje.

Chris en Marleen en de ganse familie De Buysser – Decroock wil ik danken voor hun interesse en steun met in het bijzonder mijn bobonneke en pepé…

Het thuisfront…
Broer
Ik wens je heel veel succes toe in “the world of 2D imaging”
Mama, Papa
Ik kan jullie niet genoeg bedanken voor alles wat jullie gedaan hebben en steeds doen. Jullie gaven me een heleboel bagage mee en maakten me tot de mens die ik nu ben. Dikke knuffel

Mijn Wim…
Jij leerde me misschien wel de belangrijkste les: Relativeren en genieten van het leven. Bedankt om er telkens weer voor mij te zijn en me op tijd bij te sturen. Onze reis is nog maar net begonnen…

Klaartje

Contents

Outline of the study

Overzicht van het onderzoek

Chapter 1: Thermal expansion of materials 1

1 Thermal expansion in solids 2
1.1 The nature of thermal expansion 2
1.2 Definition of the linear and volume expansion 4
1.3 The thermodynamic Grüneisen functions 6
1.4 Thermal expansion behaviour of ceramics in general 8

2 Mechanisms for Negative thermal expansion 10
2.1 Phase transitions 10
2.2 Phonons 12
2.3 Electronic and Magnetic transitions 12
2.4 Negative Thermal Expansion of geometrical origin 15
2.5 Examples of Negative Thermal Expansion in framework structures 17

3 Isotropic negative thermal expansion behaviour in the AM_2O_8 – family 30
3.1 Introduction 30
3.2 Strong isotropic negative thermal expansion in ZrW_2O_8 30
3.3 Application of ZrW_2O_8 materials 43

4 References 44

Chapter 2: Experimental Techniques 53

1 X-Ray Diffraction 54
1.1 XRD in general 54
1.2 Indexing and refinement of the unit cell parameters 56
1.3 Rietveld Refinement 58

2 EXAFS analysis 59
2.1 Introduction 59
2.2 X-ray absorption 59
2.3 Synchrotron radiation 62

3 Morphological analysis 64
3.1 Scanning Electron Microscopy 64
3.2 Density measurements 65
3.3 Particle size measurements 66

4 Thermal analysis 67
4.1 Thermogravimetric Analysis – Differential Thermal Analysis 67
4.2 Differential Scanning Calorimetry 67
4.3 Thermal Mechanical Analysis 68

5 IR and Raman Spectroscopy 70
6 Mechanical analysis: three-point bending test 71
7 Luminescence measurements 72
7.1 Absorption - Excitation 72
7.2 Relaxation – Emission 72
7.3 Experimental set-up 74
8 References 75

Chapter 3: Conventional synthesis methods for ZrW_2O_8 materials 77
1 Synthesis methods 78
2 Conventional solid state reaction 79
2.1 Phase diagram of ZrW_2O_8 80
2.2 Characterization of ZrO_2 and WO_3 oxides 80
2.3 Preparation of the ZrO_2 – WO_3 oxide powder mixtures 83
2.4 Synthesis and characterization of ZrW_2O_8 86
3 Conclusions 91
4 References 92

Chapter 4: Sol-gel synthesis methods for ZrW_2O_8 materials 95
1 Sol-gel chemistry 96
1.1 Hydrolysis 97
1.2 Condensation reactions 97
2 Description of the Zirconium and Tungsten salts 99
2.1 Zirconyl chloride 99
2.2 Zirconyl nitrate 101
2.3 Zirconium hydroxyl acetate 103
2.4 The aqueous chemistry of the zirconium salts 105
2.5 Ammonium metatungstate 106
2.6 The aqueous chemistry of the tungstate salts 108
3 Citrate-gel processing of ZrW_2O_8 109
3.1 Coordinative properties of citric acid 109
3.2 Screening of ideal sol-gel conditions for the preparation of the precursor gels 111
3.3 Synthesis of ZrW_2O_8 116
4 EDTA-gel synthesis of ZrW_2O_8 124
4.1 Coordinative properties of Ethylene diamine tetraacetic acid 124
4.2 Synthesis and preparation of the precursor solution 124
4.3 Synthesis of ZrW_2O_8 128
5 Conclusions 131
6 References 132

Chapter 5: Luminescent properties and EXAFS analysis of the sol-gel precursors 135

1 Luminescence of the precursor gels 136

2 EXAFS analysis of the precursor solutions 141
2.1 EXAFS of scheelite reference materials 142
2.2 EXAFS of wolframite reference materials 144
2.3 EXAFS of the sol-gel precursor solutions 147

3 Conclusions 151

4 References 152

Chapter 6: Synthesis and characterization of ZrW_2O_8 composites 155

1 Composites in general 156
1.1 Introduction 156
1.2 Synthesis of composites 157
1.3 Properties of composites 158
1.4 Thermal expansion properties of composites 159

2 State of the art of ZrW_2O_8 composites 160
2.1 Al-ZrW_2O_8 composites 160
2.2 Cu-ZrW_2O_8 composites 160
2.3 ZrW_2O_8 – cement based composites 161
2.4 ZrW_2O_8 substrates 161

3 Preparation of ZrO_2 – ZrW_2O_8 composites 162
3.1 Introduction 162
3.2 Conventional processing of ZrO_2 – ZrW_2O_8 ceramic composites 162
3.3 Synthesis of ZrO_2 – ZrW_2O_8 composites by a novel in situ method using oxides precursors 163
3.4 Synthesis of ZrO_2 – ZrW_2O_8 composites by the in situ method using sol-gel precursors 166

4 Analysis of the composites 167
4.1 X-ray analysis and morphology studies 167
4.2 Flexural strength of the ZrO_2 – ZrW_2O_8 composites 170
4.3 Thermomechanical analysis 174

5 Conclusions 179

6 References 181

Chapter 7: Synthesis and analysis of Zr-substituted $Zr_{1-x}M_xW_2O_8$ materials 183

1 Introduction 184

2 Synthesis 185

3 X-ray analysis and thermomechanical properties of the substituted materials 186

4 DSC analysis of the substituted materials 194
4.1 Experimental set-up 194
4.2 Calorimetric data of the substituted materials 198
4.3 Pre-treatment of the samples 201

5 Conclusion 203

6 References 204

Summary and conclusion

Samenvatting en besluit

List of symbols and abbreviations

Crystallographic data

Scientific work

Outline of the study

In today's world there is a continued quest to develop high performance materials with excellent mechanical properties and resistance against extreme circumstances. A material is characterized by a large number of parameters and one of the most important parameters is its thermal expansion coefficient which describes the change in the dimensions of the material under influence of a temperature change. The positive thermal expansion of the majority of materials is widely found and can be easily explained by the asymmetry of the vibrational potential well. Nevertheless, there are some families of materials which will exhibit shrinkage of their volume upon a temperature increase and this phenomenon is the subject in the present study.

ZrW_2O_8 is one of the most popular negative thermal expansion materials known. It is a ceramic compound with isotropic negative thermal expansion due to its cubic crystal structure. Its thermodynamical stability range is situated between 1105 °C and 1257 °C whereas this material is kinetically stable between - 273 °C and 770 °C. The thermal expansion of our best samples can go up to -10×10^{-6} °C^{-1}. This parameter is superior in comparison with other materials with negative thermal expansion behaviour. Clearly, negative thermal expansion materials, alone or in combination with other kinds of materials, are very interesting in the development of new high performance materials with tuned thermal expansion.

The aim of this PhD research is threefold. First of all, a pure, crystalline material was synthesized and emphasis was put on the **synthetic routes** from different precursors (soluble or non-soluble) to ZrW_2O_8. The crystallinity, morphology and thermal expansion of the materials obtained are described in detail. Secondly, ZrW_2O_8 was screened for its potential in the processing of ZrW_2O_8 **composite materials with**

tuned thermal expansion. This study also aimed at obtaining a better insight in the mechanism involved in the phase transition occurring in ZrW_2O_8. **Substitution** of the Zr atom helped us to understand the different aspects influencing this transition.

As all research starts with an extensive literature research, the most important facts and figures are written down in *Chapter 1*. This chapter describes the thermal expansion of materials in general and reveals some mechanisms which lead to negative thermal expansion. ZrW_2O_8 is built from tetrahedrons and octahedrons linked to each other in a so-called open framework structure. Low frequency librations result in a global shrinkage of the unit cell. This mechanism is described in detail. Other framework families and their specific - positive or negative - anisotropic or isotropic - thermal expansion behaviour are shown also there.

Detailed studies of materials and material properties need high quality equipment. In *Chapter 2* the different experimental techniques and parameters used in this work are briefly presented. The techniques are grouped as follows: (1) structural characterization by X-rays (diffraction and EXAFS); (2) morphology characterization by SEM, density and particle size; (3) thermal analysis by TMA, TGA-DTA and DSC; (4) mechanical properties by using a three-point bending test (5) identification of the different species by IR and Raman and (6) photoluminescence measurements.

As described above, this study emphasizes the different synthetic routes to obtain pure ZrW_2O_8. *Chapter 3* describes the conventional synthesis method using ZrO_2 and WO_3 as precursor materials and using different milling techniques whereas *Chapter 4* is reserved for the sol-gel synthesis methods using water soluble precursor salts and complexing agents such as citric acid and EDTA. The crystallinity of the phases formed, particle sizes, morphology and thermal expansion are the main properties screened in these two chapters. The morphology of the precursor solutions obtained by the citrate – gel method are examined more in detail in *Chapter 5* by Extended X-ray Absorption Fine Structure measurements and photoluminescence measurements.

Chapter 6 highlights the exploration of ZrW_2O_8 as matrix material in ZrO_2 – ZrW_2O_8 composite materials. The influence of the composition on the thermal expansion behaviour is examined as well as on the mechanical properties of these composites. These composites allow the preparation of ceramic materials with a tuned thermal expansion. This could be a step towards the development of high performance materials. As these composites still exhibit a phase transition, *Chapter 7* concentrates on the shift in the phase transition temperature and represents the study of Sn and Ti substituted ZrW_2O_8 materials. This chapter attempts to explain the mechanism followed during phase transition and the influence of the substitution ion properties on the thermal expansion behaviour of $Zr_{1-x}M_xW_2O_8$.

Most part of this research was already published or accepted for publication in several A1 publications. The bibliographic references to these articles are given at the beginning of each chapter.

Overzicht van het onderzoek

De ontwikkeling van nieuwe materialen stelt erg hoge eisen. Ze moeten uitstekende mechanische eigenschappen bezitten en bestand zijn tegen extreme omstandigheden. Alhoewel een materiaal wordt gekenmerkt door een groot aantal eigenschappen, is de thermische expansie één van de belangrijkste materiaaleigenschappen. De thermische expansie geeft weer hoe het volume en de afmetingen van het materiaal zullen veranderen onder invloed van temperatuurschommelingen. De meeste materialen zetten uit bij verwarming wat te wijten is aan de asymmetrische Morse-potentiaalcurve. Er zijn echter ook materialen die het tegengestelde gedrag vertonen. Deze familie kreeg de naam NTE materialen mee: Negatieve Thermische Expansie materialen.

ZrW_2O_8 is één van de meest besproken en bestudeerde NTE materialen. Het is een keramisch materiaal met isotrope negatieve thermische expansie, te danken aan de kubische kristalstructuur. ZrW_2O_8 is thermodynamisch stabiel tussen 1105 °C en 1257 °C terwijl zijn kinetische stabiliteit het ganse gebied tussen -273 °C en 770 °C inneemt. De thermische expansie coëfficiënt kan waarden tot -10×10^{-6} $°C^{-1}$ aannemen. Al deze eigenschappen zorgen er voor dat ZrW_2O_8 superieur is in vergelijking met andere materialen die negatief thermisch expansie gedrag vertonen. Het spreekt voor zich dat NTE materialen op zichzelf of in combinatie met andere materialen een uitstekend startpunt vormen met het oog op ontwikkeling van hoogtechnologische materialen met thermische expansie op maat.

Het onderzoeksgebied van dit proefschrift is drieledig. Eerst en vooral werd er een zuiver kristallijn materiaal gesynthetiseerd. Daarvoor werd in dit werk grote aandacht besteed aan de ontwikkeling en optimalisatie van verschillende **synthesemethoden**

vertrekkende van de oplosbare of niet-oplosbare precursoren om uiteindelijk kristallijn ZrW_2O_8 te verkrijgen. De kristalstructuur, morfologie en thermische expansie werden in detail bestudeerd. ZrW_2O_8 werd ook gescreend als potentiële kandidaat in de ontwikkeling van **composietmaterialen met thermische expansie op maat.** Tenslotte wil deze studie ook een duidelijker beeld scheppen van het mechanisme dat achter de fasetransitie schuilt. **Substitutie** van de Zr positie bracht een aantal parameters aan het licht die deze transitie beïnvloeden.

Alle onderzoek begint met een grondig literatuuronderzoek weergegeven in *Hoofdstuk 1*. Dit hoofdstuk beschrijft het thermische expansiegedrag van materialen in het algemeen en toont een aantal mechanismen die kunnen leiden tot negatieve thermische expansie. ZrW_2O_8 is opgebouwd uit tetraëders en octaëders die deel uitmaken van een open netwerk structuur. Rotaties en vibraties met een lage frequentie leiden tot het verkleinen van de eenheidscel bij toenemende temperatuur. Dit mechanisme wordt in detail besproken. Het thermische expansiegedrag van enkele andere open netwerk structuur materialen wordt ook even vermeld.

Studies van materialen en materiaaleigenschappen vereisen meetapparatuur van hoge kwaliteit. *Hoofdstuk 2* vermeldt de gebruikte experimentele technieken. De theoretische aspecten worden kort aangehaald. De technieken worden als volgt gegroepeerd: (1) structurele karakterisatie met behulp van X-stralen (diffractie en EXAFS); (2) morfologische studie met behulp van SEM, dichtheidsmetingen en deeltjesgrootte; (3) thermische analyse met TMA, TGA-DTA en DSC; (4) mechanische eigenschappen werden gemeten met een driepuntsbuigtest (5) identificatie gebeurde ondermeer met IR en Raman en (6) fotoluminescentie metingen.

Zoals hierboven vermeld, gaat de aandacht in dit werk uit naar verschillende synthese methoden die uiteindelijk leiden tot ZrW_2O_8. *Hoofdstuk 3* beschrijft een conventionele synthese methode die ZrO_2 en WO_3 als precursor materiaal gebruikt terwijl *Hoofdstuk 4* voorbehouden is voor de sol-gel synthese methoden die wateroplosbare precursor zouten en complexantia zoals citroenzuur en EDTA gebruiken. Analyse van de kristalstructuur van de gevormde fasen, deeltjesgroottes, morfologie en thermische expansie zijn de belangrijkste parameters die in deze twee hoofdstukken bestudeerd

worden. De eigenschappen van de precursoroplossing verkregen door de citraat gel methode werden onderzocht in *Hoofdstuk 5* met behulp van "Extended X-ray Absorption Fine Structure" metingen en fotoluminescentie.

Hoofdstuk 6 toont de exploratie van ZrW_2O_8 als matrix materiaal in ZrO_2 – ZrW_2O_8 composiet materialen. De invloed van de samenstelling van de composieten op het thermisch expansie gedrag werd onderzocht evenals de andere mechanische eigenschappen van deze composieten. Hierdoor werd het mogelijk om keramische materialen te synthetiseren met een thermische expansie op maat. Dit kan een grote stap voorwaarts betekenen in de ontwikkeling van hoogtechnologische materialen. Deze composieten vertonen echter nog steeds een fasetransitie. Daarom concentreert *Hoofdstuk* 7 zich op het verschuiven van de fasetransitietemperatuur door het substitueren van de Zr positie met Sn^{4+} en Ti^{4+} ionen. Dit hoofdstuk probeert het mechanisme van die fasetransitie te verklaren en de invloed van de substituenten op het thermisch expansie gedrag van $Zr_{1-x}M_xW_2O_8$ te verklaren.

Een deel van dit onderzoek werd reeds gepubliceerd of is aanvaard tot publicatie in verscheidene A1 tijdschriften. De bibliografische gegevens van deze artikels worden vermeld aan het begin van elk hoofdstuk.

Chapter 1

Thermal expansion of materials

This chapter summarizes the theoretical principles and formulae concerning the thermal expansion in solid materials. Positive thermal expansion is more common in daily life and therefore the mechanisms behind the negative thermal expansion (NTE) are discussed in more detail. The classification of the different families of negative expansion materials is given with some examples. The negative thermal expansion of ZrW_2O_8 is widely explored and the most important features are mentioned.

1 Thermal expansion in solids

1.1 The nature of thermal expansion [1, 2]

Most solid materials expand upon heating and will contract when they are exposed to a decrease in temperature. However, it is not uncommon for materials to contract upon heating. Examples in this field are many tetrahedrally bonded crystals at low temperature and β-quartz at high temperature.

Thermal expansion can be defined as the temperature dependence of the geometrical parameters under specified conditions. Although most of the time the external length is measured to determine the thermal expansion, the changes in unit cell parameter, as determined from XRD analysis, will also show the thermal expansion of the unit cell in detail. The applied conditions can vary according to the different measurements. In general, the materials are exposed to constant pressure.

From an atomic perspective, thermal expansion is reflected by a change in the average distance between the atoms with increasing temperature. This phenomenon can be understood by using the potential well of a diatomic molecule (figure 1). This potential well illustrates the relation between the potential energy and interatomic spacing. As the temperature rises the vibrational energy will also increase. This will have a positive effect on the average vibrational amplitude of an atom. The interatomic distance is calculated by the mean position of the atoms and due to the asymmetric curvature of the potential well the interatomic distance will increase as the temperature shifts to higher values.

For each class of materials (polymers, ceramics or metals) the atomic bond energy will affect the curvature of the potential well. For strongly bonded atoms, the minimum of the potential well will reach lower values and the curve will become narrower and more symmetric. This means that the effect of the temperature will be less than in the case of weakly bonded atoms.

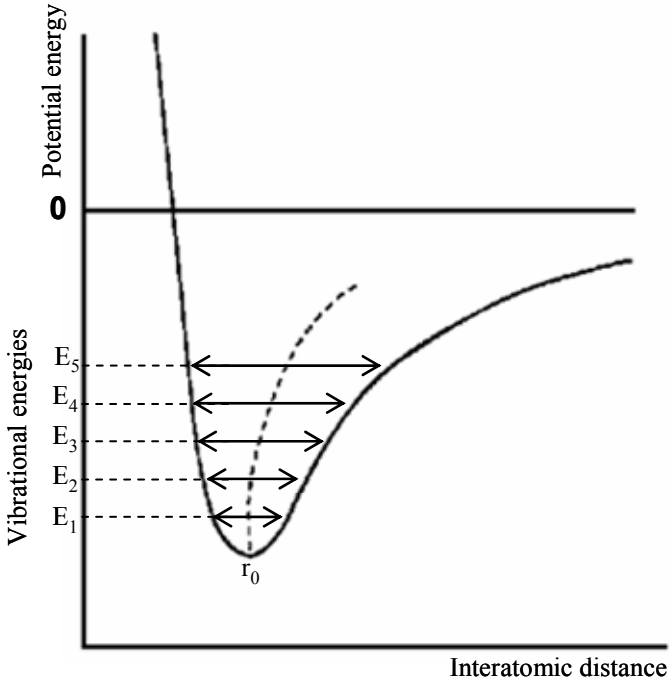

Figure 1: Potential well of a diatomic molecule

The potential well reveals the most generally accepted mechanism for thermal expansion as it states that the atomic vibrations will give rise to thermal expansion because of anharmonicity. Nevertheless, it is a simplified model as it uses isolated diatomic molecules which are not representative of ceramic materials. Furthermore, it doesn't explain the principle behind negative thermal expansion. The model's main weakness is that only the longitudinal component of the vibrational mode is used. In solid materials the transversal vibrational motion may give rise to a second mechanism pulling the atoms towards one another and decreasing the interatomic spacing (figure 2).

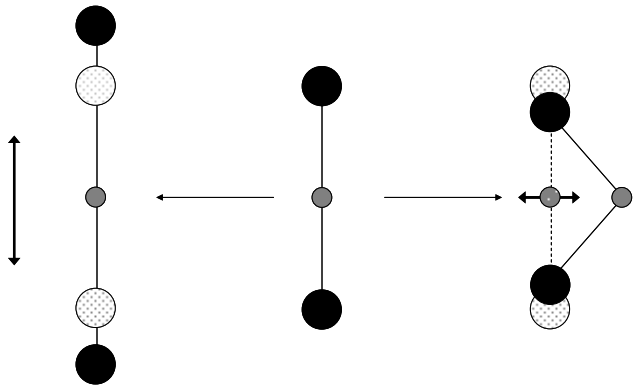

Figure 2: Longitudinal (left) and transversal (right) component of the vibration mode

The two mechanisms will have an opposite effect on the interatomic spacing and the resulting expansion will be positive or negative depending on which effect is more pronounced. The transverse effect will become dominant in solids with an open structure where vibrations occur for which the components of relative motion have large transversal components along all bond directions.

Non-vibrational contributions can also occur and may be spectacular, especially at low temperatures where the vibrational effects are small. In principle, any contribution to the free energy (electronic, magnetic …) is dependent on strain and therefore affects the thermal expansion.

1.2 Definition of the linear and volume expansion [1, 3]

To compare the thermal expansion behaviour of different kinds of materials, there is a need for a quantitative analysis of the dimension change. Changing the temperature must change the internal pressure and, as a consequence, the dimensions will be adjusted to minimize the Gibbs free energy. The magnitude of change is partially controlled by the elastic stiffness of the solid.

The thermodynamic relation between the volume thermal expansion coefficient β, pressure P, volume V, compressibility χ and entropy S is given by the following equation.

$$\beta = \left(\frac{d(\ln V)}{dT}\right)_P = \chi_T \left(\frac{dP}{dT}\right)_V = \chi_T \left(\frac{dS}{dV}\right)_T \qquad [1]$$

The sign of dS/dV determines the sign of the expansion coefficient. In most cases, the entropy becomes smaller under increasing pressure and the volume is reduced. This leads towards positive values for dS/dV and β. However, as mentioned above there are solids for which the entropy increases under increasing pressure which will result in a negative thermal expansion coefficient.

Equation 1 is widely known in a slightly adjusted form (equation 2) which gives a direct relation between the volume thermal expansion coefficient and the volume (V) of the materials at different temperatures (T).

$$\beta = \left(\frac{d(\ln V)}{dT} \right)_P = \left(\frac{V_2 - V_1}{V_1} \right) \left(\frac{1}{T_2 - T_1} \right) \quad [2]$$

Linear thermal expansion is defined in the same way as the volumetric expansion with the exception of length l instead of volume V.

$$\alpha = \left(\frac{d(\ln l)}{dT} \right)_P = \left(\frac{l_2 - l_1}{l_1} \right) \left(\frac{1}{T_2 - T_1} \right) \quad [3]$$

For materials with isotropic or cubic symmetry, the linear thermal expansion is independent of the direction. For these materials there is a simple relation between the volume and their linear thermal expansion coefficient as mentioned in equation 4.

$$\beta = 3 \times \alpha \quad [4]$$

For anisotropic materials the expansion is defined relative to specific directions, most frequently the crystallographic vectors along the a-, b- and c-axis. For hexagonal, trigonal and tetragonal crystals the thermal expansion is symmetric according to the principal axis of symmetry. This results in two independent coefficients of linear expansion, $\alpha_{\parallel}$ along the axis and $\alpha_{\perp}$ normal to the axis. For materials with orthorhombic symmetry the three crystallographic axes are at right angles to each other, with three independent linear expansion coefficients α_a, α_b and α_c. For monoclinic and triclinic systems, there is also a temperature variation of the angles between the axes. All these different linear thermal expansion coefficients must be taken into account to describe the thermal expansion behaviour of these materials.

1.3 The thermodynamic Grüneisen functions

Grüneisen established the experimental pattern of behaviour for many crystalline materials before 1920 and summarized this in his 1926 review [4]. He observed that in many solids at normal and elevated temperature, the ratio of the thermal expansion coefficient to the heat capacity C is roughly constant with temperature as can be seen in equation 5.

$$\beta = \frac{\gamma C_P \chi_S}{V} = \frac{\gamma C_V \chi_T}{V} \qquad [5]$$

In this equation C_P and C_V are the heat capacities of a mole of volume V at constant pressure and constant volume respectively. χ_S and χ_T are the adiabatic and isothermal values of the compressibility of the material. The parameter γ is known as the Grüneisen parameter.

The anharmonicity of the pair potential gives rise to a volume dependence of the frequency (ν_i) described by the Grüneisen parameter.

$$\gamma_i = -\frac{d \ln \nu_i}{d \ln V} \qquad [6]$$

For positive thermal expansion materials, Grüneisen parameters with a value between 1 to 3 are typical. Negative thermal expansion materials are characterized by a negative Grüneisen parameter. This means that the vibrations which increase in frequency as the volume increases will give rise to the global shrinkage of the material. When a string is plucked, a transversal vibration is induced. When the plucked string is stretched, the sound produced by the guitar will shift to higher frequencies [5].

To estimate the thermal expansion of a material, the distribution among the different vibration modes must be known. The total vibrational Grüneisen function is a weighted average of all the γ_i's.

$$\gamma_{vib} = \frac{\sum_i c_i \gamma_i}{\sum_i c_i} \qquad [7]$$

In this equation c_i stands for the contribution of a specific vibrational mode to the total heat capacity C_V which can be given by equation 8.

$$C_V = \sum_i c_i \qquad [8]$$

The vibrational contribution to the volume thermal expansion coefficient is given by:

$$\beta = \frac{\gamma_{vib} C_{vib} \chi_T}{V} \qquad [9]$$

Transversal vibration modes are most frequently less energetic than the longitudinal modes and are therefore activated at lower temperatures. At low temperatures, these vibrational modes can dominate the Grüneisen parameter. This can be observed in a series of Rubidium halides, Si, Ga, CuCl… Below -151 °C, negative thermal expansion behaviour can be observed as can be seen in figure 3.

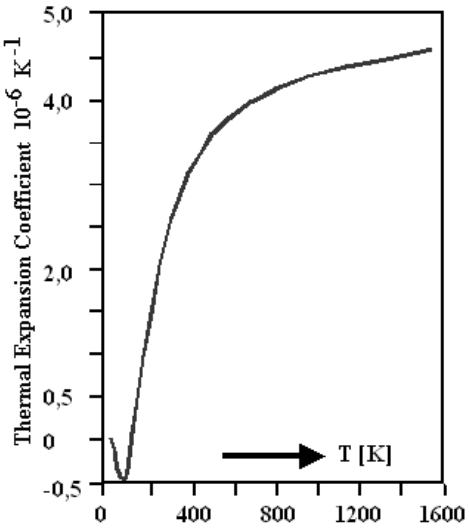

Figure 3: Thermal expansion behaviour of Si

1.4 Thermal expansion behaviour of ceramics in general

Relatively strong interatomic bonding forces are found in many ceramic materials as reflected in their comparatively low thermal expansion coefficients. Typical values are in the range between 0.5 – 15 $\times$ 10^{-6} °C^{-1}. For non-crystalline ceramics and those having a cubic crystal structure α_l is isotropic. Otherwise the thermal expansion is anisotropic and, in fact, some ceramic materials will contract upon heating in some crystallographic directions while expanding in others [2].

Ceramic materials that are to survive larger temperature changes must possess relatively low thermal expansion coefficients and need to expand preferably in an isotropic way. Otherwise these brittle materials may experience fracture as a consequence of non-uniform dimensional changes caused by a thermal shock.

The thermal expansion properties for a variety of materials are given in table 1 .

Material	α ($\times$ 10^{-6} °C^{-1})
Al	23.6 *(between 0 °C and 100 °C)*
Cu	17.0 *(between 0 °C and 100 °C)*
Au	14.2 *(between 0 °C and 100 °C)*
Fe	11.8 *(between 0 °C and 100 °C)*
Ni	13.3 *(between 0 °C and 100 °C)*
W	4.5 *(between 0 °C and 100 °C)*
Invar	1.6 *(between 0 °C and 100 °C)*
Al_2O_3	7.6 *(between 20 °C and 1000 °C)*
Fused SiO_2	0.4 *(between 20 °C and 1000 °C)*
α-ZrW_2O_8	-9.1 *(between -270 °C and 30 °C)*
MgO	13.5 *(at 100°C)*
Polyethylene	106 – 198 *(at room temperature)*
Polypropylene	145 – 180 *(at room temperature)*
Polystyrene	90 – 150 *(at room temperature)*
Teflon	126 – 216 *(at room temperature)*
Nylon 6,6	144 *(at room temperature)*

Table 1: Tabulation of the thermal expansion properties

The thermal expansion of ceramics can be divided into 4 groups:

(1) negative thermal expansion $\alpha < 0\ °C^{-1}$

(2) very low expansion $0\ °C^{-1} < \alpha < 2 \times 10^{-6}\ °C^{-1}$

(3) low expansion $2 \times 10^{-6}\ °C^{-1} < \alpha < 8 \times 10^{-6}\ °C^{-1}$

(4) high expansion $\alpha > 8 \times 10^{-6}\ °C^{-1}$.

Different thermal expansion coefficients will lead towards different relative length changes with varying temperature. In figure 4 some examples are given. The slope of the curves will increase for higher thermal expansion coefficients. The middle region represents the very low expansion materials. These are very useful for industrial applications as there is nearly no dimension change. The upper region is occupied by positive expansion ceramic materials such as alumina and some metal alloys. The area below $\Delta L/L = 0$ is occupied by the NTE materials from which ZrW_2O_8 is chosen as a representative.

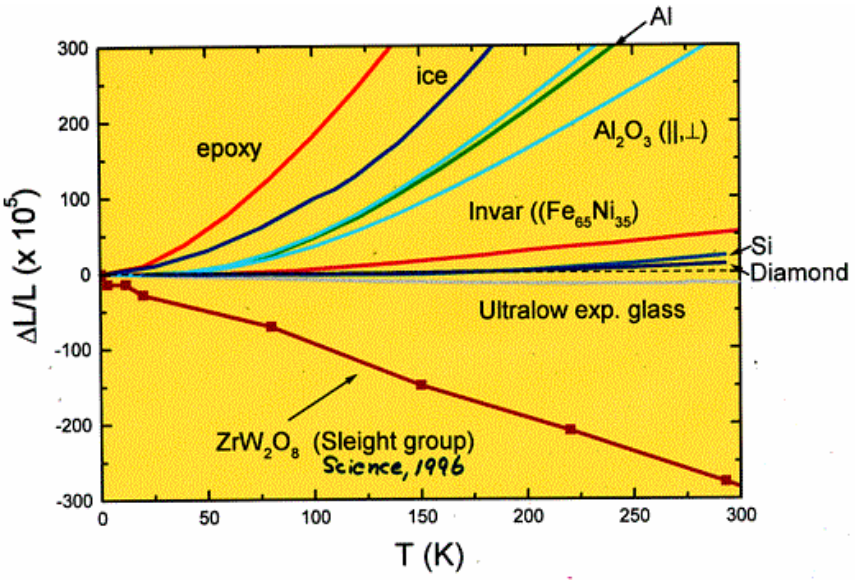

Figure 4: Relative length difference according to temperature

2 Mechanisms for Negative thermal expansion

Negative thermal expansion can be induced by several mechanisms which will be described in the following paragraph such as phase transitions, phonons, electronic - magnetic transitions and the negative thermal expansion of geometrical origin.

2.1 Phase transitions [5-7]

There must be a structural phenomenon which overrules the normal tendency to expand at increasing temperatures in case of a material displaying negative thermal expansion. In some situations, a decrease in the average bond distance, at least over a narrow temperature range, can be detected.

The contribution to the overall valence bond sum from a given bond can be approximated by the following expression with r_0 equal to a constant for an E – X combination of elements [8]. The individual bond valences are equivalent to the number of bonding electrons distributed within the bond.

$$\nu = \exp\left[\frac{r - r_0}{0.37}\right] \qquad [10]$$

This leads to an exponential decrease in bond strength with increasing bond length as can be seen in figure 5. It can be understood that the average bond length in an undistorted MO_6 octahedron will always be shorter than the average bond length in a distorted octahedron. This effect can be attributed to the fact that anion-anion repulsions are minimized as polyhedra become more regular.

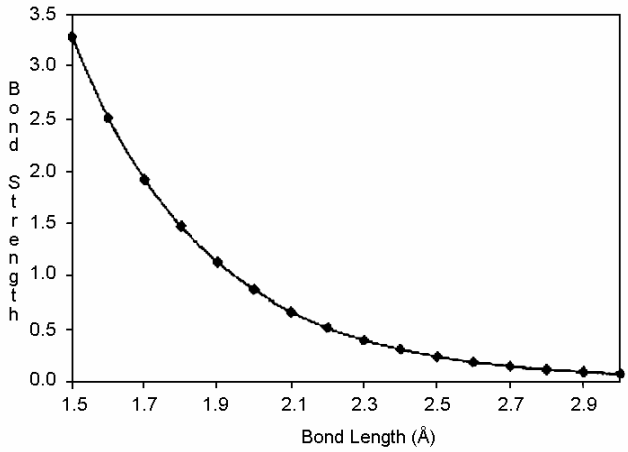

Figure 5: The form of a typical bond length-bond strength plot [5]

A suitable example to explain this phenomenon is $PbTiO_3$. At room temperature $PbTiO_3$ is a ferroelectric material with a tetragonal structure. The ferroelectric – paraelectric phase transition is situated around 490 °C. At temperatures above 490 °C, lead titanate is cubic with regular PbO_{12} and TiO_6 polyhedra. Below the phase transition temperature $PbTiO_3$ contains highly distorted polyhedra. The polyhedra will regularize as they approach the phase transition. This effect contributes to a decrease in cell volume as the temperature is increased. In the tetragonal structure there is thermal expansion along the a - and b - axis and thermal contraction along the c axis as shown in figure 6. Once $PbTiO_3$ becomes cubic it shows normal positive thermal expansion.

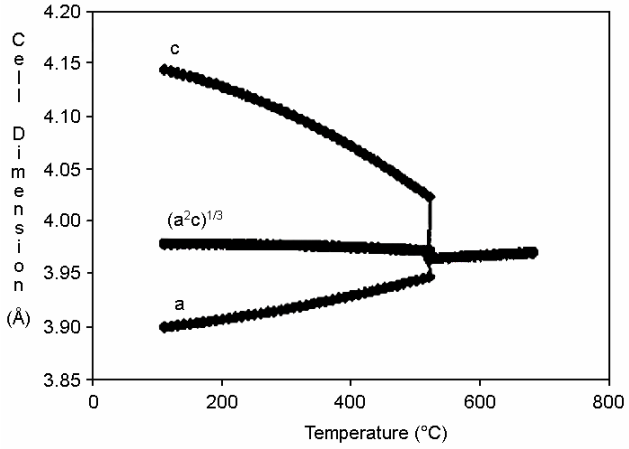

Figure 6: Cell parameters of $PbTiO_3$ as it approaches the tetragonal - cubic phase transition [5]

2.2 Phonons [7, 9, 10]

Lattice vibrations or phonons play a major part in thermal expansion. As already discussed in this chapter, transversal thermal motion of the oxygen atom in an e.g. M-O-M linkage can induce shrinkage of the unit cell upon heating. If the M-O bonds are strong enough they will show negligible thermal expansion. As the temperature increases, the average displacement of the oxygen atom will increase and the vibration will pull the metal atoms together. This mechanism can operate in any crystal system.

2.3 Electronic and Magnetic transitions [11-13]

Besides ceramic materials, some metals and alloys display negative or low thermal expansion behaviour.

For materials with a significant magnetoelastic coupling, the normal positive thermal expansion can be compensated by a large contraction due to changes in the magnetic structure. Invar, $Fe_{0.65} - Ni_{0.35}$, and some transition metals as Mn and Cr show this behaviour. RE_2Fe_{17} (RE: Y, Lu) exhibits negative thermal expansion.

In 1897 Guillaume discovered that an iron-nickel alloy with a nickel concentration of around 35 atomic percent exhibits nearly no dimension change as the temperature increases. Invar has a thermal expansion coefficient of 0.02×10^{-6} °C^{-1} in a wide temperature range. The discovery of the so-called Invar effect was a stimulus for many scientists to reveal the mechanism. Weiss introduced the 2γ – state model. According to this model, there are two possible states for face-centred γ – Fe: the ferromagnetic high-volume state and the antiferromagnetic low-volume state. Thermal excitations between these two states are supposed to compensate for the usual lattice expansion related to the anharmonic effects of the lattice vibrations. Recently studies were published which suggest that the invar-system consists of multiple magnetic states [13]. The magnetic transition is a continuous process from a high volume ferromagnetic state to disordered states with non-collinear spin alignments with similar energies and lower volumes.

YbGaGe is an electrically conductive intermetallic compound with a negligible volume change between -170 and 130 °C. YbGaGe crystallizes in the hexagonal $P6_3/mmc$ space group. Figure 7 shows a detail of the crystal structure with an indication of GaGe layers (A-D). There are 4 of these layers in the unit cell and they sandwich the Yb atoms. Yb(1) atoms are lying between the A-B and C-D layers and the Ga atoms provide the binding sites for these Yb atoms whereas for the Yb(2) the Ge atoms show the closest approach.

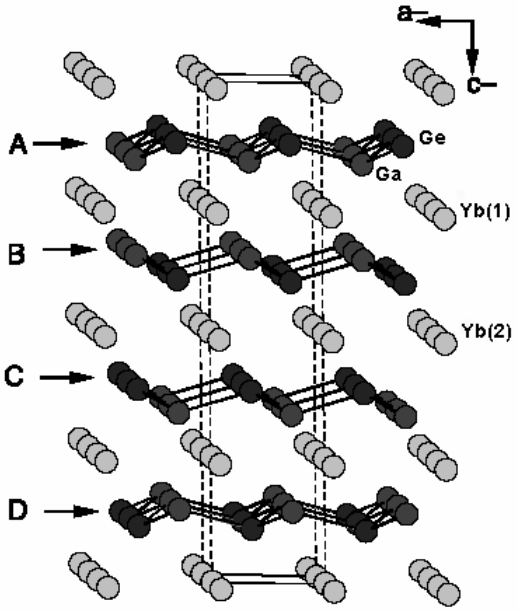

Figure 7: Crystal structure details YbGaGe [12]

Studies by a research group at Michigan State University suggest that the low thermal expansion response to an increasing temperature is due to a temperature induced valence transition in the Yb atoms. Yb(1) has a mixed valency +2/+3 whereas Yb(2) has a fixed valency of +2 [12]. With an increase in valence, a smaller radius will be obtained.

The temperature induced valence transition is drawn in figure 8. The negative thermal expansion depends on the overlap of the Yb 4f and Ga 4p bands. As the temperature increases, the electron density shifts from the Yb 4f band to the Ga 4p band. The Yb shrinks in size due to its higher valence state whereas at the Ga ion a negligible increase in size is created. Strong negative thermal expansion along 2 axes is compensated by a strong normal thermal expansion along the third axis.

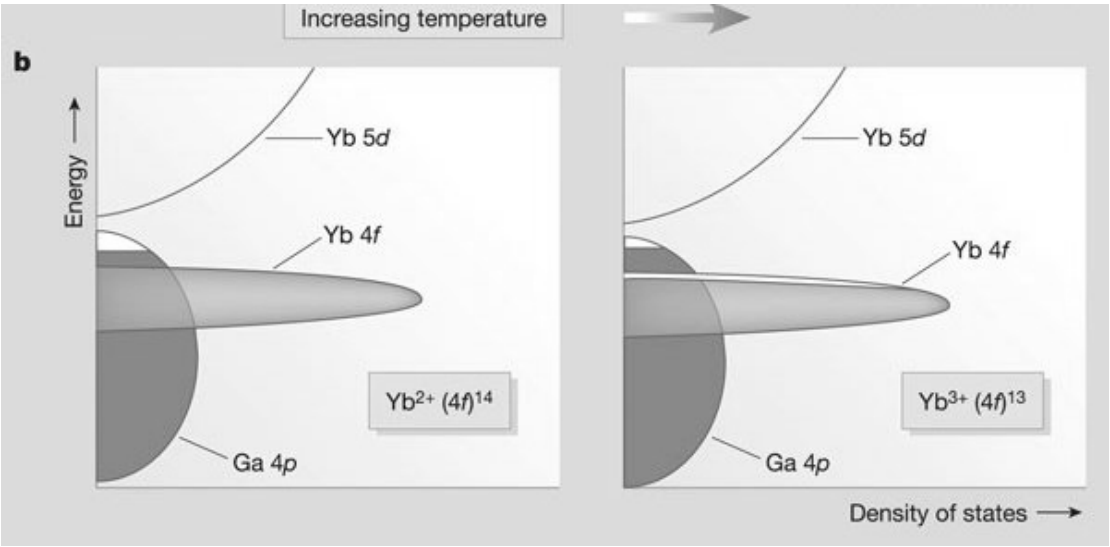

Figure 8: Valence degeneracy as a function of temperature [11]

This induced valence change is also indicated by magnetic susceptibility measurements. Yb^{3+} ($4f^{13}$) is a paramagnetic ion with a calculated free ion molar susceptibility of 4.54 BM and Yb^{2+} is diamagnetic. As the temperature rises, the magnetic behaviour of YbGaGe changes due to the larger population of paramagnetic Yb^{3+}.

$Sm_{2.75}C_{60}$ materials can also be situated in this category [14, 15]. $Sm_{2.75}C_{60}$ displays large negative thermal expansion behaviour in the temperature range -268.9 °C – -241 °C due to a quasi continuous valence change from the larger Sm^{2+} towards the smaller $Sm^{2.3+}$ ion. This material exhibits not only negative thermal expansion but shows a lattice collapse upon application of pressure. Synchrotron X-ray powder diffraction measurements at ambient temperature have shown that the $Sm_{2.75}C_{60}$ structure contracts and at 3.95 GPa an abrupt phase transformation accompanied by a more pronounced lattice shrinkage sets in. This phase transformation can be interpreted as a discontinuous valence change if Sm from the +2.3 towards the +3 state. This leads to a smaller size of the rare-earth ions and a collapse of the unit cell parameters. The observed pressure and temperature response is similar to that of strongly correlated Kondo insulators like SmS with a Sm^{2+} ($4f^6$) → Sm^{3+} ($4f^5 5d^1$) electron transfer.

2.4 Negative Thermal Expansion of geometrical origin [16-19]

Negative thermal expansion can arise as a geometrical effect in framework structures. These are crystal structures consisting of rather stiff atomic units such as AX_4 tetrahedra and AX_6 octahedra which are joined by shared X-atoms at the corners. Most frequently the place of the X-atom is taken by oxygen atoms. Framework structures can be recognized in ZrV_2O_7 and ZrW_2O_8, β-quartz, some zeolites…

The mechanism which will lead towards negative thermal expansion is a combination of the geometrical effect of the flexible framework structures associated with the rotation of the rigid structural units (i.e. bond bending at the shared oxygen or other corner atoms). Figure 9 shows an ideal structure with lattice constant a_0 and the result of rotating squares by an angle θ. A global shrinkage of the lattice is illustrated.

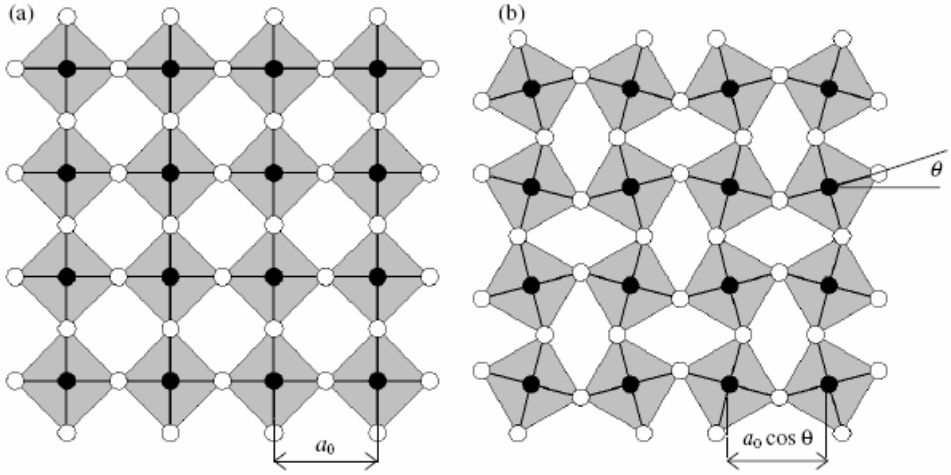

Figure 9: (a) square lattice of rigid MO_4 unit modes (b) Rotational displacements inducing a contraction of the lattice [19]

The area A(θ) of the 2D-cell is reduced and is given by equation 11.

$$A(\theta) = a_0^2\left(1-\eta_A\theta^2\right) = A_0\left(1-\eta_A\theta^2\right) = A_0\cos^2\theta \qquad [11]$$

with η_A: a geometrical calculable constant (equal to 1 in the case above) and A_0: the area occupied by the unit cell when no rotations occur. Fluctuating positive and negative rotations are a manifestation of the thermal agitation.

In this case, as the temperature rises, the angle θ by which the lattice will deform will increase resulting in a decrease of the unit cell.

$$\langle A(\theta)\rangle_T = A_0\left(1-\eta_A\langle\theta^2\rangle_T\right) \qquad [12]$$

where $\langle A\rangle_T$ decreases and $\langle\theta^2\rangle_T$ increases with T.

Applying the principle of equipartition of energy to the potential energy of oscillation, the rotation due to thermal fluctuation can be written as follows:

$$\frac{1}{2}I\nu^2\langle\theta^2\rangle_T = \frac{1}{2}k_B T \qquad [13]$$

Here I is the moment of inertia of the units, ν is the vibrational frequency and k_B is known as the Boltzmann's constant. Combining equations 12 and 13 leads towards an expression including temperature and vibrational frequency.

$$\langle A(\theta)\rangle_T = A_0\left(1-\eta_A\frac{k_B T}{I\nu^2}\right) \qquad [14]$$

Taking a closer look at equation 14, one can conclude that thermal agitation will cause a deformation of the ideal lattice structure by a reduction of one or more lattice parameters. Lower frequency modes will have a larger impact resulting in a larger absolute value of the negative thermal expansion coefficient.

The rotations described in this section are called Rigid Unit Modes or RUM's. They are characterized by large amplitudes and low frequencies. They involve no changes in the intrapolyhedral bond distances or bond angles. In some materials these low frequency vibrations are accompanied by small distortions of the polyhedra. These are called Quasi-Rigid Unit Modes or QRUM's and these can also give rise to negative thermal expansion. In structures where neither RUM's nor QRUM's can occur, large negative thermal expansion is unlikely.

Open framework structures where the following restrictions are taken into account have the tendancy to result in negative thermal expansion materials [6, 9].

- the framework oxygen is coordinated to just two metal ions
- framework structure exhibits a topology which support low-energy transverse vibrational modes
- the angle of the M – O – M linkage is 180°
- transversal motion of the oxygen will pull the metal ions closer together
- the thermal expansion of the M – O bond can be neglected due to the high strength of this bond. (M = W^{6+}, V^{5+}, Si^{4+}…)
- No interstitial framework cations are present

2.5 Examples of Negative Thermal Expansion in framework structures

The two most common polyhedra building blocks in framework oxide structures are tetrahedra (MO_4) and octahedra (AO_6). If all polyhedra are corner-sharing with all oxygen atoms in two-fold coordination, the generic composition of a framework structure is $A_xM_yO_{3x+2y}$. A network consisting only of corner sharing octahedra will have AO_3 as formula whereas a pure tetrahedral composition will end up with the MO_2 formula. In the following paragraphs a number of these families are discussed with extra attention to their thermal expansion behaviour. In the following paragraph several families such as MO_2, AO_3, AMO_5, AM_2O_7, AM_2O_8, $A_2M_3O_{12}$ and CN bridged framework materials are described.

2.5.1 MO_2 family [19]

Among the family of MO_2 or $MO_{4/2}$ networks there is the group of framework silicates and aluminophosphates which consists of almost ideal $SiO_{4/2}$, $AlO_{4/2}$ or $PO_{4/2}$ tetrahedra connecting to each other by sharing corners. Most of these framework structures contain interstitial ions or molecules which have a significantly impact on the thermal expansion properties. Those which lack interstitial ions or molecules frequently show NTE behaviour.

RUM's are known to exist in the common crystalline forms of SiO_2: quartz, tridymite and cristobalite. Strong negative thermal expansion has been found for the pure SiO_2 zeolites, ITQ-1, SSZ-23, CIT-5 and ITQ-3 from 50 – 500 °C and above [20-24]. The tetrahedral framework structure of the siliceous zeolite CIT-5 can be seen in figure 10. The aluminophosphates ($AlPO_4$) are built from of alternating $AlO_{4/2}$ and $PO_{4/2}$ tetrahedra [25]. It has been shown that these materials have an unusual large negative linear thermal expansion coefficient (-11.7×10^{-6} °C^{-1}) over the temperature range -260 °C – 70 °C. The hexagonal crystal structure exhibits negative thermal expansion along the a- and c- axes.

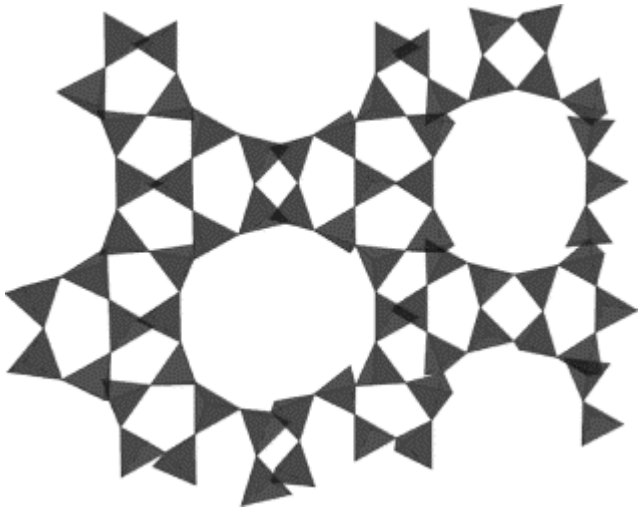

Figure 10: The structure of CIT-5 as corner sharing $SiO_{4/2}$ tetrahedra [16]

The unusual and useful thermal expansion properties of β-eucriptite ($LiAlSiO_4$) have been known for many years [26, 27]. On heating from room temperature the hexagonal a- and b-cell edges increase. However there is a pronounced contraction of the c-cell edge resulting in a very low volume expansion material. The framework structure can be compared with β-quartz where some of the Si^{4+} atoms are replaced by Al^{3+} atoms. Charge compensating Li^+ ions reside in the interstitial sites, resulting in a material with a high ionic conductivity.

2.5.2 AO_3 family [16, 28]

Several different network structures are known in this family. Thermal expansion has been studied in the cubic crystal structures. These cubic networks consist of corner-shared $MO_{6/2}$ octahedra. This model is easily illustrated with the cubic ReO_3 structure as is shown in figure 11. The Re – O – Re bond angles are 180°. Bending of these linkages results in a volume decrease of the entire unit cell. Other examples in this field are TaO_2F and NbO_2F. RUM's appear in these oxides resulting in "rocking motions" along each of the three axes resulting in a very low positive thermal expansion. The low value is caused by the combination of the transversal vibrations and the anharmonicity of the potential well of the Re – O bonds.

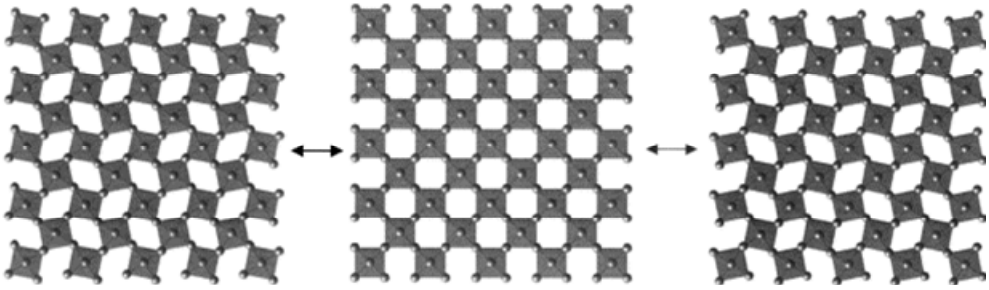

Figure 11: Rocking motions within the ReO_3 structure [28]

2.5.3 AMO_5 or $AOMO_4$ family [6, 16, 29, 30]

From the overall stochiometry two combinations are possible: two 5+ valency cations or one 4+ and one 6+ valency cation. So far only the first combination has been examined for thermal expansion. The A cations can be Nb, Ta, Mo or V. The screened M cations are P, V, As, S, Mo. They form a large family with corner-sharing tetrahedra and octahedra. Each $AO_{6/2}$ octahedron shares corners with four $MO_{4/2}$ tetrahedra and 2 other octahedra whereas the tetrahedron shares corners with four $MO_{6/2}$ octahedra.

The most famous member of this family is $NbOPO_4$ which is composed of NbO_6 octahedra and PO_4 tetrahedra. Three polymorphs of $NbOPO_4$ have been reported. It is interesting to see that the high temperature polymorphs show more explicit negative thermal expansion behaviour related to a higher symmetry.

The monoclinic ($P2_1/c$) polymorph transforms in the orthorhombic (Pnma) form at higher temperatures (figure 12) and both polymorphs show the same connectivity of the octahedra and tetrahedra throughout the transition. The length of the a-axis of the monoclinic phase will decrease with increasing temperature whereas in the orthorhombic polymorph a decrease of all axes is noticed.

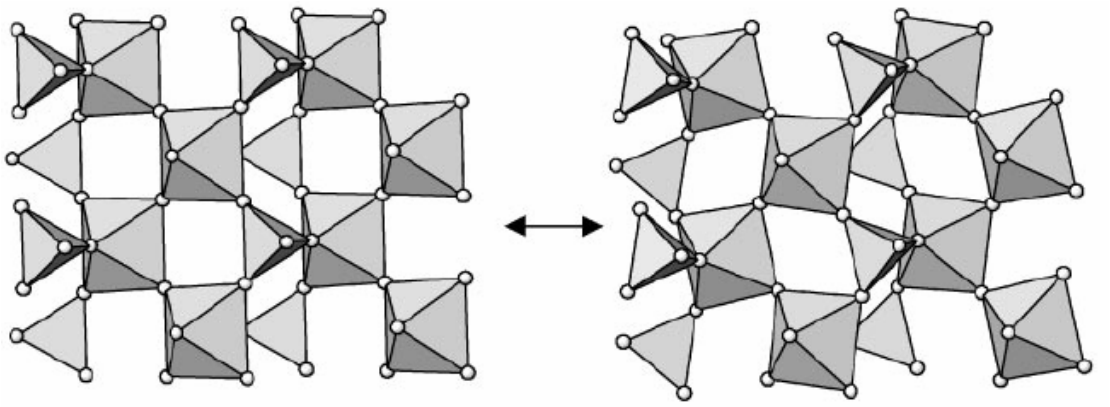

Figure 12: Orthorhombic, high T phase (left) and monoclinic, low T phase (right) [29]

The tetragonal polymorph undergoes a phase transition at about 200 °C. The low temperature phase (P4/n) is transformed in a high temperature (P4/nmm) phase. The c-cell edges show positive thermal expansion in both phases. The a- and b-cell edges show positive thermal expansion below the transition and negative thermal expansion after the transition. Both phases are given in figure 13.

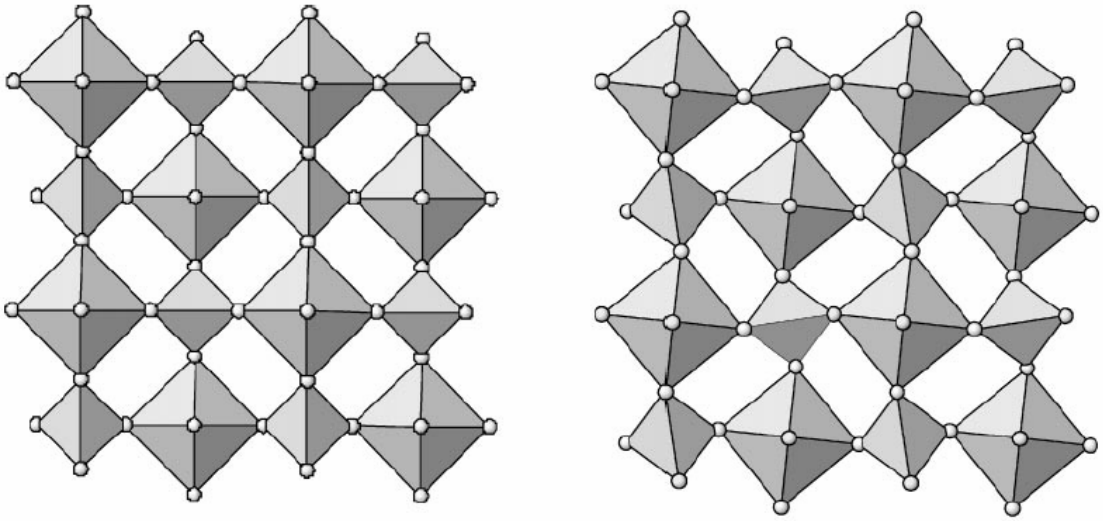

Figure 13: The high- (left) and low- (right) temperature phase of tetragonal $NbOPO_4$ [29]

2.5.4 AM_2O_7 and AM_2O_8 families [6, 19]

The AM_2O_7 phases (with A: Ti, Zr, Hf, Sn and M: P or V) are mostly cubic structures which display isotropic negative thermal expansion under specified conditions. The network structure is composed of AO_6 octahedra corner-sharing with M_2O_7 polyhedra. These can be seen as a combination of two tetrahedra sharing one oxygen atom. In figure 14 the thermal expansion behaviour of some members of the AM_2O_7 family is displayed. As can be seen from this figure, the tendency to exhibit negative thermal behaviour will increase as the unit cell edge increases. This can be understood as follows: RUM's can not occur in these materials as small changes in the polyhedra are necessary to allow these rotations. Therefore Quasi-RUM's are present in this family. As the polyhedra become larger, it is easier for them to change shape due to the decreased anion-anion distances within the polyhedra. The negative thermal expansion behaviour of AM_2O_7 materials is strongly dependent on the more facile rocking motions of the larger polyhedra. ZrV_2O_7, HfV_2O_7, ThP_2O_7 and UP_2O_7 show negative thermal expansion behaviour.

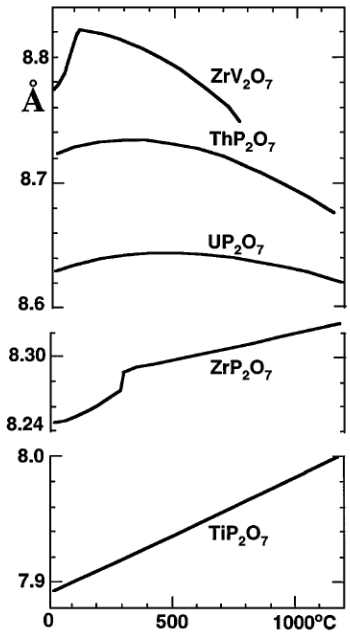

Figure 14: Thermal expansion for some cubic AM_2O_7 compounds [6]

Several members of the cubic AM_2O_7 family have a network collapse phase transition with decreasing temperature. Below this transition, the thermal expansion is positive and more normal. The structural changes through these transitions have been studied in detail for ZrV_2O_7 and ZrP_2O_7 [31-36]. At room temperature, both of these compounds have a 3 × 3 × 3 superstructure relative to their high-temperature structure as given in figure 15.

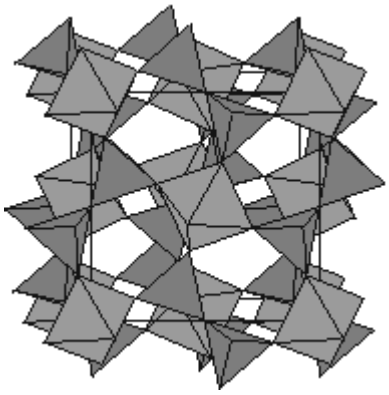

Figure 15: The high-temperature ideal cubic structure of ZrV_2O_7 [32]

These phase transitions can be seen in the diagram showing the cell parameter of ZrV_2O_7 versus temperature (figure 16). The cell edge at room temperature is 8.765 Å. The structure is a superstructure so the actual length of the a-axis is three times this size: 26.293 Å. As the temperature increases, the cell parameter value increases. At 70 °C however the material undergoes a phase transition resulting in an incommensurated structure with the following dimensions: ~3a × ~3a × ~3a. At 160 °C, a second phase transition occurs and induces a transformation of the superstructure to a simple cubic cell. This phase shows strong negative thermal expansion behaviour with $\alpha_l = -7.1 \times 10^{-6}$ °C^{-1} between 130 and 230 °C. Starting from room temperature one can say that the material will expand to its maximum volume, undergoes a phase transition and contracts by the transversal movements of the V – O – V bridging oxygen atoms in the framework structure.

The origin of the incommensurate intermediate phase is somewhat unclear. A possible explanation is that this phase is related with a low energy arrangement of the polyhedra within the ZrV_2O_7 structure. In the superstructure, there are 108 octahedra and 216 tetrahedra. There is more than one possibility to arrange these units in a way

that retains the framework topology and involves minimal polyhedral distortion. As the temperature rises, another arrangement can be more favourable and a phase transition will be induced.

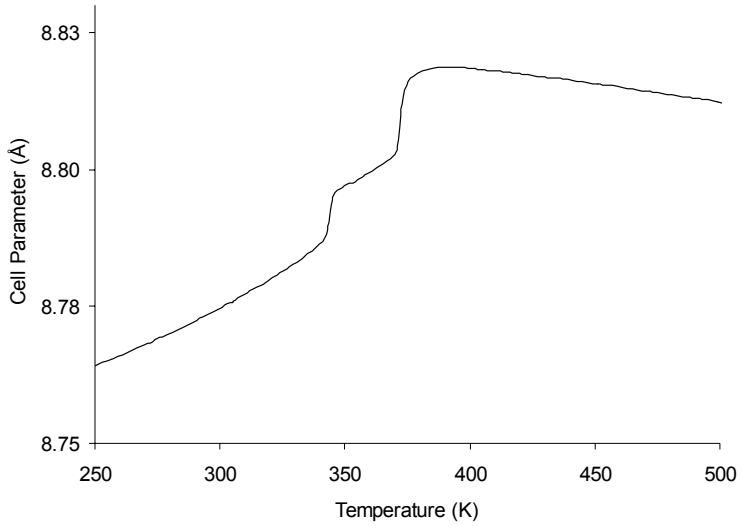

Figure 16: Thermal expansion curve of ZrV_2O_7 [37]

The thermal expansion properties of ZrP_2O_7 (figure 17) are somewhat similar. There is a phase transition at 300 °C inducing a transformation from a superstructure (Pbca) to a simple cubic structure.

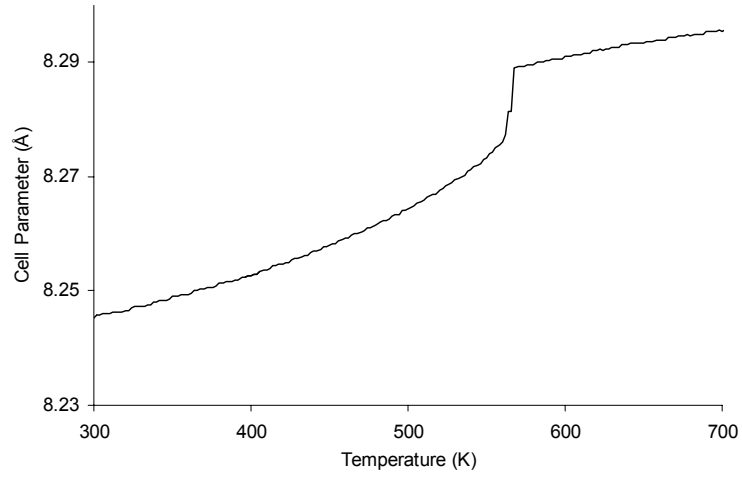

Figure 17: Thermal expansion of ZrP_2O_7 [35]

The thermal expansion coefficient of the latter is 5.4×10^{-6} °C^{-1} between 330 and 430 °C. In comparison with ZrV_2O_7 no negative thermal expansion is noticed after the

phase transition. This discrepancy lies in the angles between the M – O – M linkages. In the case of the pyrovanadates, the bond angle is 180 ° for 2 V – O – V linkages and the four others are free to bend away from 180 ° whereas for the pyrophoshate compounds an angle of 130 – 160 ° is measured and this will interfere with the Quasi-RUM's resulting in a very low positive thermal expansion.

The cubic structures of the AM_2O_8 family and the cubic ones of the AV_2O_7 family are closely related to each other as can be seen in figure 18. They both consist of AO_6 octahedra and MO_4 tetrahedra. In the case of ZrW_2O_8 these tetrahedra share 3 oxygen atoms with neighbouring octahedra and they end up with one free oxygen atom. In the AM_2O_7 family, the other oxygen atom is shared with a tetrahedron resulting in an intra-tetrahedral link. ZrW_2O_8 exhibits negative thermal expansion over its entire stability range to its decomposition temperature at 1260 °C. ZrW_2O_8 and other AM_2O_8 related structures will be discussed in §3.

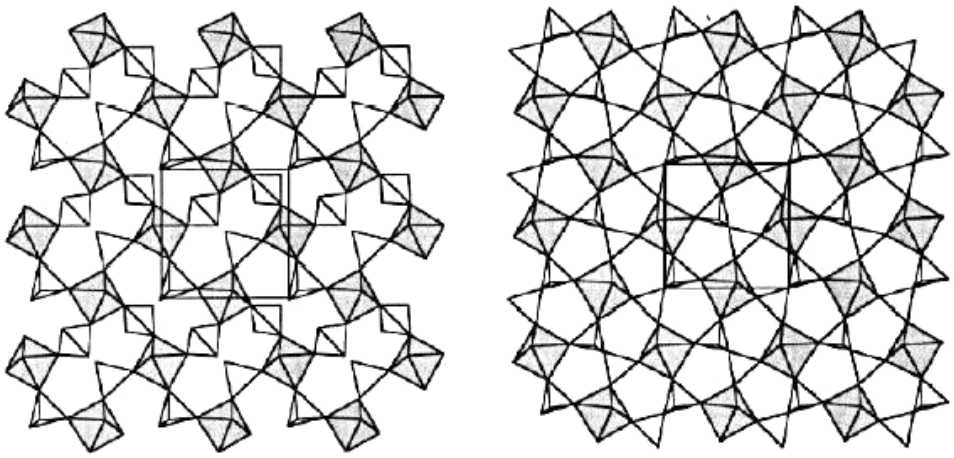

Figure 18: Crystal structure of ZrW_2O_8 (left) and ZrV_2O_7 (right) [38]

2.5.5 $A_2M_3O_{12}$ or $A_2(MO_4)_3$ family [6, 7, 9, 16, 19, 39]

This family of materials forms a network of corner-shared AO_6 octahedra and MO_4 tetraedra. There is a large variety of materials known which can be situated within this family. The A cation place can be taken in a trivalent cation with a radius size between Al^{3+} (0.672 Å) and Gd^{3+} (1.075 Å) such as Sc^{3+}, Y^{3+}, Fe^{3+}, Lu^{3+}, Dy^{3+}, Ho^{3+}, Tm^{3+}… The M cations are known by their 6+ valency and in most of the cases W^{6+} or Mo^{6+} can be found in these structures. Sometimes the trivalent cation is replaced by a

higher valency cation such as Zr^{4+} and Hf^{4+}. The M cation is then replaced by a lower valency cation to respect to neutrality of the compound: e.g. $Zr_2WP_2O_{12}$, $Hf_2WP_2O_{12}$., $Zr_2WMoP_2O_{12}$ and $Hf_2MoP_2O_{12}$.

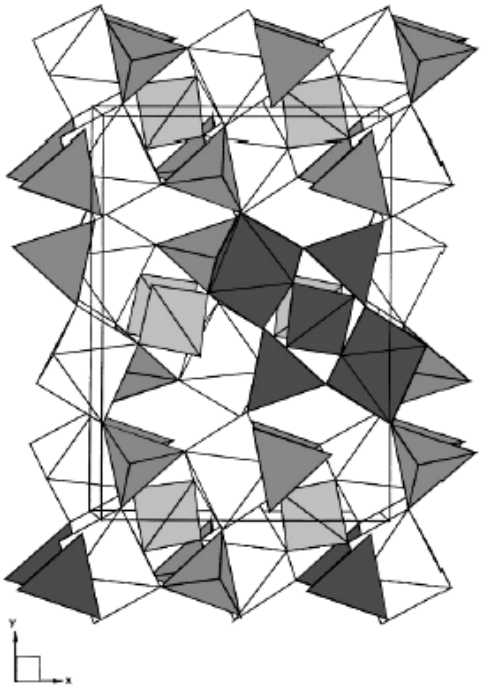

Figure 19: Open framework structure of $Sc_2(WO_4)_3$: orthorhombic phase [40]

The relatively open framework structure of $Sc_2(WO_4)_3$ is shown in figure 19. The orthorhombic crystal structure of this family of materials results in an anisotropic thermal expansion linked to the a-, b- and c-axis. A decrease in a- and c-parameters can be noticed whereas the b-parameters show normal thermal expansions. The magnitudes of these individual changes are such that an overall decrease of the cell volume is observed.

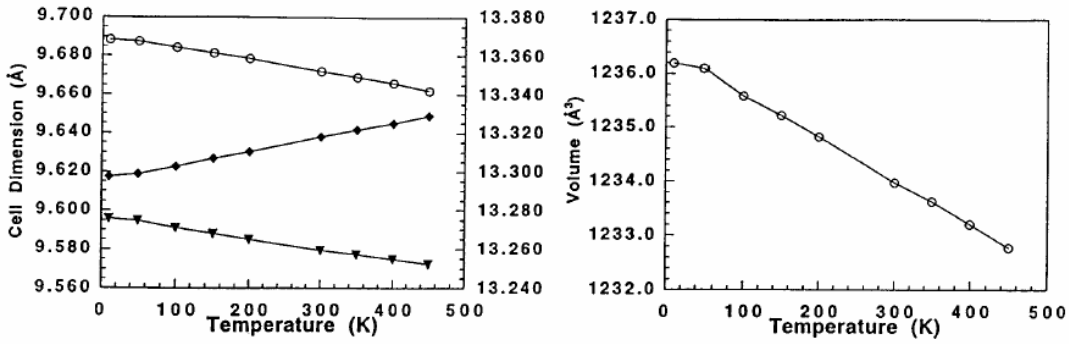

Figure 20: Thermal expansion of the cell parameters and the cell volume of $Sc_2(WO_4)_3$ [41]

Some members of the $Sc_2(WO_4)_3$ family undergo volume reducing phase transitions, also known as a network collapse transition, from the high temperature orthorhombic phase to a monoclinic structure at low temperature. The temperature of this transition varies from < -260 °C for $Sc_2(WO_4)_3$ till 1050 °C for $Fe_2(MoO_4)_3$. As an example the evolution of the cell volume of $Sc_2(MoO_4)_3$ as a function of temperature is shown in figure 21. On cooling down, a drastic cell volume decrease is noticed around -200 °C. The data for some other members of the $A_2M_3O_{12}$ are gathered in table 2.

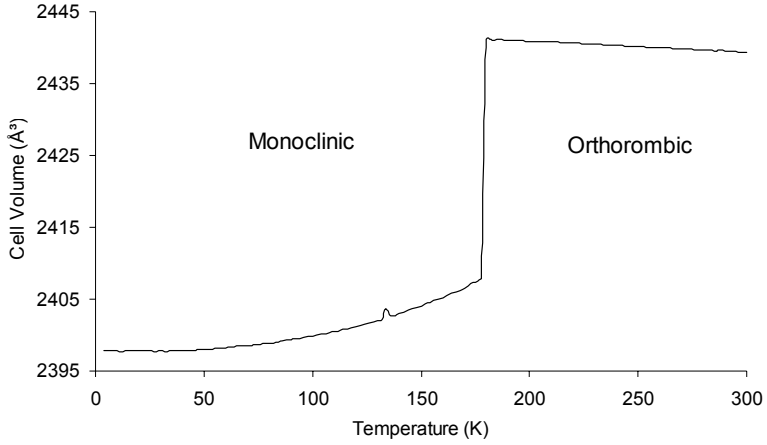

Figure 21: Temperature dependence of the cell volume of $Sc_2(Mo_4)_3$ [42]

Compound	Transition Temperature	α_l ($\times 10^{-6}$ °C^{-1}) After transition	References
$Sc_2(WO_4)_3$	Below -260 °C	-2.2	9, 40
$Sc_2(MoO_4)_3$	-100 °C	-1.72	9, 42, 43
$Fe_2(MoO_4)_3$	1050 °C		9
$Lu_2(WO_4)_3$	Below 100 °C	-6.8	6, 39
$Al_2(WO_4)_3$	Below RT	2.2	41, 44
$(HfMg)(WO_4)_3$	Below RT	-3.3	45
$Al_{2x}(HfMg)_{1-x}(WO_4)_3$	Below RT	-0.8	46
$Y_2(WO_4)_3$	Below -260 °C	-7	47-49
$Y_2Mo_4O_{15}$	Below 100 °C	7	50
$Dy_2Mo_4O_{15}$	Below 100 °C	5.75	50
$Ho_2Mo_4O_{15}$	Below 100 °C	11.4	50
$Tm_2Mo_4O_{15}$	Below 100 °C	5.4	50
$Zr_2P_2WO_{12}$	Below -260 °C	-3	9, 41

Table 2: Data of the AM_3O_{12} family

A possible cause of the network collapse is oxygen-oxygen attraction [41]. Such oxygen-oxygen attractive forces must be balanced against repulsive forces arising from the fact that oxygen is expected to have some negative charge in a metal oxide compound. The effective charge in a metal oxide compound will be directly related to the electronegativity of the cations present. As the electronegativity of the A cation rises the effective charge on oxygen decreases. The oxygen-oxygen repulsion decreases and the oxygen-oxygen attractive forces causes the network collapse transition to occur at higher temperatures as can be seen in figure 22. The electronegativity of W^{6+} is less than that of Mo^{6+} and hereby the phase transition of a $A_2(MoO_4)_3$ compound is always higher than the $A_2(WO_4)_3$ materials.

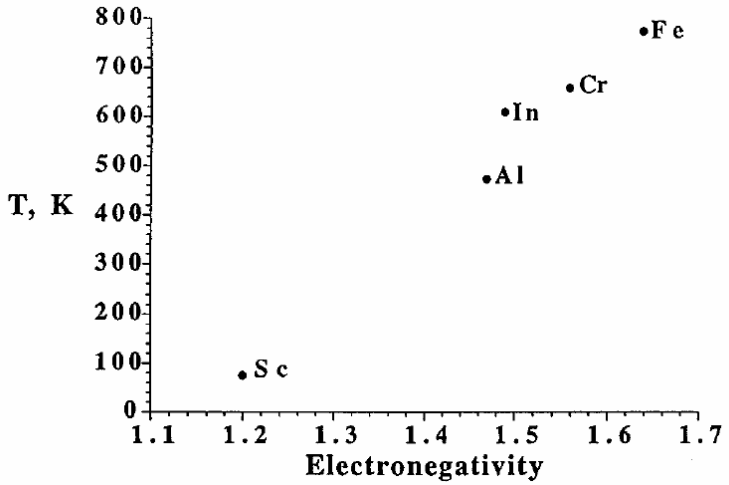

Figure 22: Structure collapse temperature plotted against electronegativity of A^{3+} [41]

The $A_2M_3O_{12}$ family well illustrates that strong negative thermal expansion behaviour can occurs without RUM's. Strong NTE behaviour has been observed for some members of the family after the network collapse transition and the transformation from the monoclinic phase to the orthorhombic crystal structure. Presumably vibrational modes are frozen out in the monoclinic phase and are released after the phase transition at higher temperatures. No classical RUM's can be identified but Quasi-RUM's are more likely in this family.

The NZP materials are also part of the AM_3O_{12} family [26, 51-54]. NZP's are based on $NaZr_2P_3O_{12}$ and a wide variety of adaptations can be made to the basic stochiometry by substitutions at all three non-oxygen sites. One of such series is $M_{0.5}Ti_2(PO_4)_3$ where M is a divalent cation such as Ca, Sr (SrTP), Ba or Pb. Closely related to this

series are $NaTi_2(PO_4)_3$ (NTP) and $La_{0.33}Ti_2(PO_4)_3$ (LaTP). Some NZP-type phoshates have the following stochiometry $PbM^{3+}M^{4+}P_3O_{12}$ with M^{3+} = Cr, Fe or In; M^{4+} = Ti, Zr, Hf or Sn. All types of combinations can be made such as $PbFeZrP_3O_{12}$, $Pb_{0.5}Mo_2P_3O_{12}$ and many more.

The crystal structure of the prototype composition $NaZr_2P_3O_{12}$ has a rhombohedral symmetry (R-3c) and the basic structure consists of a framework of corner-shared PO_4 tetrahedra and ZrO_6 octahedra which form chains along the c-axis. This polyhedral interconnection gives rise to interstitial sites with distinct geometries. In NZP itself, all the MI or trigonal anti-prismatic sites are filled with Na^+ ions whereas by suitable substitution at other sites the MI sites can be made partially or completely vacant as in the case of $Ca_{0.5}Zr_2(PO_4)_3$ (50% vacancy), $La_{0.33}Zr_2(PO_4)_3$ (67% vacancy) or $NbZr(PO_4)_3$ (100% vacancy). An example of the differences in site occupancy is given in figure 23. Occupancy by divalent cations lowers the symmetry to R-3 implying alternate ordering of cations and vacancies along the c-axis.

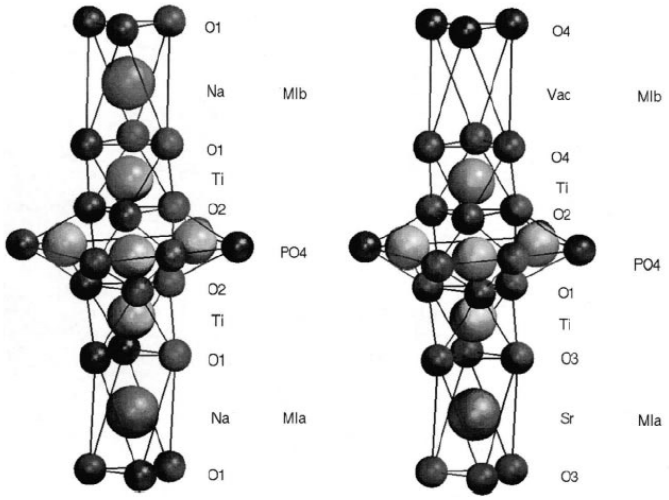

Figure 23: Site occupancy in NTP (left) and SrTP (right) crystal structures [51]

The substitution of the Na^+ ions has its effect on the thermal expansion of NZP-based materials. Pure NZP has an anisotropic thermal expansion with expansion along the c-axis and contraction along the a-axis whereas the divalent cations reverse the anisotropy resulting in an expansion along the a-axis and a contraction along the c-axis. Substitution will lead to a large variety of thermal expansion coefficients ranging from negative over low thermal expansion to positive values.

2.5.6 Cyanide-bridged framework materials [55-57]

The oxide-based framework materials are the most widely studied members of the negative thermal expansion materials. Nevertheless, anomalously large and negative thermal expansion has been reported for $Zn(CN)_2$, $Cd(CN)_2$, $Fe[Co(CN)_6]$. The crystal structure of $Zn(CN)_2$ is shown in Figure 24 and this material has a thermal expansion coefficient of - 16.9×10^{-6} °C^{-1} in the temperature range between -250 °C and 100 °C.

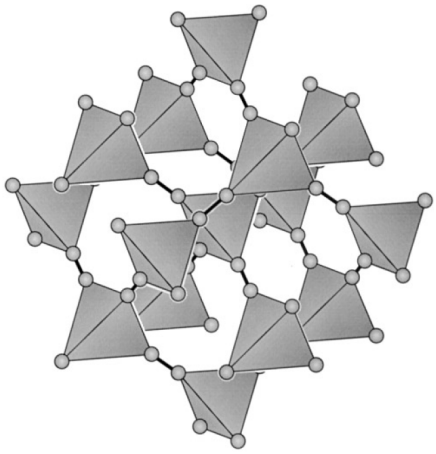

Figure 24: Crystal structure of $Zn(CN)_2$ [58]

These cyanide-bridged framework materials have cubic crystal structures containing rigid molecular polyhedra but the M – O – M linkages are now replaced by cyanide-metal bridges: M – (CN) – M. This linear M – (CN) – M linkages might give rise to a local NTE effect. Two transverse vibrational modes similar to the bending mode of the M – O – M bridges are possible and these are shown in. The first (a) involves displacement of the C and N atoms away from the M – M axis in the same direction, (b) shows the displacement in opposite directions. Both modes bring the anchoring metal atoms closer together.

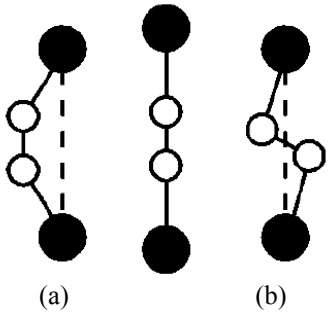

Figure 25: Representation of local vibration modes [56]

3 Isotropic negative thermal expansion behaviour in the AM_2O_8 – family

3.1 Introduction

As can be deduced from their molecular formulae, there is a strong relationship between the AM_2O_8 and the AM_2O_7 families. AM_2O_8 compounds consist of a network where each $MO_{4/2}$ tetrahedron shares three corners with surrounding $AO_{6/2}$ octahedra and has one free oxygen atom. The isotropic negative thermal expansion makes this family of materials very interesting. Most materials exhibiting negative thermal expansion exhibit anisotropic expansion. This phenomenon renders them very brittle and therefore not usable for technological applications. There are some other ceramic materials which show isotropic negative thermal expansion such as amorphous SiO_2, Cu_2O, ZrV_2O_7…[59]. In 1996 a highly unusual behaviour was observed for ZrW_2O_8 and HfW_2O_8. These compounds showed high isotropic negative thermal expansion over a large temperature range [60].

3.2 Strong isotropic negative thermal expansion in ZrW_2O_8

ZrW_2O_8 was first synthesized in 1959 by heating an encapsulated mixture of ZrO_2 and WO_3 at 1200 °C followed by a quenching step [61]. The obtained powders exhibit a cubic crystal structure which is unstable at room temperature [62]. According to a phase diagram of the ZrO_2 – WO_3 binary system published by Chang in 1967 and given in figure 26, ZrW_2O_8 is stable at temperatures ranging from 1105 till 1257 °C [63]. When the material is cooled down rapidly by immersion into liquid nitrogen, metastable ZrW_2O_8 at room temperature can be obtained. Increasing the temperature will decompose the material into its oxides ZrO_2 and WO_3 at 800 °C. In 1968 Martinek and Hummel revealed the negative thermal expansion behaviour in ZrW_2O_8 [64].

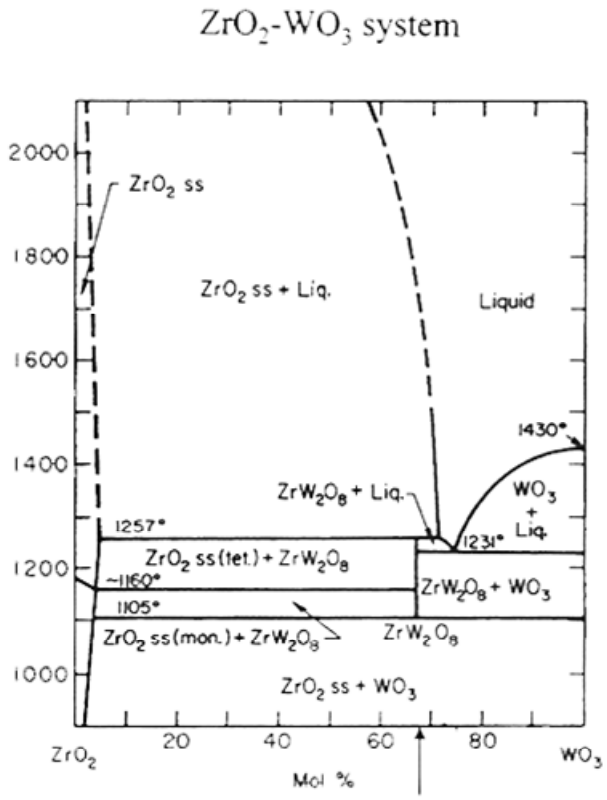

Figure 26: ZrO_2-WO_3 binary phase diagram [63]

In 1996 the material gained more interest when Evans, Mary and Sleight reported the isotropic negative thermal expansion of ZrW_2O_8 until the decomposition temperature at 777 °C [60]. The temperature dependence of the cell parameter of ZrW_2O_8 over its entire stability range is given in figure 27. The thermal expansion coefficient between -273 °C and 150 °C is -9.7×10^{-6} °C^{-1}. Around 150 – 170 °C, there is discontinuity in the measured cell parameter caused by an order-disorder transition. After this transition the negative thermal expansion behaviour of ZrW_2O_8 is maintained but the thermal expansion coefficient has a smaller absolute value.

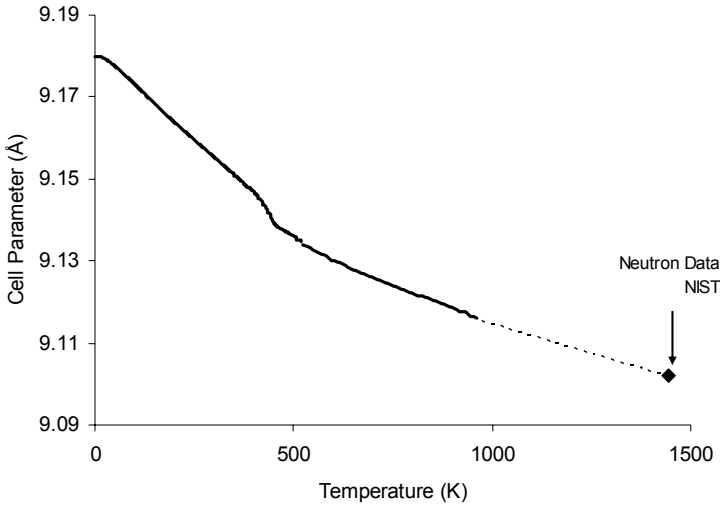

Figure 27: Thermal expansion behaviour of ZrW_2O_8. The dotted line is an extrapolation between the experimental data below 1000 K and the data collected at 1443 K [5]

3.2.1 Crystal structures of ZrW_2O_8 [60, 65-68]

Being part of the AM_2O_8 family, zirconium tungstate has ZrO_6 octahedra and WO_4 tetrahedra as building blocks. The tetrahedra are connected with three oxygen atoms to the octahedra with zirconium as central atom and each WO_4 unit has one free oxygen atom. The crystal structure of ZrW_2O_8 at room temperature can be seen in figure 28. The arrangement of the WO_4 groups is as such that pairs of tetrahedra lie along the main three-fold axis of the cubic unit cell with an asymmetric W···O – W bridge. This geometry results in one short W – $O_{terminal}$ bond (1.7 Å). The distance between this oxygen atom and the W of an adjacent tetrahedron is significantly longer (2.4 Å).

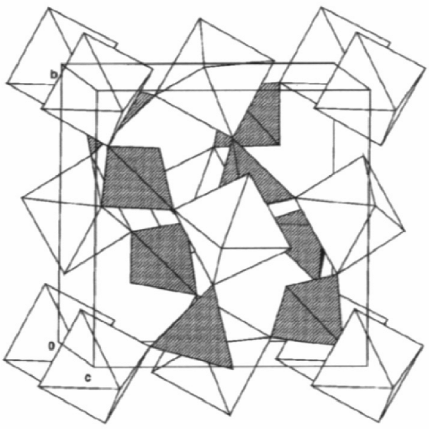

Figure 28: Crystal structure of α-ZrW_2O_8 [60]

Under ambient conditions zirconium tungstate (α-ZrW_2O_8) is a cubic compound with spacegroup $P2_13$. Zirconium tungstate maintains its negative thermal expansion over two phase transitions, one at ambient pressure and 160 °C to β-ZrW_2O_8 and the other at room temperature and pressures above 0.2 GPa to γ-ZrW_2O_8. β-ZrW_2O_8 has a cubic symmetry with Pa-3 as spacegroup whereas the γ-polymorph has an orthorhombic structure ($P2_12_12_1$). The crystallographic identity cards with the unit cell parameters of all three polymorphs are given in table 3. The fractional atomic coordinates are only mentioned for the alpha and beta phases.

α-ZrW_2O_8 $P2_13$	Atom	x/a	y/b	z/c
Cell parameters at 20 °C		a 9.1569(3)		
	Zr1	0.0004(3)	0.0004(3)	0.0004(3)
	W1	0.3409(3)	0.3409(3)	0.3409(3)
	W2	0.6009(3)	0.6009(3)	0.6009(3)
	O1	0.0529(3)	-0.2069(3)	-0.0619(4)
	O2	0.0697(4)	-0.0575(3)	0.2132(3)
	O3	0.4914(4)	0.4914(4)	0.4914(4)
	O4	0.2322(3)	0.2322(3)	0.2322(3)
β-ZrW_2O_8 Pa-3	Atom	x/a	y/b	z/c
Cell parameters at 210 °C		a 9.1371(5)		
	Zr1	0.0000(0)	0.0000(0)	0.0000(0)
	W1	0.3394(5)	0.3394(5)	0.3394(5)
	W2	0.6035(5)	0.6035(5)	0.6035(5)
	O1	0.0549(3)	-0.2089(2)	-0.0671(3)
	O3	0.5055(0)	0.5055(0)	0.5055(0)
	O4	0.2322(4)	0.2322(4)	0.2322(4)
γ-ZrW_2O_8 $P2_12_12_1$	Atom	x/a	y/b	z/c
Cell parameters at 20 °C		a 9.0608(2)	b 27.0141(6)	c 8.9191(2)

Table 3: Crystallographic identity cards of α-ZrW_2O_8 [60], β-ZrW_2O_8 [60] and γ-ZrW_2O_8

a. *α -β -phase transition* [5, 60, 67, 69, 70]

ZrW_2O_8 shows dynamic oxygen disorder at unusually low temperatures. This disorder is understood to be responsible for an order-disorder phase transition observed at 150 – 180 °C in which the space group symmetry changes from $P2_13$ to Pa-3. The transition is related with the orientation of the WO_4 tetrahedra along the three-fold axis. At room temperature these tetrahedra are ordered and all point in a definite direction. In the high temperature β-phase the direction in which the WO_4 tetrahedra point becomes dynamically disordered. The interaction between two WO_4 as mentioned above can be seen as a W_2O_8 unit. The α to β transition involves a formal inversion of the W_2O_8 groups.

Two mechanisms illustrated in figure 29 can be proposed for this inversion. On the left side, Figure 29(a) shows a "coupled S_N2" mechanism in which the formation of a W_1-O_3 bond leads to cleavage of the W_1-O_4 bond and a local inversion of tetrahedra. This process can occur in a cooperative way throughout the crystal or proceed via the local process as mentioned in equation 15.

$$4\ WO_4^{2-} \rightarrow W_2O_7^{2-} + W_2O_9^{6-} \qquad [15]$$

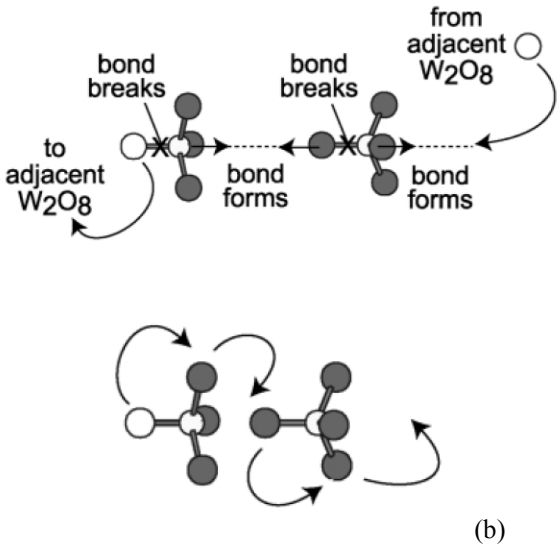

Figure 29: Schematic diagrams showing two possible mechanisms for oxygen exchange [69]

An alternative mechanism is mentioned in the figure 29(b). Adjacent tetrahedra could rotate as a whole in a "ratchet" motion causing mutual exchange between all oxygen sites. ^{17}O NMR is an ideal technique to study these two mechanisms as can be seen in figure 30. Peaks first broaden and then coalesce with rising temperature. The chemical shift of the single broad centre band peak at 229 °C tends towards the weighted mean of all those observed at low temperature (487 ppm). This indicates that all sites are involved in exchange at high temperature and that the mechanism involved in the order-disorder phase transition is most likely the "ratchet" motion. β-ZrW_2O_8 shows isotropic negative thermal expansion with $\alpha_l = -5 \times 10^{-6}$ °C^{-1}.

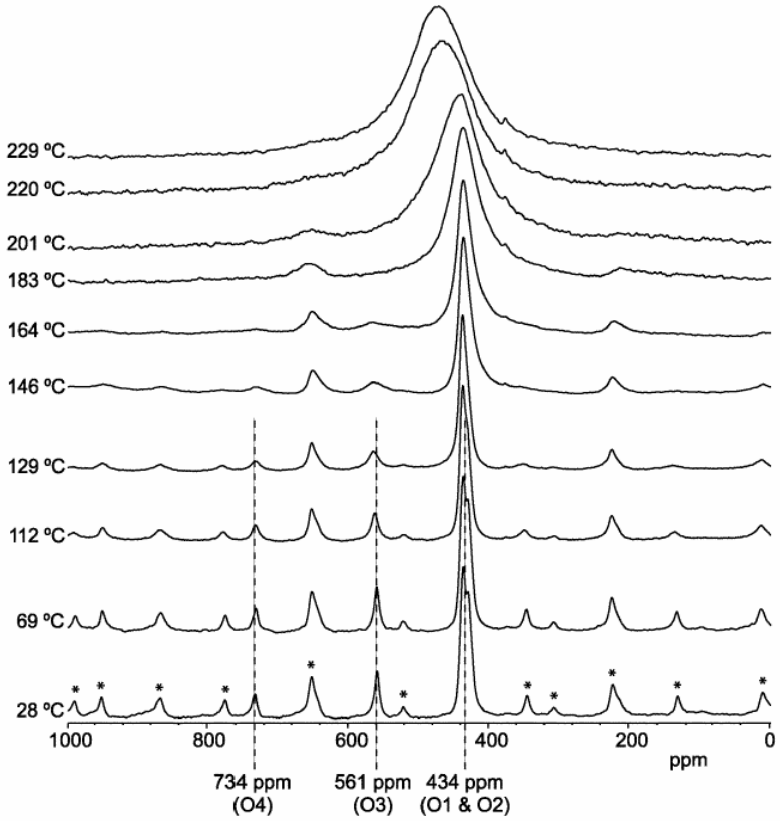

Figure 30: Variable temperature ^{17}O MAS spectra of ZrW_2O_8 [69]

b. *α - γ -phase transition* [71-78]

At room temperature, the cubic α-phase is stable below 0.21 GPa, above this pressure there is a first-order transition to the orthorhombic γ-phase. The orthorhombic phase is metastable after the release of pressure. At low temperature, its thermal expansion is also negative but an order of magnitude smaller than for the α-phase. Upon increasing temperature, the thermal expansion of the γ-phase passes through zero at -45 °C and is slightly positive at room temperature. Above room temperature (120 °C) the metastable γ-phase transforms back into the cubic α-phase. The orthorhombic unit cell is closely related to the cubic phase but with a tripled b-axis as can be seen in figure 31. The mechanism involved in the transition from α to γ is again related to migration of oxygen atoms in the lattice. The relative volume change at the α-γ-transition is -5%.

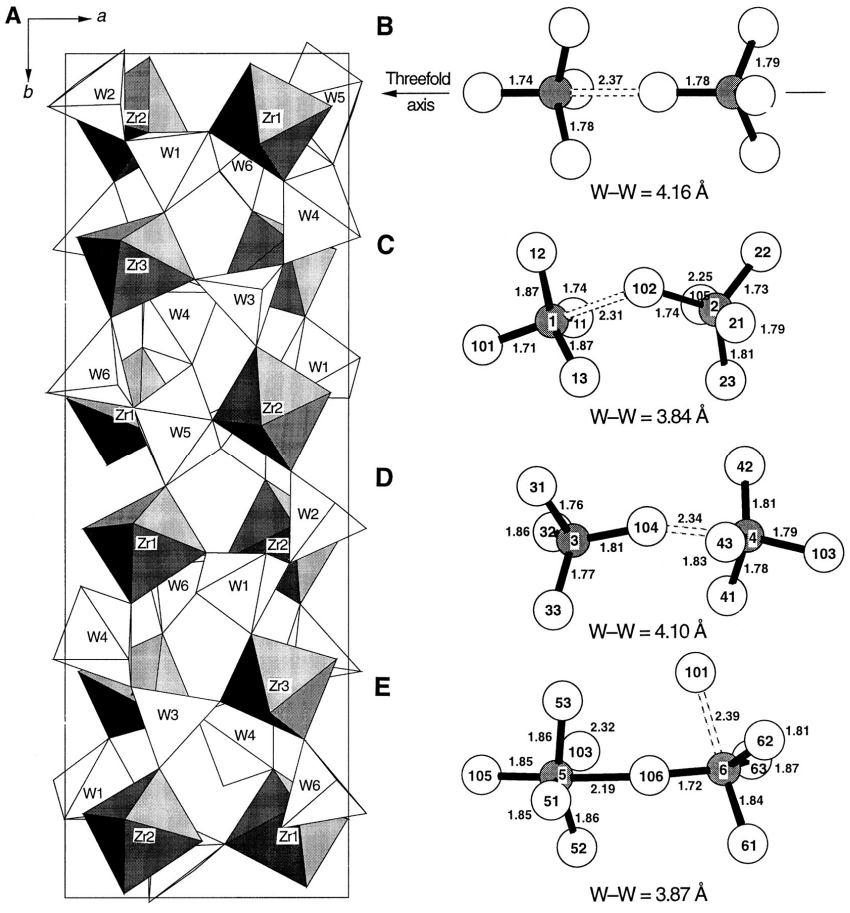

Figure 31: (A) Polyhedral representation of the structure of γ-ZrW_2O_8. (B) Schematic representation of the 2 WO_4 groups of α-ZrW_2O_8 viewed perpendicular to the threefold axis (C, D and E) Representations of the W coordination environments in γ-ZrW_2O_8 [71]

There are two reasons for this decrease. First, there is a significant decrease in the non-bonding W···O distance leading to an increase in the bonding nature of this interaction. Secondly, in α-ZrW_2O_8 the WO_4 groups are constrained by symmetry to lie on a threefold axis and thus their $W - O_{terminal}$ vectors are collinear. At the phase transition all threefold axes are destroyed and the W···O – W bond angles can deviate from 180°. Hereby a closer packing of the WO_4 groups is possible. The overall coordination of W(5) is increased from 4 to 6, that of O(103) from 1 to 2.

The increase of the average coordination numbers decreases the flexibility of the structure. Hereby the number of low-energy vibrational modes, which require minimal distortion of the polyhedra is markedly decreased. This reduction leads to a corresponding decrease in magnitude of the negative thermal expansion: $\alpha_l = -1 \times 10^{-6}\ °C^{-1}$ between -250 – 25 °C .

Upon further compression ZrW_2O_8 irreversibly amorphizes above 1.5 GPa. After release of the pressure and re-heating the sample, the material recrystallizes into cubic ZrW_2O_8. In-situ heating of cubic ZrW_2O_8 at high pressures leads towards new polymorphs which are quenchable at ambient conditions. One of them is a α-type U_3O_8-type in wich the Zr and W atoms are six-fold coordinated and statistically disordered [79] Amorphous ZrW_2O_8 has a positive thermal expansion as all low energy-modes responsible for negative thermal expansion behaviour in α-ZrW_2O_8 are to be frozen in the amorphous phase. A simple heat treatment could induce partially relaxation of the amorphous to the crystalline state and hereby the thermal expansion can be tuned [80].

3.2.2 Mechanisms behind the Negative Thermal Expansion

It was first suggested that a large transversal vibration of the oxygen atom in the middle of the W – O – Zr linkage, which requires corresponding rotations of the polyhedra, is the primary origin of negative thermal expansion in this material [60, 67]. The inherent flexibility of an ideal ZrW_2O_8 was modelled. It was found that this connectivity could support a cell reduction from 9.3 Å to 8.8 Å without distortions of the polyhedra (figure 32). Figure 33 shows the calculated effect on the cell parameter by libration of the rigid ZrO_6 octahedra.

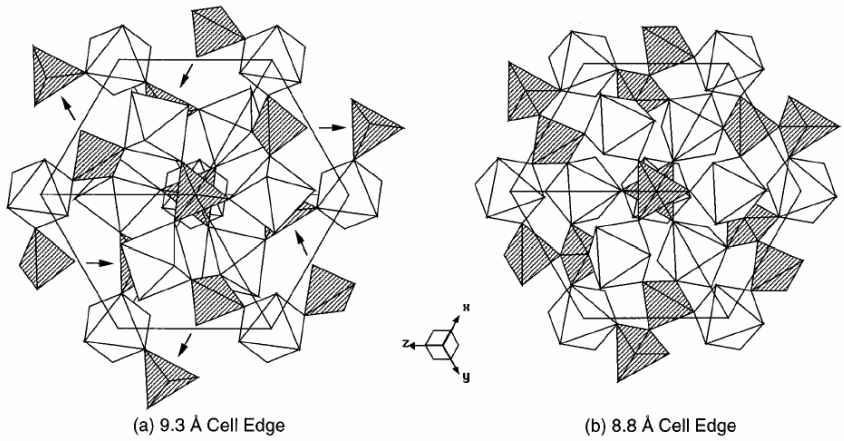

Figure 32: Polyhedral representation of idealized structures down [111]at (a) a cell edge of 9.3 Å and (b) at a cell edge of 8.3 Å [60]

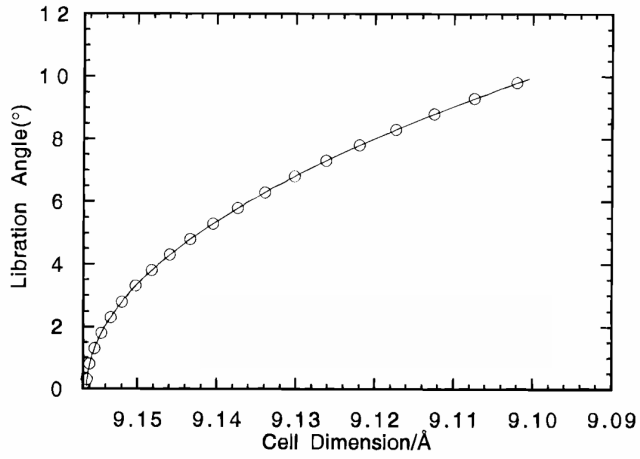

Figure 33: Tilt angle of ZrO_6 octahedra as a function of cell dimension [60]

The calculation of Rigid Unit Modes in these materials points out that RUM's are possible in ZrW_2O_8. The low-frequency rotations of the RUM's contribute mainly to the negative thermal expansion behaviour in ZrW_2O_8 [38]. The thermodynamics of this system have been investigated by several groups in the recent years. High pressure Raman studies [74, 75], inelastic neutron scattering [81], temperature dependence of the cell parameter [82, 83] and specific heat data [84] were used to find evidence for these low – frequency phonon modes [85-87]. As mentioned in §1.3, negative thermal expansion behaviour is related to negative Grüneisen parameters. Using the modes between 1.5 meV and 8.5 meV, the Grüneisen parameter was found to be large and negative and these modes are most relevant for the contraction of the material. Fitting of specific heat data indicates the large influence of the 3.3 meV optical phonons as can be seen in the insert in figure 34 using 2 Einstein modes (3.3 and 5.8 meV) and 2 Debye modes (with θ_D = 650 and 200 K). High-pressure Raman studies have indicated that modes much higher than 8 meV also contribute significantly to negative thermal expansion in ZrW_2O_8. The phonon density of states and observed Raman mode energies are compared in figure 34. Some of the phonons with energies above 8 meV have negative Grüneisen parameters and will exhibit negative thermal expansion behaviour.

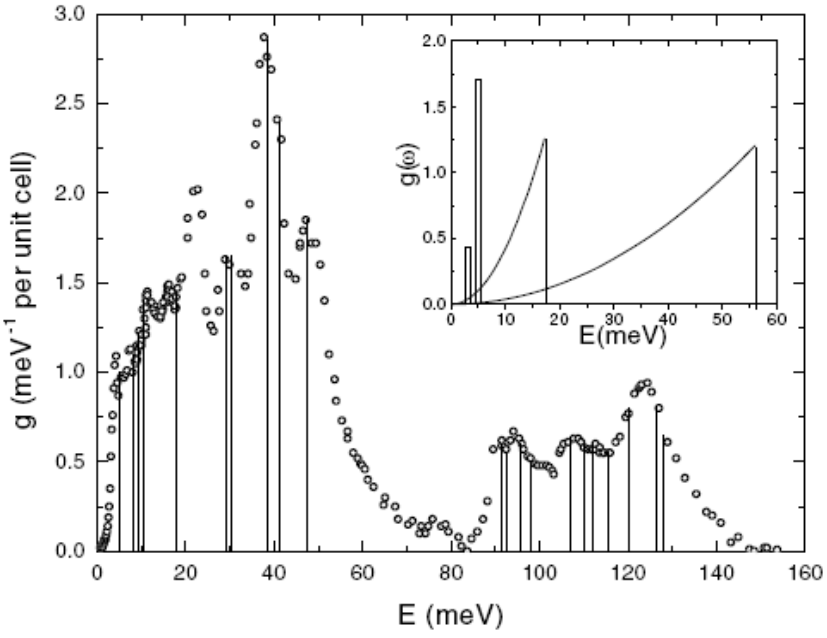

Figure 34: Comparison of phonon density of states g(E) and observed Raman mode energies. The inset shows the density of states fitted to the specific heat data [74]

The local structure of ZrW_2O_8 was studied by X-ray absorption fine structure experiments at the W L_{III} and Zr K-edge [88, 89]. These studies indicated that the stiffness of the Zr – O –W linkages makes it hard to believe that transversal vibrations of the middle oxygen atom in these linkages could induce such a strong negative thermal expansion. The author present a new mechanism based on the correlated motion of a WO_4 tetrahedron and its three nearest ZrO_6 octahedra. This mechanism is given in figure 35. As the tungsten atom moves up, the Zr atoms must move together to keep the W-Zr linkage rigid. This leads to a net lattice contraction.

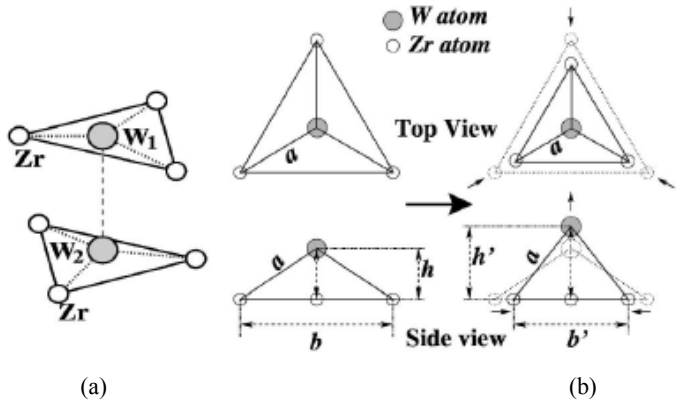

Figure 35: (a) simplified drawing of part of the structure which shows three nearest Zr atoms surrounding W(1) or W(2) atoms. (b) A rigid-tentpole model to show the constraint on the correlated motions between a W atom and it nearest Zr atoms [89]

Until this moment no new results have confirmed this mechanism. Good single crystal measurements of dispersion relation of phonons, providing sharp phonon lines, could help in identifying the nature of the soft phonons [90].

3.2.3 Substituted ZrW_2O_8 materials

The large negative thermal expansion in a broad temperature range was discussed in the previous sections. Substitution of the Zr(IV) or W(VI) site will strongly affect some properties of the material such as phase transition temperature, cell parameter, electrical characteristics and many more. The two substitution sites are individually discussed in the following parts.

a. Zr(IV) substituted materials

When substitutional solid solutions are to be formed, the ions that are replacing each other must be similar in size. For alloys the difference in radii of the metal ions is suggested to be smaller than 15%. For non-metallic systems a larger difference is allowed [91]. Another important issue is the charge neutrality of the materials; therefore it is more suitable to replace the zirconium ion by another 4+ valency ion.

In literature, the most discussed substituted material is HfW_2O_8 [60]. The Hf^{4+} ion obeys the two rules mentioned above: it has the same valency and an ionic radius in an octahedral coordination of 85 pm whereas the Zr^{4+} ion in the same surrounding has an ionic radius of 86 pm. Indeed hafnium tungstate exhibits the same remarkable negative thermal expansion properties as ZrW_2O_8. The α-phase (a = 0.913 nm at 20 °C) of the substituted material is isostructural with α-ZrW_2O_8 (a = 0.9157 nm at 20 °C). The cubic structure is composed of WO_4 tetrahedra and HfO_6 octahedra. The unusual thermal behaviour is induced by the transversal vibration of the Hf – O – W linkages. There are also a few differences between ZrW_2O_8 and HfW_2O_8. The first remarkable difference is the phase transition temperature. HfW_2O_8 shows an order-disorder transition at 190 °C whereas the phase transition temperature of ZrW_2O_8 is situated around 160 °C [92]. The increase in temperature is probably reflecting the stronger chemical bond of Hf – O in comparison to Zr – O.

Another difference is situated in the pressure-induced cubic-to-orthorhombic phase transformation [93-95]. Cubic ZrW_2O_8 only exists over a 0 – 0.21 GPa pressure range. High pressure Raman data indicate that the α - γ transition in HfW_2O_8 occurs at 0.6 – 0.9 GPa. The difference in bond strength is again of key importance.

Not only 4+ valency ions have been examined, some trivalent ions are also used to prepare substituted ZrW_2O_8 materials [96-100]. The ions used are mentioned in Table 4. The cell parameters and phase transition temperatures given are the result of a 4% substitution. The ionic radii of the substituents are larger than Zr^{4+}. Nevertheless an overall decrease in cell parameter can be noticed. It is suggested that the oxygen defect due to the difference in valency is the main reason for this decrease. The phase transition temperature is also affected by the substitution.

material	ionic radius (pm)	cell parameter (nm) [96, 98, 100]	phase transition temperature (°C)
ZrW_2O_8	86	0.9175	150-160
$Zr_{1-x}Y_xW_2O_{8-y}$	104	0.9170	130
$Zr_{1-x}In_xW_2O_{8-y}$	94	0.9165	110
$Zr_{1-x}Sc_xW_2O_{8-y}$	88.4	0.9150	90
$Zr_{1-x}Lu_xW_2O_{8-y}$	98	0.9165	100

Table 4: Data of the A^{3+} ZrW_2O_8 materials

b. W(VI) substituted materials

Besides the possibility of changing the occupancy of Zr site, the tungsten ion can also be replaced by an ion similar in valence state and ionic radius. The most studied substituted material is $ZrMo_2O_8$. The Mo(VI) ion in tetrahedral coordination has an ionic radius of 41 pm whereas a W(VI) ion in the same surrounding shows an ionic radius of 42 pm. Cubic γ-$ZrMo_2O_8$ is isostructural with β-ZrW_2O_8 and belongs to the family of materials with negative thermal expansion with $\alpha = -5 \times 10^{-6}$ °C^{-1} between -262 and 300 °C [101-103]. No phase transitions are observed in $ZrMo_2O_8$ in this specific temperature range. Recently, it has been shown that it is possible to prepare $ZrW_{2-x}Mo_xO_8$ phases over the entire composition range $0 \leq x \leq 2$ [104-106]. The phase transition temperature shifts to lower values as the amount of Mo present in the material increases. For example, the phase transition of $ZrMoWO_8$ is situated at -3 °C [107]. The oxygen migration related to this transition occurs at lower temperatures in comparison with ZrW_2O_8.

In comparison to α-ZrW_2O_8, cubic $ZrMo_2O_8$ behaves differently under pressure [108-111]. When compressed hydrostatically, γ-$ZrMo_2O_8$ transforms above 0.7 GPa to an undetermined monoclinic ϕ phase. Under non-hydrostatic conditions, cubic $ZrMo_2O_8$ amorphizes above 0.3 GPa and is transformed into the ϕ phase during heating at high pressures. There are two other known ambient pressure polymorphs of $ZrMo_2O_8$: trigonal and monoclinic. When the γ-$ZrMo_2O_8$ phase is submitted to pressures above 4 GPa, the recovered crystalline phases are ZrO_2 – MoO_3 decomposition products. The complete reversibility and higher onset pressure of γ - ϕ - transition might be advantageous for application in composites.

3.3 Application of ZrW_2O_8 materials [7, 112-114]

Isotropic negative thermal expansion materials have a wide variety of applications. Their use in composites together with the possibility to tailor the thermal expansion to a specific value by the combination of a NTE material with a positive thermal expansion material is most promising. It may resulting a whole range of new materials with a thermal expansion going on from negative over zero to positive values by adjusting the volume fraction of the components. Such a new material with controlled thermal expansion could be used in electronic devices, optical mirrors, dental fillings, fibre optic systems or in thermal packages for fibre Bragg gratings. In fibre optics, it can be used to reduce the variation in reflected wavelength due to the temperature variation of the refractive index and the thermal expansion of the fibre. The state of the art of ZrW_2O_8 composites is given in Chapter 6-§2. Amorphous ZrW_2O_8 is suggested as oxide ion conducting glass due to its high ZrO_2 content [115].

4 References

1. R.E. Taylor, *Thermal expansion of solids*, in *Data series on material properties*, Y. Ho, Editor. 1998, ASM International: Ohio.

2. W.D. Callister, *Materials Science and Engineering: An Introduction*, W. Anderson, Editor. 2000, Wiley & Sons: Danvers. p. 661-664.

3. G.K. White, *Solids - Thermal-Expansion and Contraction.* Contemporary Physics, 1993. **34**: 193-204.

4. E. Grüneisen, *Handbuch der Physik*, ed. H. Geiger and K. Scheel. Vol. 10. 1926, Berlin: Springer. 1-52.

5. J.S.O. Evans, *Negative thermal expansion materials.* Journal of the Chemical Society-Dalton Transactions, 1999: 3317-3326.

6. A.W. Sleight, *Compounds that contract on heating.* Inorganic Chemistry, 1998. **37**: 2854-2860.

7. A.W. Sleight, *Negative thermal expansion materials.* Current Opinion in Solid State & Materials Science, 1998. **3**: 128-131.

8. L. Pauling, *The principles determining the structure of complex ionic crystals.* Journal of the American Chemical Society, 1929. **51**: 1010.

9. J.S.O. Evans, T.A. Mary, and A.W. Sleight, *Negative thermal expansion materials.* Physica B, 1997. **241**: 311-316.

10. R.W. Cahn, *Materials science - The how and why of thermal contraction.* Nature, 1997. **386**: 22-23.

11. A. Sleight, *Materials science - Zero-expansion plan.* Nature, 2003. **425**: 674-676.

12. J.R. Salvador, F. Gu, T. Hogan, and M.G. Kanatzidis, *Zero thermal expansion in YbGaGe due to an electronic valence transition.* Nature, 2003. **425**: 702-705.

13. M. van Schilfgaarde, I.A. Abrikosov, and B. Johansson, *Origin of the Invar effect in iron-nickel alloys.* Nature, 1999. **400**: 46-49.

14. J. Arvanitidis, K. Papagelis, S. Margadonna, and K. Prassides, *Lattice collapse in mixed-valence samarium fulleride $Sm_{2.75}C_{60}$ at high pressure.* Dalton Transactions, 2004: 3144-3146.

15. J. Arvanitidis, K. Papagelis, S. Margadonna, K. Prassides, and A.N. Fitch, *Temperature-induced valence transition and associated lattice collapse in samarium fulleride.* Nature, 2003. **425**: 599-602.

16. J.Z. Tao and A.W. Sleight, *The role of rigid unit modes in negative thermal expansion.* Journal of Solid State Chemistry, 2003. **173**: 442-448.

17. V. Heine, P.R.L. Welche, and M.T. Dove, *Geometrical origin and theory of negative thermal expansion in framework structures.* Journal of the American Ceramic Society, 1999. **82**: 1793-1802.

18. M.T. Dove, M. Gambhir, K.D. Hammonds, V. Heine, and A.K.A. Pryde, *Distortions of framework structures.* Phase Transitions, 1996. **58**: 121-143.

19. G.D. Barrera, J.A.O. Bruno, T.H.K. Barron, and N.L. Allan, *Negative thermal expansion.* Journal of Physics-Condensed Matter, 2005. **17**: R217-R252.

20. M.P. Attfield and A.W. Sleight, *Strong negative thermal expansion in siliceous faujasite.* Chemical Communications, 1998: 601-602.

21. P. Lightfoot, D.A. Woodcock, M.J. Maple, L.A. Villaescusa, and P.A. Wright, *The widespread occurrence of negative thermal expansion in zeolites.* Journal of Materials Chemistry, 2001. **11**: 212-216.

22. D.A. Woodcock, P. Lightfoot, P.A. Wright, L.A. Villaescusa, M.J. Diaz-Cabanas, and M.A. Camblor, *Strong negative thermal expansion in the siliceous zeolites ITQ-1, ITQ-3 and SSZ-23.* Journal of Materials Chemistry, 1999. **9**: 349-351.

23. M. Gambhir, M.T. Dove, and V. Heine, *Rigid unit modes and dynamic disorder: SiO_2 cristobalite and quartz.* Physics and Chemistry of Minerals, 1999. **26**: 484-495.

24. P.R.L. Welche, V. Heine, and M.T. Dove, *Negative thermal expansion in beta-quartz.* Physics and Chemistry of Minerals, 1998. **26**: 63-77.

25. M.P. Attfield and A.W. Sleight, *Exceptional negative thermal expansion in $AlPO_4$-17.* Chemistry of Materials, 1998. **10**: 2013-2019.

26. N. Khosrovani and A.W. Sleight, *Strong anisotropic thermal expansion in oxides.* International Journal of Inorganic Materials, 1999. **1**: 3-10.

27. H.W. Xu, P.J. Heaney, D.M. Yates, R.B. Von Dreele, and M.A. Bourke, *Structural mechanisms underlying near-zero thermal expansion in beta-eucryptite: A combined synchrotron x-ray and neutron Rietveld analysis.* Journal of Materials Research, 1999. **14**: 3138-3151.

28. J.Z. Tao and A.W. Sleight, *Very low thermal expansion in TaO_2F.* Journal of Solid State Chemistry, 2003. **173**: 45-48.

29. T.G. Amos and A.W. Sleight, *Negative thermal expansion in orthorhombic $NbOPO_4$.* Journal of Solid State Chemistry, 2001. **160**: 230-238.

30. T.G. Amos, A. Yokochi, and A.W. Sleight, *Phase transition and negative thermal expansion in tetragonal $NbOPO_4$.* Journal of Solid State Chemistry, 1998. **141**: 303-307.

31. D.K. Seo and M.H. Whangbo, *Symmetric stretching vibrations of two-coordinate oxygen bridges as a cause for negative thermal expansion in $ZrV_xP_{2-x}O_7$ and AW_2O_8 (A=Zr, Hf) at high temperature.* Journal of Solid State Chemistry, 1997. **129**: 160-163.

32. I.J. King, F. Fayon, D. Massiot, R.K. Harris, and J.S.O. Evans, *A space group assignment of ZrP_2O_7 obtained by P^{31} solid state NMR.* Chemical Communications, 2001: 1766-1767.

33. K. Khosrovani, A.W. Sleight, and T. Vogt, *Structure of ZrV_2O_7 from -263 to 470 degrees C.* Journal of Solid State Chemistry, 1997. **132**: 355-360.

34. J.S.O. Evans, J.C. Hanson, and A.W. Sleight, *Room-temperature superstructure of ZrV_2O_7.* Acta Crystallographica Section B-Structural Science, 1998. **54**: 705-713.

35. R.L. Withers, Y. Tabira, J.S.O. Evans, I.J. King, and A.W. Sleight, *A new three-dimensional incommensurately modulated cubic phase (in ZrP_2O_7) and its symmetry characterization via temperature-dependent electron diffraction.* Journal of Solid State Chemistry, 2001. **157**: 186-192.

36. T. Hisashige, T. Yamaguchi, T. Tsuji, and Y. Yamamura, *Phase transition of $Zr_{1-x}Hf_xV_2O_7$ solid solutions having negative thermal expansion.* Journal of the Ceramic Society of Japan, 2006. **114**: 607-611.

37. R.L. Withers, J.S.O. Evans, J. Hanson, and A.W. Sleight, *An in situ temperature-dependent electron and x-ray diffraction study of structural phase transitions in ZrV_2O_7.* Journal of Solid State Chemistry, 1998. **137**: 161-167.

38. A.K.A. Pryde, K.D. Hammonds, M.T. Dove, V. Heine, J.D. Gale, and M.C. Warren, *Origin of the negative thermal expansion in ZrW_2O_8 and ZrV_2O_7.* Journal of Physics-Condensed Matter, 1996. **8**: 10973-10982.

39. P.M. Forster, A. Yokochi, and A.W. Sleight, *Enhanced negative thermal expansion in $Lu_2W_3O_{12}$.* Journal of Solid State Chemistry, 1998. **140**: 157-158.

40. J.S.O. Evans, T.A. Mary, and A.W. Sleight, *Negative thermal expansion in $Sc_2(WO_4)_3$.* Journal of Solid State Chemistry, 1998. **137**: 148-160.

41. J.S.O. Evans, T.A. Mary, and A.W. Sleight, *Negative thermal expansion in a large molybdate and tungstate family.* Journal of Solid State Chemistry, 1997. **133**: 580-583.

42. J.S.O. Evans and T.A. Mary, *Structural phase transitions and negative thermal expansion in $Sc_2(MoO_4)_3$.* International Journal of Inorganic Materials, 2000. **2**: 143-151.

43. W. Paraguassu, M. Maczka, A.G. Souza, P.T.C. Freire, J. Mendes, F.E.A. Melo, L. Macalik, L. Gerward, J.S. Olsen, A. Waskowska, and J. Hanuza, *Pressure-induced structural transformations in the molybdate $Sc_2(MoO_4)_3$.* Physical Review B, 2004. **69**.

44. N. Imanaka, M. Hiraiwa, G. Adachi, H. Dabkowska, and A. Dabkowski, *Thermal contraction behavior in $Al_2(WO_4)_3$ single crystal.* Journal of Crystal Growth, 2000. **220**: 176-179.

45. T. Suzuki and A. Omote, *Negative thermal expansion in $(HfMg)(WO_4)_{(3)}$.* Journal of the American Ceramic Society, 2004. **87**: 1365-1367.

46. T. Suzuki and A. Omote, *Zero thermal expansion in $(Al_{2x}(HfMg)_{(1-x)})(WO_4)_3$.* Journal of the American Ceramic Society, 2006. **89**: 691-693.

47. D.A. Woodcock, P. Lightfoot, and C. Ritter, *Negative thermal expansion in $Y_2(WO_4)_3$.* Journal of Solid State Chemistry, 2000. **149**: 92-98.

48. S. Sumithra and A.M. Umarji, *Hygroscopicity and bulk thermal expansion $Y_2W_3O_{12}$.* Materials Research Bulletin, 2005. **40**: 167-176.

49. P.M. Forster and A.W. Sleight, *Negative thermal expansion in $Y_2W_3O_{12}$.* International Journal of Inorganic Materials, 1999. **1**: 123-127.

50. L. Sebastian, S. Sumithra, J. Manjanna, A.M. Umarji, and J. Gopalakrishnan, *Anomalous thermal expansion behaviour of $Ln_2Mo_4O_{15}$ (Ln = Y, Dy, Ho, Tm).* Materials Science and Engineering B-Solid State Materials for Advanced Technology, 2003. **103**: 289-296.

51. P. Lightfoot, D.A. Woodcock, J.D. Jorgensen, and S. Short, *Low thermal expansion materials: a comparison of the structural behaviour of $La_{0.33}Ti_2(PO_4)_3$, $Sr_{0.5}Ti_2(PO_4)_3$ and $NaTi_2(PO_4)_3$.* International Journal of Inorganic Materials, 1999. **1**: 53-60.

52. D.A. Woodcock and P. Lightfoot, *Comparison of the structural behaviour of the low thermal expansion NZP phases $MTi_2(PO_4)_3$ (M=Li, Na, K).* Journal of Materials Chemistry, 1999. **9**: 2907-2911.

53. D.A. Woodcock, P. Lightfoot, and C. Ritter, *Mechanism of low thermal expansion in the cation-ordered Nasicon structure.* Chemical Communications, 1998: 107-108.

54. G. Buvaneswari and U.V. Varadaraju, *Synthesis of new network phosphates with NZP structure.* Journal of Solid State Chemistry, 1999. **145**: 227-234.

55. K.W. Chapman, M. Hagen, C.J. Kepert, and P. Manuel, *Low energy phonons in the NTE compounds $Zn(CN)_2$ and $ZnPt(CN)_6$.* Physica B-Condensed Matter, 2006. **385**: 60-62.

56. A.L. Goodwin and C.J. Kepert, *Negative thermal expansion and low-frequency modes in cyanide-bridged framework materials.* Physical Review B, 2005. **71**.

57. S. Margadonna, K. Prassides, and A.N. Fitch, *Zero thermal expansion in a Prussian blue analogue.* Journal of the American Chemical Society, 2004. **126**: 15390-15391.

58. D.J. Williams, D.E. Partin, F.J. Lincoln, J. Kouvetakis, and M. O'Keeffe, *The disordered crystal structures of $Zn(CN)_2$ and $Ga(CN)_3$.* Journal of Solid State Chemistry, 1997. **134**: 164-169.

59. A.W. Sleight, *Isotropic negative thermal expansion.* Annual Review of Materials Science, 1998. **28**: 29-43.

60. J.S.O. Evans, T.A. Mary, T. Vogt, M.A. Subramanian, and A.W. Sleight, *Negative thermal expansion in ZrW_2O_8 and HfW_2O_8.* Chemistry of Materials, 1996. **8**: 2809-2823.

61. J. Graham, A.D. Wadsley, J.H. Weymouth, and L.S. Williams, *A new ternary oxide, ZrW_2O_8.* Journal of the American Ceramic Society, 1959. **42**: 570.

62. S. Nishiyama, T. Hayashi, and T. Hattori, *Synthesis of ZrW_2O_8 by quick cooling and measurement of negative thermal expansion of the sintered bodies.* Journal of Alloys and Compounds, 2006. **417**: 187-189.

63. L.L.Y. Chang, *Condensed phase relations in the systems ZrO_2-WO_2-WO_3 and HfO_2-WO_2-WO_3.* Journal of the American Ceramic Society, 1967. **44**: 211-215.

64. C. Martinek and F.A. Hummel, *Linear Thermal Expansion of Three Tungstates.* Journal of the American Ceramic Society, 1968. **51**: 227-228.

65. C.A. Perottoni, J.E. Zorzi, and J.A.H. da Jornada, *Entropy increase in the amorphous-to-crystalline phase transition in zirconium tungstate.* Solid State Communications, 2005. **134**: 319-322.

66. J.S.O. Evans, W.I.F. David, and A.W. Sleight, *Structural investigation of the negative-thermal-expansion material ZrW_2O_8.* Acta Crystallographica Section B-Structural Science, 1999. **55**: 333-340.

67. T.A. Mary, J.S.O. Evans, T. Vogt, and A.W. Sleight, *Negative thermal expansion from 0.3 to 1050 Kelvin in ZrW_2O_8.* Science, 1996. **272**: 90-92.

68. J.M. Gallardo-Amores, U. Amador, E. Moran, and M.A. Alario-Franco, *XRD study of ZrW_2O_8 versus temperature and pressure.* International Journal of Inorganic Materials, 2000. **2**: 123-129.

69. M.R. Hampson, P. Hodgkinson, J.S.O. Evans, R.K. Harris, I.J. King, S. Allen, and F. Fayon, *The nature of oxygen exchange in ZrW_2O_8 revealed by two-dimensional solid-state O-17 NMR.* Chemical Communications, 2004: 392-393.

70. M.R. Hampson, S. Allen, I.J. King, C.J. Crossland, P. Hodgkinson, R.K. Harris, F. Fayon, and J.S.O. Evans, *Synthesis and NMR studies of O-17 enriched $AM_{(2)}O_{(8)}$ phases.* Solid State Sciences, 2005. **7**: 819-826.

71. J.S.O. Evans, Z. Hu, J.D. Jorgensen, D.N. Argyriou, S. Short, and A.W. Sleight, *Compressibility, phase transitions, and oxygen migration in zirconium tungstate, ZrW_2O_8.* Science, 1997. **275**: 61-65.

72. J.S.O. Evans, J.D. Jorgensen, S. Short, W.I.F. David, R.M. Ibberson, and A.W. Sleight, *Thermal expansion in the orthorhombic gamma phase of ZrW_2O_8.* Physical Review B, 1999. **60**: 14643-14648.

73. J.D. Jorgensen, Z. Hu, S. Teslic, D.N. Argyriou, S. Short, J.S.O. Evans, and A.W. Sleight, *Pressure-induced cubic-to-orthorhombic phase transition in ZrW_2O_8.* Physical Review B, 1999. **59**: 215-225.

74. T.R. Ravindran, A.K. Arora, and T.A. Mary, *High-pressure Raman spectroscopic study of zirconium tungstate.* Journal of Physics-Condensed Matter, 2001. **13**: 11573-11588.

75. T.R. Ravindran, A.K. Arora, and T.A. Mary, *High pressure behavior of ZrW_2O_8: Gruneisen parameter and thermal properties.* Physical Review Letters, 2000. **84**: 3879-3882.

76. Z. Hu, J.D. Jorgensen, S. Teslic, S. Short, D.N. Argyriou, J.S.O. Evans, and A.W. Sleight, *Pressure-induced phase transformation in ZrW_2O_8 - Compressibility and thermal expansion of the orthorhombic phase.* Physica B-Condensed Matter, 1997. **241**: 370-372.

77. A.K.A. Pryde, M.T. Dove, and V. Heine, *Simulation studies of ZrW_2O_8 at high pressure.* Journal of Physics-Condensed Matter, 1998. **10**: 8417-8428.

78. L.H. Ouyang, Y.N. Xu, and W.Y. Ching, *Electronic structure of cubic and orthorhombic phases of ZrW_2O_8.* Physical Review B, 2002. **65**: 4.

79. A. Grzechnik, W.A. Crichton, K. Syassen, P. Adler, and M. Mezouar, *A new polymorph of ZrW_2O_8 synthesized at high pressures and high temperatures.* Chemistry of Materials, 2001. **13**: 4255-4259.

80. J. Catafesta, J.E. Zorzi, C.A. Perottoni, M.R. Gallas, and J.A.H. da Jornada, *Tunable linear thermal expansion coefficient of amorphous zirconium tungstate.* Journal of the American Ceramic Society, 2006. **89**: 2341-2344.

81. R. Mittal, S.L. Chaplot, H. Schober, and T.A. Mary, *Origin of negative thermal expansion in cubic ZrW_2O_8 revealed by high pressure inelastic neutron scattering.* Physical Review Letters, 2001. **86**: 4692-4695.

82. W.I.F. David, J.S.O. Evans, and A.W. Sleight, *Direct evidence for a low-frequency phonon mode mechanism in the negative thermal expansion compound ZrW_2O_8.* Europhysics Letters, 1999. **46**: 661-666.

83. R. Mittal and S.L. Chaplot, *Phonon density of states and thermodynamic properties in cubic and orthorhombic phases of ZrW_2O_8.* Solid State Communications, 2000. **115**: 319-322.

84. A.P. Ramirez and G.R. Kowach, *Large low temperature specific heat in the negative thermal expansion compound ZrW_2O_8.* Physical Review Letters, 1998. **80**: 4903-4906.

85. G. Ernst, C. Broholm, G.R. Kowach, and A.P. Ramirez, *Phonon density of states and negative thermal expansion in ZrW_2O_8.* Nature, 1998. **396**: 147-149.

86. K. Wang and R.R. Reeber, *Mode Gruneisen parameters and negative thermal expansion of cubic ZrW_2O_8 and $ZrMo_2O_8$.* Applied Physics Letters, 2000. **76**: 2203-2204.

87. T.R. Ravindran, A.K. Arora, and T.A. Mary, *Anharmonicity and negative thermal expansion in zirconium tungstate.* Physical Review B, 2003. **67**: 4.

88. D. Cao, F. Bridges, G.R. Kowach, and A.P. Ramirez, *Correlated atomic motions in the negative thermal expansion material ZrW_2O_8: A local structure study.* Physical Review B, 2003. **68**: 14.

89. D. Cao, F. Bridges, G.R. Kowach, and A.P. Ramirez, *Frustrated soft modes and negative thermal expansion in ZrW_2O_8.* Physical Review Letters, 2002. **89**: 215902-215906.

90. S.L. Chaplot, *Negative thermal expansion in ZrW_2O_8 - Do we give up the concept of normal mode?* Current Science, 2005. **88**: 347-349.

91. A.R. West, *Solid Solutions*, in *Solid state chemistry and its applications*. 1987, Wiley: Chichester. p. 358-374.

92. Y. Yamamura, N. Nakajima, and T. Tsuji, *Calorimetric and x-ray diffraction studies of alpha-to-beta structural phase transitions in HfW_2O_8 and ZrW_2O_8.* Physical Review B, 2001. **6418**: art. no.-184109.

93. B. Chen, D.V.S. Muthu, Z.X. Liu, A.W. Sleight, and M.B. Kruger, *High-pressure Raman and infrared study of HfW_2O_8.* Physical Review B, 2001. **6421**: art. no.-214111.

94. J.D. Jorgensen, Z. Hu, S. Short, A.W. Sleight, and J.S.O. Evans, *Pressure-induced cubic-to-orthorhombic phase transformation in the negative thermal expansion material HfW_2O_8.* Journal of Applied Physics, 2001. **89**: 3184-3188.

95. Y. Yamamura, N. Nakajima, T. Tsuji, Y. Iwasa, K. Saito, and M. Sorai, *Heat capacity and Gruneisen functions of negative thermal expansion compound HfW_2O_8.* Solid State Communications, 2002. **121**: 213-217.

96. T. Tsuji, Y. Yamamura, and N. Nakajima, *Thermodynamic properties of negative thermal expansion materials ZrW_2O_8 substituted for Zr site.* Thermochimica Acta, 2004. **416**: 93-98.

97. T. Hashimoto, J. Kuwahara, T. Yoshida, M. Nashimoto, Y. Takahashi, K. Takahashi, and Y. Morito, *Thermal conductivity of negative-thermal-expansion oxide, $Zr_{1-x}Y_xW_2O_8$ (x-0.00, 0.01)-temperature dependence and effect of structural phase transition.* Solid State Communications, 2004. **131**: 217-221.

98. N. Nakajima, Y. Yamamura, and T. Tsuji, *Synthesis and physical properties of negative thermal expansion materials $Zr_{1-x}M_xW_2O_{8-y}$ (M = Sc, In, Y) substituted for Zr(IV) sites by M(III) ions.* Solid State Communications, 2003. **128**: 193-196.

99. Y. Morito, K. Takahashi, S.R. Wang, H. Abe, A. Katoh, and T. Hashimoto, *Press-free preparation method of dense negative-thermal-expansion oxide, $Zr_{1-x}Y_xW_2O_{8-delta}$ (x=0.00-0.02) ceramic using reactive sintering.* Journal of the Ceramic Society of Japan, 2002. **110**: 807-812.

100. Y. Yamamura, M. Kato, and T. Tsuji, *Synthesis and phase transition of negative thermal expansion materials $Zr_{1-x}Lu_xW_2O_{8-y}$.* Thermochimica Acta, 2005. **431**: 24-28.

101. C. Lind, A.P. Wilkinson, C.J. Rawn, and E.A. Payzant, *Preparation of the negative thermal expansion material cubic $ZrMo_2O_8$.* Journal of Materials Chemistry, 2001. **11**: 3354-3359.

102. C. Lind, A.P. Wilkinson, Z.B. Hu, S. Short, and J.D. Jorgensen, *Synthesis and properties of the negative thermal expansion material cubic $ZrMo_2O_8$.* Chemistry of Materials, 1998. **10**: 2335-2337.

103. S. Allen and J.S.O. Evans, *Negative thermal expansion and oxygen disorder in cubic $ZrMo_2O_8$.* Physical Review B, 2003. **68**.

104. C. Closmann, A.W. Sleight, and J.C. Haygarth, *Low-temperature synthesis of ZrW_2O_8 and Mo-substituted ZrW_2O_8.* Journal of Solid State Chemistry, 1998. **139**: 424-426.

105. L. Huang, Q.G. Xiao, H. Ma, G.B. Li, F.H. Liao, C.M. Qi, and X.H. Zhao, *Phase behaviors of the $ZrMo_{2-x}W_xO_8$ (x=0.2-2.0) system and the preparation of an Mo-rich cubic phase.* European Journal of Inorganic Chemistry, 2005: 4521-4526.

106. U. Kameswari, A.W. Sleight, and J.S.O. Evans, *Rapid synthesis of ZrW_2O_8 and related phases, and structure refinement of $ZrWMoO_8$.* International Journal of Inorganic Materials, 2000. **2**: 333-337.

107. J.S.O. Evans, P.A. Hanson, R.M. Ibberson, N. Duan, U. Kameswari, and A.W. Sleight, *Low-temperature oxygen migration and negative thermal expansion in $ZrW_{2-x}Mo_xO_8$.* Journal of the American Chemical Society, 2000. **122**: 8694-8699.

108. C. Lind, D.G. VanDerveer, A.P. Wilkinson, J.H. Chen, M.T. Vaughan, and D.J. Weidner, *New high-pressure form of the negative thermal expansion materials zirconium molybdate and hafnium molybdate.* Chemistry of Materials, 2001. **13**: 487-490.

109. T. Varga, A.P. Wilkinson, C. Lind, W.A. Bassett, and C.S. Zha, *Pressure-induced amorphization of cubic $ZrMo_2O_8$ studied in situ by X-ray absorption spectroscopy and diffraction.* Solid State Communications, 2005. **135**: 739-744.

110. A. Grzechnik and W.A. Crichton, *Structural transformations in cubic $ZrMo_2O_8$ at high pressures and high temperatures.* Solid State Sciences, 2002. **4**: 1137-1141.

111. A.M.K. Andersen and S. Carlson, *High-pressure structures of alpha- and delta-$ZrMo_2O_8$.* Acta Crystallographica Section B-Structural Science, 2001. **57**: 20-26.

112. H. Mavoori and S. Jin, *Low thermal-expansion copper composites via negative CTE metallic elements.* Jom-Journal of the Minerals Metals & Materials Society, 1998. **50**: 70-72.

113. X.C. Li, F. Prinz, and J. Seim, *Thermal behavior of a metal embedded fiber Bragg grating sensor.* Smart Materials & Structures, 2001. **10**: 575-579.

114. S. Yilmaz, *Phase transformations in thermally cycled Cu/ZrW_2O_8 composites investigated by synchrotron x-ray diffraction.* Journal of Physics-Condensed Matter, 2002. **14**: 365-375.

115. S. Jacob, J. Javornizky, G.H. Wolf, and C.A. Angell, *Oxide ion conducting glasses - Synthetic strategies based on liquid state and solid state routes.* International Journal of Inorganic Materials, 2001. **3**: 241-251.

Chapter 2

Experimental Techniques

During this thesis a large number of techniques were used to identify and characterize the synthesized materials. To clarify the main purpose and the possibilities of these techniques a short overview is given in the following chapter. The knowledge present within the research group of Solid State Chemistry combined with a large range of available apparatus within the group and abroad was explored. The main issue of this chapter is to reveal some of the most important features of the different techniques relevant to the study of negative thermal expansion materials. For more detailed information we can refer to literature and the manuals of the used equipment.

1 X-Ray Diffraction [1, 2]

In this thesis X-ray diffraction was used for identification of the powder, obtaining information about crystallinity, crystallite sizes, unit cell refinement and quantitative analysis. All measurements were collected on a Siemens D5000 diffractometer at the Department of Solid State Physics of the Ghent University.

1.1 XRD in general

X-rays were discovered in 1895 by the German physicist Roentgen and were so named because their nature was unknown at that time. Unlike ordinary light, these rays are invisible. However they travel in straight lines and affect photographic film in the same way as light. In addition, they are much more penetrating than light and can easily pass through the human body, wood, relatively thick pieces of metal and other "opaque" objects.

In powder diffraction, characteristic X-rays (for example Cu-Kα_1, λ=1.54060 Å and Cu-Kα_2, λ=1.54443 Å) are used to examine the powder specimens. Copper anodes are by far the most common. Single crystal monochromators are usually used to produce a beam of a narrower wavelength distribution.

The incident beam and the diffracted beam are always coplanar and the angle between both beams is 2θ. The Bragg law describes the conditions upon which the diffracted beams interact constructively resulting in a diffraction peak in the pattern according to:

$$n\lambda = 2d \cdot \sin\theta \qquad [1]$$

In this equation λ is the wavelength of the radiation used, d is the inter-planar spacing and θ is the angle between the incident or diffracted beam and the relevant crystal plane. The letter n refers to the order of diffraction. Figure 1 is a representation of the Bragg law.

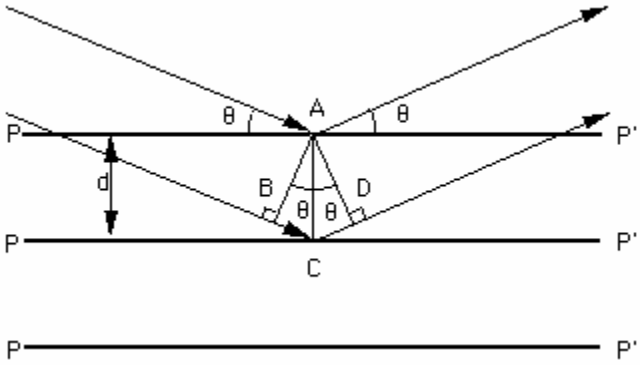

Figure 1: Representation of Bragg's Law

During the measurement the incident angle (θ) varies while the scintillation detector is rotated by 2θ. This means that the detector will receive a signal when at the surface of the powder crystals are orientated in such a way that the (hkl) plane with inter-plane distance $d_{(hkl)}$ is parallel with the surface and the angle θ obeys the Bragg Law. This set-up is referred to as the Bragg-Brentano geometry. The general set-up for a diffractometer with a secondary monochromator is given in figure 2. The divergence of the beam can be controlled by a divergence slit positioned after the source. The divergence of the diffracted beam is controlled by the receiving slit and detector slit.

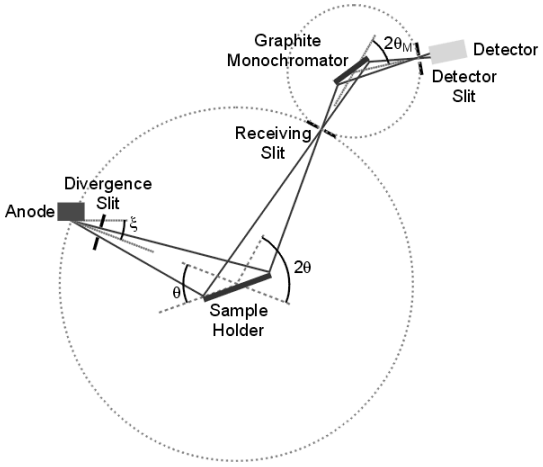

Figure 2: Bragg-Brentano set-up for a diffractometer with a secondary monochromator

A step scanning Siemens D5000 diffractometer equipped with a graphite monochromator and a scintillation detector was used in standard measurements. The step width was 0.02 2θ and the step time was 1.2 s.

1.2 Indexing and refinement of the unit cell parameters [3]

The combination of the reflection positions (in 2θ values) and their relative intensities is characteristic for the crystal structure. It is therefore of great importance to examine the diffraction patterns in the correct way. The dimensions of the unit cell will determine the peak positions. From the Bragg law d spacings can be calculated and these are related to the unit cell as can be seen by the following formulae for cubic symmetry and first order diffraction.

$$\frac{1}{d^2} = \frac{h^2 + k^2 + l^2}{a^2} \qquad [2]$$

$$a = \frac{\lambda}{2\sin\theta}\sqrt{h^2 + k^2 + l^2} \qquad [3]$$

The most important equation used for the indexing of the diffraction patterns is the reciprocal space metric tensor equation.

The relation between the d spacings in a material and the d^* spacings in the reciprocal lattice is $1/d = d^*$. The reflection indices h, k and l are related to d^* according the vector equation:

$$d^* = h\vec{a}^* + k\vec{b}^* + l\vec{c}^* \qquad [4]$$

$$d^{*2} = \vec{d}.\vec{d} \qquad [5]$$

Yielding:

$$\frac{1}{d^2} = h^2a^{*2} + k^2b^{*2} + l^2c^{*2} + 2klb^*c^*\cos\alpha^* + 2hla^*b^*\cos\beta^* + 2hka^*b^*\cos\gamma^* \qquad [6]$$

Equation 6 is often written with the six parameters (A-F) as the reciprocal space metric tensor equation.

$$\frac{1}{d^2} = Ah^2 + Bk^2 + Cl^2 + Dkl + Ehl + Fhk \qquad [7]$$

In the case of cubic symmetry this equation can be simplified as follows.

$$\frac{1}{d^2} = Ah^2 + Bk^2 + Cl^2 \qquad [8]$$

In a unit cell refinement procedure the quantity that is minimized is represented by:

$$\sum_{n}^{N} w_n \left(2\theta_{n(obs)} - 2\theta_{n(calc)}\right)^2 \qquad [9]$$

where, w_n is the weight of the observation and according to the Bragg Law.

$$2\theta_{n(calc)} = 2\sin^{-1}\left(\frac{\lambda\sqrt{Ah^2 + Bk^2 + Cl^2}}{2}\right) \qquad [10]$$

Practically, A-F are refined and the lattice parameters are derived from them. The least square calculation yields estimated standard deviations which are a measure of the precision of the refined parameters.

In this thesis, the program UNITCELL [4] was used to refine the unit cell parameters. Unlike most existing cell refinement programs it does not require initial estimates for cell constants. It uses a non-linear least squares fit method, which allows the refinement to be carried out on the actual observed data. A minimum of 20 reflections was used as input in the program. The reflection positions were corrected by adding 6 m% LaB_6 (SRM660a) as internal standard. The data were collected on the Siemens D5000 diffractometer (0.02 2θ, 1s step time and detector slit = 0.02°).

A second method to retrieve precise lattice parameters is the Nelson-Riley extrapolation function.

$$\frac{\cos^2\theta}{\sin\theta} + \frac{\cos^2\theta}{\theta} \qquad [11]$$

In this method the lattice parameter is plotted as a function of the extrapolation

function and the precise lattice parameter is calculated by the use of the least square method at x = 0.

1.3 Rietveld Refinement [5, 6]

In crystallography, structure refinement is of the greatest importance. The starting model which is an approximate model of the structure is refined by the least-squares refinement so that the final calculated diffraction pattern resembles the observed measured data. The quantity minimized in the least-squares refinement is the residual S_y:

$$S_y = \sum_i w_i (y_{iobs} - y_{icalc})^2 \qquad [12]$$

where $w_i = 1/y_{iobs}$, with y_{iobs} the observed intensity in the diffractogram at the i-th step and y_{icalc} the calculated intensity at the i-th step.

There are several model parameters that can be refined. First of all there are structural parameters which will have a large influence on the peak position and furthermore the instrumental parameters which will mostly affect the peak intensities. An overview is given in table 1.

Instrumental	Structural
Zero-error: 2θ error	scale factor: s
peak shape parameter: η	fractional atomic coordinates: x_i, y_i and z_i
peak width parameters: U, V, W	anisotropic temperature factor
Unit cell metric tensor: A-F	isotropic temperature factor
	site occupancy factor

Table 1: Refinable parameters in a Rietveld Refinement.

The program FULLPROF [7] was used to refine structures of several materials. A large number of programs for indexing, space group determination, calculation of bond angles and bond distance… are included in the FullProf Suite software package.

2 EXAFS analysis [8, 9]

2.1 Introduction

X-ray absorption fine structure (XAFS) refers to the details of how X-rays are absorbed by an atom at energies near and above the core-level binding energies of that atom. XAFS is in fact the modulation of an atom's X-ray absorption probability due to the chemical and physical state and environment of an atom. XAFS spectra are sensitive to the oxidation state, coordination chemistry and the distances, coordination number and type of atoms immediately surrounding the absorbing element. As a result XAFS provides a practical way to determine the chemical state and local atomic structure for a selected atom. XAFS measurements do not require crystallinity of the materials and can be performed on solid materials and on dissolved species. The X-ray absorption spectrum is divided into two areas: X-ray near-edge spectroscopy or XANES and extended X-ray absorption fine-structure spectroscopy or EXAFS. XANES is strongly sensitive to oxidation states and coordination chemistry of the selected atoms whereas EXAFS is suitable to determine distances, coordination number and species of the neighbouring atoms.

2.2 X-ray absorption

X-ray absorption can be understood as an X-ray photon which is absorbed by an electron in a tightly bound quantum core level of an atom as can be seen in figure 3. If the binding energy of the electron is less than that of the X-ray, the electron may be removed from its quantum level. The energy in excess is given to a photo-electron that is ejected from the atom. This phenomenon is known as the photo-electric effect. The photo-electron must be treated as a wave whose wavelength λ is given by the de Broglie relation:

$$\lambda = \frac{h}{p} \qquad [13]$$

where p is the momentum of the photo-electron and h is Planck's constant.

The momentum of the photo-electron can be determined by the free electron relation:

$$\frac{p^2}{2m} = h\nu - E_0 \qquad [14]$$

where m is the mass of the electron, hν is the energy of the X-ray photon and E_0 represents the binding energy of the photo-electron.

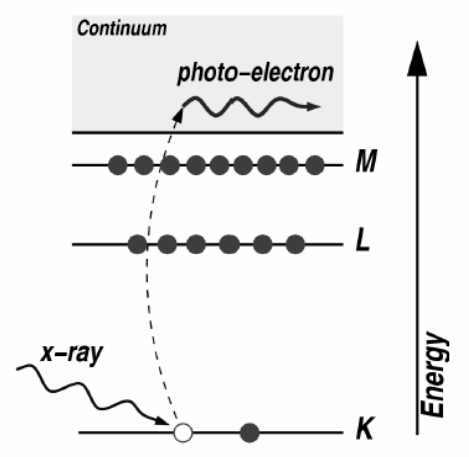

Figure 3: The photo-electric effect

X-ray absorption is immediately related to the absorption coefficient μ as in the Lambert- Beer law

$$I = I_0 e^{-\mu t} \qquad [15]$$

where I_0 is the X-ray intensity of the incident radiation, I is the intensity of the transmitted radiation and t is the thickness of the sample.

The EXAFS fine-structure function χ(E) can be defined as:

$$\chi(E) = \frac{\mu(E) - \mu_0(E)}{\Delta\mu_0(E)} \qquad [16]$$

where μ(E) is the measured absorption coefficient, $\mu_0(E)$ is a smooth background function representing the absorption of an isolated atom and $\Delta\mu_0$ is the measured jump in the absorption μ(E) at the threshold energy E_0 as given in figure 4. The typical

damped oscillatory structure at energy above E_0 is superposed on the absorption of the isolated atom.

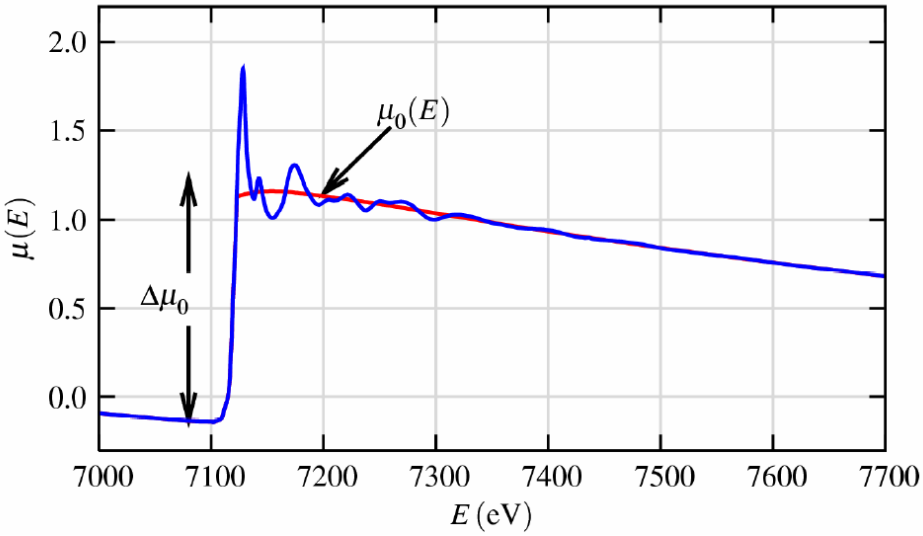

Figure 4: XAFS spectrum for FeO

EXAFS is best understood in terms of the wave behaviour and the interference with the neighbouring atoms. The expression for the EXAFS is then χ(k) with

$$k = \sqrt{\frac{2m(E-E_0)}{\hbar^2}} \qquad [17]$$

where E_0 is the absorption edge energy , ħ is the reduced Planck's Constant (h/2π) and m is the electron mass.

The photo-electron can be represented as an outgoing wave. The surrounding atoms will scatter the outgoing wave and the final state is the superposition of the outgoing and scattered waves. The backscattered wave will add or substract from the outgoing wave at the centre depending on their relative phase. The total amplitude of the electron wave function will be enhanced or reduced and thus modifying the probability of absorption of the X-ray correspondingly. How the phase varies with the wavelength of the photo-electron depends on the distance between the centre atom and backscattering atom. The variation of the backscattering strength as a function of energy of the photo-electron depends on the type of atom responsible for the backscattering.

The different frequencies apparent in $\chi(k)$ correspond to different near – neighbour coordination shells which can be described and modelled according to the EXAFS equation:

$$\chi(k) = \sum_j \frac{N_j f_j(k) e^{-k^2 \sigma_j^2}}{kR_j^2} \sin\left[2kR_j + \delta_j(k)\right] \qquad [18]$$

where f(k) and δ(k) are scattering properties of the atoms neighbouring the excited atom, N is the number of neighbouring atoms, R is the distance to the neighbouring atom and σ^2 is the disorder in the neighbour distance. The EXAFS equation allows to determine N, R and σ^2 knowing the scattering amplitude f(k) and the phase-shift δ(k). Fourier transformation of the EXAFS equation results in a radial atomic distribution plot.

2.3 Synchrotron radiation [10]

X-ray absorption measurements need an intense and energy-tunable source of X-rays. Synchrotron radiation is very suitable for EXAFS experiments. The experimental set-up of the synchrotron present at the European Synchrotron Radiation Facility (Grenoble) consists of 3 major parts as can be seen in Figure 5. First of all, electrons emitted by an electron gun are accelerated in a 200 MeV linear accelerator (linac) and then transmitted to a second part, the booster synchrotron. They are accelerated to reach an energy level of 6 billion electron volts (6 GeV). These high energy electrons are injected into a large storage ring (844 meters in circumference) where they circulate in a vacuum environment at a constant energy for many hours. The beam is guided into the pseudo-circular orbit by 64 bending magnets and is focused by 320 quadrupoles. The optimal beam intensity can reach 200 mA.

The storage ring includes straight and curved sections. The electrons pass through different types of magnets as they travel round the ring. When the electrons pass through the bending magnets, they are deflected from their straight path by several degrees. This change in direction causes them to emit synchrotron radiation. This synchrotron light consists of very bright X-rays. The beam of X-rays is collimated and very intense. The second type of magnets are the focusing magnets which are used to

keep the electron beam small and well-defined. These restrictions are necessary to obtain a very bright X-ray beam. The last type of magnets consists of undulators which force the electron beam to follow a wavy trajectory. This generates a much more intense beam of radiation than in the case of the bending magnets. Those magnets are given schematically in the upper part of figure 5: from left to right – Bending magnets – Focussing magnets – Undulators.

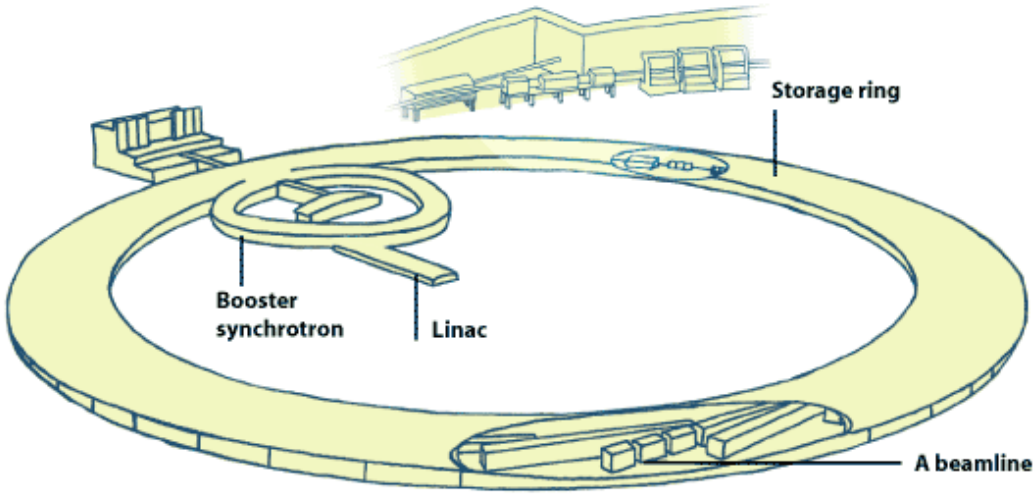

Figure 5: Experimental set-up of the ESRF synchrotron

The synchrotron beams emitted by the electrons are directed towards the "beamlines" which surround the storage ring in the experimental hall. The beamlines include an optics cabin housing the optical systems used to tune the X-ray beam to the desired experimental characteristics (size, energy …). Next to the optics cabin, there is an experimental cabin which contains the support mechanism and sample environment. One or more detectors record the information produced as a result of the interaction between X-ray beam and sample. A control cabin allows control of experiment and the data collection. Each beamline is designed for use with a specific technique of for a specific type of research. Our experiments were performed at the DUBBLE beamline with financial support of NWO and FWO.

3 Morphological analysis

3.1 Scanning Electron Microscopy [11]

SEM is an electron microscopy measurement and is mostly based on the following electron interaction with the specimen: secondary electrons, backscattered electrons and X-rays. Usually a standard SEM detects secondary electrons. This results in a picture of the morphology of the studied material.

A schematic diagram of the main components of the SEM equipment is shown in figure 6.

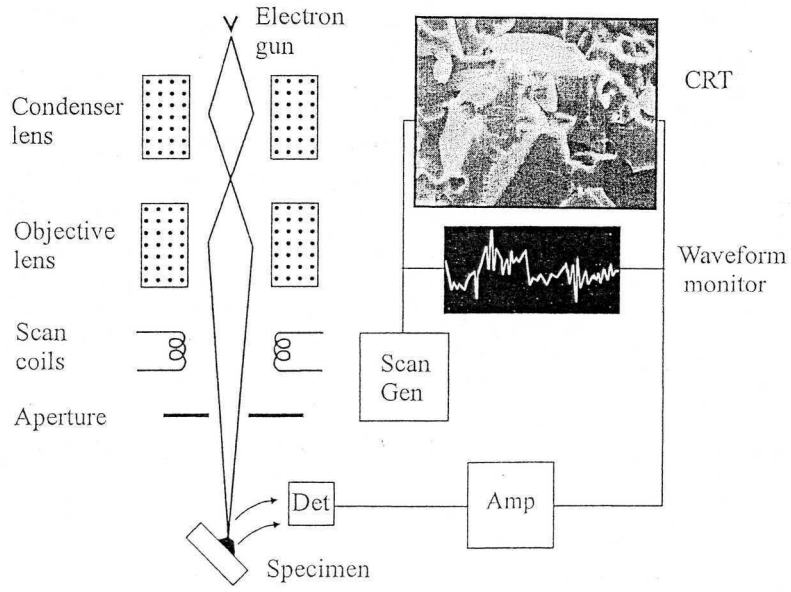

Figure 6: Schematic diagram of the main components of a SEM

A field emission gun is used as electron source to obtain higher resolution in comparison to the thermoionic emission types. The electrons are accelerated to an energy which is usually between 1 keV and 30 keV. Two or three condenser lenses demagnify the electron beam. It may have a diameter of only 2-10 nm as it hits the specimen. The objective lens is used to further demagnify the filament image producing a probe of a specific diameter on the surface of the specimen. The distance between the aperture and the specimen is known as the work distance.

X-rays can be formed as secondary effect due to electron interaction. Characteristic X-rays can be used to identify the specimen by SEM-EDX (Energy dispersive analysis of X-rays). This was very useful in the identification of Zr(40), W(74) and O(8). In this thesis the Zr Kα and W Lα lines were used for quantification. Simultaneous SEM and EDX were performed on a FEI-200F (FEI).

3.2 Density measurements [12]

Knowing the density of the material is of utmost importance. The presence of pores (open or closed) reduces the density. The volume of the material can be defined by its bulk, real or apparent volume. There are different kinds of definition of density each with their own special feature. All these terms are explained as follows.

- Open pores: pores in direct contact with the environment
- Closed pores: pores encapsulated in the material and therefore not in contact to the environment
- Bulk or geometrical volume: external measured volume of the sample
- Real volume: volume occupied with sample material (Bulk volume – volume (open + closed pores)
- Apparent volume: Bulk volume – volume (open) pores
- Geometrical density: ratio of the mass of the sample to the geometrical volume
- Apparent density: ratio of the mass of the sample to the apparent volume
- Theoretical density: calculated using mass and volume of the unit cell.
- Porosity (%): $100\,\% - \frac{geometrical\ density}{theoretical\ density} \text{x} 100\,\%$ [19]

The *geometrical density* is the ratio of the mass of the sample to the bulk volume measured with the use of a micrometer.

The *apparent density* was determined using an AccyPyc 1330 pycnometer (Micromeritics). This is a gas impregnation-type pycnometer.

3.3 Particle size measurements [13]

The particle size of a powder mixture is quantifiable in many different ways such as microscopy and SEM. Crystallite size can be determined by line broadening in X-ray diffractograms. In this work, a non-imaging technique was used. Laser diffraction is a suitable tool to measure the particle size and particle size distribution. The measurements were carried out on a Malvern Particle Sizer, Series 2600c.

Low power Helium-Neon laser light is used to form a collimated and monochromatic light beam. The beam is sent through a cell in which the sample material is dispersed in a liquid. The particle size will influence the angle under which the laser light is been scattered. The scattered and unscattered light passes the receiver lens and falls onto the detector planes. The detector consists of 31 concentric planes. Each plane represents a certain range of particle sizes. By software calculations a differential and cumulative distribution pattern is generated. From the cumulative distribution curve, the median size d_{50} and also d_{90} and d_{10} can be determined. The d_{10} size represents the particle size below which 10% of the distribution is situated. The particle sizer can screen different ranges of particle size depending on the kind of lenses (Beam expander lens or range lens) used. The ranges are given in table 2.

Range Lens (mm)	Beam Expander lens (mm)	Particle size range (μm)
63	10	1.2-118
100	10	1.9-188
300	10	5.8-564
600	18	11.6-1128
800	18	15.5-1503
1000	18	19.4-1880

Table 2: Ranges of particles size according to the lenses used.

4 Thermal analysis

Thermal analysis of materials focuses the response of a material to applied heat. In this chapter a range of techniques based on the changes in length, weight, heat capacity or exo/endothermal reaction heat are mentioned.

4.1 Thermogravimetric Analysis – Differential Thermal Analysis [12, 15]

Thermogravimetric Analysis (TGA) measures weight changes in a material as a function of temperature (or time) under a controlled atmosphere. Simultaneously, the temperature difference (DTA) is measured between the sample and a reference (Al_2O_3). This temperature difference can be due to a difference in heat capacity between sample and reference. Reactions in the sample will be indicated by a positive (exothermal) or a negative (endothermal) peak in the DTA spectrum. The equipment used for this application was a SDT 2690 (TA instruments).

4.2 Differential Scanning Calorimetry [16]

Differential Scanning Calorimeters (DSC) measures temperatures and heat flows associated with thermal transitions in a material as a function of time and temperature. The sample heat capacity is determined from the heating power, baseline and sensitivity calibrations. Transition enthalpies are calculated by integration of the peak in the power versus temperature curve.

$$\Delta H_{tr} = K_{\phi}(T)A \qquad [21]$$

Where ΔH_{tr} is the enthalpy associated with the transition, $K_{\phi}(T)$ is an instrument-dependent factor and A is the peak area above the baseline.

The measurements were performed at Hogent on DSC 2910 (TA Instruments).

4.3 Thermal Mechanical Analysis [17, 18]

Interesting information can be obtained by measuring the expansion or contraction of a sample under negligible loads. The bulk thermal expansion of the materials was analysed by a TMA 2940 Thermomechanical Analyzer as can be seen in figure 7.

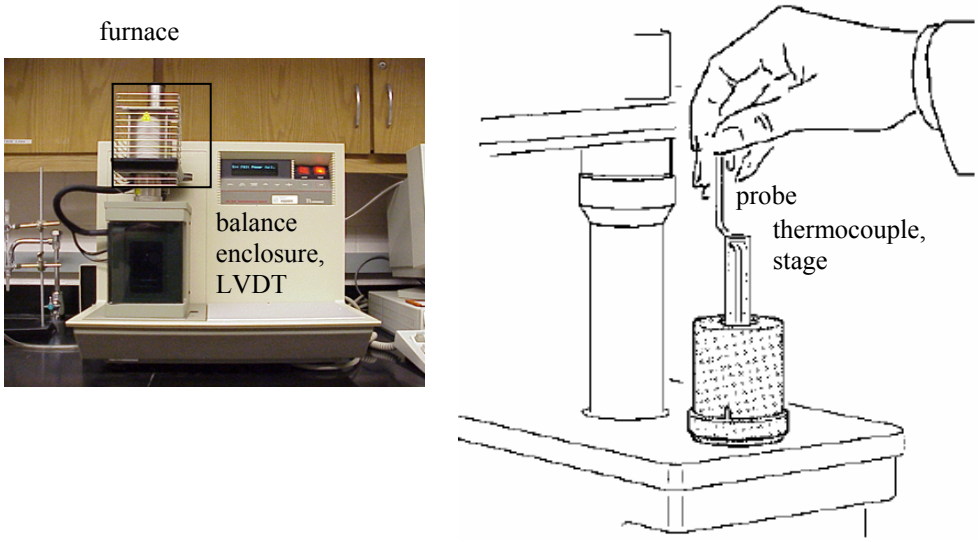

Figure 7: TMA 2940 Thermomechanical Analyzer

The instrument is constructed with the following parts:

- The balance enclosure surrounds the TMA balance mechanism which exerts a specified force on the sample.
- The probe assembly is interchangeable for making several different measurements on the various sample materials. The macro expansion probe is used during these measurements. This type of probe (∅ = 6 mm) covers a larger sample surface and gives a more representative reading.
- The stage is an interchangeable component that supports the sample during measurements.
- The furnace assembly surrounds the stage in order to heat the sample. It contains the integral cooling container and the furnace monitor chromel/alumel thermocouple.
- The weight tray holds the weight to exert a known force to the sample.

- The linear variable differential analyzer (LVDT) measures the length changes of the sample during the thermal program. This is based on a linear movement of a small magnet located at the end of the probe into coils, which generates a very precise position signal.

The experiments yield a bulk thermal expansion coefficient according to:

$$\frac{dl}{dt} = l_0 \cdot \alpha \cdot \frac{dT}{dt} \qquad [22]$$

where dl/dt is the measured length change derived to the time, l_0 is the initial length, α is the bulk thermal expansion coefficient and dT/dt is the applied heating rate.

Measurements were performed between room temperature and 300 °C using a heating rate of 5 °C/min and a load of 0.5 N on 2 mm thick bars. The materials were examined with extra attention to the bulk thermal expansion coefficient and the phase transition temperature at which the order-disorder reaction occurs. A typical TMA graph is given in figure 8. The second order transition will also result in a discontinuous behaviour in the thermal expansion coefficient. During the thermal contraction measurement the α-value is stable and then drops drastically in the region around the transition temperature and rises again to form the almost constant α-value of the β-structure of ZrW_2O_8.

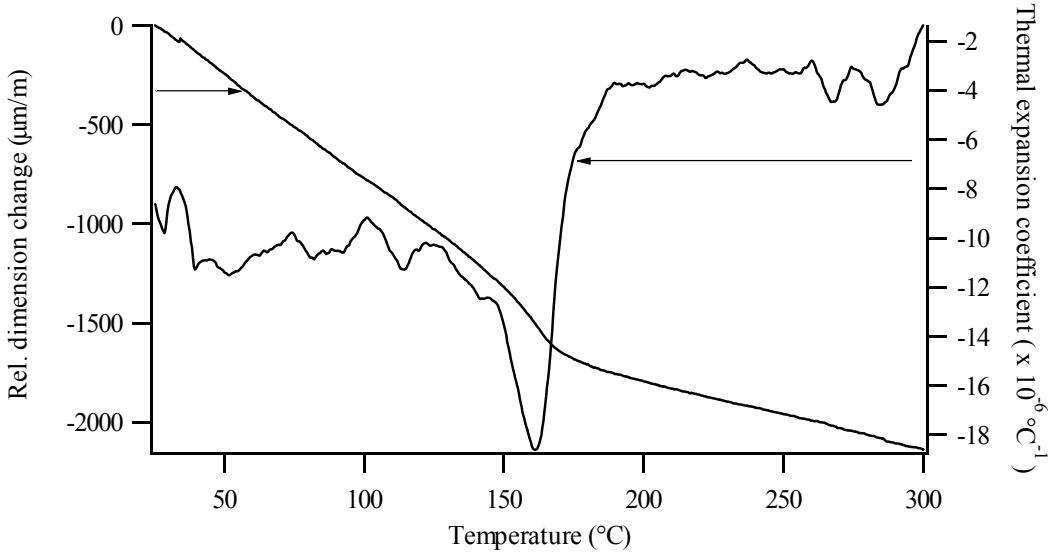

Figure 8: Typical TMA graph with indication of the relative dimension change and the bulk thermal expansion coefficient

5 IR and Raman Spectroscopy [19, 20]

The IR-spectra were collected using a Mattson Research Series I FT-IR spectrometer. The Raman-spectra were collected using a Bruker FT spectrophotometer Equinox 55S equipped with a Raman module FRA 106. The spectrophotometer is provided with a Neodymium Yttrium Aluminum garnet laser. The most important peaks of ZrW_2O_8 in IR/Raman [21] are mentioned in table 3. The phase transition will induced a change in the spectral view in the IR measurements. The Raman spectra will experience broadening of the peaks. No extra peaks are included due to the Raman inactive vibrations coupled with the phase transition. The increase in temperature will harden some of the vibration modes whereas others are softened.

IR (cm^{-1})		Raman (cm^{-1})		
298K	473K	298K	473K	assignments
		1028_m	1024_m	
999_w		966_w	932_m	ν (WO_4)
908_m	914_w	929_m	896_m	
871_m	873_w	901_m		
		887_w		
800_s	801_w	859_w		
760_m	741_w	789_s	783_s	ν_{as} (WO_4)
739_m	720_w	733_m	739_m	
646_w	688_w			
	668_s			(O-W-O-W-O)
$(600\text{-}400)_w$	$(650\text{-}450)_w$			
	419_m			(O-W-O-W-O)
		382_w	380_w	δ_{as} (WO_4)
		331_m		δ (WO_4)
		308_w		
		271_w		
		234_w		lattice modes
		144_m	148_w	
		103_w		
		84_w		
		65_m	59_m	
		40_m	39_w	

Table 3: IR and Raman data at 298 and 273K (m = medium, w = weak)

As can be seen in table 3 the differences occur in the IR-region below 1000 cm^{-1}. In this far-IR area most metal-metal and metal-oxygen vibrations are situated.

6 Mechanical analysis: three-point bending test [22, 23]

The three-point bending test is a suitable way of testing the mechanical properties of solid materials. These measurements were performed at the Laboratory of Mechanical Construction and Production at Ghent University. The used equipment is an Instron™ Series 4500 linked with a Series IX Automated Materials Testing System. The shape of the measured sample is rectangular with the following dimensions: 2 mm x 2 mm x 13 mm. The dimensions of the samples are too small to obtain correct values of the mechanical properties but the method is suitable to deliver data which can be compared relative to one another.

The stress at fracture is known as the flexural strength (σ_f). For samples with a rectangular cross-section σ_f equals:

$$\sigma_f = \frac{3.F.L}{2.b.d^2} \qquad [23]$$

In this equation F is the load at fracture, L is the distance between the two support points, d is the height and b is the width of the rectangular bar.

Another parameter which defines the strength of the material is the modulus of bending. Ceramic materials have the tendency to break before or at the elastic limit. The modulus of bending is the ratio of the applied stress to the strain. Hereby, the modulus is calculated using the strain and stress at the moment of fracture.

$$E = \frac{L^3}{4b.d^3}\frac{\Delta F}{\Delta D} \qquad [24]$$

where ΔD and ΔF are respectively the strain and applied stress.

7 Luminescence measurements [24-26]

A luminescent material can emit radiation after absorption of the excitation energy which can be many types of energy. Photoluminescence is excited by electromagnetic radiation, cathodoluminescence by a beam of energetic electrons, electroluminescence by an electric voltage, chemiluminescence by a chemical reaction and so on. The photoluminescence process can be described as follows. The exciting radiation is absorbed by a luminescent center, raising it to an excited state. The excited state returns to the ground state by emission of radiation. Some materials exhibit only non-radiative return to the ground state and are non-luminescent species.

7.1 Absorption - Excitation

In optical absorption, the center is promoted from its ground state to an excited state. This absorption depends on the energy level of the individual ions. For example, compounds like $CaWO_4$ have strong and broad bands in their absorption spectra. Nevertheless, the electronic configuration of the W ion is a d^0 configuration. Transition metal ions with d^0 configuration can exhibit charge transfer from the ligand to the d^0 ion. An electron is hereby excited from a non-bonding orbital (ligand) to an anti-bonding orbital (ion). The same phenomenon occurs in d^{10} configurations such as Zn^{2+}.

7.2 Relaxation – Emission

The principle of excitation-emission is given in a configurational coordinate diagram (figure 9). The two parabolas represent the ground state (g) and excited state (e). The minima of the parabolas represent the equilibrium distances and these are shifted by ΔR due to the fact that the chemical bond is different in the ground and the excited state. Absorption brings the center in a high vibrational level of the excited state. The center returns first to the lowest vibrational level in the excited state. Hereby, the excess of energy is passed to the surroundings and the center undergoes relaxation. During this relaxation process, there is usually no (visible) emission. From this lowest vibrational level of the excited state, the system can return to the ground state

spontaneously by emission of radiation. By emission, the center reaches the higher vibrational level of the ground state. This process is followed by relaxation to the lowest vibrational level of the ground state. The energy difference between the maximum of the excitation band and the emission band is defined as the Stokes shift and is given in figure 10. Complexes of transition metal ions with a formally empty d shell show intense broad-band emission with a large Stokes shift (10000 – 20000 cm^{-1}).

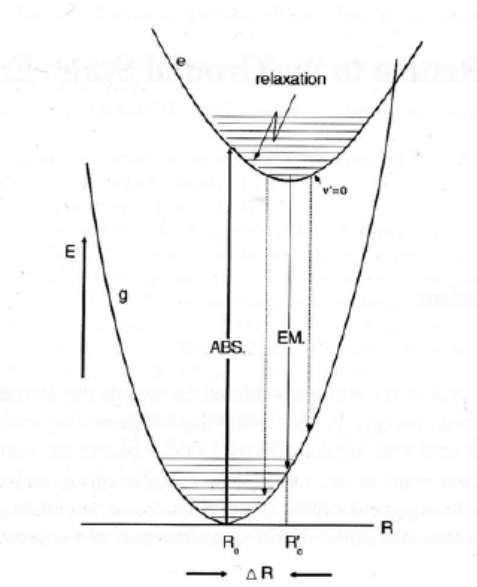

Figure 9: Configurational coordinate diagram [24]

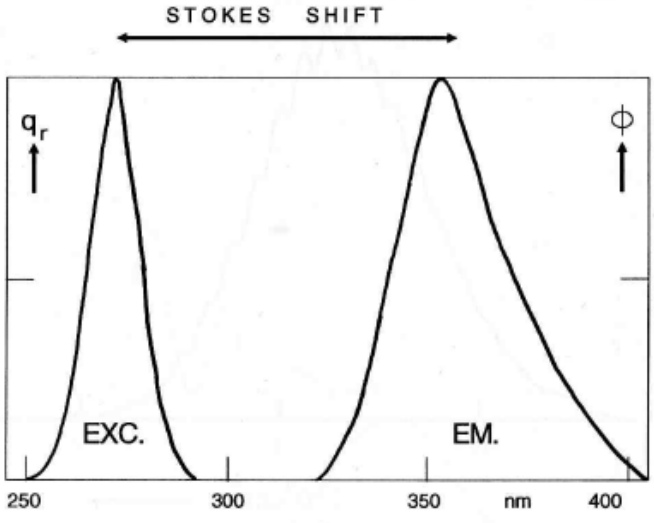

Figure 10: Emission and excitation spectra of Bi^{3+} luminescence in LaOCl:Bi^{3+} [24]

7.3 Experimental set-up

A FS920 steady state fluorescence spectrometer (Edinburgh Instruments) was used to record high quality photoluminescent excitation and emission spectra (250 – 800 nm). A scheme of the spectrometer can be seen in figure 11. A continuous xenon arc lamp spectrum is used from which the energy (wavelength) of the excitation light is selected by two diffraction grating monochromators. The excitation beam is split in two parts: one part is focused towards a Si-diode reference detector and the other part continues towards the sample. The emission is collected by a lens and focused on the emission monochromator. The emission spectrum itself is recorded with a Hamamatsu 928 photomultiplier tube with a spectral response from 250 – 800 nm.

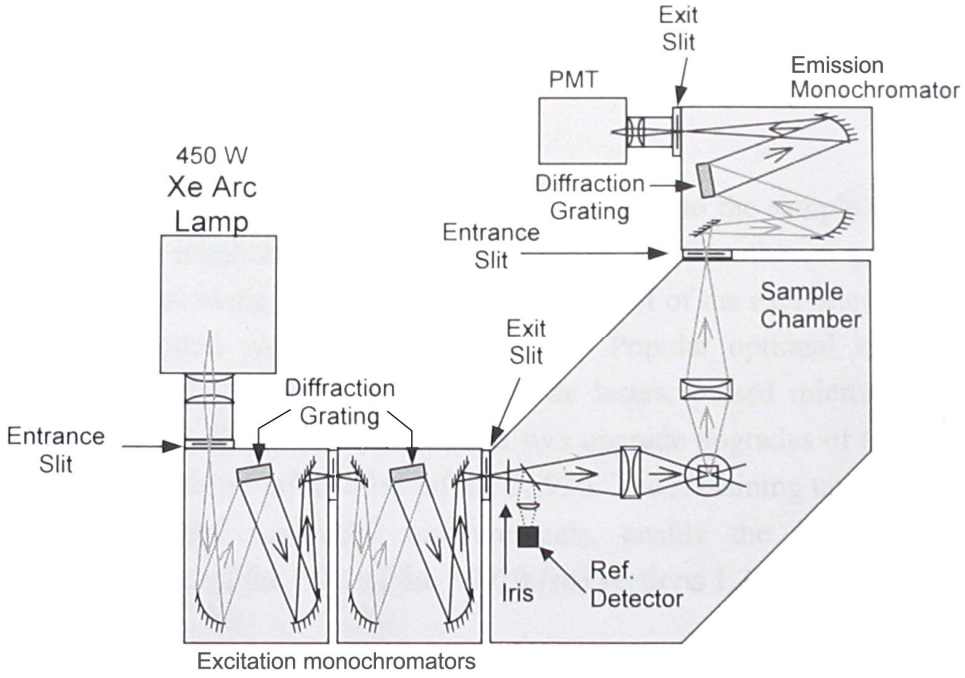

Figure 11: Experimental set-up of the spectrophotometer used in luminescence measurements

There are two different kinds of luminescence measurements. Excitation spectra are obtained by variation of the wavelengths of the excitation light beam while monitoring the emission intensity at a fixed wavelength. Emission spectra are collected after excitation at a chosen wavelength and the emission is recorded in a broad wavelength range.

8 References

1. B.D. Cullity, *Elements of X-Ray Diffraction*. Addison-Wesley Series in Metallurgy and Materials. 1978, Reading, Massachusetts: Addison-Wesley Publishing Company Inc. 553.

2. B.E. Warren, *X-ray Diffraction*. 1969, Reading, Massachusetts: Addison-Wesley Publishing Company.

3. A.R. West, *Basic Solid State Chemistry*. Second ed. 1999, Chichester, England: Whiley & Sons. 480.

4. T.J.B. Holland and S.A.T. Redfern, *Unit cell refinement from powder diffraction data: The use of regression diagnostics.* Mineralogical Magazine, 1997. **61**: 65-77.

5. C. Giacovazzo, H.L. Monaco, D. Viterbo, F. Scodari, G. Gilli, G. Zanotti, and M. Catti, *Fundamentals of Crystallography*, ed. Giacovazzo. 1992, Oxford: Oxford University Press. 653.

6. H.M. Rietveld, Journal of Applied Crystallography, 1969. **2**: 65.

7. S. Rodriguez-Carvajal, *FULLPROF: A program for Rietveld Refinement and Pattern Matching Analysis.* Abstracts of the Satellite Meeting on Powder Diffraction of the XV Congress of the IUCr., 1990: 127.

8. M. Newville, *Fundamentals of EXAFS*. 2004, University of Chigago, IL: Chigago.

9. D.C. Koningsberger and R. Prins, *X-ray Absorption: Principles, Applications, Techniques of EXAFS, SEXAFS and XANES*. 1988, Toronto: John Wiley & Sons.

10. ESRF, *A light for Science*. 2007, European Synchrotron Radiation Facility: Grenoble p. 12.

11. B.C. De Cooman, *Cursus Materiaalkundige Observatietechnieken*. 2000: Universiteit Gent.

12. I. Van Driessche, *Cursus Anorganische chemie: Anorganische Vaste Stoffen*. 2002: Universiteit Gent.

13. T. Vande Cavey, *Het gebruik van deeltjesgrootte-analyse via laserdiffractie bij de synthese van keramische materialen*. 2003, Hogeschool Antwerpen.

14. S.J. Gregg and K.S.W. Sing, *Adsorption, Surface Area and Porosity*. 1967, London: Academic Press.

15. M.E. Brown, *Introduction to Thermal Analysis: Techniques and Application*. 1988, London: Chapman and Hall.

16. TA instruments, *MDSC: Operator's Manual.*

17. R.E. Taylor, *Thermal expansion of solids*. 1998: ASM International.

18. TA instruments, *TMA 2940 Thermomechanical Analyzer: Operator's Manual*. 1999.

19. L. Moens, *Cursus Analytische Chemie: Spectroscopische Analysemethoden*. 2000: Universiteit Gent.

20. F. Verpoort, *Cursus Anorganische Chemie: Grondslagen van Moleculaire Spectroscopie*. 2000: Universiteit Gent.

21. J.S.O. Evans, T.A. Mary, T. Vogt, M.A. Subramanian, and A.W. Sleight, *Negative thermal expansion in ZrW_2O_8 and HfW_2O_8.* Chemistry of Materials, 1996. **8**: 2809-2823.

22. E. Bruneel, *Supergeleidende composieten op basis van $Bi_{1,5}Pb_{0,5}Sr_2Ca_2Cu_3O_x$*. 2001, Universiteit Gent.

23. W.D. Callister, *Materials Science and Engineering: An Introduction*, ed. W. Anderson. 2000, Danvers: Wiley & Sons.

24. G. Blasse and B.C. Grabmaier, *Luminescent Materials*. 1994, Heidelberg: Springer-Verlag.

25. P.F. Smet, *Study of $BaAl_2S_4$:Eu and SrS:Cu,Ag as blue emitting materials for thin film electroluminescence*. 2005, Universiteit Gent.

26. A. Goeminne, *Cursus Anorganische Chemie: Symmetrie en Chemische Binding - Transitiemetaalchemie*. 2000: Universiteit Gent.

Chapter 3

Conventional synthesis methods for ZrW_2O_8 materials

The study of every material starts with the synthesis of its pure phase material. Several different synthetic approaches are used in this work and will be discussed individually in the Chapters 3 and 4. The influence of the synthetic routes on the purity, crystallinity, thermomechanical properties and morphology are described in detail. The first synthetic route mentioned is the conventional solid state reaction using commercially available oxides (ZrO_2 and WO_3) and is the most explored synthetic way to prepare ZrW_2O_8. The main goal is the preparation of a homogeneous oxide precursor mixture. The conventional solid state reaction is described here as it is the basic synthesis for the composite materials described in Chapter 6 and substituted materials mentioned in Chapter 7.

1 Synthesis methods

Several methods to synthesize ZrW_2O_8 have been published in the literature and they can be divided into two classes depending on the precursor materials used: starting from commercially available pure oxides ZrO_2 and WO_3 in powder form and using the conventional solid state reactions [1-3] or starting from solutions of commercial salts of zirconium and tungsten using a so-called wet chemical procedure. Mixtures of dissolved salts possess the obvious advantage over classical ceramic techniques that very homogeneous precursors in the liquid state can be obtained and that is possible to maintain this level of homogeneity in the solid precursor state which remains after removal of the solvent (Chapter 4). An overview of the different synthetic approaches is given in figure 1.

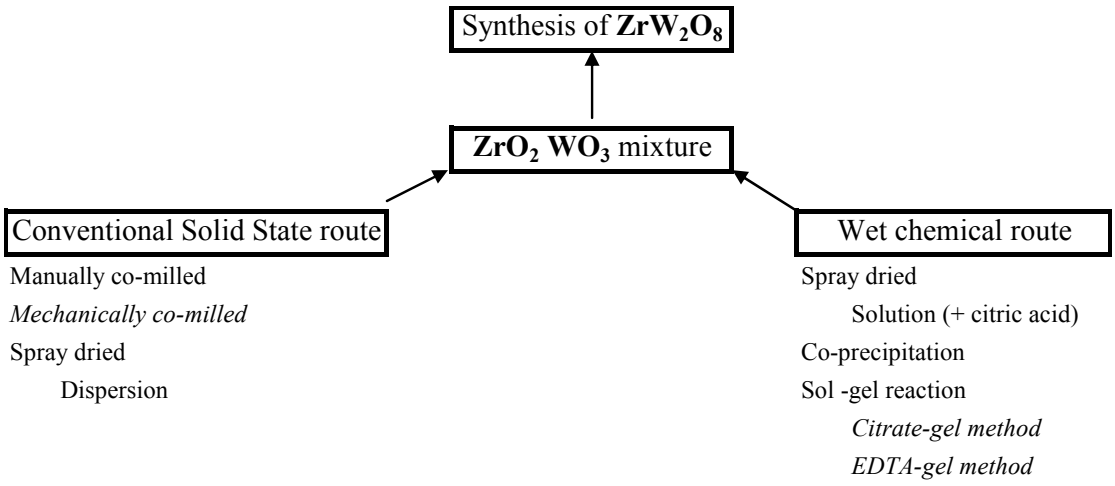

Figure 1: Overview of the synthetic routes for ZrW_2O_8

On the left side of this figure the conventional methods are given starting from ZrO_2 and WO_3 in powder form while on the right part of the scheme the methods starting from the salts can be seen. These salts can be spray dried from a solution [4, 5]. Co-precipitation is also a synthetic route starting from the salts and resulting in cubic ZrW_2O_8. Alternative synthetic routes are the *citrate-gel method* and *EDTA-gel method* providing homogeneous oxide mixtures and ultra-pure ZrW_2O_8. The following synthetic routes are used in this work: a conventional solid state route with mechanically co-milled powders and the wet chemical routes using the citric-gel and EDTA-gel method.

2 Conventional solid state reaction

The synthesis of ZrW_2O_8 by conventional solid state reaction has been reported many years ago [6, 7]. ZrO_2 oxide powder is mixed with WO_3 in a 1 : 2 ratio. This powder mixture is then thermally treated in order to prepare the negative thermal expansion phase ZrW_2O_8. The most important drawback of this synthetic route is the difficulty to prepare a very homogenous oxide powder mixture. This is hindered by the large particle sizes of the starting products. Thus, two different milling methods are described in this chapter. A schematic overview of the conventional synthetic route described in this chapter is mentioned in figure 2.

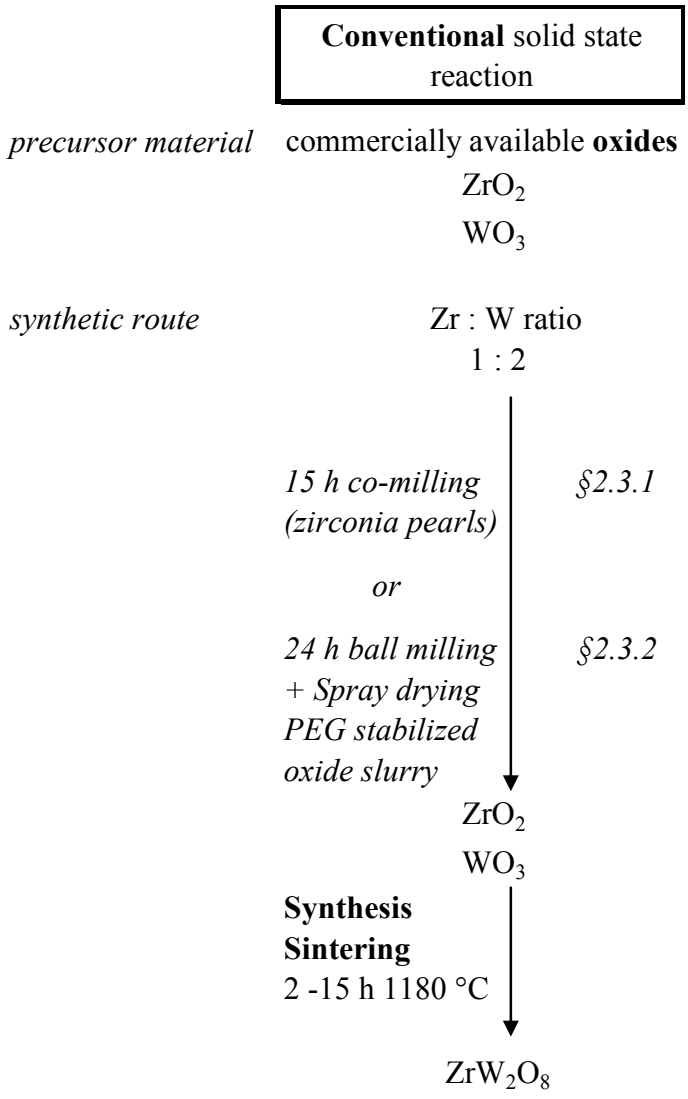

Figure 2: Detailed description of the conventional synthetic route

2.1 Phase diagram of ZrW_2O_8

The phase diagram published by Chang [6] (Chapter 1-§3, figure 24) shows the phase relations in the ZrO_2 – WO_3 system. A mixture containing 33 mol% ZrO_2 and 66 mol% WO_3 will lead towards the formation of pure ZrW_2O_8 when a temperature of 1105 °C is reached. The ZrW_2O_8 compound melts incongruently at 1257 °C to form ZrO_2 and a liquid phase. Below 1105 °C a dissociation of the negative thermal expansion material to ZrO_2 and WO_3 can be seen.

2.2 Characterization of ZrO_2 and WO_3 oxides

The materials used were purchased from Sigma - Aldrich (Germany). The product label mentioned a particle size less than 5 μm for ZrO_2 whereas the particle size of the WO_3 oxide powder is stated to have an average value of 20 μm.

2.2.1 ZrO_2 [8-10]

ZrO_2 is a white crystalline powder which can exhibit three different crystal structures. At room temperature, ZrO_2 exists as a monoclinic crystal which is converted to the tetragonal phase above 1200 °C. The material has a cubic structure at very high temperatures (> 2370 °C). Several oxides (MgO, CaO and Y_2O_3), which can dissolve in zirconia, slow down or eliminate these phase changes. When sufficient amounts of these oxides are added, the high temperature cubic structure can be maintained down to room temperature. The crystallographic information of the ZrO_2 polymorphs is given in table 1. The commercially obtained ZrO_2 powder has a monoclinic crystal structure with a theoretical density of 5.85 g/cm^3.

	Monoclinic	Tetragonal	Cubic
Space Group	$P2_1/c$	$P4_2/nmc$	Fm3m
Lattice constants [11]	a = 5.145 Å	a = 3.588 Å	a = 5.12 Å
	b = 5.208 Å	c = 5.188 Å	
	c = 5.311 Å		
	β = 99.23°		

Table 1: Crystallographic information of the ZrO_2 polymorphs extrapolated to room temperature

2.2.2 WO_3 [12-14]

Tungsten trioxide adopts at least five distinct crystallographic modifications between absolute zero and its melting point at 1700 K. When the temperature is decreased from the melting point the crystallographic symmetry for WO_3 changes as follows: tetragonal – orthorhombic – monoclinic – triclinic – monoclinic. The known polymorphs and their temperature ranges are given in table 2. All of the polymorphs of WO_3 can be described as distortions from the cubic ReO_3 structure (Chapter 1-§2.5.1). WO_3 undergoes at least four phase transitions, each one resulting from a change in octahedral tilting and/or cooperative tungsten shifts. Figure 3 illustrates the crystal structure of the triclinic polymorph of WO_3 with WO_6 octahedra as building blocks.

Phase	Symmetry	Space group	Temperature range (K)
α - WO_3	Tetragonal	P4/nmm	1010 – 1170
β - WO_3	Orthorhombic	Pmnb	600 – 1170
γ - WO_3	Monoclinic	$P2_1/n$	290 – 600
δ - WO_3	Triclinic	P-1	230 – 290
ε - WO_3	Monoclinic	Pc	0 – 230

Table 2: The thermal stability ranges of the WO_3 polymorphs at ambient pressure [13]

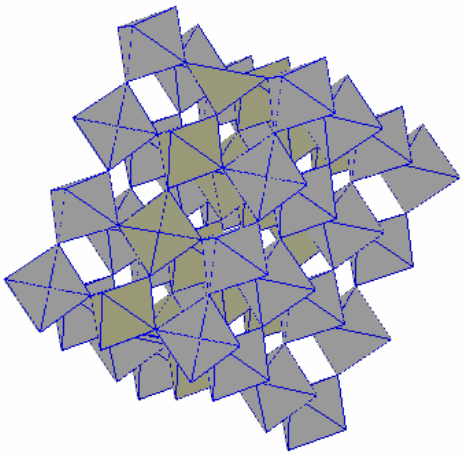

Figure 3: Crystal structure of Triclinic WO_3

The thermodynamically stable polymorph of WO_3 at room temperature is stated to be triclinic. Nevertheless the material often contains a mixture of the triclinic and monoclinic phase (table 3). It is very hard to distinguish these two phases by X-ray diffraction because of the small differences in unit cell dimensions as can be seen in table 3. The commercially obtained WO_3 is a green, crystalline powder and is most probably a mixture of triclinic (ρ = 7.282 g/cm^3) and monoclinic polymorphs (ρ = 7.278 g/cm^3).

	Triclinic [14]	Monoclinic [12]
Space Group	P-1	$P2_1/n$
Lattice constants [11]	a = 7.309Å	a = 7.301 Å
	b = 7.522 Å	b = 7.539 Å
	c = 7.686 Å	c = 7.689 Å
	α = 89.85°	
	β = 90.91°	β = 90.89°
	γ = 90.94°	

Table 3: Crystallographic information of triclinic and monoclinic WO_3

2.3 Preparation of the ZrO_2 – WO_3 oxide powder mixtures

ZrO_2 – WO_3 mixtures are prepared by milling in order to reduce the particle size of the oxide powders and to improve the homogeneity of the mixtures. Mechanical milling techniques used in this work consist of tumbler milling or a planetary ball mill.

2.3.1 Preparation of the oxide mixture by tumbler milling assisted by zirconia pearls

ZrO_2 – WO_3 powder mixtures in a 1 : 2 stochiometric ratio (1.05 g ZrO_2, 3.95 g WO_3) are brought into a horizontally disposed glass container (15 cm^3) and 5g zirconia pearls (Ø = 3.15 mm) are added in a 1 : 1 mass ratio. The glass recipient is closed firmly and the powder mixture is put on the rollers for 15 h. Figure 4 schematically shows how the milling time influences the particle size. 97 % decrease in particle size (d_{90}) is obtained after a period of 5 h. An additional milling period of 10 h is added to increase the homogeneity of the powder mixture. No further decrease in particle size can be seen during this time.

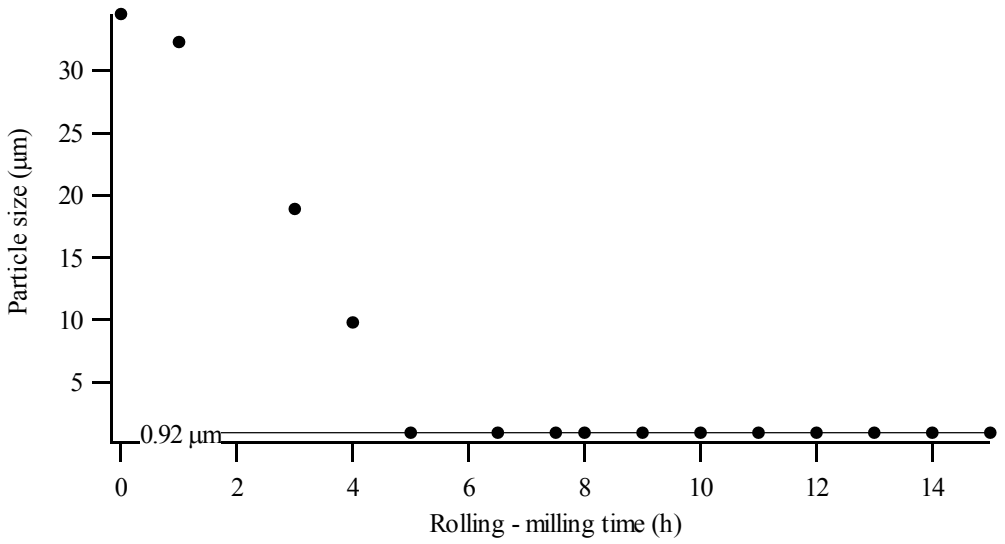

Figure 4: Influence of tumbler milling on the particle size (d_{90} value) of the oxide mixture

The particle sizes of the commercially obtained oxides powders and the powder mixtures before and after milling are given in table 4.

Material	Particle size	
	d_{50} (µm)	d_{90} (µm)
ZrO_2 (commercial)	3.15	6.54
WO_3 (commercial)	18.68	40.78
ZrO_2-WO_3 powder mixture before milling	7.92	34.54
ZrO_2-WO_3 powder mixture after 15 h tumbler milling	0.64	0.92

Table 4: Particle sizes of non-milled and milled powders

The oxide mixtures are pressed at 750 MPa into bars (2 mm × 2 mm× 13 mm). The next step is the thermal treatment at 1180 °C to synthesize ZrW_2O_8 which will be discussed in §2.4. The bars are very fragile before high temperature thermal treatment.

2.3.2 Preparation of the oxide mixture by ball milling and spray drying

The commercially available oxide powders are individually milled in this preparation route. 20 g of the oxide powders (15.8 g WO_3 and 4.2 g ZrO_2) are mixed and put in an agate mortar (50 cm^3) with 2 agate balls (Ø = 20 mm). By the use of this planetary ball mill, the powders are crushed for 24 h. As can be seen in table 5 the particle sizes are reduced in comparison with the non-milled commercial powders (table 4).

Material	Particle size	
	d_{50} (µm)	d_{90} (µm)
ZrO_2 (ball-milled, 24h)	1.06	5.14
WO_3 (ball-milled, 24h)	0.62	0.94
ZrO_2-WO_3 powder mixture (spray drying of the slurry)	0.79	2.12

Table 5: Powder specification after ball-milling and spray-drying of the slurry

The milled powders are mixed manually. For further manipulation of the mixed powders, they need to be pressed into bars. As mentioned before, it is very difficult to obtain nice and firm bars using small oxide particles. Therefore polyethylene glycol is added as pressing aid. The spray drying technique is used to obtain a thin layer of PEG around the oxide particles. This additive possesses the benefit of reducing the friction during pressing of the bars. Therefore the desired mixture of ball milled oxides is suspended in 250 ml deionised water together with 3 mass% polyethylene glycol (calculated on the mass of the oxides). The preparation of the slurry and stirring improves the homogeneity of the mixture. The water is removed using the spray drying technique (Büchi 190 mini spray dryer) with a 0.5 mm nozzle and a feeding rate of 5 ml per minute at inlet temperatures close to 250 °C. The set-up of the spray drying equipment is given in figure 5. The spray drying process consists of 4 major steps. (1) **Spraying of the liquid phase** – slurry into little droplets, (2) **Mixing** of the spray with a drying medium, (3) **Drying**: heat transfer of the gas to the droplets results in a mass transfer from the droplets to the gas molecules and (4) **Separation** of the formed particles from the gas medium.

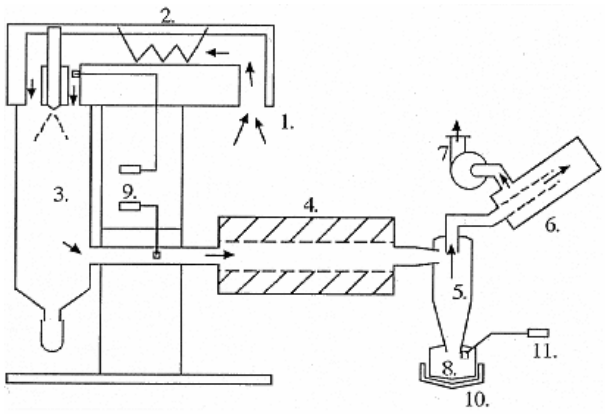

Figure 5: Schematic overview of a modified Büchi Spray Dryer: (1) Air inlet, (2) Oven, (3) Dry Chamber, (4) Quartz oven, (5) Cyclone, (6) Water cooling, (7) Aspirator, (8) Collector, (9) In- and outlet Temperature sensors, (10) heating (collector) and (11) Temperature sensor (collector)

The powder assembled in the reservoir consists of PEG coated ZrO_2 and WO_3 oxide particles. The final step is shaping of the oxide mixture (0.3 g) in small bars under the same conditions as mentioned above. This bars, compared to these obtained in the previous procedure, gained more strength due to the presence of the polyethylene glycol.

2.4 Synthesis and characterization of ZrW_2O_8

High temperature treatment of the oxide mixture induces the formation of ZrW_2O_8. The bars are inserted in a preheated furnace at 1180 °C for a period of 2-15 h. Afterwards the bars are immediately immersed into liquid nitrogen. This quenching step is necessary to avoid the decomposition of ZrW_2O_8 into ZrO_2 and WO_3 at temperatures below 1105 °C. Thus the metastable ZrW_2O_8 phase can be obtained at room temperature.

The X-ray diffraction pattern of an oxide mixture obtained by the ball milling – spray drying method described above and before thermal treatment is given in figure 6. From this diffraction pattern monoclinic ZrO_2 and triclinic (and monoclinic) WO_3 can be identified. Figure 7 shows the diffractograms of both ball milled and tumbler milled precursors after heat treatment. The materials obtained are largely identical and the majority phase is ZrW_2O_8.

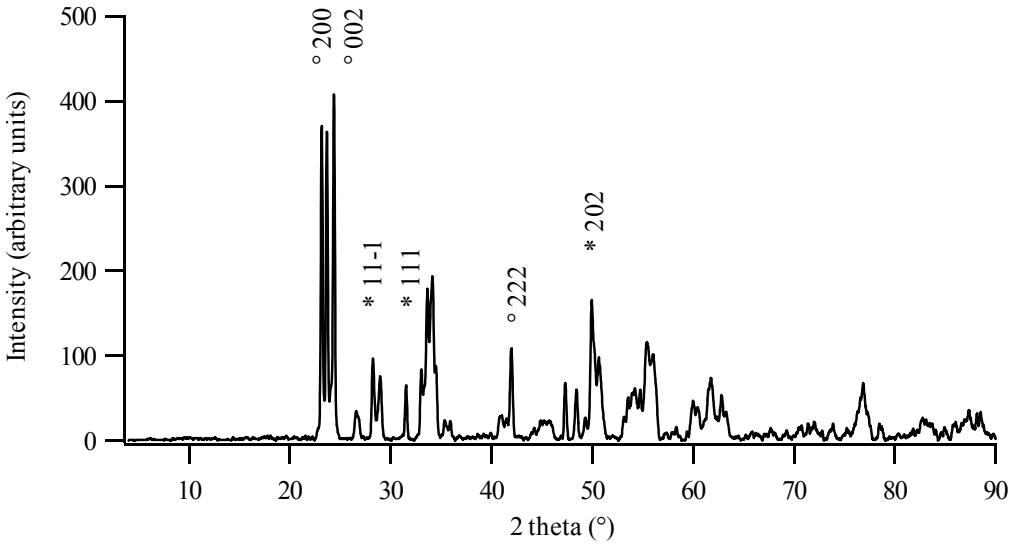

Figure 6: XRD-pattern of ZrO_2 – WO_3 oxide mixture (°): WO_3 reflections; (*) ZrO_2 reflections

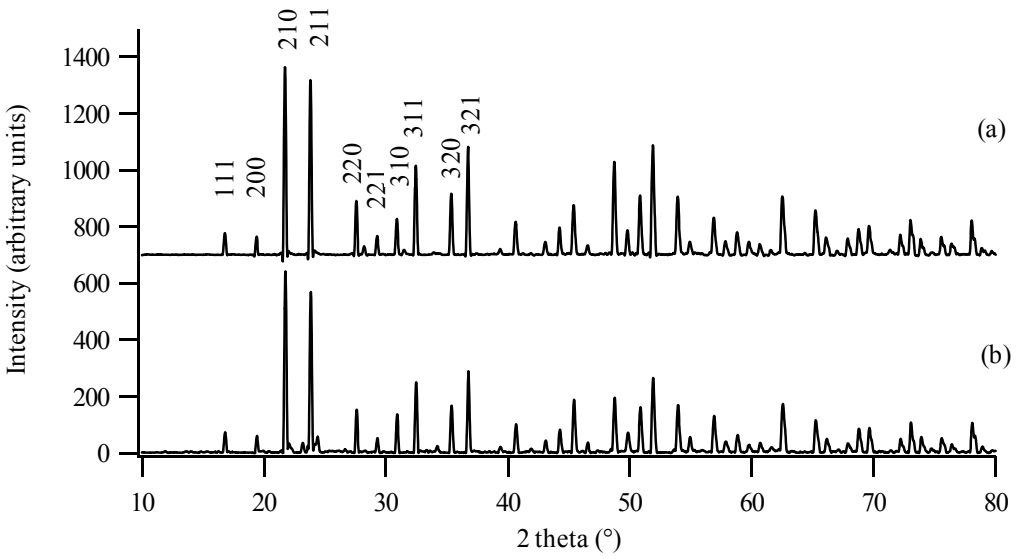

Figure 7: XRD-pattern of ZrW_2O_8 obtained by conventional solid state reaction. The ZrO_2 – WO_3 oxide mixtures are prepared by (a) tumbler milling or (b) ball milling - spray drying

Rietveld refinement was performed on ZrW_2O_8 obtained by conventional solid state reaction with tumbler-milling prepared oxide mixture. The input data[15] are mentioned in figure 8. The following parameters were refined: scale, background polynomial parameters, x,y,z positions, zero position, cell parameter a, U,V,W, shape. The output data with cell parameter a: 9.1585(1) are given in figure 9. The results of the refinements are given in figure 10. Chi^2 of the refinement is 7.38 (R_{exp}: 9.72; R_{wp}: 26.2 and $R(F^2)$: 11.3. The results show good resemblance with the data published by Mary *et al* [16].

Spacegroup : $P2_13$

a : 9.1569(3) Å α : 90°
b: 9.1569(3) Å β : 90°
c: 9.1569(3) Å γ : 90°

atom	occupancy	x/a	y/b	z/c
Zr1	1/3	0.0004(3)	0.0004(3)	0.0004(3)
W1	1/3	0.3409(3)	0.3409(3)	0.3409(3)
W2	1/3	0.6009(3)	0.6009(3)	0.6009(3)
O1	1	0.0529(3)	-0.2069(3)	-0.0619(4)
O2	1	0.0697(4)	-0.0575(3)	0.2132(3)
O3	1/3	0.4941(4)	0.4941(4)	0.4941(4)
O4	1/3	0.2322(3)	0.2322(3)	0.2322(3)

Figure 8: Input data for Rietveld refinement of ZrW_2O_8

a: 9.1585(1)	Å	α : 90°
b: 9.1585(1)	Å	β : 90°
c: 9.1585(1)	Å	γ : 90°

Figure 9: Output data file of the Rietveld refinement of ZrW_2O_8

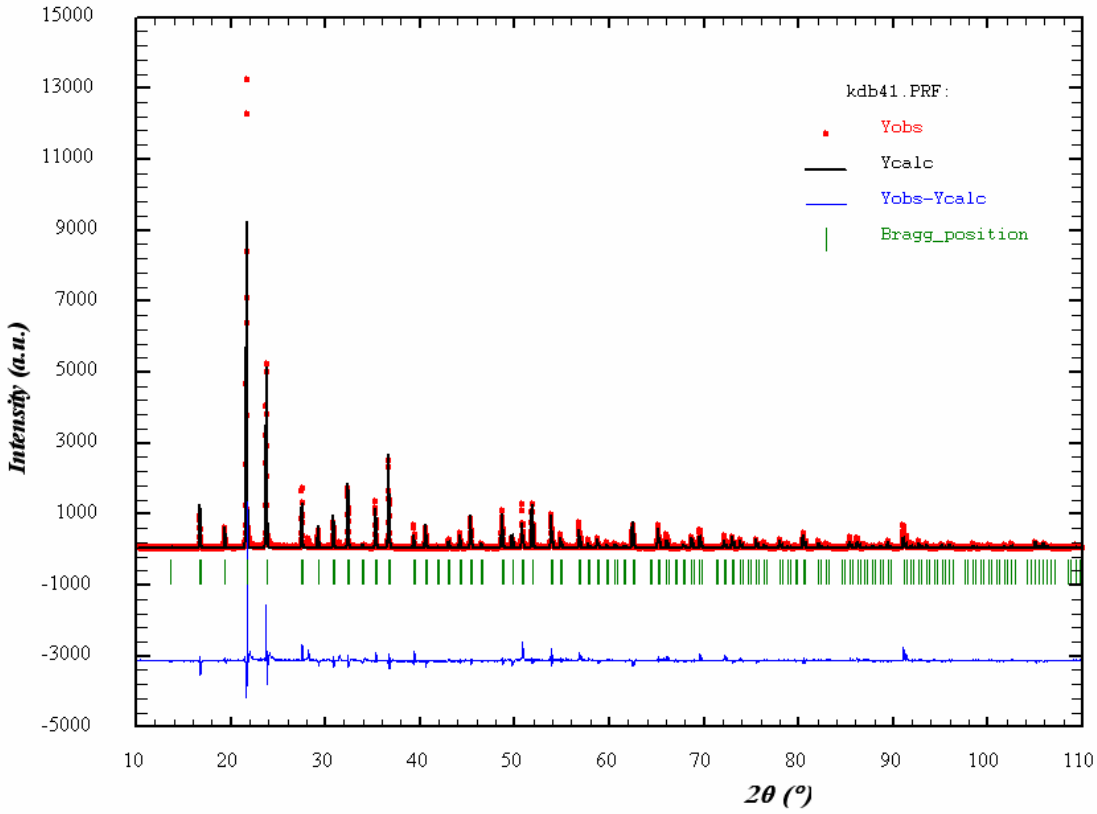

Figure 10: Graphical overview of Rietveld refinement of ZrW_2O_8

In addition to X-ray analysis as identification technique, Raman spectroscopy is very useful to determine whether the synthesis has been successful or not. The Raman spectrum of ZrW_2O_8 (figure 11) can be unraveled with the use of the table with Raman data (Chapter 2-§4). The most pronounced W – O vibrations are indicated.

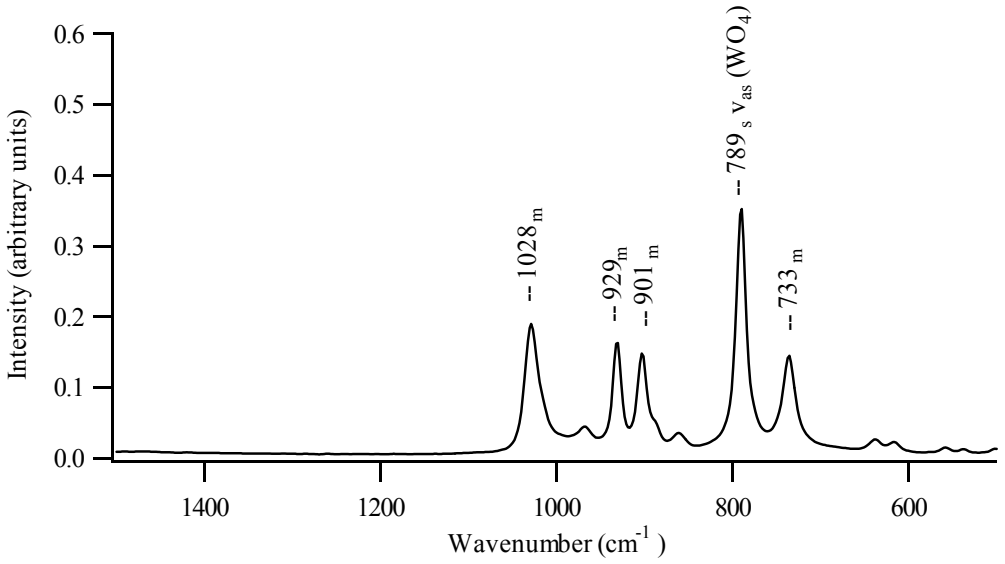

Figure 11: Raman spectrum of α-ZrW_2O_8 prepared by tumbler milled precursors after heat treatment

Finally, the thermal mechanical behaviour of the ZrW_2O_8 bars is tested and the results are shown in figure 12. The phase transition temperature, determined as the temperature at which the thermal expansion coefficient changes drastically, is determined as 162 °C from the derivative curve. The thermal expansion coefficient of the α-ZrW_2O_8 polymorph is -9.71 × 10^{-6} °C^{-1} (slope of the relative dimension change curve between room temperature and 125 °C) whereas for the β-phase a value of - 3.19 × 10^{-6} °C^{-1} (slope of the relative dimension change curve between 200 °C and 300 °C) can be noted.

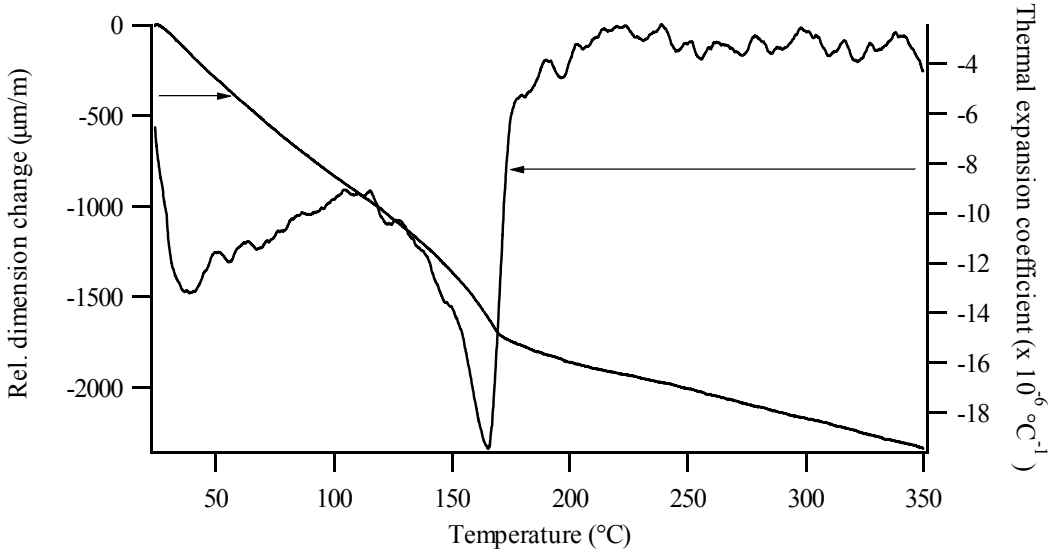

Figure 12: Thermal expansion properties of ZrW_2O_8 (oxide mixture - ball milling - spray drying)

Another important parameter is the morphology of the synthesized material. A scanning electron micrograph image of ZrW_2O_8, synthesized from PEG coated oxide powders heated at 1180 °C for 2h, is shown in figure 13. The evaporation of the polyethylene glycol at elevated temperatures causes pores within the ZrW_2O_8 samples. These results are compared with ZrW_2O_8 samples prepared out of tumbler milled oxide mixtures (figure 14). No PEG was present in the precursor mixture so no pores should be present. Nevertheless large pores can be seen presumably due to the evaporation of WO_3 and to poor stacking of the powder during pressing. The sublimation of WO_3 above 1130 °C can not be neglected and will affect the porosity of the ZrW_2O_8 sintered materials.

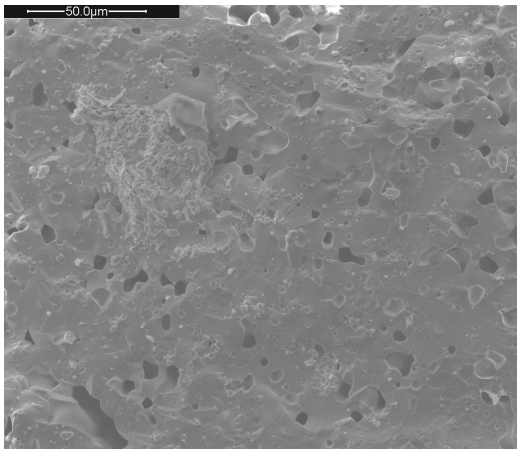

Figure 13: SEM micrograph of ZrW_2O_8 (oxide mixture prepared by ball milling - spray drying)

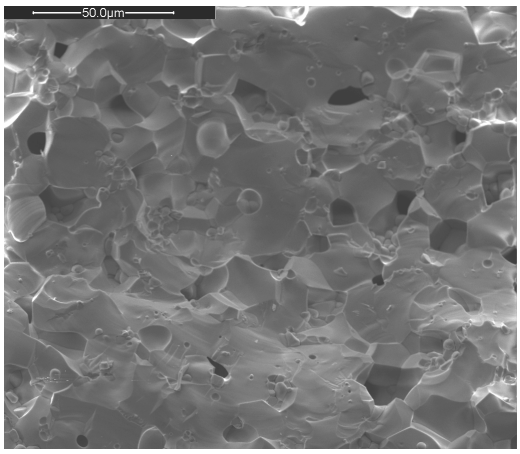

Figure 14: SEM micrograph of ZrW_2O_8 (oxide mixture prepared by tumbler - milling)

3 Conclusions

The conventional solid state reaction is a suitable synthesis method for the preparation of ZrW_2O_8. Conventional solid state reactions use commercially available oxides as precursor material. The oxides can be applied after co-milling in a tumbler mill or ball-milling. Ball milled powders are dispersed in a PEG slurry and spray dried to improve the homogeneity and to coat the oxide particles with a thin polyethylene glycol layer. This layer reduces the friction while pressing resulting in firm bars before the heat treatment. The oxide mixtures are submitted to a suitable temperature treatment including a high temperature treatment at 1180 °C for several hours which results in α - ZrW_2O_8.

The destruction of PEG at high temperatures leads to pores which can be detected by SEM. No organic material is used for the oxide mixtures which are treated in a tumbler mill. Nevertheless, pores can be seen in these materials after heat treatment. These pores are most likely due to poor stacking of the powder during pressing and evaporation of WO_3.

Alternatives can be found in the wet chemical routes. Water soluble salts, used as precursor material, can improve the homogeneity drastically. In the next chapter, sol-gel routes are described for the synthesis of ZrW_2O_8 material.

4 References

1. T. Hashimoto, T. Katsube, and Y. Morito, *Observation of two kinds of phase transitions of ZrW_2O_8 by power-compensated differential scanning calorimetry and high-temperature X-ray diffraction.* Solid State Communications, 2000. **116**: 129-132.

2. Y. Yamamura, N. Nakajima, and T. Tsuji, *Heat capacity anomaly due to the alpha-to-beta structural phase transition in ZrW_2O_8.* Solid State Communications, 2000. **114**: 453-455.

3. U. Kameswari, A.W. Sleight, and J.S.O. Evans, *Rapid synthesis of ZrW_2O_8 and related phases, and structure refinement of $ZrWMoO_8$.* International Journal of Inorganic Materials, 2000. **2**: 333-337.

4. C. De Meyer, L. Vandeperre, I. Van Driessche, E. Bruneel, and S. Hoste, *Processing effects on the microstructure observed during densification of the NTE-compound ZrW_2O_8.* Crystal Engineering, 2002. **5**: 469-478.

5. C. De Meyer, I. Van Driessche, and S. Hoste, *Synthesis of the negative thermal expansion compound ZrW_2O_8 by the spray drying technique.* Key Engineering Materials, 2002. **206-2**: 11-14.

6. L.L.Y. Chang, *Condensed phase relations in the systems ZrO_2-WO_2-WO_3 and HfO_2-WO_2-WO_3.* Journal of the American Ceramic Society, 1967. **44**: 211-215.

7. J. Graham, A.D. Wadsley, J.H. Weymouth, and L.S. Williams, *A new ternary oxide, ZrW_2O_8.* Journal of the American Ceramic Society, 1959. **42**: 570.

8. R.H. French, S.J. Glass, F.S. Ohuchi, Y.N. Xu, and W.Y. Ching, *Experimental and Theoretical Determination of the Electronic-Structure and Optical-Properties of 3 Phases of Zro2.* Physical Review B, 1994. **49**: 5133-5141.

9. C.J. Howard, R.J. Hill, and B.E. Reichert, *Structures of the Zro2 Polymorphs at Room-Temperature by High-Resolution Neutron Powder Diffraction.* Acta Crystallographica Section B-Structural Science, 1988. **44**: 116-120.

10. J. Bailar, H. Emeléus, R. Nyholm, and A. Trotman-Dickenson, *Comprehensive Inorganic Chemistry*. 1973, Oxford: Pergamon Press Ltd.

11. P. Southon, *Structural evolution during the preparation and heating of nanophase zirconia gels*. 2000, University of Technology: Sydney.

12. P.M. Woodward, A.W. Sleight, and T. Vogt, *Structure Refinement of Triclinic Tungsten Trioxide.* Journal of Physics and Chemistry of Solids, 1995. **56**: 1305-1315.

13. P.M. Woodward, A.W. Sleight, and T. Vogt, *Ferroelectric tungsten trioxide.* Journal of Solid State Chemistry, 1997. **131**: 9-17.

14. T. Vogt, P.M. Woodward, and B.A. Hunter, *The high-temperature phases of WO_3.* Journal of Solid State Chemistry, 1999. **144**: 209-215.

15. J.S.O. Evans, T.A. Mary, T. Vogt, M.A. Subramanian, and A.W. Sleight, *Negative thermal expansion in ZrW_2O_8 and HfW_2O_8.* Chemistry of Materials, 1996. **8**: 2809-2823.

16. T.A. Mary, J.S.O. Evans, T. Vogt, and A.W. Sleight, *Negative thermal expansion from 0.3 to 1050 Kelvin in ZrW_2O_8.* Science, 1996. **272**: 90-92.

Chapter 4

Sol-gel synthesis methods for ZrW_2O_8 materials

Novel sol-gel synthetic routes using water soluble precursor salts are described as a synthetic path for negative thermal expansion materials. These synthetic routes involve an adapted citrate-gel method and a sol-gel method with the use of EDTA as complexing agent and are described in detail.

Chapter 4-§3 is adapted from:

"Aqueous sol-gel processing of precursor oxides for ZrW_2O_8 synthesis"

K. De Buysser, P.F. Smet, B. Schoofs, E. Bruneel, D. Poelman, S. Hoste and I. Van Driessche

Published in Journal of Sol-Gel Science and Technology, 43 (2007) 347-353

"EDTA assisted sol-gel synthesis of ZrW_2O_8"

K. De Buysser, I. Van Driessche and S. Hoste

Submitted to Journal of Sol-Gel Science and Technology

1 Sol-gel chemistry [1]

The citrate-gel method described in this chapter is a sol-gel process [2-7]. The name sol-gel is an abbreviation for solution-gelling. This method employs judiciously chosen metal salts and complexants at a specific pH to form a stable, quasi solid gel in which homogeneity at the ionic level is preserved. The gel can be thermally reacted to form the required ceramic phases at elevated temperatures. This method has the potential technological advantages in comparison with other synthetic approaches, not only to achieve homogeneous mixing of the component cations on atomic scale, but also to form fibres or films from gels as shown in figure 1.

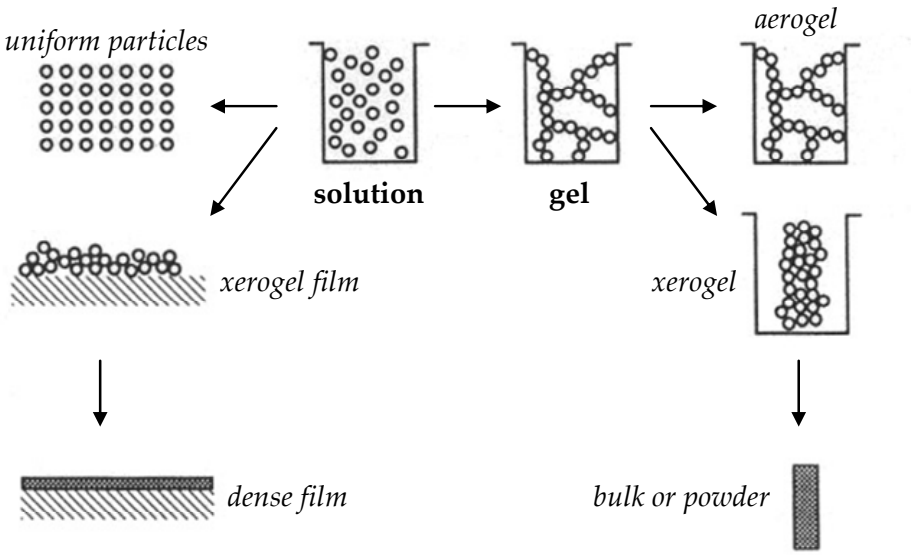

Figure 1: Overview of the sol-gel process [1]

The most demanding issue of sol-gel synthesis is the ability to prepare a stable precursor solution which can be transformed into a homogeneous gel. Hydrolysis of the metal cations and condensation (olation and oxolation) are the main reactions involved in the transformation of the solution to the gel.

1.1 Hydrolysis

When dissolved in pure water, metal cations, M^{z+}, are solvated by water molecules according to figure 2. There are three types of metal - ligands combinations present in hydrolysates depending of the water acidity and charge of the cation.

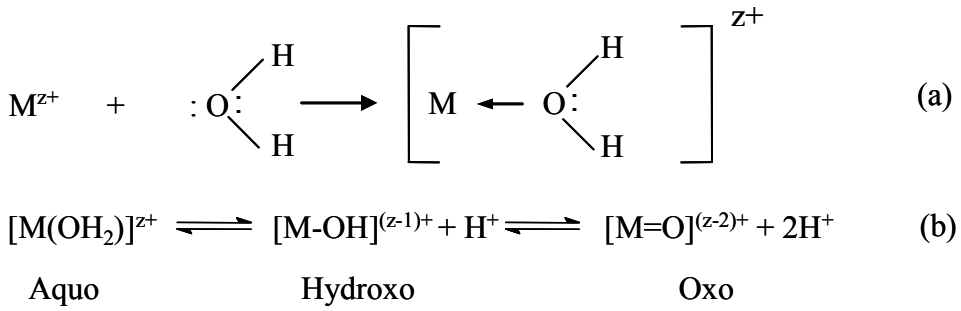

Figure 2: (a) Hydratation of cations (b) Different kinds of ligands obtained under controlled hydrolysis

1.2 Condensation reactions

Condensation reactions are chemical reactions which include the elimination of a small molecule such as H_2O, HCl… Two different types of condensation reactions are present in the aqueous sol-gel chemistry: olation and oxolation.

1.2.1 Olation

Olation is a condensation process in which a hydroxyl bridge is formed between two metal centers. The olation reaction corresponds to the nucleophilic addition of a negatively charged hydroxyl group onto a positively charged hydrated metal cation. Two examples of olation reactions are given in figure 3. Polycation species can be formed by olation reactions such as the zirconyltetramer mentioned in §2.4.

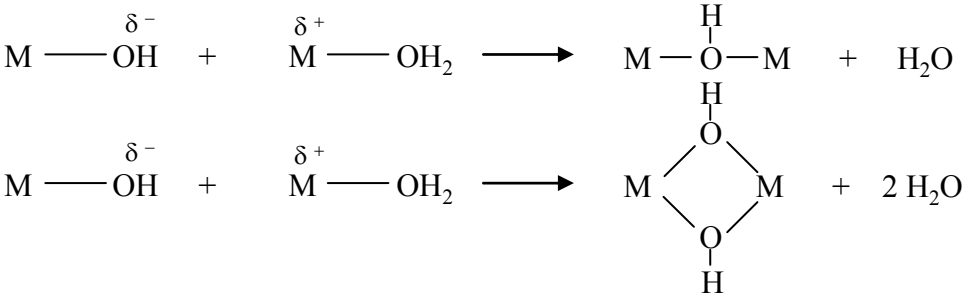

Figure 3: Olation mechanisms with formation of hydroxyl bridges

1.2.2 Oxolation

Oxolation is a condensation reaction in which an oxo bridge is formed between two metal centers. For coordinately unsaturated metals, oxolation can lead to edge- or face-share polyhedra as can be seen in figure 4(a). Nucleophillic addition followed by water elimination will form M – O – M bonds in the case of coordinately saturated metals (figure 4(b)).

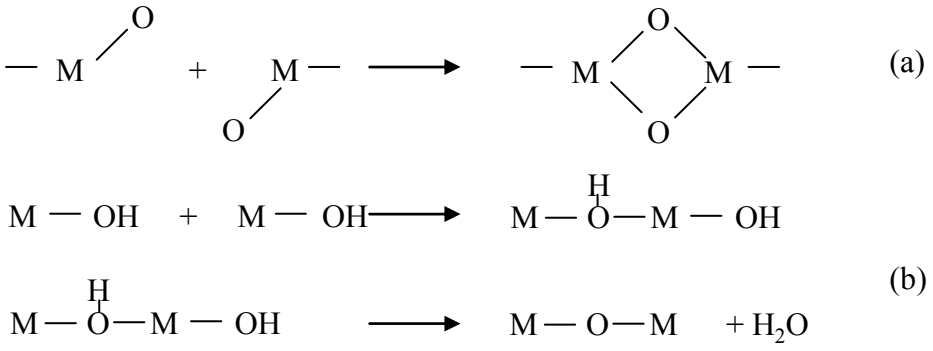

Figure 4: Oxolation reaction in coordinately unsaturated (a) and saturated (b) metal centers

2 Description of the Zirconium and Tungsten salts

Water soluble salts are utilized in our wet chemical routes. Three different kinds of zirconium salts are used: zirconyl nitrate ($ZrO(NO_3)_2.xH_2O$), zirconyl chloride ($ZrOCl_2.xH_2O$) and zirconium hydroxy acetate ($Zr(OH)_3OAc.xH_2O$). Ammonium metatungstate ($(NH_4)_6H_2W_{12}O_{40}.xH_2O$) is used as tungsten salt. These salts are characterized and described in the next sections §2.1 – 5.

2.1 Zirconyl chloride [1, 8-10]

2.1.1 Structure of zirconyl chloride

The structure of the $ZrOCl_2.xH_2O$ or $Zr(OH)_2Cl_2.(x-1)H_2O$ salt has been identified by X-ray diffraction. The crystalline structure consists of discrete $[Zr_4(OH)_8.16H_2O]^{8+}$ 'cyclic tetramer' cations, separated from each other in the lattice by chloride anions and water molecules. The four zirconium cations are at the corners of a slightly distorted square and are linked to each other by bridging hydroxyl-groups along each edge. Four water molecules around each Zr^{4+} ion complete the eight-fold coordination as can be seen in figure 5.

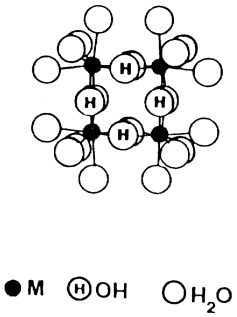

Figure 5: Structure of the zirconyl cyclic tetramer [1]

2.1.2 Thermal decomposition

TGA-DTA analysis gives detailed information about thermal decomposition of zirconyl chloride as can be seen in figure 6. The first small endothermic peak at 79 °C can be attributed to the loss of weakly bonded water. The next two endothermic peaks

coupled with a major weight loss are attributed to loss of water and hydrogen chloride. A small endothermic peak at 337 °C would be induced by halide removal [11-13]. The thermal decomposition is complete at 460 °C and ZrO_2 is formed. ZrO_2 crystallizes at 471 °C as can be seen by the small exothermic peak in the DTA signal.

The TGA-DTA data are used to determine the exact degree of hydration. Using the remain weight percentage of 39.72 % represented by ZrO_2 the exact molecular structure of the starting materials can be calculated: $Zr(OH)_2Cl_2.6.33H_2O$. Figure 7 and table 1 outline the reactions that most possible take place during the decomposition of zirconyl chloride.

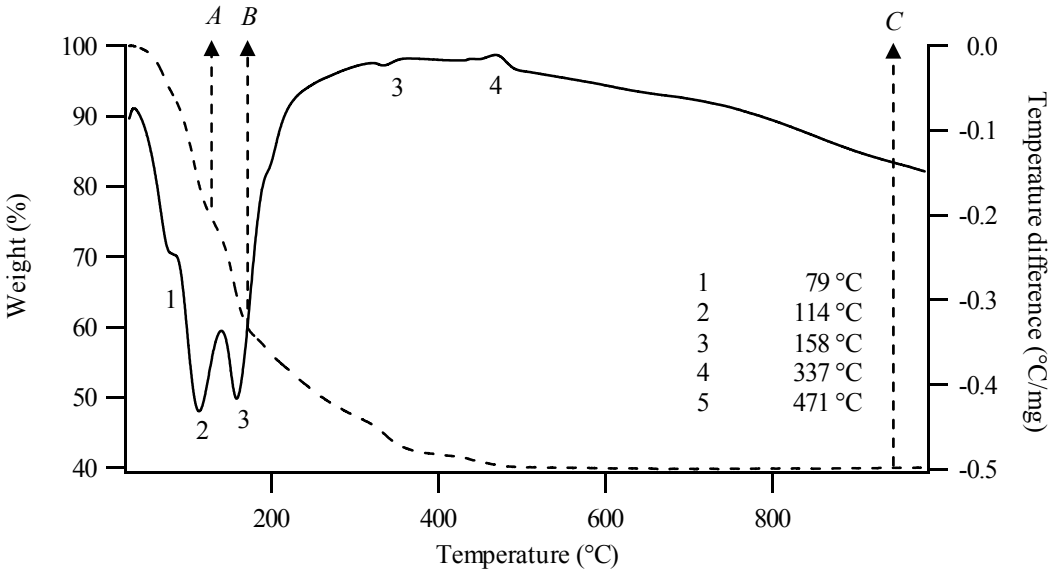

Figure 6: TGA-DTA analysis of zirconyl chloride - TGA signal (----) DTA signal (—)
Experiment performed under air, heating rate 5 °C /min, RT till 1000 °C

$$Zr(OH)_2Cl_2.6.33H_2O \longrightarrow Zr(OH)_2(H_2O)_3Cl_2 + 3.33\ H_2O \quad (1)$$

$$Zr(OH)_2(H_2O)_3Cl_2 \longrightarrow Zr(OH)_2Cl_2 + 3\ H_2O \quad (2)$$

$$Zr(OH)_2Cl_2 \longrightarrow ZrO_2 + 2\ HCl \quad (3)$$

Figure 7: Decomposition reactions of zirconyl chloride

	Reactions	Theoretical weight loss	Experimental weight loss
A	(1)	80.65 %	80.25 %
B	(2)	63.22 %	61.71 %
C	(3)	39.72 %	39.72 %

Table 1: Overview of the weight losses of zirconyl chloride detected by TGA-DTA

2.2 Zirconyl nitrate [10]

2.2.1 Structure of zirconyl nitrate

Zirconyl nitrate or $ZrO(NO_3)_2.xH_2O$ is the result of a hydrolysis reaction of zirconium nitrate ($Zr(NO_3)_4$) in water and acid solutions. The crystalline structure was solved from powder XRD data and the formula is better stated as $Zr(OH)_2(NO_3)_2.(4+x)H_2O$ ($x \leq 6$). The structure is made up of parallel cationic chains, with the repeating unit $[Zr(OH)_2(NO_3)(H_2O)_2]^+$ as can be seen in figure 8.

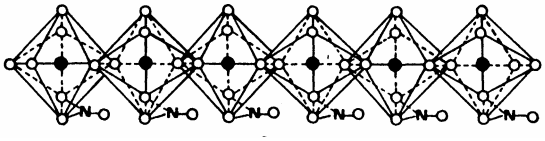

Figure 8: Cationic chains in zirconyl nitrate [10]

The zirconium atoms within each chain are linked by double hydroxyl bridges and each zirconium is coordinated by four bridging hydroxyl groups, two water molecules and a bidentate nitrate group. This structure can be visualized as 'cyclic-tetramers" that have been opened up and joined into a chain, with a nitrate group coordinated to each zirconium atom. For each zirconium atom, there are also 2 to 3 water molecules and an additional nitrate group located in between the chains. Half of the nitrate groups present in the formula are directly coordinated to the zirconium atoms and the other half are ionically bound between the chains in the crystal lattice.

2.2.2 Thermal decomposition

The thermal decomposition behaviour of zirconyl nitrate is given in figure 9. The first two peaks in the DTA signal can be attributed to endothermic reactions correlated with the loss of weakly bonded water and the conversion of uncoordinated nitrate groups to NO_x. The exothermic crystallization peak of ZrO_2 can be seen at 469 °C. The remaining weight percentage after complete decomposition being 37.16 % results in a hydration degree of 4.6 in the starting material $Zr(OH)_2(NO_3)_2.4.6H_2O$. The decomposition reactions and the corresponding weight losses are given in table 2.

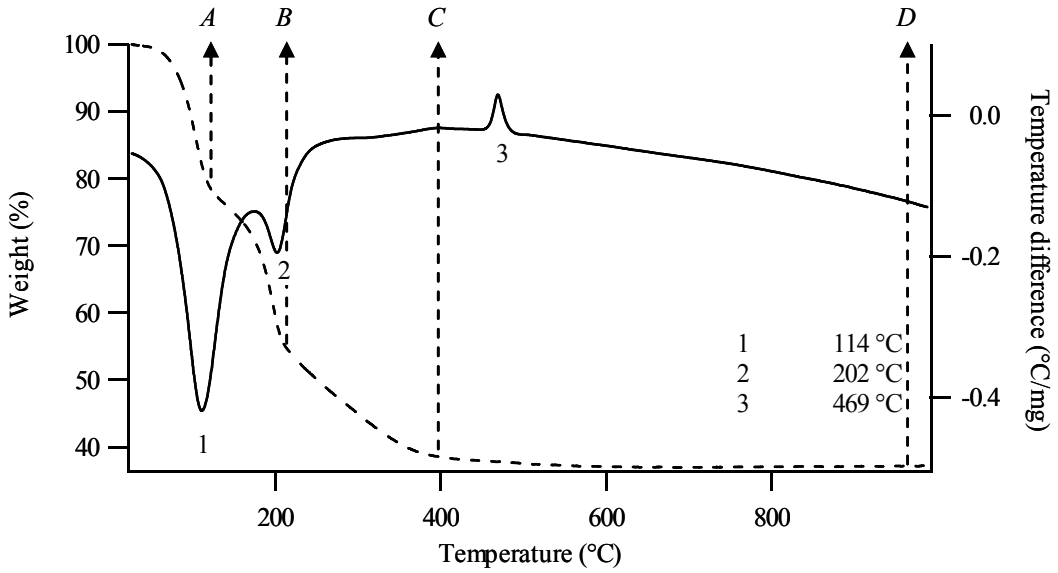

Figure 9: TGA-DTA analysis of zirconyl nitrate - TGA signal (----) DTA signal (—)
Experiment performed under air, heating rate 5 °C /min, RT till 1000 °C

$$Zr(OH)_2(NO_3)_2.4.6H_2O \longrightarrow Zr(OH)_2(H_2O)(NO_3)_2 + 3.6\,H_2O \quad (4)$$

$$2\,Zr(OH)_2(H_2O)(NO_3)_2 \longrightarrow Zr_2O_2(OH)_2(NO_3)_2 + 2\,NO_x + 3\,H_2O \quad (5)$$

$$Zr_2O_2(OH)_2(H_2O)(NO_3)_2 \longrightarrow Zr_2O_3(OH)_2 + 2\,NO_x + H_2O \quad (6)$$

$$Zr_2O_3(OH)_2 \longrightarrow 2\,ZrO_2 + H_2O \quad (7)$$

Figure 10: Decomposition reactions in zirconyl nitrate

	Reactions	Theoretical weight loss	Experimental weight loss
A	(4)	80.46 %	79.35 %
B	(5)	56.14 %	55.03 %
C	(6)	39.87 %	38.78 %
D	(7)	37.16 %	37.16 %

Table 2: Overview of the weight losses of zirconyl nitrate detected by TGA-DTA

2.3 Zirconium hydroxyl acetate [11-13]

2.3.1 Structure of zirconium hydroxyl acetate

Zirconium hydroxyl acetate also called zirconium oxy hydroxy acetate can be chemically expressed as follows: $Zr(OH)_3OAc.xH_2O$ or $ZrO(OH)OAc.(x+1)H_2O$ with the acetate group acting as a bidentate ligand. This compound is a basic zirconium acetate and can be precipitated from a $ZrO_2.xH_2O$ – acetic acid solution [14]. Mostly the chemical formula is given as follows: $Zr(OH)_x(OAc)_y.zH_2O$ with $x+y = 4$.

2.3.2 Thermal decomposition

Only a few peaks can be detected in the DTA signal obtained by the decomposition of zirconium hydroxyl acetate. The first endothermic peak at 41 °C is caused by the loss of weakly bonded water. The exothermic peak at 334 °C is due to the loss of acetate and hydroxyl groups and is associated with a large weight loss. Full loss of all carbon material is not achieved before 800 °C [15] as can be seen by a small endothermic peak at 723 °C accompanied by a small weight loss. All material is then converted into ZrO_2 with a remaining weight percentage of 57.77 % corresponding to a hypothetical molecular formula $Zr(OH)_3OAc.\ 0.67H_2O$. The decomposition reaction and the corresponding weight losses are given in figure 12 and table 3.

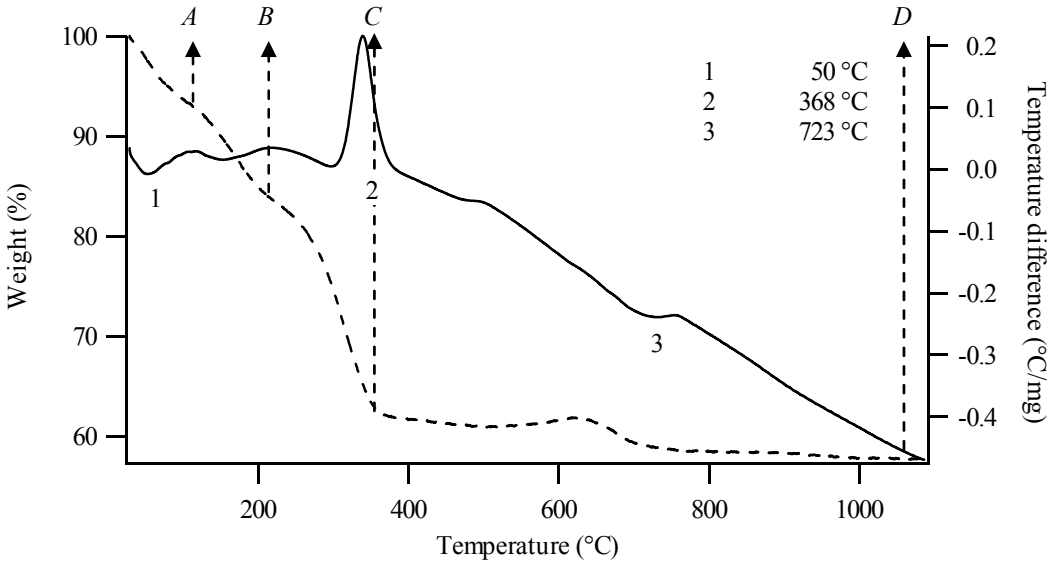

Figure 11: TGA-DTA analysis of zirconium hydroxy acetate - TGA signal (----) DTA signal (—) Experiment performed under air, heating rate 5 °C /min, RT till 1000 °C

$$Zr(OH)_3OAc.0.66H_2O \longrightarrow Zr(OH)_3OAc + 0.66\,H_2O \quad (8)$$

$$2\,Zr(OH)_3OAc \longrightarrow Zr_2O_2(OH)_2(OAc)_2 + 2\,H_2O \quad (9)$$

$$Zr_2O_2(OH)_2(OAc)_2 \longrightarrow Zr_2O_3(OH)_2 + 4\,CO_2 + 3\,H_2O \quad (10)$$

$$Zr_2O_3(OH)_2 \longrightarrow 2\,ZrO_2 + H_2O \quad (11)$$

Figure 12: Decomposition reactions in zirconium hydroxy acetate

	Reactions	Theoretical weight loss	Experimental weight loss
A	(8)	94.34 %	93.03 %
B	(9)	85.90 %	83.53 %
C	(10)	61.99 %	62.13 %
D	(11)	57.77 %	57.77 %

Table 3: Overview of the weight losses of zirconium hydroxyl acetate detected by TGA-DTA

2.4 The aqueous chemistry of the zirconium salts [10]

The chemistry of zirconium salt solutions is quite extensive. The Zr^{4+} compounds are very easily hydrolyzed (see §2.1). The zirconium atom favours seven or eight-fold oxygen coordination and in solution it will be surrounded by water or hydroxyl groups.. A number of polycation species can be formed in solution. The zirconium atoms are linked by hydroxyl (Zr-OH-Zr) bridges within these polynuclear species. The basic repeating structural unit is $[-Zr(OH)_2^{2+}-]$ with each zirconium atom linked to others by two hydroxyl bridges. Any given solution may have a range of species present, each with different units and degrees of hydrolysis. There are three main factors that control the size and structure of the cation species. *Solution* and *pH* determine the degree of hydrolysis and the equilibrium size of species, while the *anion* present may form complexes, thus influencing the bonding and geometry. Some anions, such as chloride interact very weakly, while others such as sulphate can form strong complexes and will compete with the hydroxyl groups to form bridges.

$ZrOCl_2$ solutions only contain the cyclic tetramer species, with $Zr_4(OH)_8^{8+}$ as polynuclear species core framework. The structure of the tetramer species consists of four zirconium atoms at the corners of a square, each joined by two bridging hydroxy groups (OH^b) along the edges. This is in strict correlation with the structure observed in solid $ZrOCl_2.xH_2O$ crystals. When dissolved in water, four water molecules and four hydroxy ($OH^{'}$) ligands will complete the eight-fold coordination around each zirconium atom and give a formula of $[Zr_4(OH^b)_8(OH')_h(H_2O)_{16-h}]^{(8-h)+}$. The example with h=8 is given in figure 13.

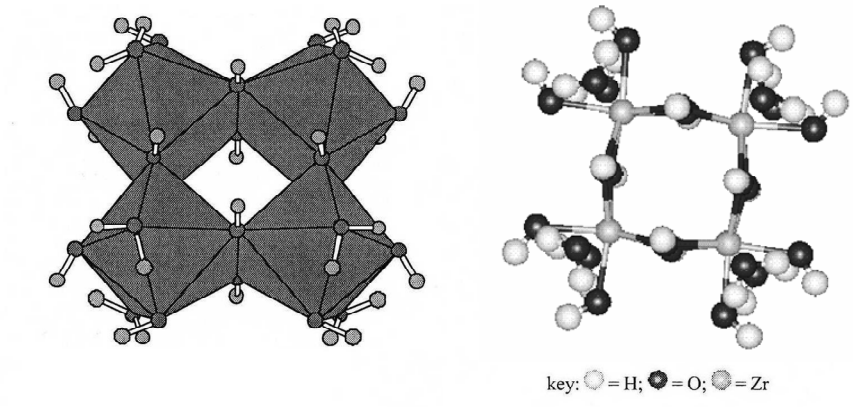

Figure 13: Illustration of the cyclic-tetramer cation (with h = 8) [10]

Although the polynuclear zirconyl species described in the previous section are reasonably stable at low pH, they are easily hydrolysed and thus susceptible to condensation reactions to form larger oligomers as can be seen in figure 14.

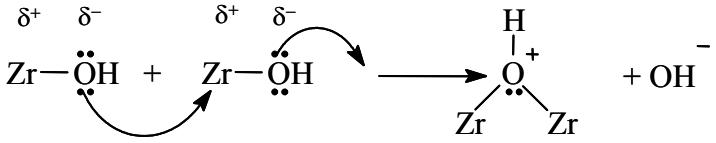

Figure 14: Condensation reaction between hydrolyzed zirconyl species

The condensation process may continue as a polymerization reaction to form colloidal particles and/or precipitates. The rate of condensation between species is particularly sensitive to the pH of the solution. The appearance of turbidity, indicating the precipitation of a solid, was observed in the range of pH 1.9 – 2.3. Coagulation of the precipitate occurs at pH 3.5. The condensation reactions are greatly accelerated at elevated temperatures (above 80 °C). When polymerisation is allowed above 90 °C, precipitation and crystallisation of the monoclinic zirconia phase takes place.

2.5 Ammonium metatungstate [8, 16-18]

2.5.1 Structure of ammonium metatungstate

The structure of the metatungstate anion $[H_2W_{12}O_{40}]^{6-}$ shown in figure 15, is composed of four identical 'tritungstate' groups. Each of these groups is made up of 3 WO_6 octahedra joined by shared edges. The four 'tritungstate' groups are then attached to each other by corner sharing, thus forming a cavity in which the two protons of the metatungstate ion are situated. The protons are strongly bonded and are necessary to maintain the stability of the structure.

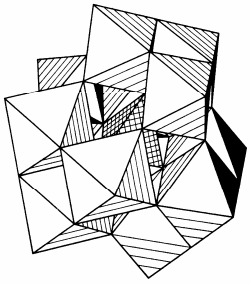

Figure 15: Structure of the metatungstate anion [8]

2.5.2 Thermal decomposition

The thermal decomposition of $(NH_4)_6H_2W_{12}O_{40}.xH_2O$ yields WO_3. The TGA-DTA data are given in figure 16.

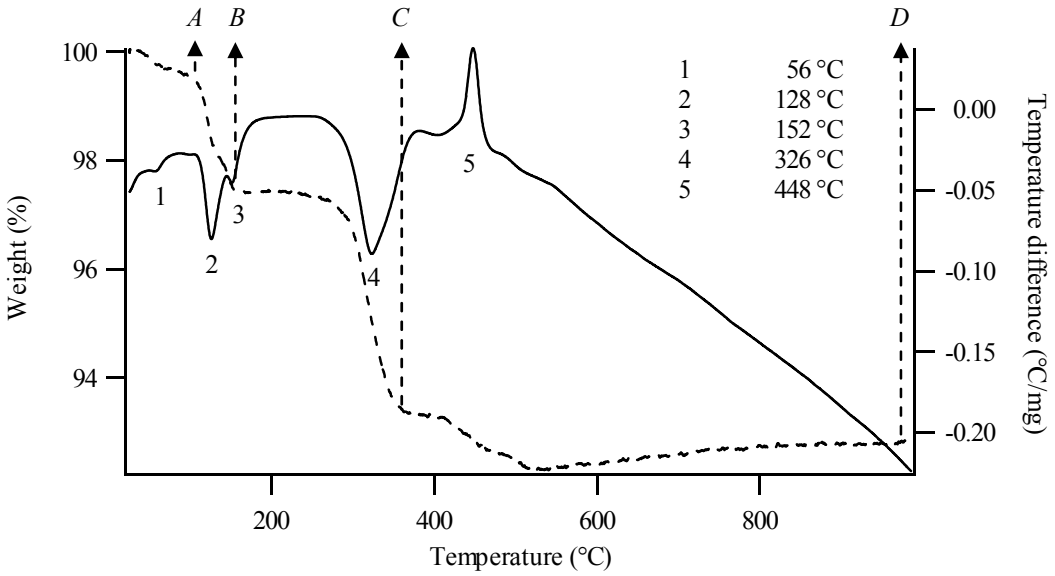

Figure 16: TGA-DTA analysis of ammonium metatungstate – TGA signal (dotted line) DTA signal (line) Experiment performed under air, heating rate 5 °C /min, RT till 1000 °C

4 endothermic peaks can be seen and attributed to the loss of H_2O and NH_3 gasses. The exothermic peak at 448 °C is the result of the decomposition of the intermediate $H_2W_{12}O_{40}$ product into crystalline WO_3. The remaining weight percentage of 92.86 % yields a hydration degree of 1.98 and gives the following formula: $(NH_4)_6H_2W_{12}O_{40}.1.98H_2O$.

	Experimental weight loss	Comments
A	99.37 %	Loss of 1 molecule H_2O or NH_3
B	97.44 %	Loss of 3.2 molecules H_2O or NH_3
C	93.33 %	Loss of 6.8 molecules H_2O or NH_3
D	92.86 %	Loss of 0.78 molecules of H_2O and formation of 12 molecules of WO_3

Table 4: Overview of the weight losses of ammonium metatungstate detected by TGA-DTA

2.6 The aqueous chemistry of the tungstate salts

Dissolving trioxides of tungsten in aqueous alkali will result in solutions containing WO_4^{2-} ions and simple tungstates such as $(NH_4)_2WO_4$ with a tetrahedral surrounding. These tungsten solutions can absorb large quantities of strong acid by mechanisms leading to formation of isopolytungstates with octahedral surrounding. When the tungsten solution is acidified, precipitates of colloidal tungsten oxide also called tungsten acid ($WO_3.H_2O$) are eventually formed. A lot of different polyanions are formed when the pH is varied between those two extremes. A simplified overview is given in figure 17. The polyanions are formed by condensation reactions with slow equilibration between the different species. The most important species are the paratungstates and metatungstates. The formation of the polyanions is influenced by concentration, temperature, counter anion and acidity.

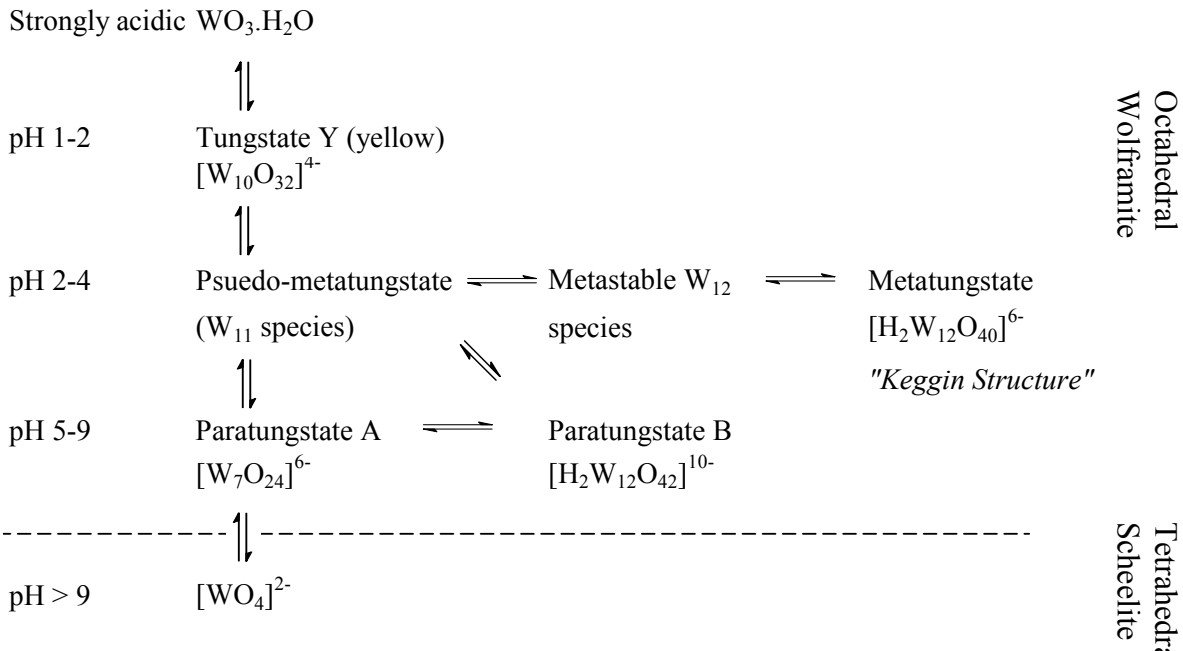

Figure 17: Reaction scheme for the condensation of tungstate ions in aqueous solutions

There is equilibrium between the tetrahedral tungstate and the metatungstate as given below.

$$18\,H^+ + 12WO_4^{2-} \rightleftharpoons H_2W_{12}O_{40}^{6-} + 8H_2O$$

3 Citrate-gel processing of ZrW_2O_8

3.1 Coordinative properties of citric acid

In the so-called citrate gel process, citric acid (figure 18) acts as a metal-ion complexant to assure the formation of a homogeneous and stable precursor solution. Citric acid is very suitable as complexant due to the presence of four potential coordinating functional groups and it simultaneously forms a three-dimensional network using its different functional groups (One -OH and three -COOH groups). The formation of this three-dimensional network in the liquid state insures the homogeneity and applicability by maintaining a liquid sol-gel state but reducing the mobility of ionic and chelated species.

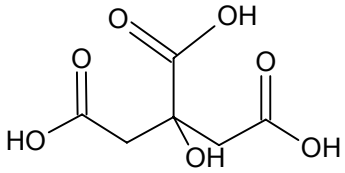

Figure 18: Molecular structure of citric acid

Rajendran et al [19] described the citrate coordination in the zirconyl tetramer in which only the carboxylgroups are involved in the complexation as shown in figure 19. In our opinion, the structure of the tetramer is not correct as the zirconium atoms are linked by oxygen atoms instead of hydroxyl bridges as stated in §2.4.

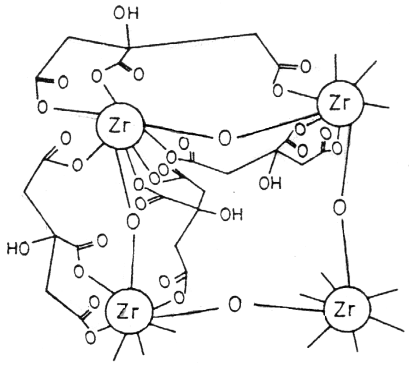

Figure 19: Coordination of the zirconyl tetramer by citric acid [19]

The coordination of citric acid is investigated using IR. Characteristic symmetric and asymmetric carboxylate stretching modes are found around 1400 cm^{-1} and 1600 cm^{-1} respectively. No free carboxyl groups remain after the complexation as indicated by the absence of a band around 1720 cm^{-1}.The typical C-O stretch associated with a tertiary hydroxyl group, R_3C-OH lies around 1050 cm^{-1} – 1100 cm^{-1} in citric acid and can also be detected in the gel compound.

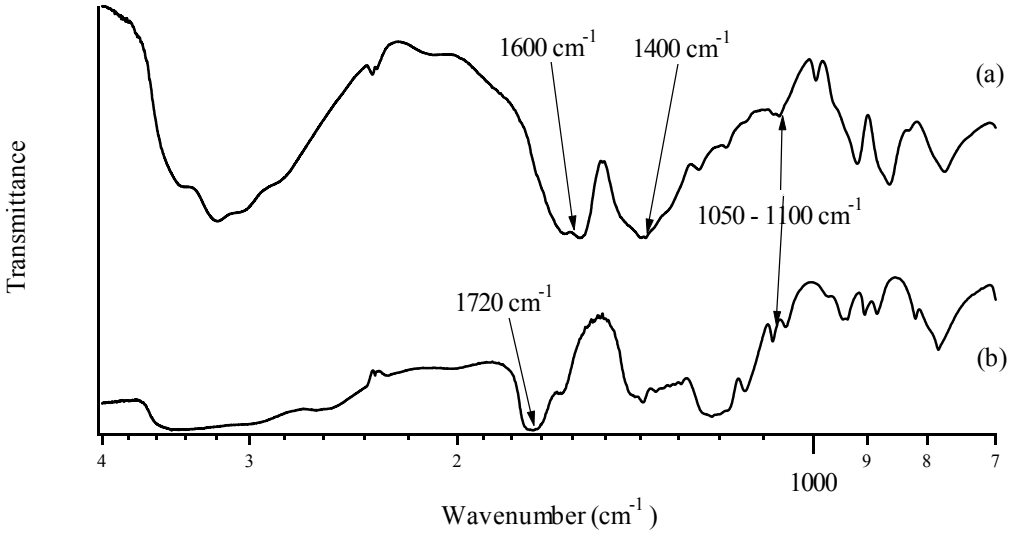

Figure 20: IR spectra of (a) gel obtained from a solution containing zirconium oxychloride, ammonium metatungstate and citric acid as chelating compound and (b) citric acid

The coordination has already been studied by TGA-DTA analysis [20]. Therefore, the thermal decomposition of the complexes is analysed by simultaneous TGA-DTA and additional information is collected by IR-spectroscopy of thermally treated powders in a muffle furnace. The experiments are carried out from room temperature to 900 °C. The typical R_3C-OH stretch at 1050 cm^{-1} – 1100 cm^{-1} is still present in the IR-spectra of powders which are heated from room temperature up till 300 °C. At higher temperatures, the stretch mode disappears. The thermal decomposition mechanism of pure citric acid describes the loss of the tertiary hydroxyl group at 140 °C [21, 22]. In our case, the tertiary hydroxyl group is thus very probably stabilized due to the coordination of this tertiary C-OH group to the metal cations. Hereby, it can be infered that all functional groups of citric acid are involved in the complexation.

3.2 Screening of ideal sol-gel conditions for the preparation of the precursor gels

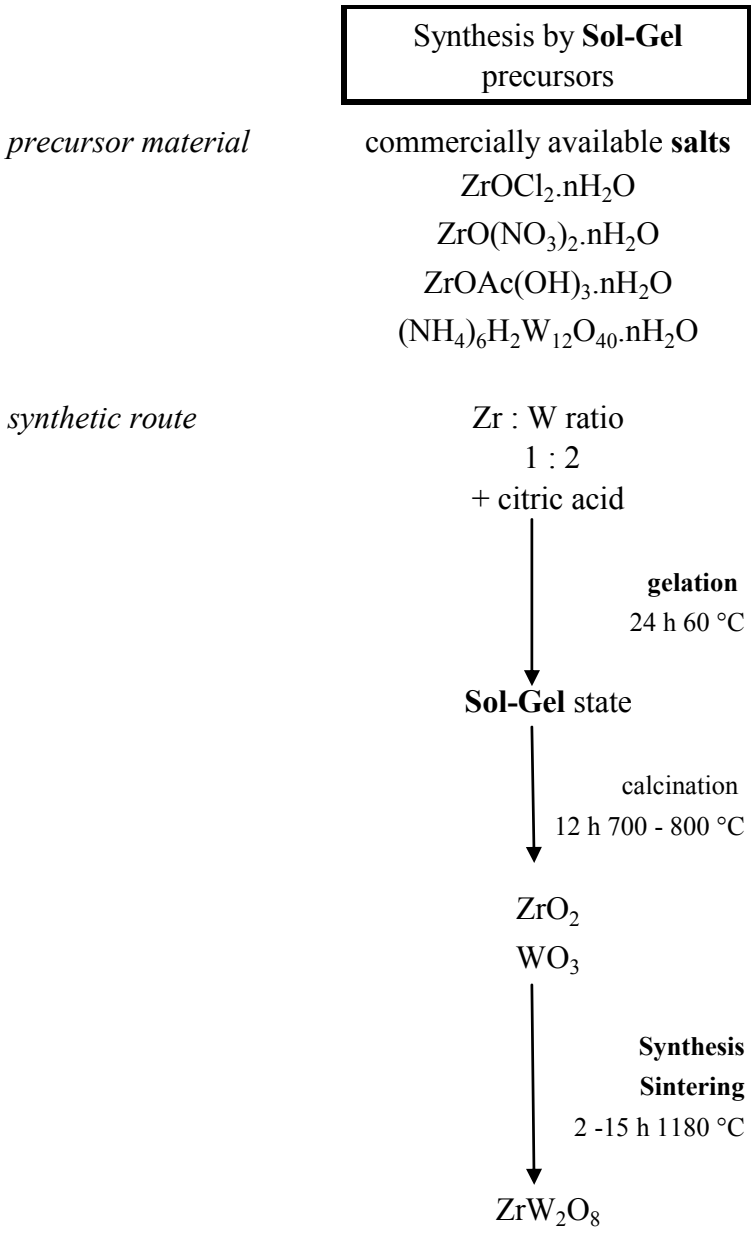

Figure 21: Detailed description of the sol-gel synthetic route

Figure 21 mentions the different synthesis steps in the citrate-gel process of ZrW_2O_8. As can be seen in this figure, the first important step is the mixing of the metals salts and the formation of a homogenous precursor solution. Storing these solutions in the drying furnace at 60 °C for a period of 24 h will induce olation and oxolation reaction resulting in a highly viscous gel network.

At room temperature, $ZrOCl_2.xH_2O$ (6.20 g, 20 mmol) was dissolved in 50 mL water whereas 50 mL water was added to $(NH_4)_6H_2W_{12}O_{40}.xH_2O$ (9.99 g, 3.33 mmol). Mixing of those two solutions would immediately induce the precipitation of Zr^{4+}-ions when dissolved in an aqueous solution of $(NH_4)_6H_2W_{12}O_{40}.xH_2O$. This would induce co-precipitation of the salts. The complexing agent citric acid (CA) was added to the Zr^{4+} solution to avoid the precipitation. It is necessary to determine the metal ions/complexant ratio and pH needed in the synthesis. Therefore the metal ions/complexant ratio was varied from 1 to 6 whereas NH_4OH was added to vary the pH between 0 and 7. The different combinations are mentioned below and photographs of the gel after 12 h in the drying furnace at 60 °C are given. This temperature treatment induces the transformation of solution to gel.

3.2.1 $ZrOCl_2.xH_2O$ - $(NH_4)_6H_2W_{12}O_{40}.xH_2O$ – citric acid (Ratio Zr^{4+} : CA 1:1)

Mixing of the $ZrOCl_2.xH_2O$: citric acid solution (1:1) and the aqueous ammonium metatungstate solution resulted in the formation of a white precipitation. The pH of the mixed solution was 0.03, addition of NH_4OH dissolved the precipitate at pH 6.82. The solution was transferred to a Petri disk and placed in a drying furnace for 24 h at 60 °C. Figure 22 shows that no clear gel is obtained and a white cackled product is left behind in the Petri disk. These conditions are thus not suitable for the sol-gel synthesis of ZrW_2O_8.

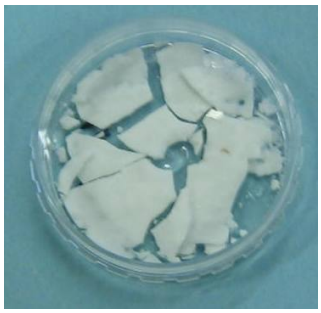

Figure 22: $ZrOCl_2.xH_2O$ - $(NH_4)_6H_2W_{12}O_{40}.xH_2O$ citrate gel (1:1 - pH 6.83)

3.2.2 $ZrOCl_2.xH_2O$ - $(NH_4)_6H_2W_{12}O_{40}.xH_2O$ – citric acid (Ratio Zr^{4+} : CA 1:2)

The ratio of zirconium ion : citric acid was increased to 1:2. The concentrations of metal salts used were kept constant. The solution obtained by mixing the two solutions was a clear and colourless solution with a pH value of 0. NH_4OH was added in small amounts to obtain several samples with varied pH values. All samples were submitted to a gel step and the results are shown below in figure 23. The sample with the lowest pH resulted in a precipitation of all salts whereas the more basified samples obtained a "jelly" structure but with traces of white precipitation. For further use, a clear gel is an absolute necessity.

Figure 23: $ZrOCl_2.xH_2O$ - $(NH_4)_6H_2W_{12}O_{40}.xH_2O$ citrate gel (1:2)

3.2.3 $ZrOCl_2.xH_2O$ - $(NH_4)_6H_2W_{12}O_{40}.xH_2O$ – citric acid (Ratio Zr^{4+} : CA 1:3)

A further increase of the zirconium ion : citric acid ratio was necessary and the results are shown in figure 24. All samples yielded high viscosity gels but again precipitation was detected but less pronounced than in the earlier mentioned samples. The aqueous solution obtained before gelling was clear and colourless (pH 0).

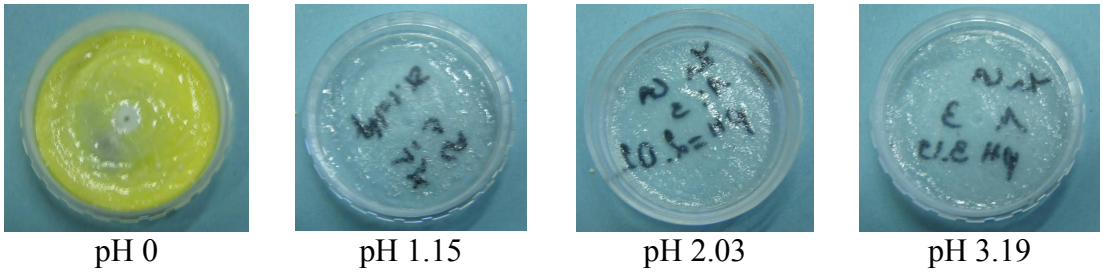

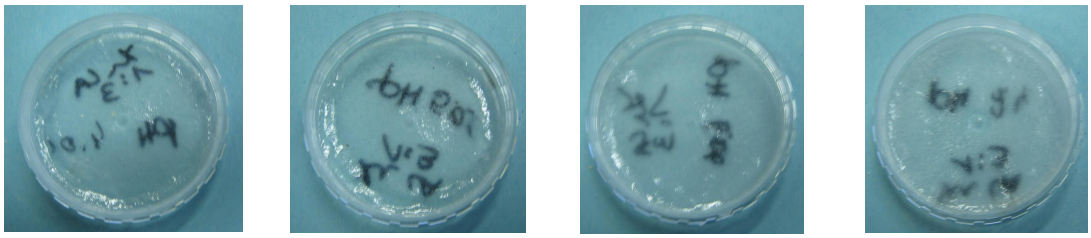

pH 4.06 pH 5.06 pH 6.06 pH 7.40

Figure 24: $ZrOCl_2.xH_2O$ - $(NH_4)_6H_2W_{12}O_{40}.xH_2O$ citrate gel (1:3)

3.2.4 $ZrOCl_2.xH_2O$ - $(NH_4)_6H_2W_{12}O_{40}.xH_2O$ – citric acid (Ratio Zr^{4+} : CA 1:4)

As can be seen from figure 25, an extra amount of citric acid till the zirconium ions : citric acid ratio reached a value of 1:4 was not sufficient to obtain clear gels after the gelation at 60 °C. A diminution of precipitates can be seen which is most pronounced as the pH of the precursor solution increases. The ideal parameters for the precursor solution will be most likely a zirconium ion : citric acid ratio above 1:5 and pH values around 7.

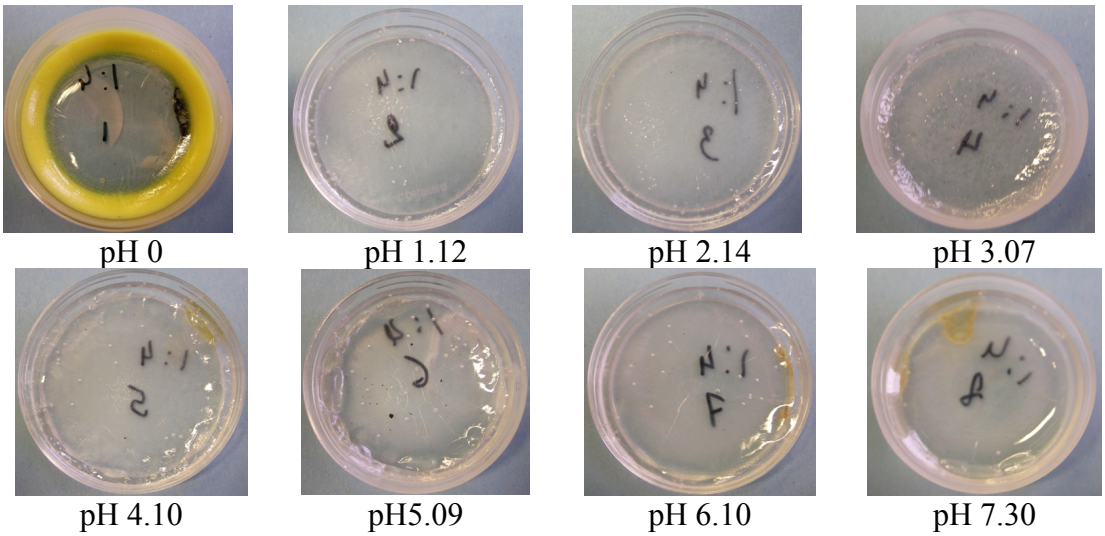

pH 0 pH 1.12 pH 2.14 pH 3.07

pH 4.10 pH5.09 pH 6.10 pH 7.30

Figure 25: $ZrOCl_2$ - $(NH_4)_6H_2W_{12}O_{40}.xH_2O$ citrate gel (1:4)

3.2.5 $ZrOCl_2.xH_2O$ - $(NH_4)_6H_2W_{12}O_{40}.xH_2O$ – citric acid (Ratio Zr^{4+} : CA: 1:5)

As already suggested by the previous experiment a clear gel was indeed obtained using a 1:5 ratio and adding NH_4OH until pH 7.17 was reached. The last picture in figure 26 shows a clear, transparent gel without the presence of any precipitates. This could be a suitable candidate for further synthesis.

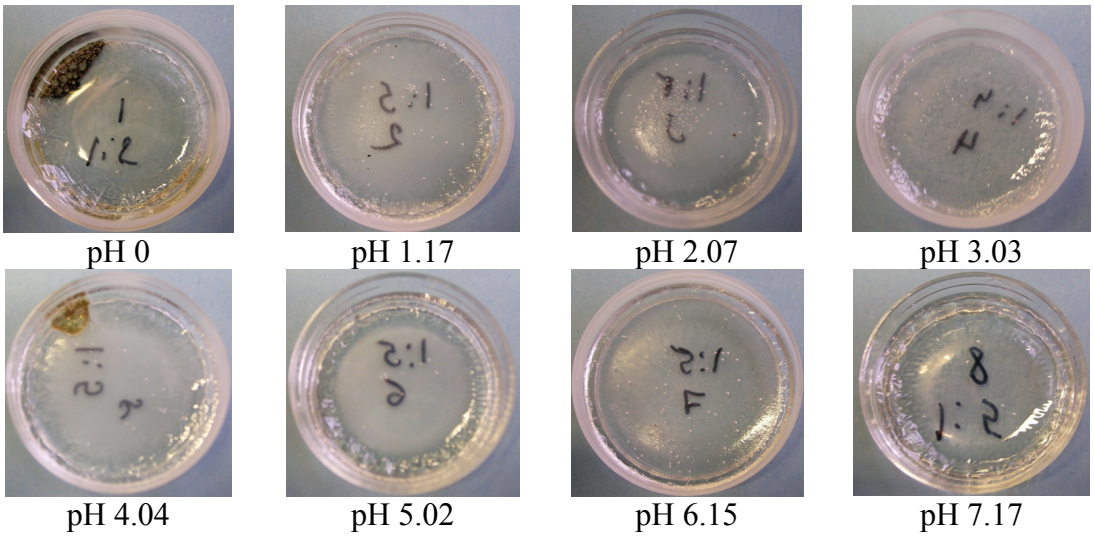

Figure 26: $ZrOCl_2.xH_2O$ - $(NH_4)_6H_2W_{12}O_{40}.xH_2O$ citrate gel (1:5)

3.2.6 $ZrOCl_2.xH_2O$ - $(NH4)_6H_2W_{12}O_{40}.xH_2O$ – citric acid (Ratio Zr^{4+} : CA 1:6)

The aqueous solutions with a zirconium ion : citrate ratio of 1:6 described in this work yielded perfectly clear and colourless solutions with a low pH (1.4) due to the use of citric acid. Samples at varied pH were put aside in the drying furnace to allow gelling of the precursor solutions. The results are given in figure 27. Clear and colourless gels were obtained at each pH value. We decided to use a zirconium ion : citric acid ratio of 1: 6 at a pH value of 7 for all further experiments. Although the whole pH range of 1-7 was suitable, a value of 7 is safer when keeping the possible industrial application of this synthetic route in mind.

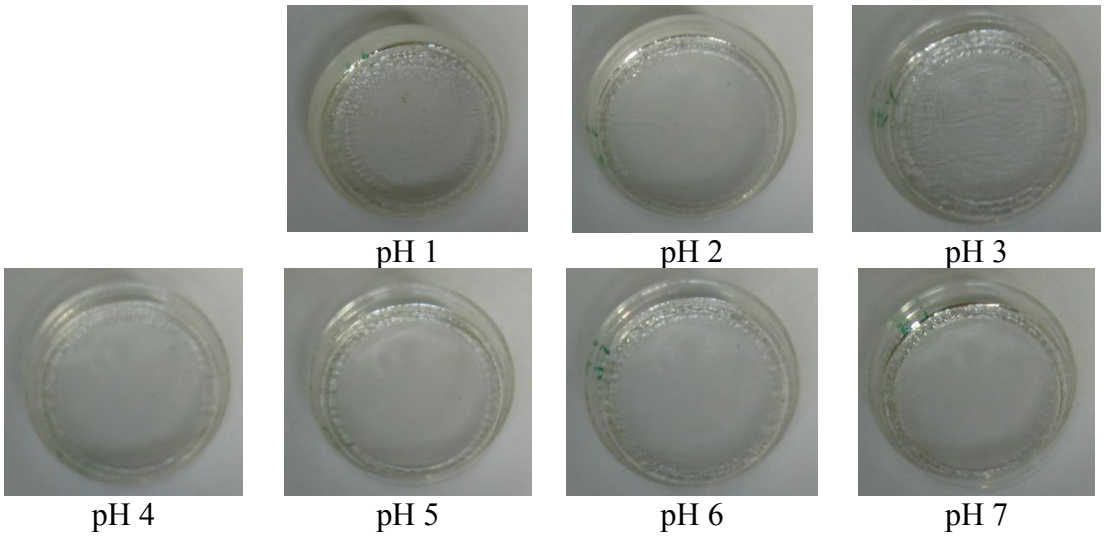

Figure 27: $ZrOCl_2.xH_2O$ - $(NH_4)_6H_2W_{12}O_{40}.xH_2O$ citrate gel (1:6)

Similar tests were performed for the gels using $ZrOAc(OH)_3$ and $ZrO(NO_3)_2$. In a zirconium ion : citric acid ratio of 1:6, NH_4OH must be added until pH 7 is reached in case of the zirconium oxynitrate salts. To avoid precipitation in the case of the $ZrOAc(OH)_3$ based gels, the amount of NH_4OH necessary is higher and stable gel is obtained at pH 10. All gels were colourless immediately after removal out of the furnace. This is an important observation in view of later findings in relation to photochromic behaviour.

3.3 Synthesis of ZrW_2O_8

After preparation of the precursor gels, a thermal treatment is necessary to transform the three-dimensional gel structures into crystals of ZrW_2O_8 with negative thermal expansion. This thermal treatment consists of two steps. In the first heating step (12h at 700 / 800 °C) all organic material is removed and the gel is converted into oxides. For the zirconyl nitrate based gels, the efficient and complete removal of citric acid occurs in an autocatalytic combustion reaction induced by the presence of nitrate anions and can be formalized as follows:

$$ZrO(NO_3)_2 + {}^{1}/_{6}\,(NH_4)_6H_2W_{12}O_{40} + {}^{5}/_{9}\,C_6H_8O_7.H_2O$$

$$\downarrow$$

$$ZrO_2 + 2\,WO_3 + {}^{10}/_{3}\,CO_2 + {}^{31}/_{9}\,H_2O + N_2 + NH_3$$

The reaction is fast, yields high purity and homogeneous, crystalline foams which can be used in a further solid state reaction [23]. Comparable reactions occur in the gels manufactured with other zirconium salts.

The decomposition is associated with a gas production which leads to a spongy structure and fine oxide particles. After grounding the spongy structure in an agate mortar, these oxide mixtures were pressed at 750 MPa into small bars (2mm × 2mm × 13mm) and were subjected to a second heating step of 2 hours at 1180 °C in a preheated furnace. To avoid decomposition of ZrW_2O_8 into ZrO_2 and WO_3, this sintering process is directly followed by a quenching step from 1180 °C to -196 °C by immediate immersion into liquid nitrogen. Afterwards, the samples are allowed to heat to room temperature.

The thermal treatment of the decomposing gels was investigated by XRD. In figure 28 the diffraction peaks are given after the decomposition of a gel containing 0.2 M $ZrOCl_2.xH_2O$, 0.033 M $(NH_4)_6H_2W_{12}O_{40}.xH_2O$ and 1.2 M citric acid. The pH was set at the optimal value of 7 and the two temperatures examined were 700 °C and 800 °C. Crystalline material was only obtained above 700 °C. When we compare pattern (a) with pattern (b), not all peaks are well defined and the intensity as well as the sharpness of the peaks improved drastically when the calcination temperature is set at 800 °C. All the diffraction peaks of the oxides formed after the calcination step using the 3 different Zr^{4+} salts can be identified either as the reflections of WO_3 or ZrO_2. Figure 29 outlines the diffraction pattern of ZrW_2O_8 after sintering at 1180 °C. All peaks can be identified as α-ZrW_2O_8. The 4 most intense reflections (210), (211), (311) and (321) are indicated.

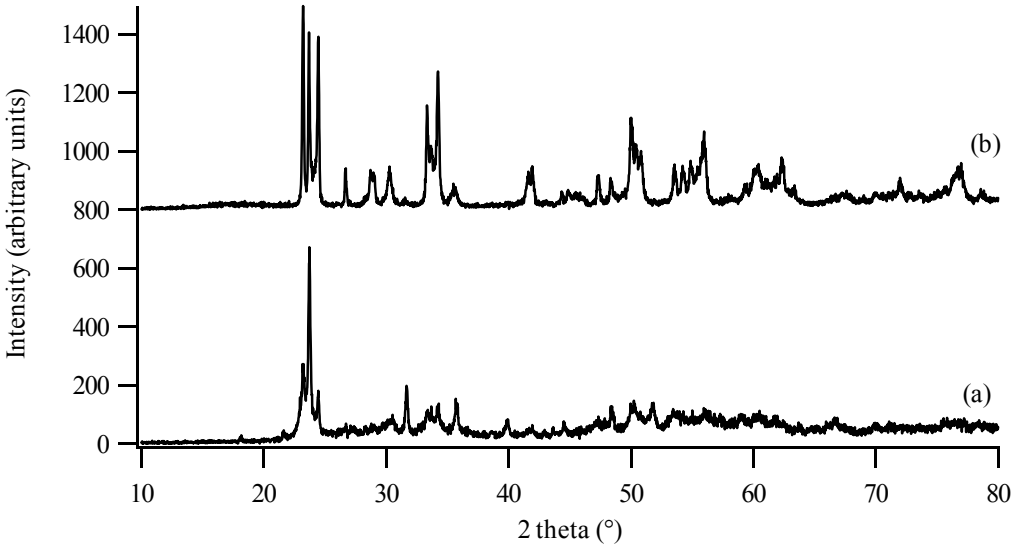

Figure 28: X-ray diffraction pattern of the precursor oxides (ZrO_2 and WO_3) - gel decomposition temperature: 700 °C (a) or 800 °C (b) - $ZrOCl_2.xH_2O$ used as Zr^{4+}-source.

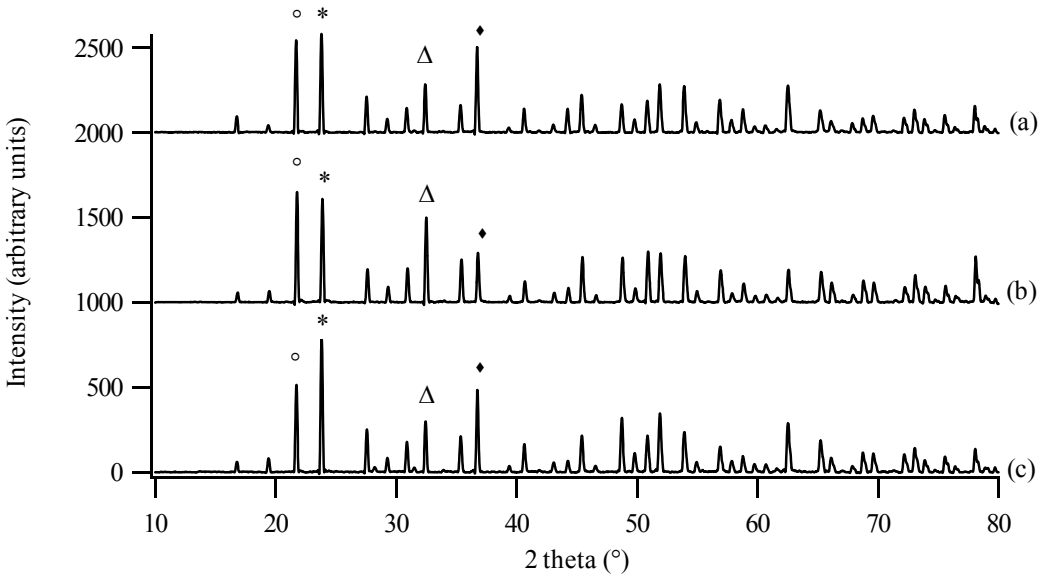

Figure 29: X-ray diffraction pattern of ZrW_2O_8 ;(a) $ZrOCl_2$ (b) $ZrO(NO_3)_2$ (c) $ZrOAc(OH)_3$ as Zr^{4+}-source. Diffraction peaks ° =(210) * =(211) Δ =(311) and • = (321)

The thermal decomposition of a $ZrO(NO_3)_2.xH_2O$ - $(NH_4)_6H_2W_{12}O_{40}.xH_2O$ citrate gel (1:6) is given in figure 30. Several endothermic and exothermic peaks can be seen. The first two peaks can be attributed to the loss of H_2O and NH_3 gasses. The exothermic peak at 247 °C accompanied by great mass losses is the autocombustion reaction mentioned above. Most of the organic material disintegrates before 500 °C is reached. Monoclinic ZrO_2 crystallizes at 471 °C and the formation of WO_3 is assembled in this exothermic peak. The formation of ZrW_2O_8 gives rise to an endothermic peak at 1180 °C.

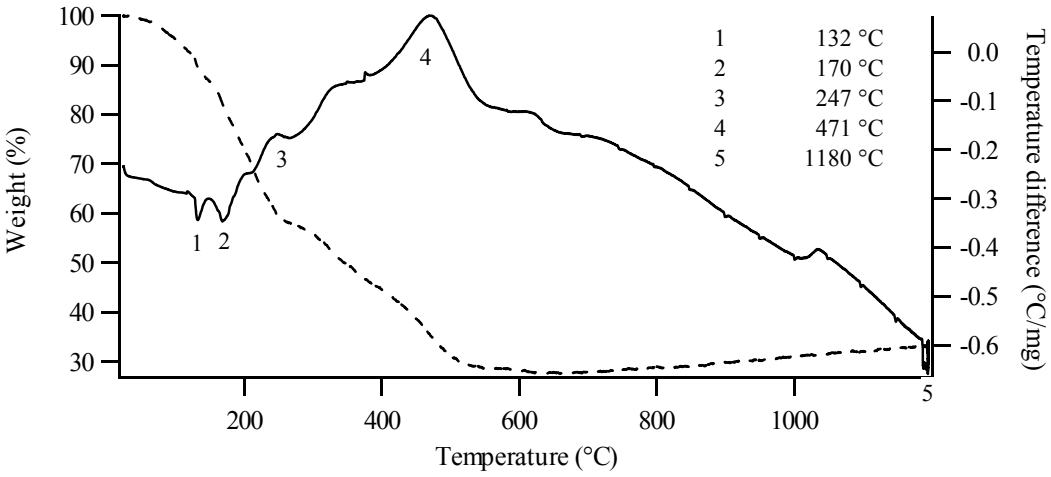

Figure 30: Thermal decomposition of a $ZrO(NO_3)_2.xH_2O$ - $(NH_4)_6H_2W_{12}O_{40}.xH_2O$ citrate gel (1:6) – TGA signal (dotted line) DTA signal (line) Experiment performed under air, heating rate 5 °C /min, RT till 1000 °C

3.3.1 High Temperature X-ray analysis

A small slice of a ZrW_2O_8 bar prepared by the sol-gel method was used to perform variable temperature X-ray analysis. In this case, $ZrOCl_2$ was used as Zr^{4+} source. Data between 10 ° and 60 ° 2 theta were collected under He atmosphere. The stepsize and steptime were respectively 0.015 ° and 0.07 s. The temperature was increased from 40 °C to 300 °C at 5 °C/min. X-ray analysis was performed every 10 °C. The results are mentioned in figure 31. A reflection at 33 ° 2theta is caused by interference of the Si-wafer on which the sample was positioned. As indicated by the insert in figure 31, the 310 reflection characteristic for the alpha phase disappears between 160 and 170 °C. This means that the phase transition took places between those two temperatures.

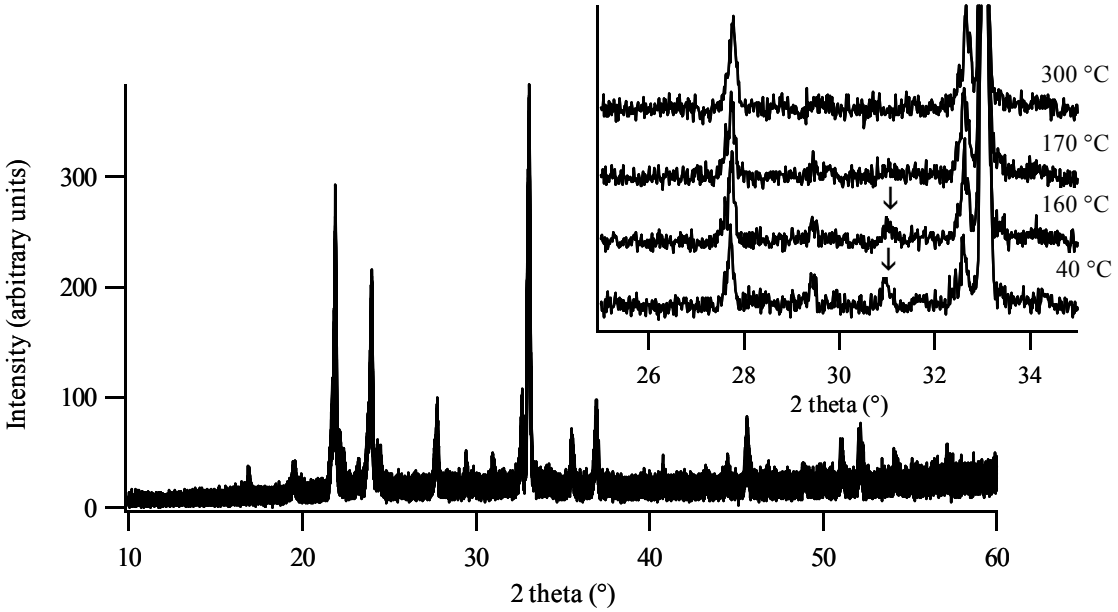

Figure 31: Variable temperature X-ray analysis of spray dried ZrW_2O_8. ↓ indicates the 310 reflection

Data points collected at the different temperatures were used to calculate the dimension changes of the cell parameter a. The exact reflection positions were determined and with the use of the Unitcell [24] software the cell parameter was calculated. The results are given in figure 32. An overall decrease in dimension of the cell parameters can be seen with a clear distinction between the alpha and the beta phase. The alpha phase is characterized by a more negative thermal expansion coefficient than in the case of β - ZrW_2O_8.

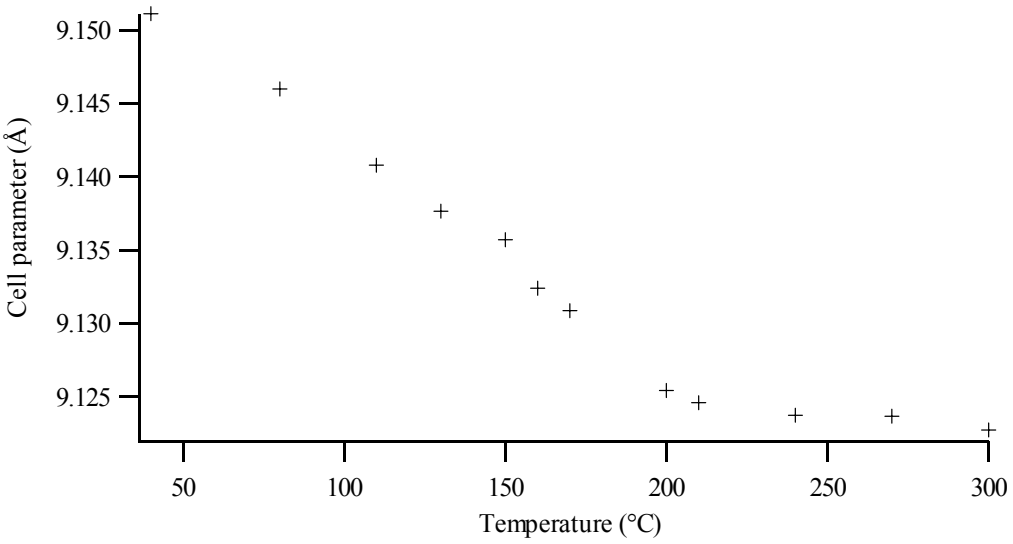

Figure 32: Evolution in cell parameter a as a function of temperature

3.3.2 Thermomechanical properties

The thermal expansion of the materials obtained after sintering at 1180 °C is given in figure 33. A drastic change in thermal expansion is noticed at 169 °C which confirms the information obtained by HT-XRD. The thermal expansion coefficients of α- and β-ZrW_2O_8 synthesized by the use of the different zirconium salts are given in table 5 together with their respective transition temperatures. Each measurement was performed 3 times. Measurements containing 3 cycles of heating to 300 °C and cooling down to room temperature were also performed in order to ascertain the absence of hysteresis.

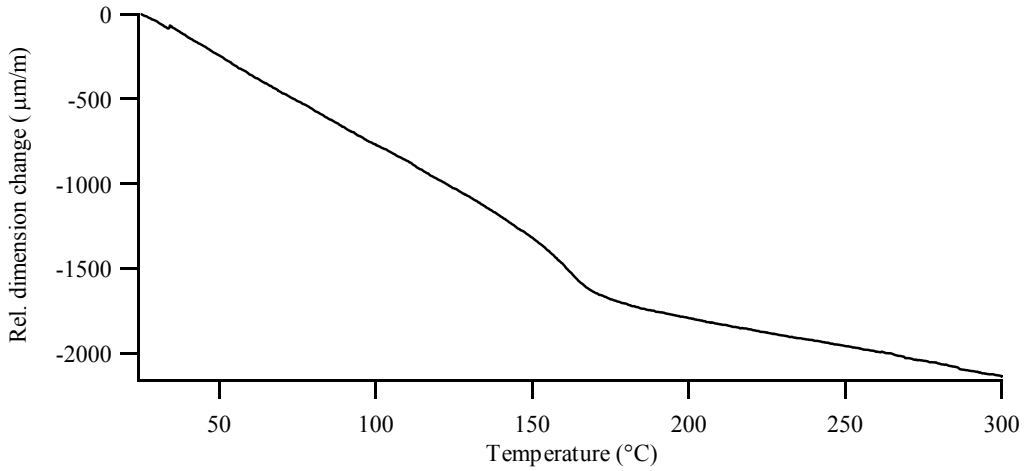

Figure 33: TMA of ZrW_2O_8 with $ZrOCl_2$ as Zr^{4+}-source

In order to relate the thermomechanical properties of the material with its structure and synthesis method, the α-values and some transition temperatures from international literature are added in table 5. The transition temperatures show negligible differences which are unlikely to affect the properties of the material. The thermal expansion coefficients of the ceramic material obtained by the sol-gel synthesis show slightly higher values in comparison with the other preparation methods. An α-value of -11×10^{-6} °C^{-1} is obtained after taking extreme precautions to prevent the WO_3 evaporation [25]. Furthermore, -10.5×10^{-6} °C^{-1} is the result obtained by an aerogel synthesis of ZrW_2O_8 [5]. The other results, obtained by a conventional solid state synthesis [26-31], all give lower values. It has to be mentioned that the analysis method used to determine the thermal expansion has also an impact on the final results. Bulk measurements used here will include the effects of microstructure whereas diffraction measurements do not.

TEC α-ZrW_2O_8 ($\times 10^{-6}$ °C^{-1}) [50 °C – 125 °C]	TEC β-ZrW_2O_8 ($\times 10^{-6}$ °C^{-1}) [200 °C – 300 °C]	Transition temperature (°C)	Reference
-10.6	-3.3	165	This work (a)
-10.5	-3.4	170	This work(b)
-10.7	-2.9	169	This work (c)
-10.5	-	-	[5] aerogel
-11	-	-	[25] extreme precautions
-9.1	-	175	[26] solid state
-8.8	-	-	[28, 29, 31] solid state

Table 5: Thermal expansion of ZrW_2O_8 obtained by sol gel synthesis with (a) $ZrOCl_2.xH_2O$, (b) $ZrO(NO_3)_2.xH_2O$ and (c)$ZrOAc(OH)_3.xH_2O$ as Zr^{4+}-source and literature data

De Meyer et al [27] have already stressed the importance of the properties of chemically prepared oxide mixtures, where homogeneity and smaller particle sizes drastically improve the sintering of the oxide mixtures. The results of this investigation are compared with the measurements of materials obtained via our sol-gel precursors. The end result is mentioned in table 6.

Material	TEC α-ZrW_2O_8 ($\times 10^{-6}$ °C^{-1})
ZrW_2O_8 containing a large amount of unreacted zirconia and tungsten oxide (spray dried oxide mixture, sintered for 5 min at 1180 °C in a quartz tube	- 4.40
Dense ZrW_2O_8 obtained by sintering spray dried powders for 1 hour at 1180 °C in a quartz tube	- 8.87
Dense ZrW_2O_8 obtained by sintering chemically prepared powders via sol-gel for 1 hour at 1180 °C in a Pt dish	- 10.6

Table 6: Thermal expansion of bulk ZrW_2O_8 materials

The quality of ceramic blocks of the negative thermal expansion material ZrW_2O_8 is strongly affected by the synthesis time and the chosen synthetic routes. Ultra-pure ZrW_2O_8 is desirable for applications where the use of composite materials with controlled thermal expansion is envisaged. Materials with positive (Cu, ZrO_2 ...) and negative thermal expansion (ZrW_2O_8) can indeed be combined to produce materials with controlled or even zero thermal expansion [31, 32]. By varying the molar ratios of the different components, different thermal expansion coefficients are obtained. It was experimentally proven by us that a 33 w% ZrW_2O_8 – 66 w% ZrO_2 results in a material which exhibits no dimensional changes as the temperature increases, on the condition that the materials used are pure and homogeneously mixed [33, 34]. The sol-gel method has proven to be a flexible tool for the preparation of the oxide mixtures in the desired molar ratios.

3.3.3 Particle size and morphology

Methods based on gelation lead towards homogeneous mixtures so that the reaction is very fast through the many particle boundaries. The diffusion distance is minimized by the small particle size which leads to fast reactions competing advantageously with the volatility of WO_3. The particle sizes of the oxide mixtures obtained by sol-gel preparation are compared with commercially available oxides in table 7 and are almost 5 times smaller than commercial WO_3 particles. As the dimensions strongly influence the sintering ability of materials, a highly pure ceramic is obtained resulting in an improved negative thermal expansion behaviour.

Material	Particle size	
	d_{50}(μm)	d_{90}(μm)
ZrO_2 (commercial, Aldrich)	3.15	6.54
WO_3 (commercial, Aldrich)	18.68	40.78
ZrO_2 – WO_3 mixture (prepared by sol-gel)	11.44	30.25

Table 7: Particle size of ZrO_2 and WO_3 oxide powders

Electron micrographs were made to compare the influence of the preparation route on the morphology and hereby the properties of the formed materials. The comparison between the fracture surfaces obtained from sintered co-milled and sol-gel synthesized powders are given in figure 34.

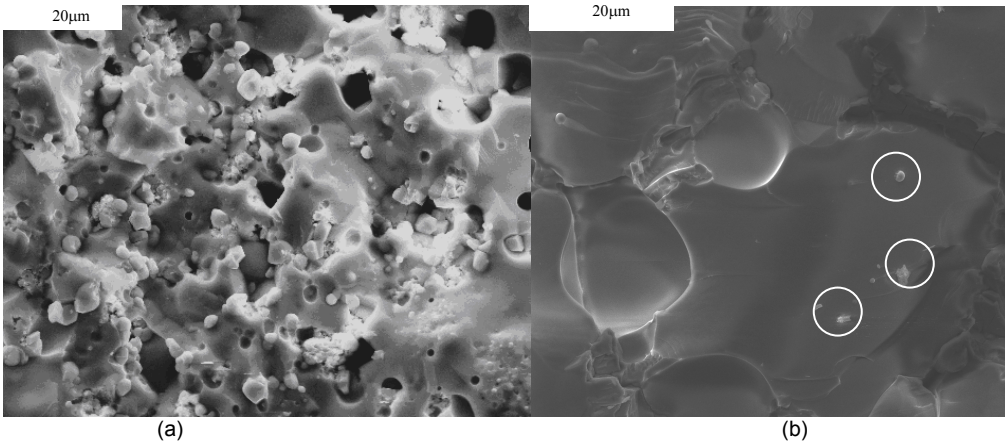

Figure 34: Electron micrographs of fracture surfaces of (a) co-milled oxide powders and (b) a sol-gel based oxide mixture sintered at 1180°C for 2 hours.

Both samples were treated for 2 hours at 1180 °C. In the case of ZrW_2O_8 prepared by sol-gel, the reaction is more complete and less unreacted material with spherical morphology is left whereas for the co-milled oxide powders more unreacted particles are still present. The particles are identified by EDAX as ZrO_2 particles. In both cases a more or less smooth matrix of zirconium tungstate can be identified. The distinct morphologies of the samples are a consequence of the initial difference in morphology and homogeneity of the oxide mixtures. The remarkable absence of pores in sol-gel based zirconium tungstate proves that the volatility of WO_3 was pushed back so that only a very small amount of unreacted ZrO_2 remains embedded in the zirconium tungstate matrix as can be seen in figure 34(b) indicated by the circles.

4 EDTA-gel synthesis of ZrW_2O_8

4.1 Coordinative properties of Ethyleen diamine tetraacetic acid [35]

Ethylene diamine tetraacetic acid, better known as EDTA, is here used as an alternative for citric acid to avoid the autocombustion reaction and hereby providing a sol-gel system which is more suitable for the preparation of thin ZrW_2O_8 layers. EDTA is a tetrabasic compound and besides the 4 carboxylic acid groups, there are two nitrogen atoms which can act as possible donor as shown in figure 35. EDTA is therefore a potentially hexadentate ligand. The conformation of the ligand can change freely by rotation around the C – C and C – N bonds. When $(EDTA)^{4-}$ coordinates to a metal ion, it actually wraps itself around the metal ion to form a octahedral surrounding.

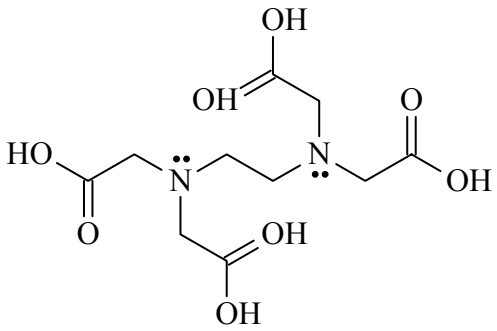

Figure 35: Chemical structure of EDTA in its acid form

4.2 Synthesis and preparation of the precursor solution

The synthesis of the Zr – W – EDTA precursor solution is twofold. In a first step, the ZrEDTA complex is formed which is then dissolved in the W – EDTA solution. The ZrEDTA complex is synthesized according to a synthesis method mentioned in literature [36-38].

4.2.1 Synthesis of $ZrEDTA.xH_2O$

$ZrOCl_2.xH_2O$ (6 g, 20 mmol) and Na_2H_2EDTA (7.44 g, 20 mmol) was dissolved in 100 mL of distilled water. A thick, white precipitation was obtained which disappeared upon heating at 100 °C. The solution was stirred at this temperature for 1

hour. Afterwards, the solution was cooled overnight. Colourless crystals were produced upon standing. The crystals were filtered off and rinsed three times with cold distilled water followed by drying for 24 hours at 110 °C. XRD analysis was performed on these crystals and the monoclinic phase of ZrEDTA (ICSD PDF 49-2452)-was identified as given in figure 36.

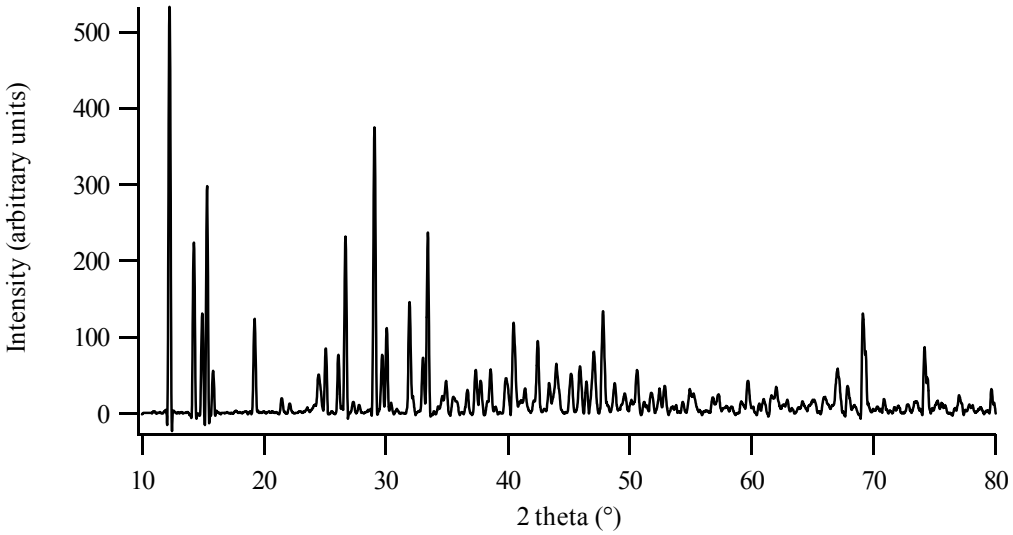

Figure 36: X-ray diffractogram of the ZrEDTA complex

The complexation by EDTA is shown schematically in figure 37. Other conformations are also possible because of the free rotation along the C – C and C – N single bonds as long as the octahedral surrounding is retained. The stability constant for ZrEDTA in water at room temperature equals $10^{29.4}$ which is very high. [39]

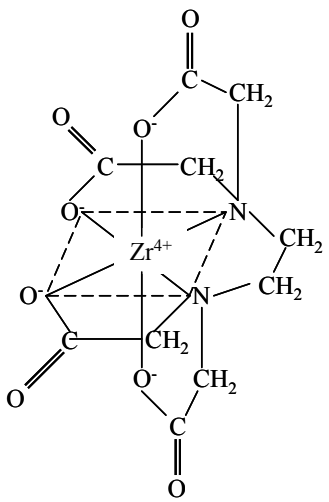

Figure 37: The coordination of EDTA around Zr^{4+}

TGA-DTA analysis was also performed to determine the amount of crystal water present. The results are given in figure 38. The DTA spectrum reveals 3 major peaks. The first endothermic signal is due to the loss of water molecules, followed by the burning-out of the EDTA ligand which results in an exothermic peak at 409 °C. The exothermic peak at 488 °C represents the crystallization of monoclinic ZrO_2. The weight percentage obtained at 1200 °C is 28.40 % which results in a molecular weight of 433.87 g/mol or ZrEDTA. $3.02H_2O$.

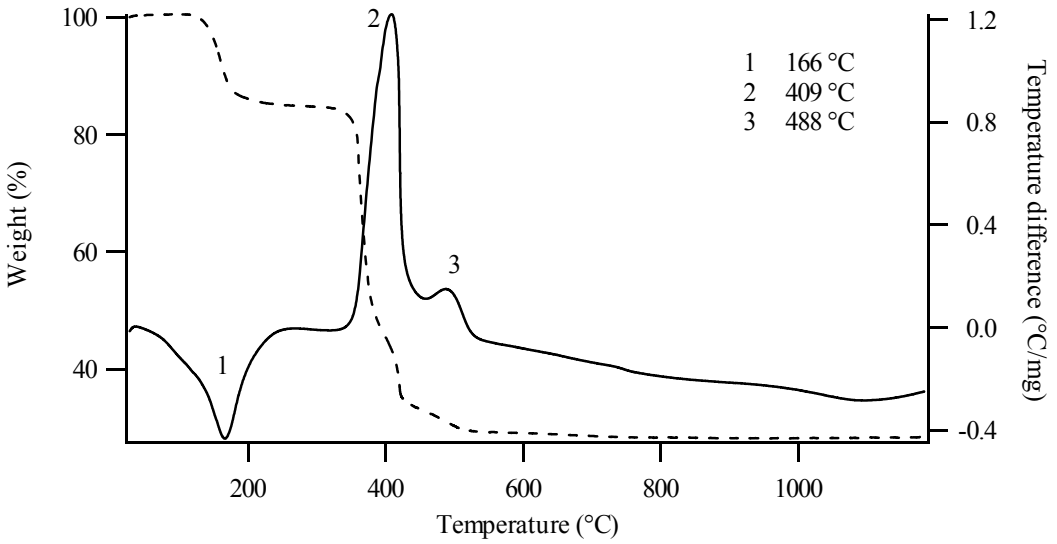

Figure 38: TGA-DTA analysis of $ZrEDTA.xH_2O$ – TGA signal (dotted line) DTA signal (line) Experiment performed under air, heating rate 5 °C /min, RT till 1000 °C

4.2.2 Synthesis of the Zr – W EDTA precursor solution

This fully characterized ZrEDTA complex was further used in the preparation of the Zr – W – EDTA precursor solution. 50 mL of a 0.2 M EDTA solution in water was prepared. 3 ml of concentrated ammonia (13 M) was added to dissolve the EDTA. $(NH_4)_6H_2W_{12}O_{40}.xH_2O$ (4.99 g, 1.67 mmol) was dissolved in the EDTA solution and the pH was adjusted with acetic acid till a pH of 4.78 was obtained. The ZrEDTA crystals (4.33 g, 10 mmol) were dissolved in the W-EDTA solution by mild heating. The pH of the Zr – W – EDTA solution was about 4.

The stability of this precursor solution and the gel was tested. The pH was increased by adding diluted ammonia (1.3 M). Precursor solutions at pH 4, 5 and 6 were put aside in a drying furnace at 60 °C for 10 hours. Further increase of the pH was not preferred because of the presence of precipitation in the precursor solution. The

results of the gelled samples are shown in figure 39. Clear gels are obtained at pH 4 whereas precipitation occurs at higher pH values. The precursor solution at pH 4 was used in further experiments.

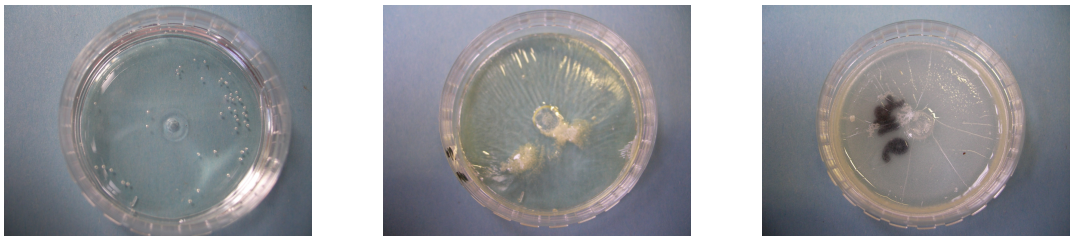

pH 4 pH 5 pH 6

Figure 39: Zr – W – EDTA gel

IR spectra (figure 40) of the pure EDTA (in its acid form), the ZrEDTA complex and the Zr –W – EDTA gel were recorded. The most important peaks are indicated such as the C-H stretch between 2950 and 2850 cm^{-1} and the C-H bending vibrations in the region 1370 – 1380 cm^{-1} and 720 – 725 cm^{-1}. Vibrations due to the carboxylic acid can be seen in the carbonyl stretch at 1700 – 1720 cm^{-1} whereas the C-O stretch results in a minimum in transmission between 1210 and 1320 cm^{-1}. C-N stretches occurring in the EDTA groups are noticeable at 1095 cm^{-1} whereas O-H stretches due to the presences of water can be seen for the ZrEDTA complex and the Zr – W – EDTA gel around 3300 cm^{-1}. This peak is very broad for the gel because of the coexistence of N-H stretch vibration as NH_4OH is used to dissolve the EDTA salt and to adjust the pH.

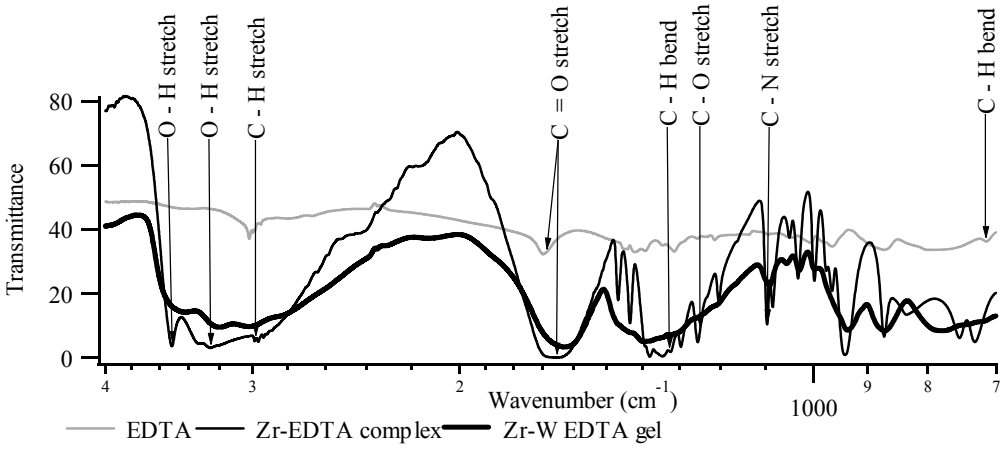

Figure 40: IR spectra of EDTA, ZrEDTA complex and Zr-W EDTA gel (pH 4)

The vibrations below 1000 cm^{-1} in the IR spectra of the ZrEDTA complex and the gel are not only caused by C-H bending vibration. Zr-N (933 cm^{-1}), W-N (957 cm^{-1}), W-O (970 – 990 $cm^{-1)}$ and Zr-O (730 – 770 cm^{-1}) stretch vibrations can be situated in this region.

4.3 Decomposition of the gel

TGA-DTA analysis was used to examine the decomposition process of the gel containing ZrEDTA dissolved in the W – EDTA solution at pH 4. The results will help to tune the thermal treatment in order to first calcine into a homogenous ZrO_2 – WO_3 mixture followed by the high temperature treatment as discussed above. Figure 41 outlines the weight percentage and the temperature difference measured during the decomposition in air. These results are compared with figure 30 in order to see the differences and similarities between the two different sol-gel systems. Two first two peaks are similar and are due to the loss of water and ammonia gases. The strong exothermic peak at 471 °C in the citrate system has shifted to higher temperature (584 °C). The EDTA complex needs higher temperature to decompose completely with production of CO_2 gas. No more decomposition processes occur above 700 °C and all material has been calcined to ZrO_2 and WO_3. Temperatures above 700 °C are suitable for further synthesis in order to obtain a pure oxide precursor mixture suitable for ZrW_2O_8 synthesis.

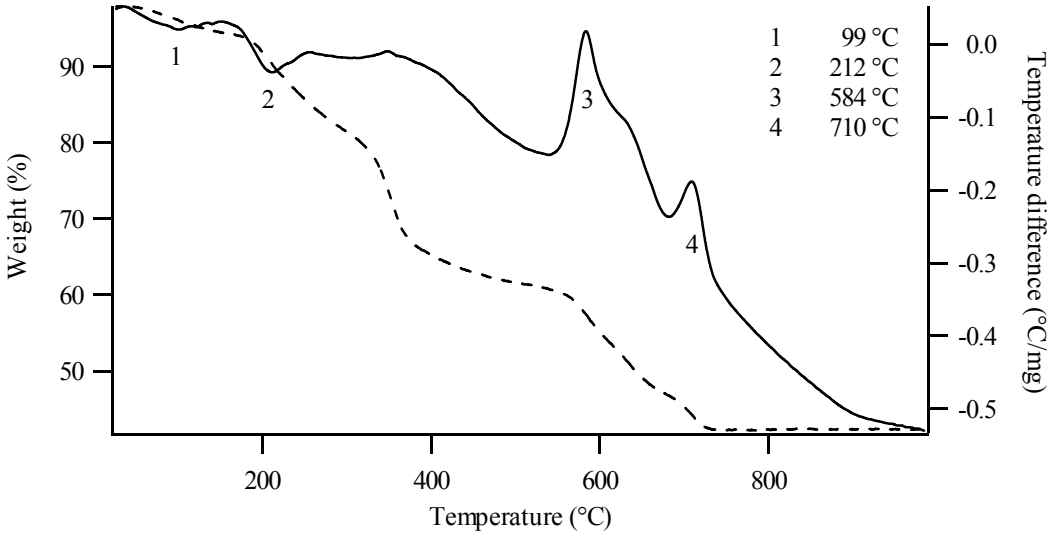

Figure 41: TGA-DTA analysis of the Zr-W EDTA gel at pH 4 – TGA signal (dotted line) DTA signal (line) Experiment performed under air, heating rate 5 °C /min, RT till 1000 °C

IR spectroscopy was used to get a better view on the different products formed during decomposition. Therefore, small amounts of the gel were heated at various temperatures (180 °C- 800 °C). The obtained powders are ground and analysed. The results are given in figure 42. The intensity stretch vibrations due to the presences of the carboxylic acid and amine functions in EDTA slowly fade to disappear completely above 750 °C. The O-H and N-H stretch vibrations disappear between 200 and 300 °C which is in correlation with the TGA-DTA analysis. Above 750 °C, absorption occurs in the region below 1000 cm^{-1} due to Zr-O and W-O vibrations.

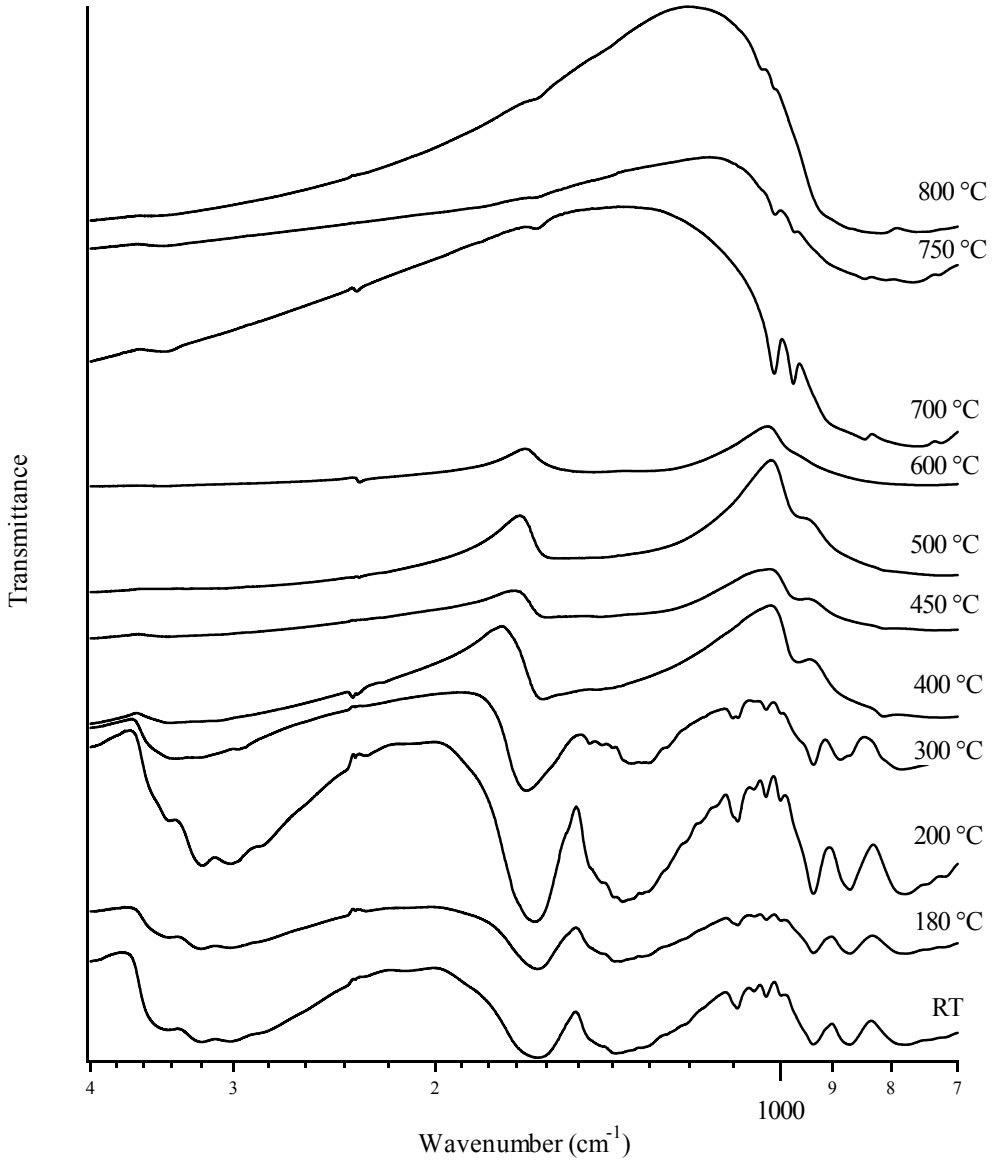

Figure 42: IR spectra of the Zr – W – EDTA gel at various temperatures

4.4 Synthesis of ZrW_2O_8

The ZrO_2 – WO_3 oxide mixture, obtained out of the Zr – W – EDTA gel after calcinations at 800 °C was submitted to X-ray analysis (figure 43 (a)). All reflections present in the diffractogram can be identified as resulting from monoclinic ZrO_2 or triclinic WO_3. This calcination step was then followed by the same high temperature treatment as described above. ZrO_2 – WO_3 powder mixtures were ground, pressed into bars and kept in a preheated furnace at 1180 °C for 2 hours. The samples were quenched afterwards in liquid nitrogen. This high temperature treatment results in pure ZrW_2O_8 as can be seen in figure 43(b).

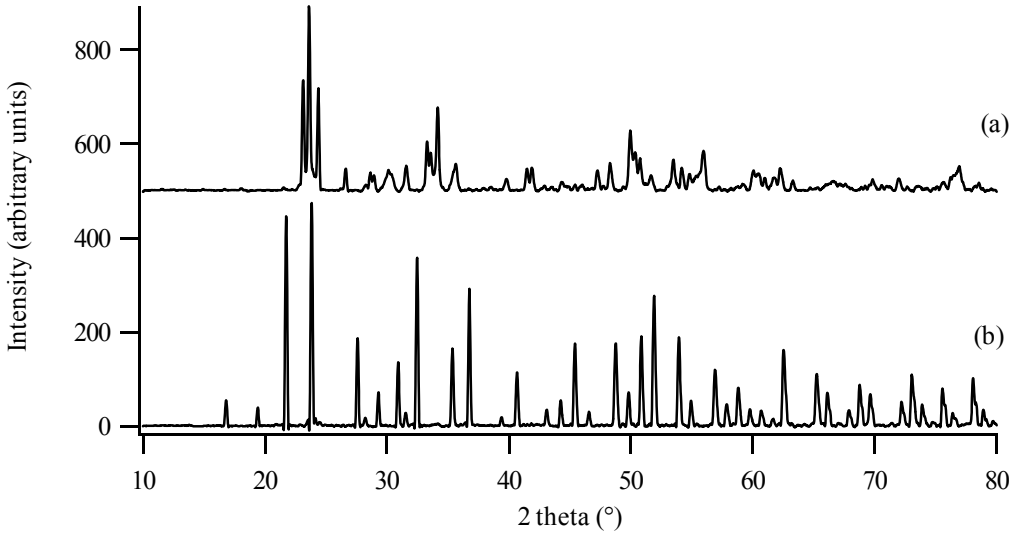

Figure 43: X-ray diffractogram of Zr – W – EDTA gel after heat treatment at (a) 800 °C (b) 1180 °C

5 Conclusions

In addition to the known synthesis methods for ZrW_2O_8 such as the conventional solid state reaction, the use of spray dried powders and the co-precipitation method, the synthesis via the citrate-gel method does produce a pure and homogenous oxide mixture and is therefore well suitable for the preparation of ZrW_2O_8. The expansion coefficient of α–ZrW_2O_8 is -10.6×10^{-6} °C^{-1} (50 °C – 125 °C) whereas that for the β-ZrW_2O_8 is -3.15×10^{-6} °C^{-1} (200 °C – 300 °C). These values are similar or higher than those obtained using synthetic techniques where extreme measures are taken to avoid volatilization. The homogeneity and the small particle sizes are the most important factors which improve the negative thermal expansion behaviour by fast diffusion and reaction along the many particle boundaries and thus avoiding volatilization of WO_3. This is proven by morphology studies of zirconium tungstate by varied synthetic routes. A negligible difference in α-β phase transition temperature is noticed. A second sol-gel synthesis method is based on EDTA as complexing agent. Pure gels are obtained which result in a homogenous powder mixture. After heat treatment pure zirconium tungstate is obtained.

Both sol-gel systems are suitable for the synthesis of ZrW_2O_8 thin layers. A well studied heat treatment is of the utmost importance as the decomposition of the gel structure includes the losses of the organic material. These losses induce the formation of gasses which have a negative influence on the morphology of the layer. A mild heating rate may slow down this process and hence improve the quality of the layers drastically.

6 References

1. C.J. Brinker and G.W. Scherer, *Hydrolysis and Condensation I Nonsilicates*, in *Sol-gel sciences : the physics and chemistry of sol-gel processing*. 1990, Academic press: San Diego, California. p. 20 - 93.

2. C. Lind, A.P. Wilkinson, Z.B. Hu, S. Short, and J.D. Jorgensen, *Synthesis and properties of the negative thermal expansion material cubic $ZrMo_2O_8$.* Chemistry of Materials, 1998. **10**: 2335-2337.

3. C. Closmann, A.W. Sleight, and J.C. Haygarth, *Low-temperature synthesis of ZrW_2O_8 and Mo-substituted ZrW_2O_8.* Journal of Solid State Chemistry, 1998. **139**: 424-426.

4. L. Noailles, B. Dunn, D. Larson, J. Starkovich, and H. Peng, *Preparation of ZrW_2O_8 xerogel and aerogels by sol-gel chemistry.* Euro Ceramics Viii, Pts 1-3, 2004. **264-268**: 363-366.

5. L.D. Noailles, H.H. Peng, J. Starkovich, and B. Dunn, *Thermal expansion and phase formation of ZrW_2O_8.* Chemistry of Materials, 2004. **16**: 1252-1259.

6. A.P. Wilkinson, C. Lind, and S. Pattanaik, *A new polymorph of ZrW_2O_8 prepared using nonhydrolytic sol-gel chemistry.* Chemistry of Materials, 1999. **11**: 101-108.

7. C. Lind and A.P. Wilkinson, *Seeding and the non-hydrolytic sol-gel synthesis of ZrW_2O_8 and $ZrMo_2O_8$.* Journal of Sol-Gel Science and Technology, 2002. **25**: 51-56.

8. J. Bailar, H. Emeléus, R. Nyholm, and A. Trotman-Dickenson, *Comprehensive Inorganic Chemistry*. 1973, Oxford: Pergamon Press Ltd.

9. C.J. Howard, R.J. Hill, and B.E. Reichert, *Structures of the Zro2 Polymorphs at Room-Temperature by High-Resolution Neutron Powder Diffraction.* Acta Crystallographica Section B-Structural Science, 1988. **44**: 116-120.

10. P. Southon, *Structural evolution during the preparation and heating of nanophase zirconia gels*. 2000, University of Technology: Sydney.

11. R.C. Paul, O.B. Baidya, R.C. Kumar, and R. Kapoor, *Zirconium (IV) Carboxylates.* Australian Journal of Chemistry, 1976. **29**: 1605-1607.

12. L.N. Komissarova, M.V. Savel'eva, and V.E. Plyushchev, *New oxide acetates of Zirconium and Hafnium.* Russian Journal of Inorganic Chemistry, 1963. **8**: 27-30.

13. L.N. Komissarova, Z.N. Prozorovskaya, and V.I. Spitsyn, *Hydroxide acetates of Zirconium and Hafnium.* Russian Journal of Inorganic Chemistry, 1966. **11**: 1089-1091.

14. L. Gmelin, *Gmelins Handbuch der anorganischen Chemie:Zirkonium*. 8 th ed. 1958, Berlin: Springer.

15. G.Y. Guo and Y.L. Chen, *Preparation and characterization of a novel zirconia precursor.* Ceramics International, 2004. **30**: 469-475.

16. D.L. Kepert, *Progress in inorganic chemistry*, ed. F.A. Cotton. 1962, New York: Interscience Publishers.

17. N.N. Greenwood and A. Earnshaw, *Chemistry of the elements*. 1984, Oxford: Pergamon Press Ltd.

18. X. Xi, Z. Nie, J. Yang, X. Fu, W. Wang, and T. Zuo, *Preparation and characterization of Ce-W composite nanopowder.* Materials Science and Engineering A, 2005. **394**: 360-365.

19. M. Rajendran and M.S. Rao, *Synthesis and Characterization of Barium Bis(Citrato) Oxozirconate(Iv) Tetrahydrate - a New Molecular Precursor for Fine-Particle $BaZrO_3$.* Journal of Materials Research, 1994. **9**: 2277-2284.

20. C. De Meyer, *Perspectives in the chemistry of negative thermal expansion materials based on ZrW_2O_8.* 2004, Universiteit Gent: Ghent.

21. A. Hardy, K. Van Werde, G. Vanhoyland, M.K. Van Bael, J. Mullens, and L.C. Van Poucke, *Study of the decomposition of an aqueous metal-chelate gel precursor for $(Bi,La)_{(4)}Ti_3O_{12}$ by means of TGA-FTIR, TGA-MS and HT-DRIFT.* Thermochimica Acta, 2003. **397**: 143-153.

22. K. Van Werde, G. Vanhoyland, D. Nelis, D. Mondelaers, M.K. Van Bael, J. Mullens, and L.C. Van Poucke, *Phase formation of ferroelectric perovskite $0.75\ Pb(Zn_{1/3},Nb_{2/3})O_3$-$0.25\ BaTiO_3$ prepared by aqueous solution-gel chemistry.* Journal of Materials Chemistry, 2001. **11**: 1192-1197.

23. T. Mimani and K.C. Patil *Solution combustion synthesis of nanoscale oxides and their composites.* Materials Physics and Mechanics, 2001: 134-137.

24. T.J.B. Holland and S.A.T. Redfern, *Unit cell refinement from powder diffraction data: The use of regression diagnostics.* Mineralogical Magazine, 1997. **61**: 65-77.

25. J.C. Chen, G.C. Huang, C. Hu, and J.P. Weng, *Synthesis of negative-thermal-expansion ZrW_2O_8 substrates.* Scripta Materialia, 2003. **49**: 261-266.

26. J.S.O. Evans, *Negative thermal expansion materials.* Journal of the Chemical Society-Dalton Transactions, 1999: 3317-3326.

27. C. De Meyer, L. Vandeperre, I. Van Driessche, E. Bruneel, and S. Hoste, *Processing effects on the microstructure observed during densification of the NTE-compound ZrW_2O_8.* Crystal Engineering, 2002. **5**: 469-478.

28. A.W. Sleight, *Isotropic negative thermal expansion.* Annual Review of Materials Science, 1998. **28**: 29-43.

29. J.S.O. Evans, Z. Hu, J.D. Jorgensen, D.N. Argyriou, S. Short, and A.W. Sleight, *Compressibility, phase transitions, and oxygen migration in zirconium tungstate, ZrW_2O_8.* Science, 1997. **275**: 61-65.

30. J.S.O. Evans, T.A. Mary, T. Vogt, M.A. Subramanian, and A.W. Sleight, *Negative thermal expansion in ZrW_2O_8 and HfW_2O_8.* Chemistry of Materials, 1996. **8**: 2809-2823.

31. E. Niwa, S. Wakamiko, T. Ichikawa, S.R. Wang, T. Hashimoto, K. Takahashi, and Y. Morito, *Preparation of dense ZrO_2/ZrW_2O_8 cosintered ceramics with controlled thermal expansion coefficients.* Journal of the Ceramic Society of Japan, 2004. **112**: 271-275.

32. H. Holzer and D.C. Dunand, *Phase transformation and thermal expansion of Cu/ZrW_2O_8 metal matrix composites.* Journal of Materials Research, 1999. **14**: 780-789.

33. P. Lommens, C. De Meyer, E. Bruneel, K. De Buysser, I. Van Driessche, and S. Hoste, *Synthesis and thermal expansion of ZrO_2/ZrW_2O_8 composites.* Journal of the European Ceramic Society, 2005. **25**: 3605-3610.

34. K. De Buysser, P. Lommens, C. De Meyer, E. Bruneel, S. Hoste, and I. Van Driessche, *ZrO_2-ZrW_2O_8 composites with tailor-made thermal expansion.* Ceramics-Silikaty, 2004. **48**: 139-144.

35. C.E. Housecroft and E.C. Constable, *Chemistry*. 3 ed. 2006, Harlow: Pearson Prentice Hall.

36. H.G. Langer, *Solid Complexes with tetravalent metal ions and ethylenediamine tetra-acetic acid (EDTA).* Journal of Inorganic & Nuclear Chemistry, 1964. **26**: 59-72.

37. Y.W. Zhang, J.T. Jia, C.S. Liao, and C.H. Yan, *Synthesis of scandia-stabilized zirconia via thermo-decomposition of precursor complexes.* Journal of Materials Chemistry, 2000. **10**: 2137-2141.

38. R.S. Sathish, U. Sujith, G.N. Rao, and C. Janardhana, *Fluoride ion detection by 8-hydroxyquinoline-Zr(IV)-EDTA complex.* Spectrochimica Acta Part a-Molecular and Biomolecular Spectroscopy, 2006. **65**: 565-570.

39. A.E. Martell and R.M. Smith, *Critical Stability Constants - Volume 1: Amino Acids*. 1974, New York: Plenum Press.

Chapter 5

Luminescent properties and EXAFS analysis of the sol-gel precursors

The precursor solutions prepared by the citrate-gel method resulted in stable blue gels at high pH values. This remarkably colour behaviour is mentioned in the previous chapter. This chapter provides extra attention to the colouring of the gels and the species present in the precursor solution. Luminescence measurements are used to identify the photoluminescent behaviour of the gels whereas EXAFS experiments are performed to clarify the species present in the precursor solution. Obviously, the chapter is limited to materials based on the citrate-gel route.

The colouring of the citrate based gels and the luminescence measurements are mentioned in the following publication:

"Aqueous sol-gel processing of precursor oxides for ZrW_2O_8 synthesis"

K. De Buysser, P.F. Smet, B. Schoofs, E. Bruneel, D. Poelman, S. Hoste and I. Van Driessche

Published in Journal of Sol-Gel Science and Technology, 43 (2007) 347-353

1 Luminescence of the precursor gels

A remarkable colour change occurs in some gels discussed in Chapter 4-§3.2 when they are exposed to sunlight after heating at 60 °C. After 72h exposure, the gels at low pH remained colourless. They exhibit a gradual colour gradation from pink to purple to blue when increasing the pH stepwise from 4 to 7.

The marked colour changes in the gels were examined with optical spectroscopy. Normally no detectable UV-Vis signal related to d-electrons is expected for free Zr^{4+}, [Kr] $4d^0$ and free W^{6+}, [Xe] $4f^{14}5d^0$. The colourless aqueous solution seemed to confirm this theory but we will demonstrate at the end of this chapter that this has another explanation. No colour was noticed immediately after transformation from solution to the sol-gel state at 60 °C and removal from the dry furnace, which is again in agreement with the presence of empty d-orbitals. Only when the gel was exposed to sunlight during several hours a range of stable colours going from light pink (pH=5) over purple to blue (pH=7) was obtained. This optical behaviour can be due to charge transfer transitions from ligand to metal. The colours are affected by pH and the sol-gel state plays in this.

To examine this puzzling optical behaviour in more detail, two series of gels were prepared with different Zr salts. Series 1 was obtained by the combination of $ZrOCl_2.xH_2O$ (6.20 g, 20 mmol) : citric acid (25.21g, 120mmol) in a 1:6 ratio with $(NH_4)_6H_2W_{12}O_{40}.xH_2O$ (9.99 g, 3.33 mmol) addition in 100 mL distilled water whereas in series 2 , $ZrO(NO_3)_2.xH_2O$ (6.63 g, 20 mmol) was used as Zr^{4+} salt. The pH was varied stepwise from 1 to 7 by adding NH_4OH. The same gradation in colour was noticed in both series, so there is no effect due to changing the Zr^{4+} salts. These gels were diluted in water and analyzed by UV-Vis. The λ_{max} of the colours formed in the sol-gel state were not affected by the dilution. In figure 1 the transmittance spectrum is given for the diluted gels of series 1. Variable absorption features at different pH between 450 nm and 750 nm were noticed. When we take a closer look at this figure, it can be seen that no difference occurs at pH 1-3. An absorption peak appears at pH 4 (520 - 540 nm) and is indicated by an asterisk. This is maintained in the other spectra (e-f) but is slightly shifted to lower energy regions. At pH 6 (spectrum (f)) an additional peak can be observed at ± 640 nm (°). As both series

exhibit the same colour behaviour the change in Zr^{4+} salts seems unlikely to affect the photochromic properties of the gels. These properties are most likely to be affected by the presence of W^{6+}-species. At this pH value, the metatungstate is transformed into the 12-tungstate with their Keggin structure [1]. These molecules are composed of $[WO_6]$ octahedra which are bonded by edge- and corner-sharing to 4 other octahedra. The transformation in different polyoxytungstate ions depends on the variation of the pH as can be seen in Chapter 4-§2.6, which can be the reason for the differences in the transmission spectra after irradiation by sunlight as was noticed in the synthesis.

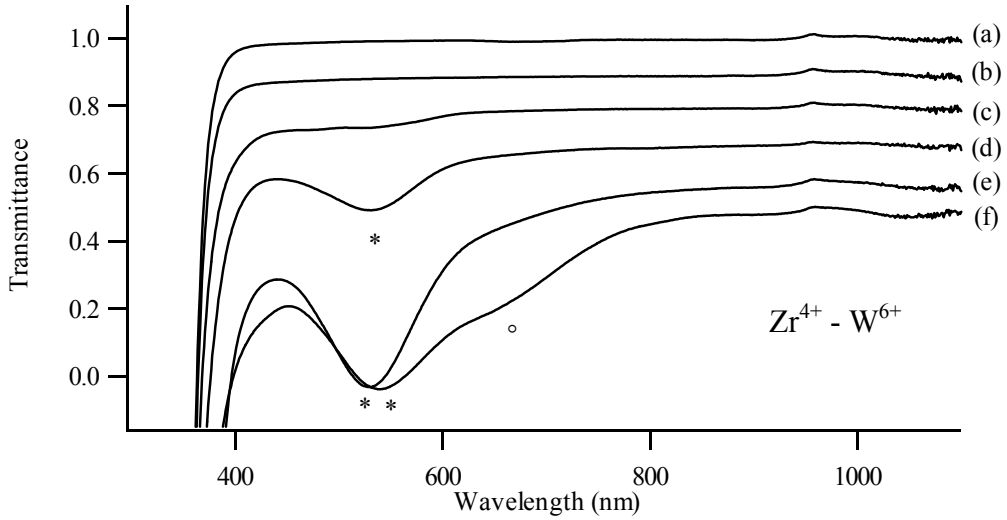

Figure 1: UV-VIS of the sol-gel precursors diluted in water at pH (a) 1 (b) 2 (c) 3 (d) 4 (e) 5 (f) 6 with $ZrOCl_2$ as Zr^{4+}-source.

A similar sol-gel sample was prepared without Zr^{4+}-salt. The pH was adjusted to obtain pH 6 and the gel indeed turned blue after irradiation by sunlight. This is an indication that W^{6+} ions are responsible for the photochromic behaviour of the gels. One sample was kept in the dark for comparison. The photochromic properties of the diluted $(NH_4)_6H_2W_{12}O_{40}.xH_2O$ – citric acid gels are studied more extensively by subjecting the sample to irradiation with a 100W – Hg lamp. The transmission spectra are shown in figure 2.

After 22 min of irradiation a different transmission pattern occurs with absorption at ± 350 nm and ± 600 nm. After a longer irradiation time of 40 min the latter shifts towards ± 560 nm. In addition absorption appears at ± 450 nm. The absorption at ± 560 nm leads to a purple tinge of the irradiated sols which is probably related to

figure 1(e-f). This photochromic effect is fully reversible as the transparency is restored by keeping the irradiated gels in the dark. Exposure of this gel to sunlight irradiation restored the original colour.

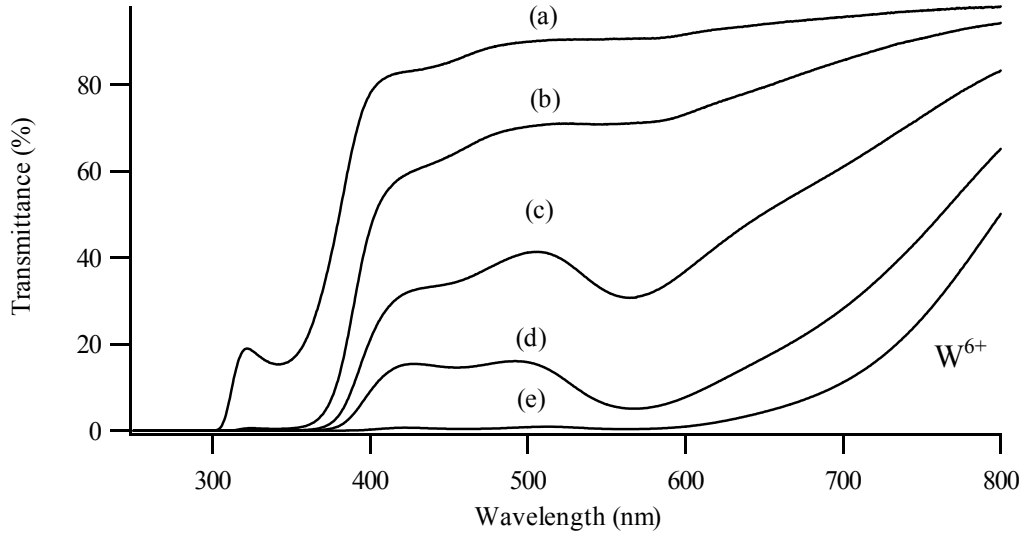

Figure 2: Transmission spectra of the samples after radiation with UV-light: (a) 0 min, (b) 2 min, (c) 22 min, (d) 40 min, (e) 130 min.

Luminescence measurements were performed on two samples for further conformation. Sample n°1 is part of the series 1 prepared as described above at pH 7 with W^{6+} and Zr^{4+} ions present and sample n°2 is a pure W^{6+} salt solution prepared under the same conditions with W : citric acid ratio of 1:2. Both solutions exhibit the same luminescence behaviour with a strong blue emission upon UV excitation. It seems that there is no contribution to the luminescence due to the presence of Zr^{4+} ions. The luminescence of zirconates is known to be excited with wavelengths shorter than 220 nm and the emission is mostly centred in the ultraviolet [2]. The blue luminescence present in the sample is thus only caused by the presence of tungstate ions.

The results of the luminescence measurements of sample n°2 are shown in figure 3. The excitation spectrum monitored at 550 nm (figure 3(a)) shows two distinct peaks situated at 365 nm and 430 nm. Excitation at 350 nm leads to a strong blue emission, with a peak wavelength of 445 nm (figure 3(b)). The Stokes shift, defined as the energy difference between excitation and emission, calculated from this spectrum is 6400 cm^{-1}. The Stokes shift is related to ΔR as given in the configurational coordinate

diagram (Chapter 2–§7.2) and a Stokes shift above 5000 cm^{-1} indicates that the optical bands involved in the excitation – emission mechanism are rather broad. Excitation at 425 nm is related to a much weaker emission band at 510 nm (figure 3(c)).

Complexes of transition metals with a formally empty d shell such as WO_4^{2-} and WO_6^{6-} often show unexpected broad band emission. The excited state is caused by a charge transfer reaction in which electronic charge has been moved from the ligands (oxygen) to the central metal ion (W). The amount of charge transfer is rather small but the electronic reorganisation is considerable. Electrons are promoted from bonding orbitals in the ground state to antibonding orbitals in the excited state.

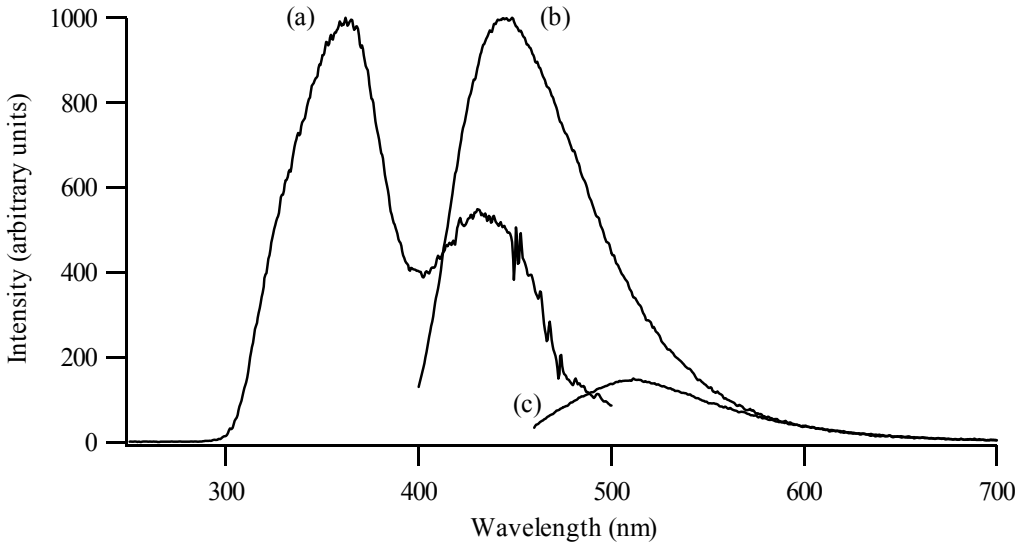

Figure 3: (a) Excitation spectrum (RT, emission wavelength of 550 nm) of a $(NH_4)_6H_2W_{12}O_{40}.xH_2O$ solution. Emission spectra after excitation at (b) 350 nm, RT (c) 425nm, RT.

As described in Chapter 4-§2.6, tungstates can be divided into two groups with different crystal coordination: Scheelites with tetrahedral surrounding around W (WO_4^{2-}) and wolframites with an octahedral surrounding around W (WO_6^{6-}). The origin of the blue emission at 450 nm as given in figure 3 (b) is generally ascribed to electronic transitions of the charge-transfer type between oxygen and tungsten within the regular lattice $(WO_4)^{2-}$ group while the green component (figure 3(c)) results from the relaxed configuration of self-trapped excitons on the d^0- octahedral groups or defects in the WO_3 groups [2-5]. An exciton is an excited state of the crystal lattice in which pairs of holes and electrons propagate together and transfer their energy to imperfections or remain self-trapped. In both cases, electron and hole recombine.

The results mentioned above suggest a mixture of tungstate octahedra and tetrahedra. But the strong blue emission caused by WO_4^{2-} anions is in contrast with the expected Keggin structure built of octahedra.

The photochromic and electrochromic behaviour of WO_3 particles is well documented [6-8] and results in blue luminescence. All the research mentioned in the literature was performed on small oxide particles, colloids or nanocrystalline films. Transparent WO_3 and WO_{3-y} films are known to become dark blue after being exposed to ultraviolet light. WO_3 nanoparticles can transform from white to blue after irradiation by a 532 nm laser due to charge transfer reactions. This observation leads us to presume the presence of nano WO_3-particles as a cause for the photochromic properties seen in our experiments.

This hypothesis is negated by the relatively short decay time of the prepared samples (<10 ns). The decay time is defined as the time in which the intensity of the emission at a certain wavelength has decreased to 37 % (1/e). The decay spectrum is obtained after excitation at one fixed wavelength and recording of decay curve at another wavelength integrated over a specific time interval: every 5 ns, 20 ns, 100 ns… The intensity at a fixed wavelength is then plotted in a so–called decay curve. Bulk materials with many neighbouring WO_6 octahedra can transfer energy more easily than in the case of the Keggin structure with a limited number of octahedra.

The absence of nanoparticles is desirable in our present study as the formation of discrete particles, even at nanoscale, should be avoided in order to maintain the homogeneity within the gel. The luminescence is thus probably caused by the tungstate anions itself and not by “bulk species”.

To explain the different optical properties of ZrW_2O_8 precursor in the gel state, our hypothesis is that the entropy present in the aqueous solution disrupts the specific electron de-excitation path so that discrete wavelengths in the visible regions are only possible in the isolated structures present in the sol-gel state [9]. Those structures apparently retain their geometric identities when redispersed into water. Further research by EXAFS is necessary to characterize these identities and will be discussed in the next section.

2 EXAFS analysis of the precursor solutions

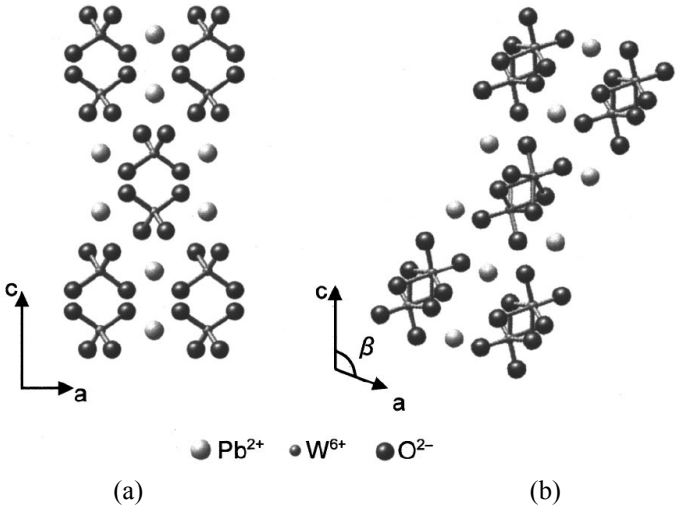

Figure 4: Projections of (a) scheelite and (b) wolframite structures of $PbWO_4$ along the b-axis. [4]

Tungstate compounds can be divided into two large groups depending on the environment of the W central atom [10]. Tungstates of calcium, strontium and barium have a tetragonal symmetry and are called scheelites or stolzites [5]. Na_2WO_4 can also be placed in this category [11]. The W atom is surrounded by 4 oxygen atoms in a tetrahedral or distorted tetrahedral surrounding. $MgWO_4$ is part of the wolframite or raspite series where the W atom is in the centre of an octahedron of with oxygen atoms. $ZnWO_4$ and $CdWO_4$ are also part of this family [12]. Some minerals such as $PbWO_4$ can be grown in both crystal structures or show respite inclusions in a scheelite structure [4]. Figure 4 shows both crystal structures for the $PbWO_4$ mineral

EXAFS analysis of the precursor solutions containing 0.02 M $(NH_4)_6H_2W_{12}O_{40}$ and 0.48 M citric acid and variable amounts of NH_4OH were performed to confirm the geometry of the species responsible for the luminescent behaviour at higher pH values as described above. These measurements reveal the coexistence of WO_4 tetrahedra and WO_6 octahedra.

Interpretation of such measurements requires reference materials. A Na_2WO_4 powder sample, 0.25 M Na_2WO_4 solution in water (pH 8.5) and $CaWO_4$ powder sample were chosen as representatives for the scheelite family. $MgWO_4$ powder and an acidified 0.25 M Na_2WO_4 solution in water (pH 1) were used as wolframite-type reference

materials. $MgWO_4$ and $CaWO_4$ were measured in powdered form as they are insoluble in water. Powder samples were suspended in grease and pressed between two paper sheets. The concentrations of the solutions are chosen as such to obtain an edge step of 1. The liquid samples were injected into a copper cell with kapton windows. The following sections will describe the different standard materials and the examined samples taken from the precursor solution at various pH values. The analysis of the EXAFS spectra (Chapter 2-§2) and the fitting was performed using the Artemis and Athena software packages [13].

2.1 EXAFS of scheelite reference materials

The absorption spectrum was collected between 9.948 and 11.172 keV. The $W_{L\ III}$ edge is situated at 10.207 keV. Figure 5 outlines the absorption spectra of Na_2WO_4 (aq) and $CaWO_4$ (s). Although they are both scheelite type of materials the fine structure superposed on the absorption is different.

Na_2WO_4 shows one maximum at 10.275 eV whereas $CaWO_4$ gives rise to two maxima situated just below the edge. Based on the information given in Chapter 2, the $\chi(k)$ functions of both samples are given in figure 6. In contrary to $CaWO_4$, the damped function of Na_2WO_4 is smoother and shows no splitting of peaks.

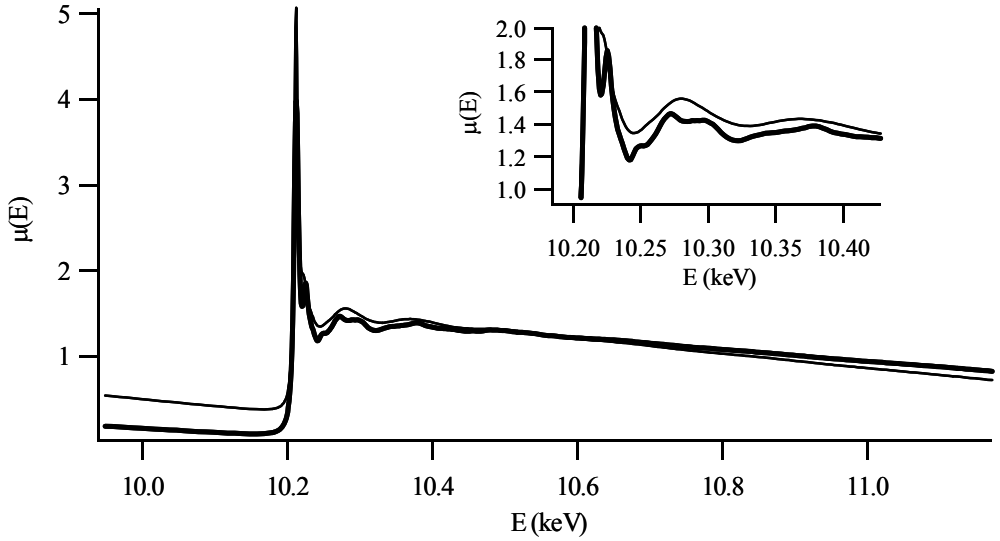

Figure 5: Absorption spectra at the W_{LIII} edge of a 0.25M Na_2WO_4 solution (thin line) and solid $CaWO_4$ (thick line) The insert is an enlargement of the absorption spectrum close to the edge.

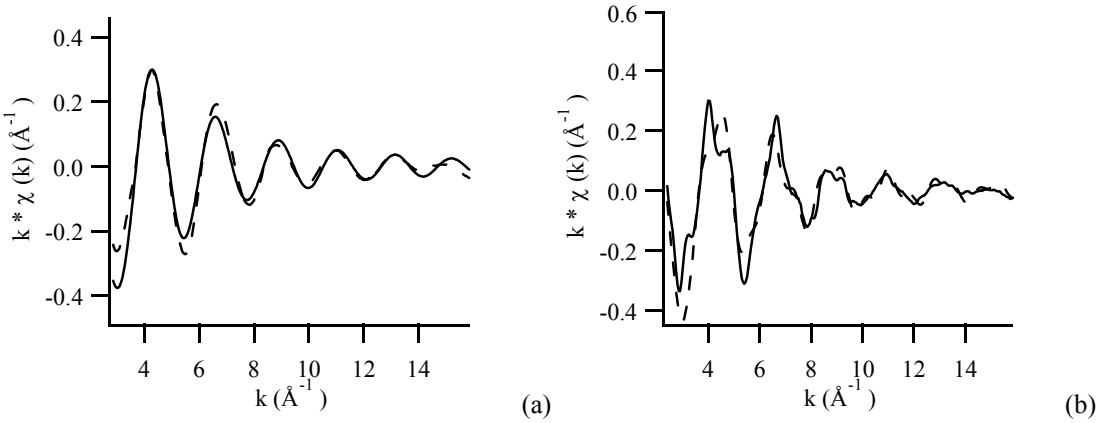

Figure 6: k*χ(k) function of (a) 0.25M Na_2WO_4 solution (pH 8.5) and (b) solid $CaWO_4$ between 3 and 16 Å. The dashed lines are the calculated k*χ(k) function using the fitting results mentioned below.

The radial atomic distribution function is obtained by Fourier transformation of the k * χ(k) function between 1.5 and 15 Å using a Kaiser – Bessel window. The results are given in figure 7. The radial atomic distribution function of the alkaline Na_2WO_4 solution shows a single intense peak at 1.4 Å (non-corrected for phase shift) which can be linked to the first coordination shell. The plot of $CaWO_4$ is more complex with 3 peaks. The first coordination shell is again situated at 1.4 Å and two addition peaks can be seen with maxima at 2.2 and 3.4 Å. The corrected values of these coordination shells are obtained by performing a fit using a suitable model. The crystal structure is well known for these standard materials and the input data are mentioned in table 1. The fit was performed for a R-range between 0.6 and 2 Å and a k-range between 2.510 and 13.7 $Å^{-1}$.

	Na_2WO_4 [14]	$CaWO_4$ [15]
Space Group	F d -3 m s	I 41/ a Z
Lattice constants	a = 9.133 Å	a = 5.2425 Å
	b = 9.133 Å	b = 5.2425 Å
	c = 9.133 Å	c = 11.3715 Å
	α = β = γ = 90°	α = β = γ = 90°
Atom coordinates	W 0; 0, 0	W 0; 0.25: 0.125
	Na 0.625; 0.625; 0;625	Ca 0; 0.25; 0.625
	O 0.3650; 0.3650; 0.3650	O 0.1497; 0.0093; 0.2097

Table 1: Crystallographic data of cubic Na_2WO_4 and tetragonal $CaWO_4$

The W – O distance of the first coordination shell is 1.769 Å (1.819 Å). The Debye-Waller factor is 1.2 $Å^2$ and the goodness of fit is 0.06 which expresses a reasonable fit. The fitting of the radial plot of $CaWO_4$ consisted of 3 different paths: scattering by 4 oxygen atoms at 1.783 Å (1.785 Å); scattering by 4 oxygen atoms at 2.900 Å (2.902 Å) and scattering by 4 Ca atoms at 3.865 Å (3.7074 Å). The XRD based values are mentioned between brackets and the global goodness of fit is 0.03.

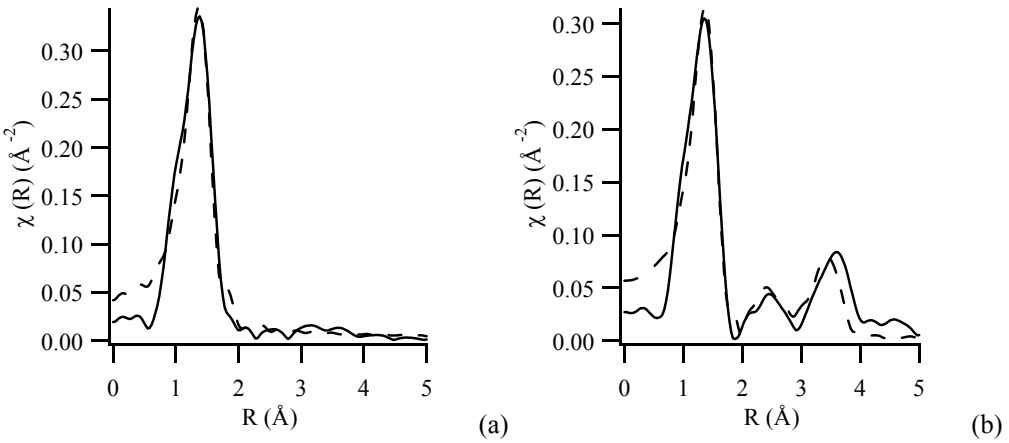

Figure 7: Radial structure plot of (a) 0.25M Na_2WO_4 solution (pH 8.5) and (b) solid $CaWO_4$ between 1 and 5 Å. The dashed lines are the calculated radial plots using the fitting results described above.

2.2 EXAFS of wolframite reference materials

As noted before, the wolframite materials ($MgWO_4$ and WO_3) are characterized by the tungsten atom surrounded by six oxygen atoms. WO_3 is built of WO_6 octahedra which are corner-sharing. An acid solution of 0.25 M Na_2WO_4 (pH 1) is measured as third reference sample. At this pH the tetrahedral surrounding is transformed in a wolframite-type with octahedral symmetry. The absorption spectra of these three samples are gathered in figure 8. The insert shows a magnification of the area close to the edge and no remarkable differences between the samples can be seen.

The radial atomic distribution plots mentioned in figure 9 are the results of a Fourier transformation of k^3- weighted $\chi(k)$ functions in the k-range 2 $Å^{-1}$ < k < 8 $Å^{-1}$ using Kaiser – Bessel windows. The radial plots of WO_3 and $MgWO_4$ exhibit a number of maxima in the R-range between 1 and 4 Å. The first peak around 1.3 Å, uncorrected for phase shift, corresponds to the first W coordination shell. In case of $MgWO_4$ these 6 oxygen atoms can be divided into 3 x 2 atoms located at the same distance from the

tungsten atom: 1.825 Å, 1.943 Å and 2.099 Å [16]. The next coordination shells are formed by W, O and Mg scattering atoms. In WO_3 the first coordination shell is made up by 6 oxygen atoms, each one with its own unique distance: 1.765 Å, 1.772 Å, 1.841 Å, 1.994 Å, 2.087 Å and 2.179 Å [17]. W and O atoms located further away from the central W atom are the building elements of the next coordination shells [18]. The average closest W – O distance in WO_3 (1. 9397 Å) is smaller than in $MgWO_4$ (1.9557 Å). This is reflected in the small shift of the radial plot to lower R values for the peak located between 1 and 2 Å.

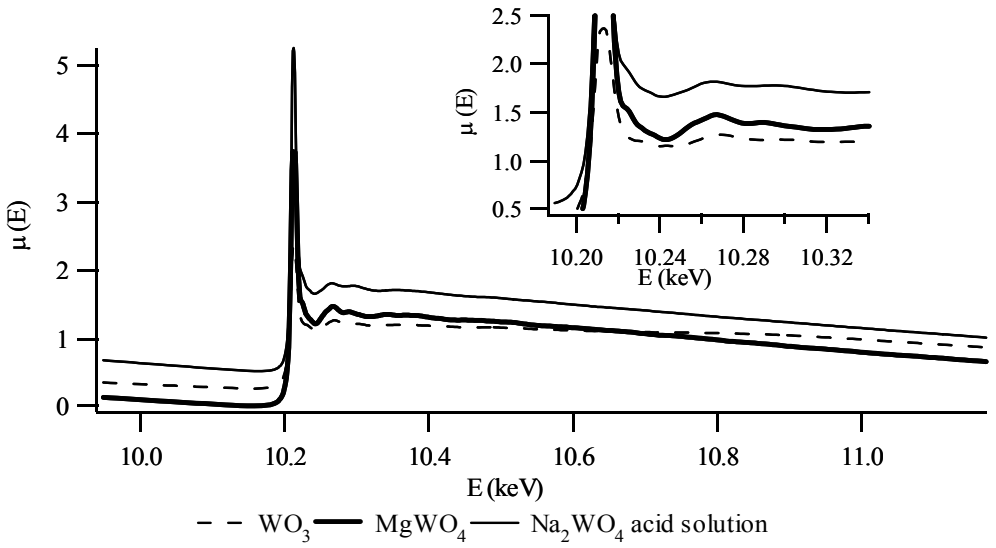

Figure 8: Absorption spectra at the W_{LIII} edge of a 0.25M Na_2WO_4 acid solution (thin line), solid $MgWO_4$ (thick line) and WO_3 (dashed line). The insert is an enlargement of the absorption spectrum close to the edge.

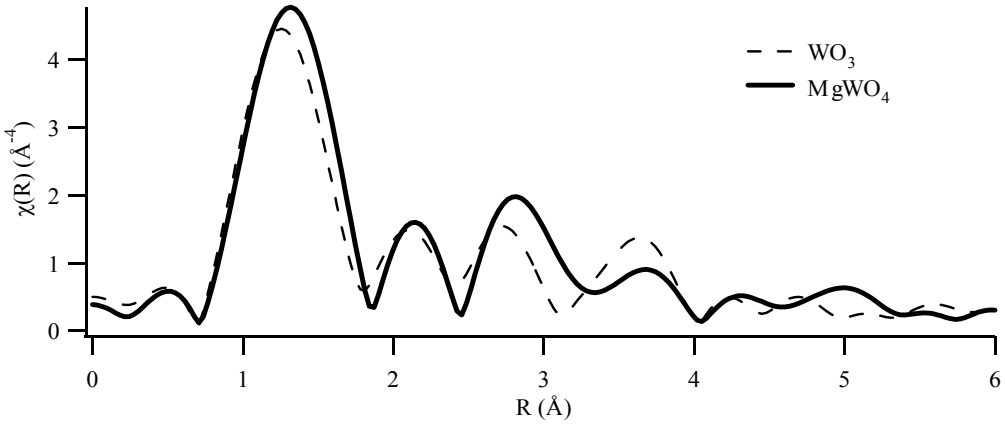

Figure 9: Radial structure plot of solid $MgWO_4$ (thick line) and WO_3 (dashed line) between 0 and 6 Å.

Figure 10 shows the k^3 weighted radial atomic distribution plots of both the alkaline and the acid solution containing 0.25 M Na_2WO_4. The W – O peak at 1.4 Å loses intensity and shifts to lower values. This is the result of destructive phase interference of multiple W – O distances which are typically found in octahedral surrounding. Acidification of tetrahedral tungstate solutions are known to form isopolytungstate anions, containing clusters of corner- and edge-shared octahedra [19]. Additional peaks between 2 and 4 Å arise from the proximity of the new-formed isopolytungstates and from W – O multiple distances.

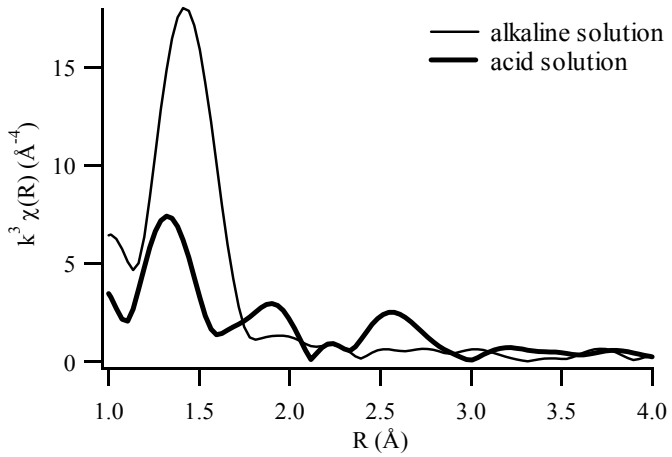

Figure 10: Radial structure plot of a 0.25M Na_2WO_4 alkaline (thin line) and an acid solution (thick line)

2.3 EXAFS of the sol-gel precursor solutions

The X-ray absorption was measured of an aqueous sample containing 0.02 M $(NH_4)_6H_2W_{12}O_{40}$ and 0.48 M citric acid. The pH of these solutions was increased stepwise from pH 1 till pH 8.5 by addition of ammonium hydroxide in order to generate the transition from octahedral to tetrahedral coordination. The absorption spectra of these samples are given in figure 11. The peak at 10.26 keV splits into two as the pH increases.

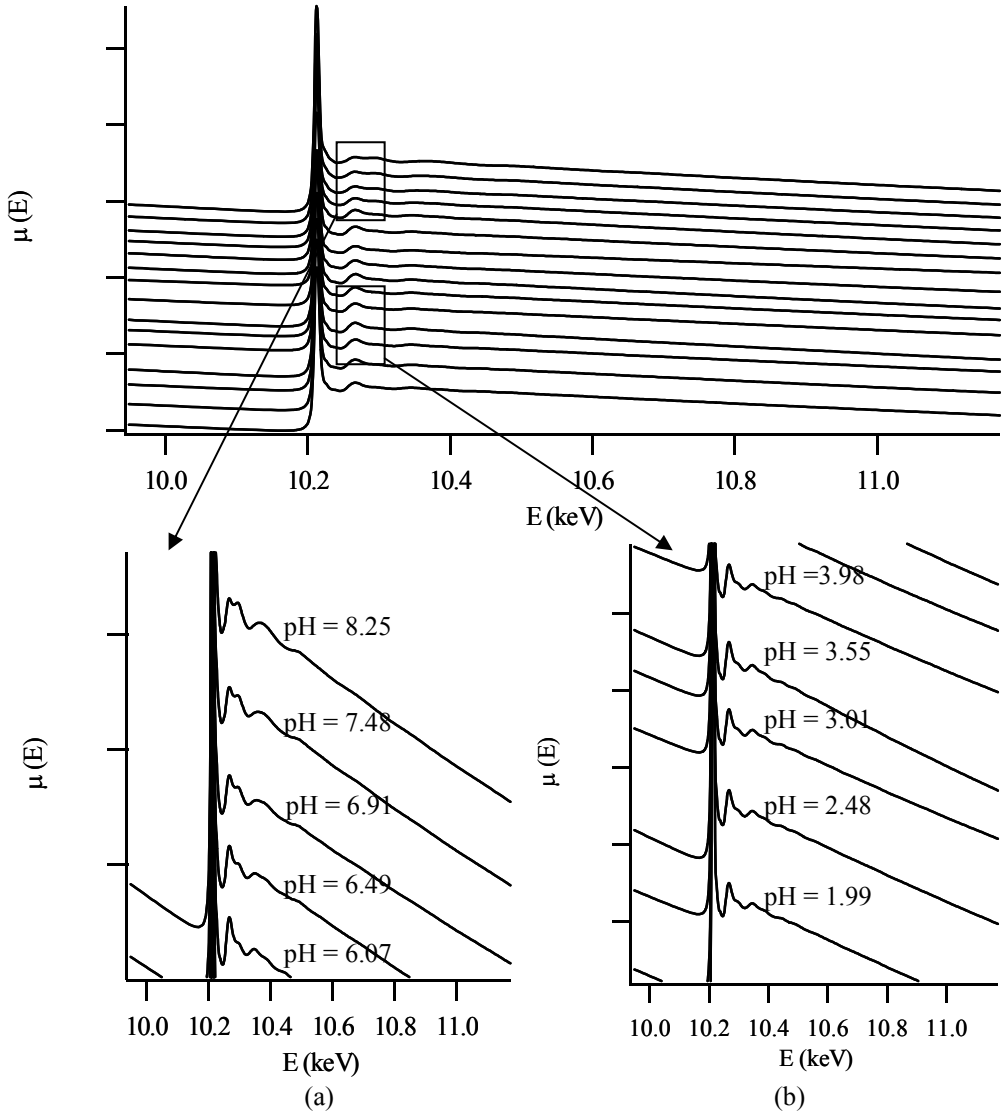

Figure 11: Absorption spectra at the W $_{LIII}$ edge of 0.02 M $(NH_4)_6H_2W_{12}O_{40}$ -0.48 M citric acid. NH_3 is added to tune the pH. The pH increases from bottom to top.

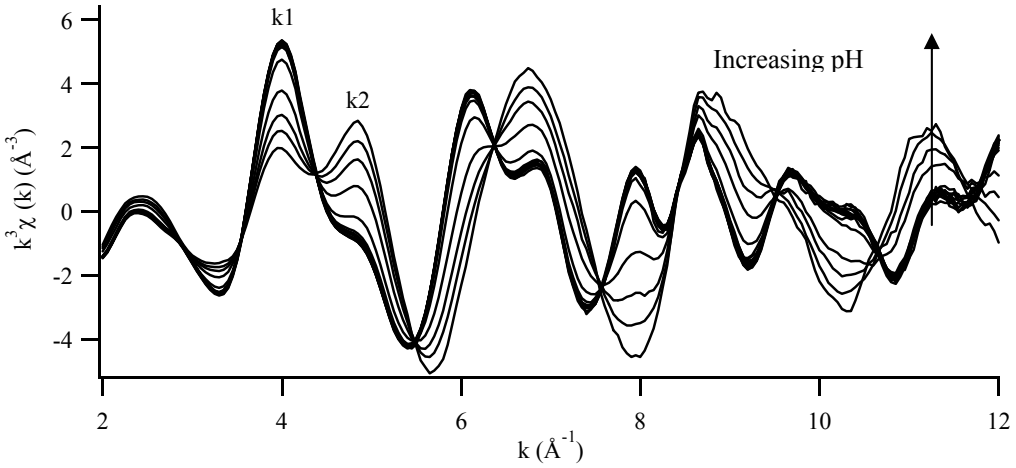

Figure 12: $k^3 * \chi(k)$ oscillatory function of the metatungstate solutions at varied pH

The changes in fine structure can easily be seen when the data are transformed into the $k^3 * \chi(k)$ oscillatory function which are plotted in figure 12 (k range: 2 - 12 Å^{-1}). Only the five samples with the highest pH value can be seen separately, the other data files overlap too closely. This differentiation starts from pH 5.5. The two peaks at 4 and 6 Å^{-1} have a shoulder peak at slightly higher Å^{-1} values. As the pH increases, the intensity of these shoulder peaks rise. The evolution of the intensities measured at k1 and k2 at various pH values are given in figure 13. A strong intensity increase starts from pH 6. The $k^3 * \chi(k)$ functions at pH 1 and pH 8.25 show remarkable resemblance with $k^3 * \chi(k)$ of respectively an acid and alkaline solution of Na_2WO_4 published by Hoffmann et al [19]. This already indicates that there is a change in coordination around the tungsten atom for the metatungstate precursor solutions as the pH is varied.

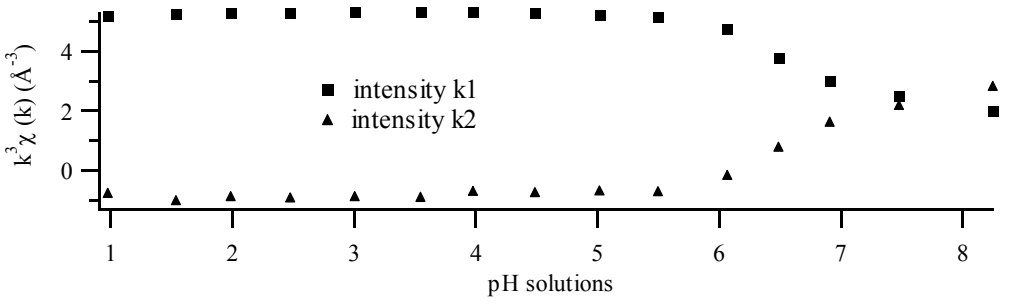

Figure 13: Intensity of $k^3 * \chi(k)$ function at 4.0 and 4.8 Å^{-1}

When oscillatory functions are Fourier transformed into radial plots, again a drastic change starting from pH 6 can be seen in figure 14. The evolution of the maxima of the two peaks at R(Å) 1 – 2 with pH is given in figure 15(a) and (b).

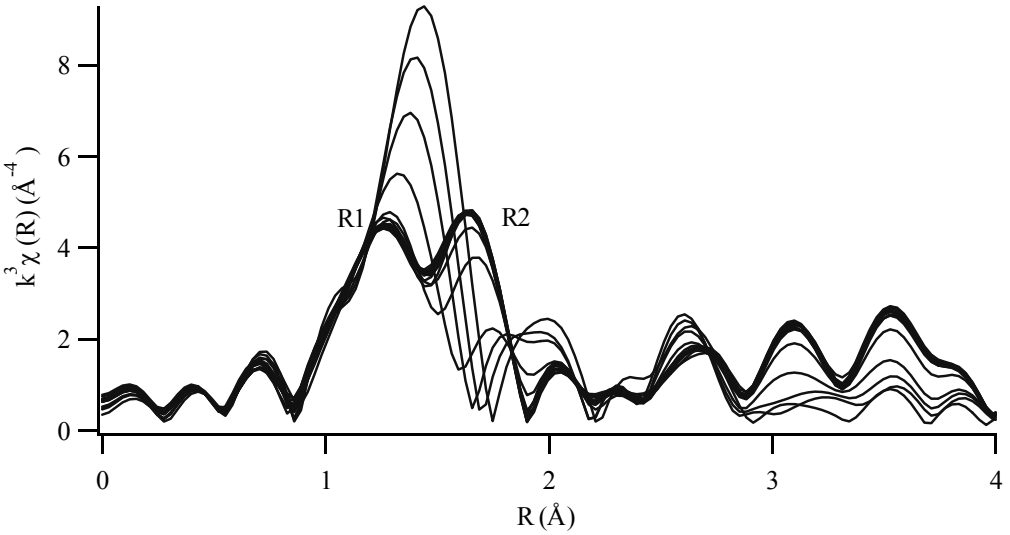

Figure 14: Radial plots of Fourier transformed of $k^3 * \chi(k)$ oscillatory function of the metatungstate solutions at various pH

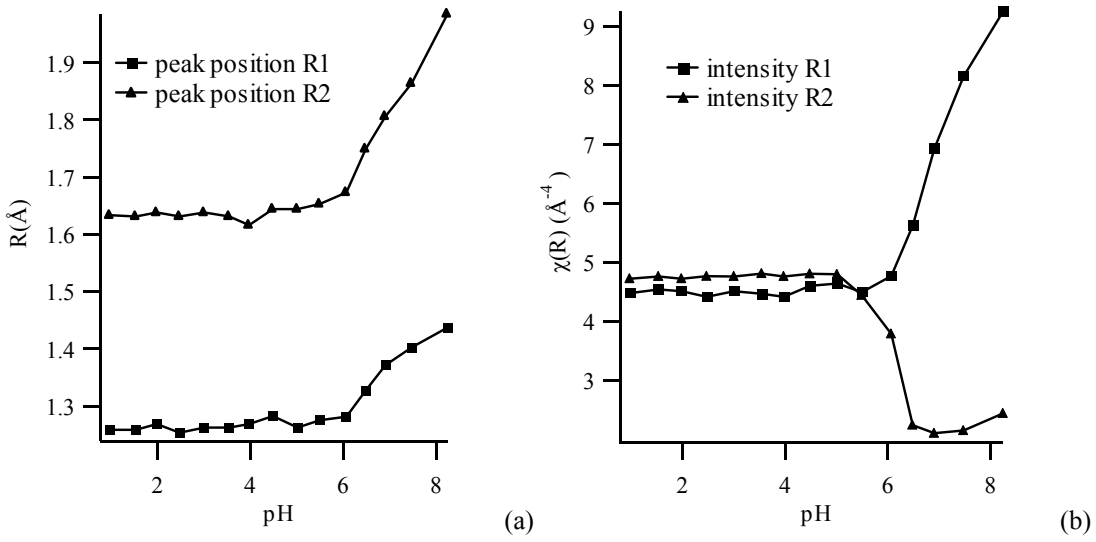

Figure 15: (a) peak positions and (b) peak intensities of R1 and R2 at various pH values

Clearly there is a shift in peak position and in peak intensity around pH 6. The change in intensity is very much like that of the Na_2WO_4 solutions. The tetrahedral (alkaline) solution has a more intense peak at 1.4 Å in comparison with the octahedral (acid) solution due to fewer multiple scatter distances.

There is also a decrease in intensity of the peaks above 3 Å. The influence of W and O atoms at larger distances becomes less dominant, probably because there is less long range order at high pH. The species seem to be more isolated. This may be interpreted that the Keggin structure present in the ammonium metatungstate species undergoes a transformation at pH 6 from the corner- and edge-shared octahedra to more independent tetrahedral–like species.

3 Conclusions

The spontaneous blue colouring of the gels by sunlight irradiation mentioned in Chapter 4 was generated by irradiation of the aqueous samples (pH 6) with a light source (wavelength 350 and 450 nm). The photoluminescence measurements revealed the presence of two bands in the emission spectrum. The blue luminescence is due to relaxation of the WO_4 tetrahedra whereas a less intense green band can be ascribed to the presence of WO_6 species. It is know that polyoxytungstates undergo structural changes as a response to changes in acidity but WO_4^{2-} anions in the tetrahedral coordination are unlikely at pH 6. The low decay time of the luminescence confirmed the presence of well dispersed molecules instead of bulk materials. The lack of bulk material is beneficial for the homogeneity in the sol-gel precursor.

EXAFS measurements of the aqueous solutions of ammonium metatungstate stabilized with citric acid were used to identify the real nature of the tetrahedral and octahedral species. The pH of these samples was gradually increased to see the influence of the acidity in the coordination around the central tungsten atom. A shift from octahedral to tetrahedral surrounding with increasing pH is suggested by differences in the radial plots.

4 References

1. R. Allman, Acta Crystallographica Section B-Structural Science, 1971. **27**: 1393.

2. A.M. Srivastava, H.A. Comanzo, and L.M. Levinson, *On the luminescence of ZrW_2O_8.* Materials Research Bulletin, 1998. **33**: 103-107.

3. M. Nikl, P. Strakova, K. Nitsch, V. Petricek, V. Mucka, O. Jarolimek, J. Novak, and P. Fabeni, *Energy transfer processes in $PbWO_4$ luminescence.* Chemical Physics Letters, 1998. **291**: 300-304.

4. M. Itoh and M. Fujita, *Optical properties of scheelite and raspite $PbWO_4$ crystals.* Physical Review B, 2000. **62**: 12825-12830.

5. V.B. Mikhailik, H. Kraus, D. Wahl, M. Itoh, M. Koike, and I.K. Bailiff, *One- and two-photon excited luminescence and band-gap assignment in $CaWO_4$.* Physical Review B, 2004. **69**.

6. N. Xu, M. Sun, Y.W. Cao, J.N. Yao, and E.G. Wang, *Influence of pH on structure and photochromic behavior of nanocrystalline WO_3 films.* Applied Surface Science, 2000. **157**: 81-84.

7. T. He, Y. Ma, Y. Cao, H.M. Liu, W.S. Yang, and J.N. Yao, *Comparison between the effects of TiO_2 synthesized by photoassisted and conventional sol-gel methods on the photochromism of WO_3 colloids.* Journal of Colloid and Interface Science, 2004. **279**: 117-123.

8. S.T. Li and M.S. El-Shall, *Synthesis and characterization of photochromic molybdenum and tungsten oxide nanoparticles.* Nanostructured Materials, 1999. **12**: 215-219.

9. I. Van Driessche and S. Hoste, *Functional Coatings by Polymer Microencapsulation*, ed. S.K. Gosh. 2006, Weinheim: VCH. 259-296.

10. A. Kuzmin and J. Purans, *Local atomic and electronic structure of tungsten ions in AWO_4 crystals of scheelite and wolframite types.* Radiation Measurements, 2001. **33**: 583-586.

11. V.N. Kolobanov, I.A. Kamenskikh, V.V. Mikhailin, I.N. Shpinkov, D.A. Spassky, B.I. Zadneprovsky, L.I. Potkin, and G. Zimmerer, *Optical and luminescent properties of anisotropic tungstate crystals.* Nuclear Instruments & Methods in Physics Research Section a-Accelerators Spectrometers Detectors and Associated Equipment, 2002. **486**: 496-503.

12. R.C. Pullar, S. Farrah, and N.M. Alford, *$MgWO_4$, $ZnWO_4$, $NiWO_4$ and $CoWO_4$ microwave dielectric ceramics.* Journal of the European Ceramic Society, 2007. **27**: 1059-1063.

13. B. Ravel and M. Newville, *ATHENA, ARTEMIS, HEPHAESTUS: data analysis for X-ray absorption spectroscopy using IFEFFIT*, in *Journal of Synchrotron Radiation*. 2005. p. 537-541.

14. K. Okada, H. Morikawa, F. Marumo, and S. Iwai, *Sodium Tungstate.* Acta Crystallographica Section B-Structural Science, 1974. **B 30**: 1872-1873.

15. M.I. Kay, B.C. Frazer, and I. Almodovar, *Neutron Diffraction Refinement of $CaWO_4$.* 1964, AIP. p. 504-506.

16. V. Kravchenko, *Crystal structure of the monoclinic form of magnesium tungstate $MgWO_4$.* Journal of Structural Chemistry, 1969. **10**: 139-140.

17. P.M. Woodward, A.W. Sleight, and T. Vogt, *Structure Refinement of Triclinic Tungsten Trioxide.* Journal of Physics and Chemistry of Solids, 1995. **56**: 1305-1315.

18. G.L. Poirier, F.C. Cassanjes, Y. Messaddeq, S.J.L. Ribeiro, A. Michalowicz, and M. Poulain, *Local order around tungsten atoms in tungstate fluorophosphate glasses by X-ray absorption spectroscopy.* Journal of Non-Crystalline Solids, 2005. **351**: 3644-3648.

19. M.M. Hoffmann, J.G. Darab, S.M. Heald, C.R. Yonker, and J.L. Fulton, *New experimental developments for in situ XAFS studies of chemical reactions under hydrothermal conditions.* Chemical Geology, 2000. **167**: 89-103.

Chapter 6

Synthesis and characterization of ZrW_2O_8 composites

The ZrO_2 - ZrW_2O_8 composites studied in this chapter have been prepared in various and sometimes innovative ways. The generalities concerning composites are discussed in §1. A more conventional method and a novel "in situ" method starting from off-stoichiometry mixtures of the pure oxide powders of ZrO_2 and WO_3 are described. The differences between these two methods are highlighted and the advantages of an adjusted sol-gel method used to prepare composites with high homogeneity is explored. This chapter draws heavily on the following publications.

Synthesis and thermal expansion of ZrO_2/ZrW_2O_8 composites

P. Lommens, C. De Meyer, E. Bruneel, K. De Buysser, I. Van Driessche, S. Hoste
Published in Journal of the European Ceramic Society, 25 (2005) 3605-3610

ZrO_2 – ZrW_2O_8 composites with tailor-made thermal expansion

K. De Buysser, P. Lommens, C. De Meyer, E. Bruneel, S. Hoste, I. Van Driessche
Published in Ceramics Silikaty, 48 (2004) 139-144

Synthesis and ZrW_2O_8 ceramics and composites from aqueous sol-gel precursors

K. De Buysser, S. Hoste, I.Van Driessche
Published in Advances in Science and Technology, 45 (2006) 218-22

1 Composites in general

1.1 Introduction

Many of today's technologies need materials with unusual combinations of properties which cannot be obtained by the traditional metal alloys, ceramics and polymeric materials. An example is the modern ski. It consists of various components, the function of each component is unique and the combination of all functions leads to the performance of the material above that of each of its components. Material property combinations and ranges have been extended by the development of composite materials [1-3].

A composite material can be defined as follows:

- It consists of two or more physical or chemically different phases which are well distributed and mixed with each other. The phases must be in close contact.
- The material exhibits certain properties which are attributed to the combination of the different phases but can not be seen in either of the isolated components.
- The material is obtained by a synthetic method.

Composites consist of a matrix phase, the continuous solid phase and the disperse phase. This phase can be in the solid, liquid or gaseous state. The properties of composites are a (not necessarily linear) function of the properties of the constituent phases, the relative amount and the geometry of the dispersed phases. This geometry can be described by the shape of the particles, the particle size, their distribution and orientation.

There are different ways to group the large family of composites. One of the possibilities is to classify them according to the matrix material used: Polymer Matrix Composites (PMC), Metal Matrix Composites (MMC) and Ceramic Matrix Composites (CMC) Another classification is built on the geometry of the dispersed

phase. A simple scheme for the classification is shown in figure 1. The three main divisions are the particle reinforced, fiber-reinforced and structural composites.

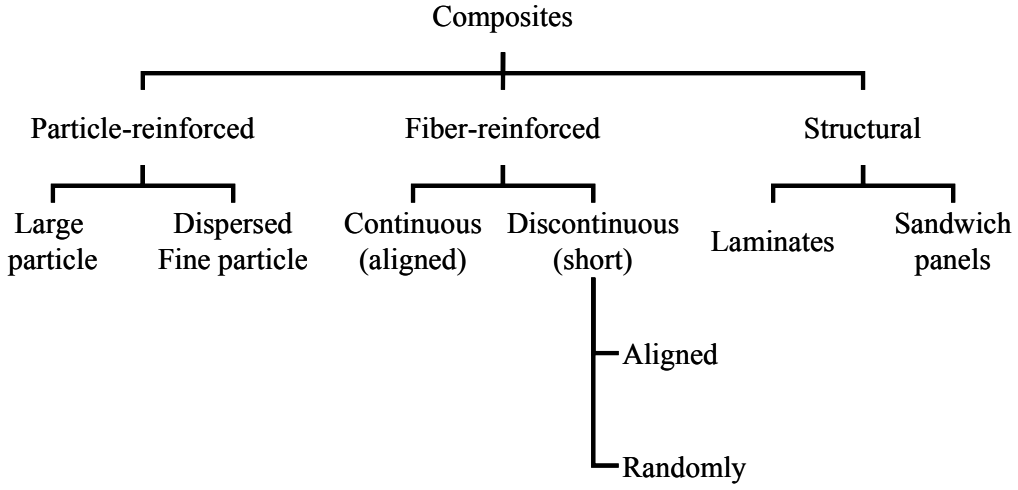

Figure 1: A classification scheme for the various composites types

The emphasis in this work is on Dispersion strengthened Ceramic Matrix Composites. Ceramic materials are somewhat limited in applicability by their mechanical properties. Their brittleness renders them mechanically inferior to metals or polymers. Nevertheless, their resistance to high temperatures makes it interesting to examine the synthesis of ceramic composites with an improved resistance to fracture and tuned properties depending on the dispersed phase used.

1.2 Synthesis of composites [4]

Once the components are chosen, the most suitable synthetic or preparation route must be developed. The most important process techniques to prepare ceramic matrix composites are stated in the following list.

First of all, there are the conventional methods. Cold pressing and sintering consist of an uni-axial pressing step followed by sintering of the material. HIP or Hot Isostatic Pressing combines the pressing and sintering step.

Some novel techniques have been developed. An in situ method is a chemical processing method in which the components gain their final structure during the reaction to form the composite. This synthesis step combines the reaction of two or

more components leading to the desired end-material together with the shaping of the composite. In this work the conventional methods are compared with such novel methods.

1.3 Properties of composites [1, 5]

Composites are synthesized with the aim of obtaining very specific properties. A dispersed phase can be added to adjust the colour or to modify the thermal expansion but in most of the cases Ceramic Matrix Composites are prepared in order to improve the fracture toughness of ceramic materials. In the new generation of CMC's particulates, fibers or whiskers of one ceramic material are embedded into the matrix of another ceramic. The influence of the increased fiber content on the mechanical properties is illustrated for SiC whisker-reinforced alumina in table 1.

Whisker Content (w%)	Fracture Strength (MPa)
0	360 ± 23
10	455 ± 55
20	655 ± 135
40	850 ± 130

Table 1: Room Temperature Fracture Strengths for various SiC whisker contents in Al_2O_3

The improvement in the fracture properties results from interactions between advancing cracks and dispersed phase particles. Crack initiation normally occurs inside the matrix phase, whereas crack propagation is impeded by the dispersed phase (i.e.particles, fibers or whiskers).

The properties of a composite material will be influenced by the properties of the individual components but also by their relative composition and the geometry. The composition of a composite material can be expressed in terms of weight fractions or weight percentages. To predict the mechanical characteristics, it is preferable to work in volume fractions or volume percentages (ν).

The rule of mixtures (Eq. 1) is a standard formula used to predict the final properties for many characteristics of the composite material. This expression gives the linear relation between the individual properties (X) where c, m and d are abbreviations

respectively of composite, matrix and dispersed phase, and the final characteristics of the composite material.

$$X_c = X_m \nu_m + X_d \nu_d \quad [1]$$

1.4 Thermal expansion properties of composites

As this work describes the exceptional negative thermal expansion behaviour of ZrW_2O_8, it is necessary to understand the thermal expansion properties of composites in general [6].

When two materials are combined into a composite, the compatibility of their thermal expansion is of the utmost importance. The difference in thermal expansion behaviour will give rise to tensions within the composite material. In a metal or polymer matrix, these tensions can be accommodated by elasticity of the material. Within ceramic matrix composites the tension will lead to cracks and fractures within the material. There is no general rule yet which allows the prediction of the differences in thermal expansion that will be tolerated or will lead to a specific deformation of the composite material.

Furthermore, the thermal expansion coefficient of a composite material will be influenced by micro-cracks, distribution of the grain sizes, properties of the grain boundaries and porosity.

For composites with a very low porosity, where there are no chemical reactions between the two components, relatively small differences in elastic moduli and the increase in temperature will not induce any cracks or sinter effects, the basic form of the rule of mixtures can be used concerning thermal expansion. Equation 1 can be rewritten to predict the thermal expansion coefficient as:

$$\alpha_c = \sum \alpha_i V_i \quad [2]$$

In this equation α_i is the thermal expansion coefficient of the individual components and V_i is the volume percentage present in the composite material.

2 State of the art of ZrW_2O_8 composites

This work stresses the different preparation methods and the resulting microstructure and mechanical properties of the ceramic composites. In order to complete this chapter on composite materials, the main features and application of composites based on NTE materials are reviewed here.

The first application for negative thermal expansion materials appears to be as component of composites to adjust the overall thermal expansion of composites to some particular value [7]. The composites with ZrW_2O_8 are a combination of the NTE material with metals or metal oxides.

2.1 Al-ZrW_2O_8 composites [8]

These composites were synthesized using Pulse Current Sintering followed by an adequate heat treatment. A wet mixing step was included in order to improve the homogeneity of the composites. The disadvantage of aluminum alloys is its large positive thermal expansion. ZrW_2O_8 was proposed as a candidate for compensating with its negative thermal expansion. An Al-75 vol% ZrW_2O_8 was stated as a nearly-zero thermal expansion material.

2.2 Cu-ZrW_2O_8 composites [9-13]

Metal matrix composites are attractive materials for application where the high thermal conductivity of metals and the low thermal expansion of ceramics are simultaneously needed. They can be used in electronic heat sinks with high heat dissipation and low thermal expansion mismatch with the silicon chip or the alumina substrate. Increasing the ceramic content of a composite will decrease its thermal expansion and the thermal conductivity. It is important to obtain a conductivity / expansion ratio as high as possible. Using Cu as a high-conductivity matrix and ZrW_2O_8 as the ceramic phase with a negative thermal expansion coefficient, the final prepared composite will potentially have a very good conductivity and a low expansion which is ideal for practical applications. Cu and ZrW_2O_8 were subjected to hot isostatic pressing (100 MPa) at 500 °C for 3 hours.

During this isostatic pressing reaction between the two phases occured resulting in a number of complex oxides containing Cu, Zr and W. A part of the α-ZrW_2O_8 phase undergoes a phase transition to the orthorhombic γ-phase under the influence of the applied pressure which results in a higher thermal expansion as expected from the literature.

2.3 ZrW_2O_8 – cement based composites [14]

Asphalt concrete or Portland cement concrete (PCC) are used in pavements as a surface layer. The temperature differential between the different layers of PCC causes deformation. The addition of low, zero or negative thermal expansion materials results in a self-compensating material composite which opens a window to many interesting practical prospects for a range of materials systems. The authors mentioned that additions of ZrW_2O_8 to a cement-sand mix showed reductions in its thermal expansion. The experimental data highlighted that zero thermal expansion was obtained with 60 w% ZrW_2O_8 addition.

2.4 ZrW_2O_8 substrates [15, 16]

Fibre Bragg gratings are applied as wavelength filters, dispersion compensators and wavelength stabilizers. The refractive index of the fibre Bragg gratings core varies as the temperature increases or decreases. The Bragg wavelength is directly coupled to this refractive index and will exhibit a temperature dependent variation. It is very important to create a system which is independent on any temperature fluctuations. ZrW_2O_8 was used as substrate to establish a hybrid system with a low thermal expansion coefficient. To obtain these substrates, ZrO_2 – WO_3 mixtures were pressed into a thin-plate shape and are heated between two platinum plates to allow the sample to heat and cool as uniformly as possible and to avoid the volatility of WO_3 during the sintering process. A plate of 3 mm × 30 mm × 55 mm was made with a thermal expansion coefficient of 10.5×10^{-6} °C^{-1}. These substrates can be used in the design of the coating of fibre Bragg gratings.

3 Preparation of ZrO_2 – ZrW_2O_8 composites

3.1 Introduction

In this chapter three different processes to prepare Ceramic Matrix Composites of ZrW_2O_8 and ZrO_2 are described. ZrO_2 is chosen because of its earlier applications in optical, electrical and energy devices and because of the absence of an intermediate phase between ZrO_2 and ZrW_2O_8 [17]. The composition ranged from 0 to 100 vol% of ZrW_2O_8. The work concerning the conventional preparation route was performed in close cooperation with dr. De Meyer. Some results were already published in her PhD thesis and the major results are recapitulated here in order to obtain a clear overview when comparing these results with those obtained in our new synthetic routes. An overview of all used preparation and synthetic routes is given in figure 14 at the end of this chapter.

3.2 Conventional processing of ZrO_2 – ZrW_2O_8 ceramic composites

In the conventional process, ZrW_2O_8 prepared using a conventional synthesis method described in Chapter 3-§2 was used as ceramic matrix. ZrO_2 was used as the dispersed phase. The flowchart in figure 2 schematically shows the preparation of the composites.

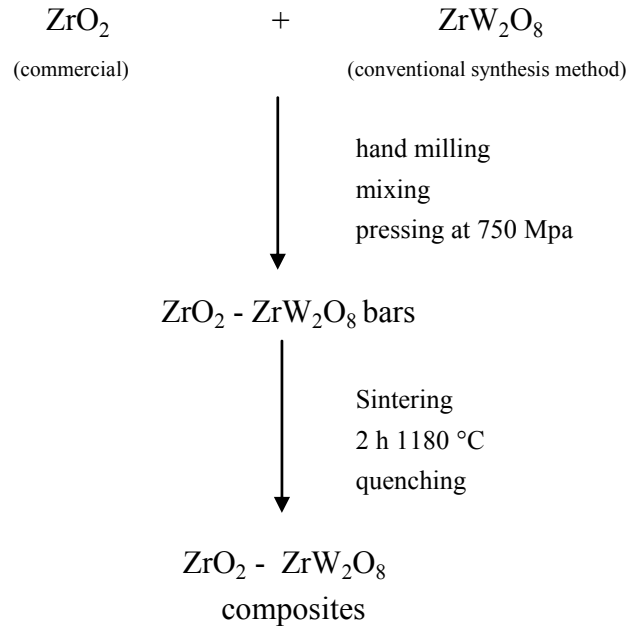

Figure 2: Synthesis scheme for the preparation of the composites

The ZrW_2O_8 and ZrO_2 powders were manually mixed in different ratios (table 2). The properties of these powders are summarized in table 3. By mixing in an agate mortar the particle sizes were reduced and the homogeneity of the mixtures was improved. The different mixtures were uni-axially, cold pressed into bars (2mm × 2mm × 13 mm – 0.3 g) at a pressure of 750 MPa. The same heat treatment procedure was used as in the synthesis of pure ZrW_2O_8. The samples were sintered at 1180 °C for 2 hours in a preheated furnace in air. Afterwards the bars were immersed in liquid nitrogen to avoid decomposition of ZrW_2O_8.

Desired w% ZrW_2O_8 in the composites	Mass ZrW_2O_8(g)	Mass ZrO_2(g)
100	10.0	0.0
80	8.0	2.0
50	5.0	5.0

Table 2: Preparation scheme for ZrO_2 – ZrW_2O_8 composites by a conventional method

Material	Particle size d_{50} (μm)	d_{90} (μm)
ZrW_2O_8	12.77	32.46
ZrO_2 (Aldrich)	3.15	6.54

Table 3: Powder specifications

3.3 Synthesis of ZrO_2 – ZrW_2O_8 composites by a novel in situ method using oxides precursors

The ZrW_2O_8 – ZrO_2 composites described here are synthesized starting from off-stoichiometry mixtures of the pure oxide powders of ZrO_2 and WO_3. This novel in situ process includes a heating step up to 1180 °C which combines the formation of ZrW_2O_8 and the sintering of the ZrW_2O_8 - ZrO_2 composite. The composites were prepared according to the scheme in figure 3. In this in situ method, commercial oxide powders were first milled in an agate ball mill for 24h in order to reduce the particle size and thus improve the homogeneity and the sintering ability of the mixture as described in chapter 3- §2.3.b. An average particle size of 0.62 μm for WO_3 and 1.06 μm for ZrO_2 was obtained. The particle size and particle size distribution of these powders are given in table 4.

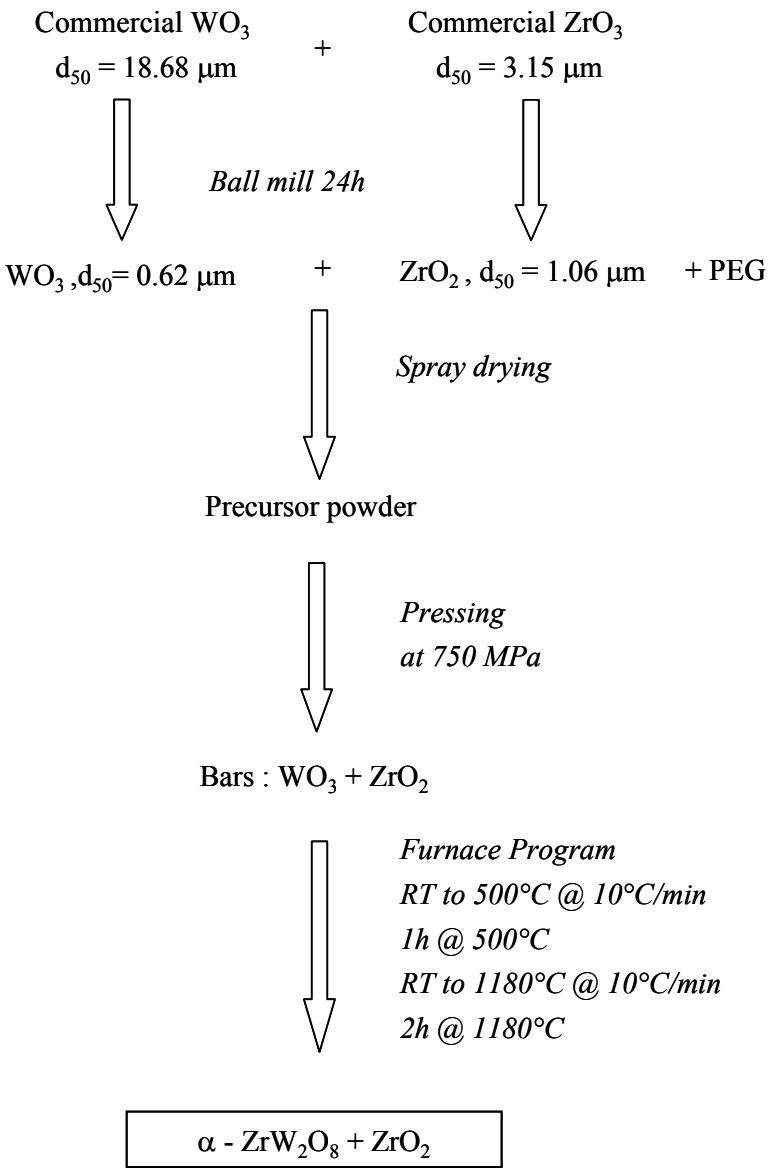

Figure 3: Synthesis scheme for composites according to the in situ method

Material	Particle size d_{50} (µm)	Particle size d_{90} (µm)
ZrO_2 (Aldrich)	3.15	6.54
ZrO_2 (milled 24h)	1.06	5.14
WO_3 (Aldrich)	18.68	40.78
WO_3 (milled 24h)	0.62	0.94

Table 4: Powder particle sizes

Bars obtained from the direct pressing of the milled powders were of poor quality. Therefore an aqueous slurry was prepared containing polyethylene glycol to stabilize the slurry. This additive possesses the additional benefit of reducing the friction during pressing of the bars. The organic material must be removed before final sintering. Thus the desired mixture of ball milled oxides was suspended in 250 ml deionised water together with 3 w% polyethylene glycol, calculated on the mass of the oxides. The amounts of oxides used in the preparation of the different composites are mentioned in table 5.

Desired w% ZrW_2O_8 in the composites	Mass WO_3(g)	Mass ZrO_2(g)	Mass PEG(g)
100	6.32	1.68	0.24
99	4.69	1.31	0.18
80	6.32	3.68	0.30
33	5.27	4.73	0.30

Table 5: Composition of the in situ composites before heat treatment

The slurry was stirred for 2 h followed by an ultrasonic treatment for 1 h to break the agglomerates down followed by spray drying using a Büchi mini spray dryer with a 0.5 mm nozzle and a feeding rate of 5 ml per minute (Inlet temperature: 160 °C; Outlet temperature: 100 °C; gas flow: 800 Nl/h). Afterwards, the powder was uni-axially, cold pressed to bars (dimensions: 2 x 2 x 13 mm) at a pressure of 750 MPa.

The bars were thermally treated under air in a covered Pt crucible in a high temperature furnace following the temperature program described in figure 3. An additional heating stage of 60 min at 500 °C ensures that all organic material will be expelled. This will have its effect on the mechanical properties of the composites as will be shown later. After heat treatment at 1180 °C, the bars were quenched in liquid nitrogen to avoid decomposition of ZrW_2O_8. Most of the bars prepared by the in situ method remain stable and show no cracks after thermal treatment. Nevertheless the bars containing less than 40 w% ZrW_2O_8 show some cracks after quenching. Examination of the mechanical properties of these samples is therefore not possible.

3.4 Synthesis of ZrO_2 – ZrW_2O_8 composites by the in situ method using sol-gel precursors

The composites were prepared under the same circumstances as the pure ZrW_2O_8 prepared by sol-gel (Chapter 4-§3) but with off-stochiometric amounts of Zr^{4+} and W^{6+} salts. The synthesis data for 100 mL precursor solution with 0.6 M metal ions in order to synthesize the different synthesized composites are given in table 6. The pH of the solution is adjusted with NH_4OH until a neutral pH value is obtained.

ZrO_2 – ZrW_2O_8 composite		# mmol $ZrO(NO_3)_2$	# mmol citric acid	# mmol $(NH_4)_6H_2W_{12}O_{40}$
w% ZrW_2O_8	vol% ZrW_2O_8			
100	100	20	120	3.33
90	91.2	26	156	2.83
80	82.2	31	186	2.33
50	53.6	45	270	1.28

Table 6: Preparation scheme for ZrO_2 - ZrW_2O_8 composites by sol-gel

4 Analysis of the composites

4.1 X-ray analysis and morphology studies

The composite bars mostly showed no cracks or shape deformation after the sintering step of 2h at 1180°C and the subsequent quenching step. This indicates that these bars are able to withstand the thermal stresses created during heating and quenching remarkably well. These stresses originate from the differences in thermal expansion coefficient between ZrW_2O_8 (-10.4×10^{-6} °C^{-1} from 0 to 100 °C and -3.4×10^{-6} °C^{-1} from 200 to 300 °C) and ZrO_2 (9.6×10^{-6} °C^{-1}). X-ray diffraction analysis confirms that only α-ZrW_2O_8 and monoclinic ZrO_2 are present as shown for a 50 w% ZrW_2O_8 composite prepared by the conventional method and a 40 w% sample prepared by an in situ method using oxide precursors in figure 4. The most intense ZrO_2 reflections are indicated by an asterisk. Not all ZrO_2 reflections were indicated for the clarity of the diffractogram.

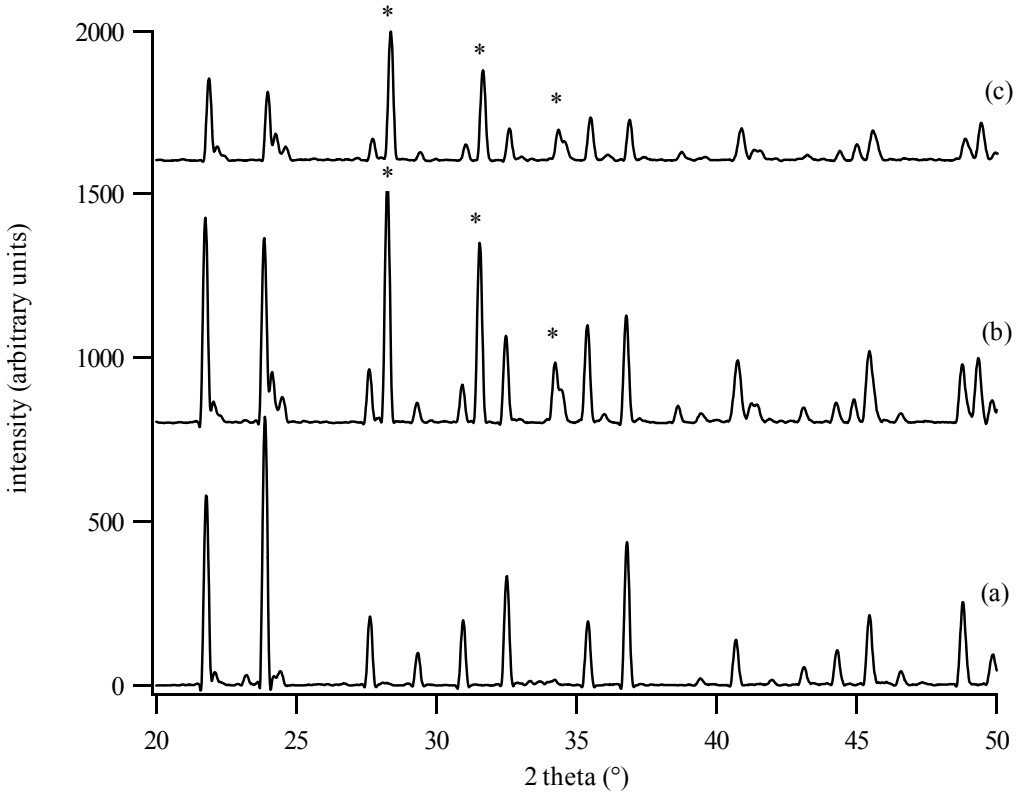

Figure 4: X-ray diffraction pattern from (a) pure α-ZrW_2O_8, (b) 50 w% ZrW_2O_8 conventional composite after sintering and (c) 40 w% ZrW_2O_8 composite prepared by an in situ method using oxide precursors (*) indicates the most characteristic reflections for monoclinic ZrO_2

The microstructure of the fractured surfaces of composites with various compositions is different as can be seen in the following SEM micrographs. The higher the ZrO_2 content of the composite materials, the more and smaller grains are present within the materials. This can be seen in their microstructures given in figure 5.

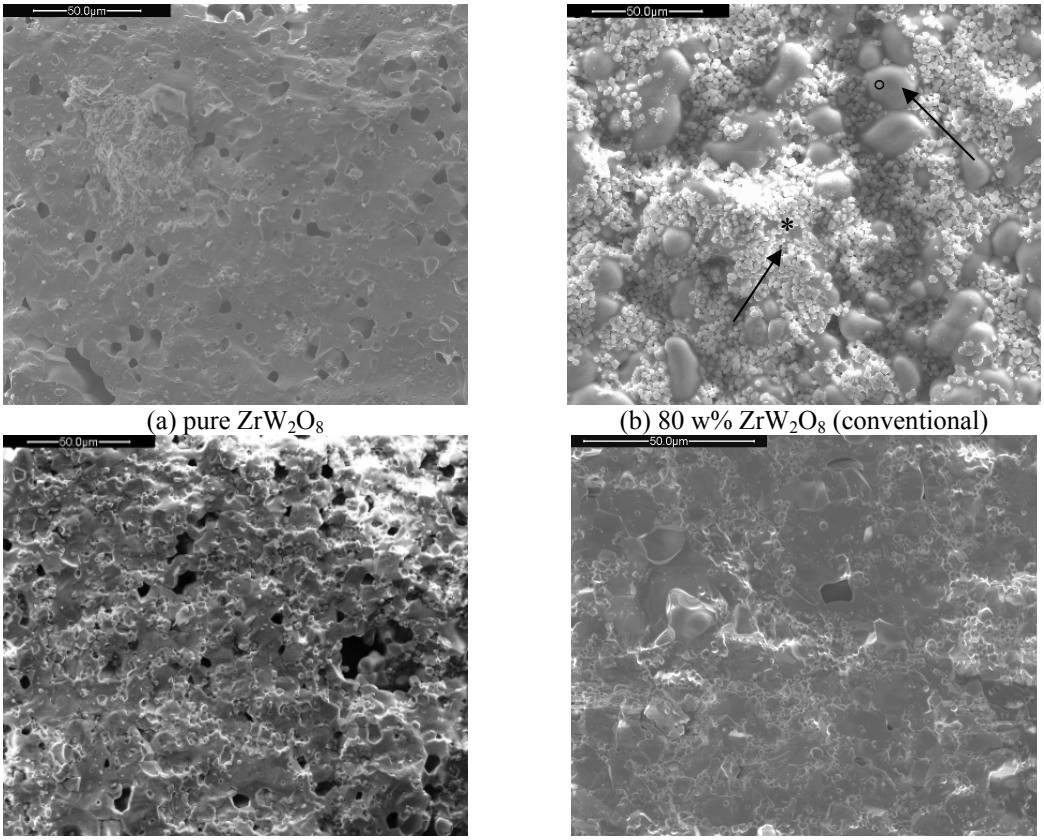

(a) pure ZrW_2O_8 (b) 80 w% ZrW_2O_8 (conventional)

(c) 80 w% ZrW_2O_8 (in situ – oxides) (d) 80 w% ZrW_2O_8 (in situ – sol-gel)

Figure 5: scanning electron micrograph of a fractured surface from a (a) 100 w% ZrW_2O_8 sample, (b) 80 w% ZrW_2O_8 composite prepared by a conventional method, (c) 80 w% ZrW_2O_8 composite prepared by an in situ method using oxide precursors and (d) 80 w% ZrW_2O_8 composite prepared by an in situ method using sol-gel precursors.

In pure ZrW_2O_8 (figure 5(a)) a totally different microstructure is found in comparison with the 80 w% composite material (figure 5(b)) prepared by a conventional method. The main reason for the difference is the high sintering temperature of ZrO_2 (2100 °C), which is considerably above the sintering step of 1180 °C in our preparation method of the composites. The ZrO_2 phase remains as loose powder between the larger ZrW_2O_8 grains. Furthermore, its presence hinders the sintering of the ZrW_2O_8 phase. This assumption was confirmed by closer investigation of the microstructure. EDAX-mapping of figure 5(b) showed that the sintered, homogeneous areas, indicated with an asterisk (*) contain Zr and W atoms while in the area

consisting of non-sintered grains, indicated with a (°), predominantly Zr atoms are found. Increasing the sintering temperature is not an option as the ZrW_2O_8 will melt at 1270 °C.

The in situ method using oxide precursors involves a spray drying step of the polyethylene stabilized slurry. This organic material is removed by an additional heat treatment at 500 °C. During this evaporation, pores are formed in the composites as can be seen in figure 5(c). The pores can also be caused by the volatilization of WO_3. The electron micrograph of the sol-gel based composites is shown in figure 5(d). Fewer pores were detected in the fractured surface of sol-gel based composite bars in comparison with the previous mentioned preparation and synthesis routes for ZrO_2 – ZrW_2O_8. The synthesis via the citrate-gel method results in a fine, pure and homogeneous oxide mixture well suitable for further synthesis.

The microstructure of the fractured surfaces of composites with identical compositions is strongly dependent on the preparation route chosen. The difference is clear. In the conventionally obtained composite (figure 5(b)), ZrO_2 loose powder remains present between the larger ZrW_2O_8 grains due to the sinter temperature of ZrO_2, which is much above that of ZrW_2O_8. The relatively better homogeneity of the in situ composite (figure 5(c-d)) can be explained by the small dimensions of the starting powder which results in a much more homogeneous mixture. Furthermore, because ZrW_2O_8 is formed in situ, the ZrO_2 grains are more dispersed in the composite. On the other hand and due to the dispersing agent used in the in situ method using oxides additional pores caused by the evaporation of the organic material and volatilization of WO_3 can be seen.

4.2 Flexural strength of the ZrO_2 – ZrW_2O_8 composites

Handling the bars is not simple because of the brittle nature of these ceramics. The mechanical properties were measured by a three-point bending test [1]. The standard test method for flexural properties of ceramic materials (C674) mentions the desired dimensions of the test specimens. The rectangular specimens are 25.4 mm by 12.7 mm in cross section and at least 114 mm in length. The samples prepared in our laboratory with the dimensions 2 mm x 2 mm x 13 mm are much too small to obtain objective results. To compare several compositions and materials with one another, I have chosen to tabulate relative flexural strengths with the flexural strength of ZrW_2O_8 (14.5 MPa) as 100%. The results are preliminary and a large margin of error should be taken into consideration.

The flexural strength σ can be calculated by the following equation:

$$\sigma = \frac{3\,L\,F}{2\,b\,h^2} \qquad [3]$$

where L is the distance between the support points, F the load at rapture, b the cross section of the sample and h is defined as the thickness.

In figure 6 the relative flexural strength is given as a function of vol% ZrW_2O_8 present in the composite prepared using an in situ method with oxide precursors. At first sight, there is no relationship between both parameters. There is no particular improvement of the mechanical properties of the materials. Besides the tuning of the thermomechanical properties by enhancing tailor made thermal expansion, any effect on the mechanical strength by ZrO_2 particles present in the ZrW_2O_8 ceramic matrix is absent. This is mainly caused by the poor sinterability of ZrO_2 at the synthesis temperature of the composites. Using polyethylene glycol as dispersant and pressing aid causes pores due to evaporation of the organic material. This may overcompensate any improvement obtained by crack deflection by the presence of ZrO_2.

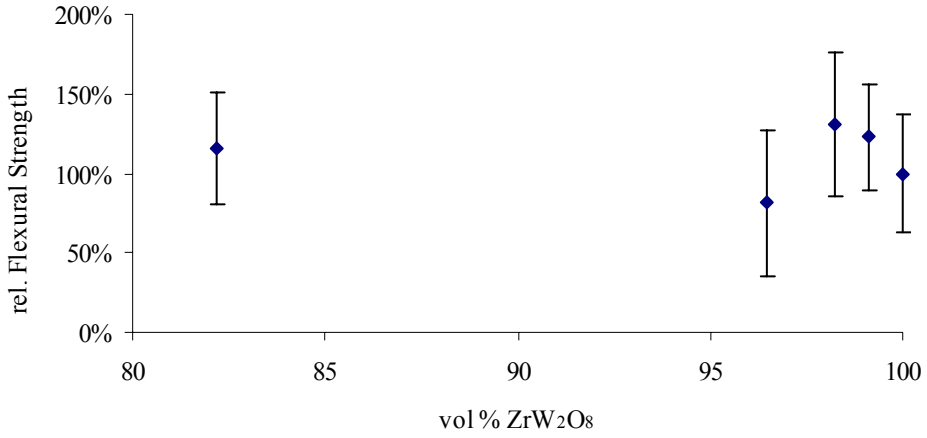

Figure 6: Evolution of the relative flexural strength in ZrW_2O_8 - ZrO_2 composites by in situ processing (oxides precursors)

The porosity and the density of materials are a major parameter in their strength. Porosity is deleterious for two reasons. First of all, the pores reduce the cross-sectional area across which a load is applied. On top of that, they can act as stress concentrators. The influence of porosity on strength is rather dramatic. When the data is converted into the volume percentage of open and closed pores present in the composite material versus the relative flexural strength, it can be seen that the flexural strength of the material drops with an increasing porosity and thus a decreasing density (figure 7).

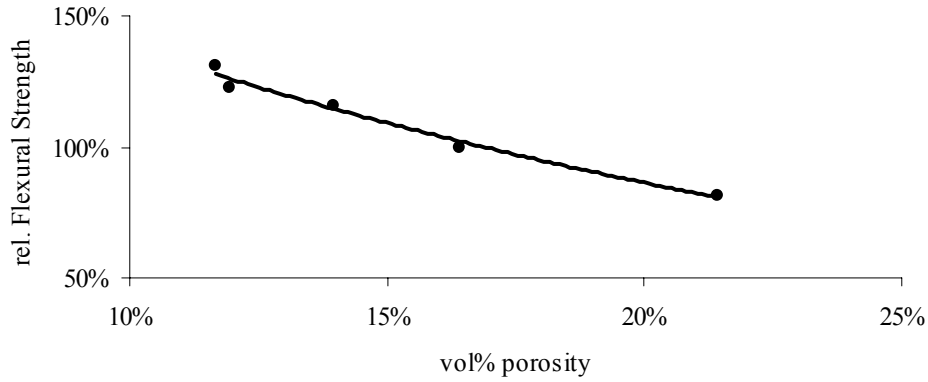

Figure 7: Relation between the relative flexural strength and vol% of open and closed pores

It was stated [1] that an exponential relationship exists between the flexural strength and the porosity as given in equation 4.

$$\sigma = \sigma_0 \exp(-nP) \qquad [4]$$

In this expression, P is the volume fraction porosity, σ is the flexural strength and σ_0 and n are experimental constants obtained by a least-squares fit.

The following experimental parameters are obtained using the data of the relative flexural strength (R^2 of the least square fit = 0.99).

σ_0 = 2.2075, a material with no porosity present can have a relative flexural strength which is more than 2 times larger that the flexural strength of the pure ZrW_2O_8 sample synthesized in this work.

n = 4.696, this parameter represents the influence of the porosity on the mechanical properties of the material. In this case a porosity of 10 vol% will decrease the flexural strength by over 35 % from the measured value for the non-porous material. Both the organic phase due to the dispergens agent and the high sintering temperature of ZrO_2 will make it very hard to prepare closed packed composites with tailor made expansion and mechanical properties suitable for industrial applications.

It is clear that the visual difference in microstructure (figure 5) must concur with differences in mechanical properties of the ceramic matrix composites. In figure 8, the flexural strengths are plotted for the pure ZrW_2O_8 phase (100 w%) and for two composites with the same composition (80 w% ZrW_2O_8) but with a different method of preparation. Only one composite was tested because the other composites prepared by the conventional method were of such poor quality that they failed before they could be tested. The flexural strength is rather similar for the pure phase and the in situ composite (oxides as precursors) whereas the composite prepared by the conventional method shows a significantly lower flexural strength which was expected from the morphological analysis. The total porosity for these composite materials prepared by the conventional processing route is 29.56 vol% calculated with the use of the geometric and theoretical densities.

Compared with the other two samples given in figure 8 (16.77 vol% for the pure ZrW_2O_8 and 14.90 vol% for the 80 w% in situ (by oxides) composite) there is a remarkable difference. The main reason for the decrease of the flexural strength is the loose ZrO_2 powder as explained above and a larger porosity. Less agglomerates of unsintered ZrO_2 can be seen in the in situ prepared samples.

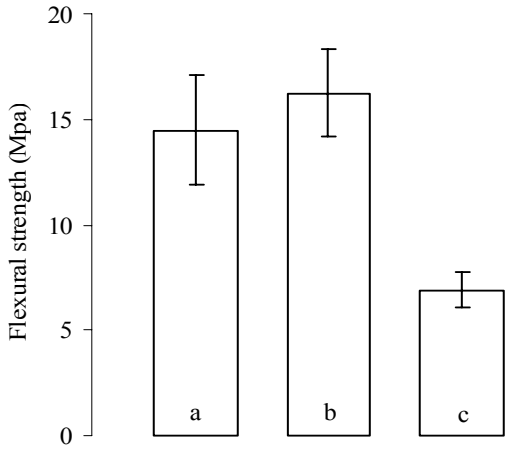

Figure 8: Relative Flexural strength for (a) pure ZrW_2O_8, (b) 80 w% in situ using oxides and (c) 80 w% conventional processing

The influence of the porosity on the flexural strength of the composites shown above was fitted to equation 4 and the R^2 of the least square fit was 0.99. The σ_0 parameter equals 2.7521 whereas n is calculated to be 5.9165.

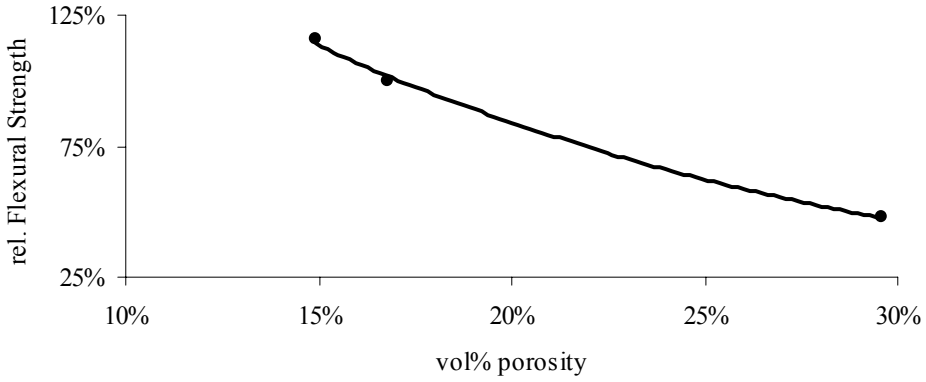

Figure 9: Relation between the relative strength and the vol% porosity of the samples mentioned in figure 8

The average porosity of the conventionally processed composites (25%) is larger than the ceramic matrix composites prepared by the in situ route using oxides (17%). Two examples are given in figure 10. In both cases the conventional route leads to a more pronounced porosity.

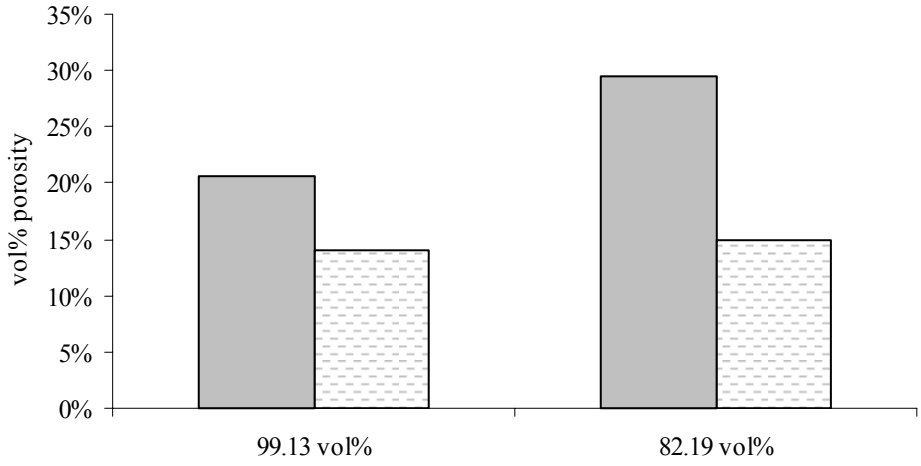

Figure 10: Comparison of the porosity in a 99.13 vol% and an 82.19 vol% ZrW_2O_8 composite. The filled blocks represent a conventional processed composite where the striped ones show the results of an in situ composite using oxides

4.3 Thermomechanical analysis

The composites consist of a mixture of positive and negative thermal expansion material. The thermal expansion coefficient is expected to increase, as the zirconium oxide content increases. In figure 11 the thermal expansion coefficients calculated from the simple "linear" rule of mixtures ($\alpha_c = \Sigma\alpha_i V_i$) at 225 °C are compared to the experimental data.

A negative deviation from the predicted values is found for all preparation and synthesis methods but the deviation is smaller for the in situ methods. The results prepared by a conventional method are lower compared with the in situ methods. The negative deviation is most pronounced in the middle of the compositional range and can be explained as follows: the rule of mixtures is only valid for a sample without voids, free of thermal stresses and when the different phases have the same elastic modulus [4, 18]. Here, none of these conditions is fulfilled. Clearly in the middle of the compositional region, where the differences in thermal expansion coefficient and

elastic modulus cause the highest stresses, the thermal expansion coefficient shows the largest deviation from the expected coefficient.

The rule of mixtures fails to predict the thermal expansion of the composite materials because it excludes the influence of the differences in mechanical properties of the matrix and the dispersed phase. A negative deviation, which can found in many other composite systems [4], can be understood as follows: the materials have a lower expansion coefficient than expected from a linear combination of the properties of the starting materials. Considerably lower volumes of ZrW_2O_8 suffice to compensate for the positive thermal expansion of the ZrO_2 phase than those calculated using this rule. A possible explanation is that the open framework structure of ZrW_2O_8 is crushed by the expanding ZrO_2 particles. The other way around is the hypothesis that the shrinkage of ZrW_2O_8 is insufficient for complete expansion of the ZrO_2 particles leading to an overestimation of the thermal expansion coefficient by the rule of mixtures.

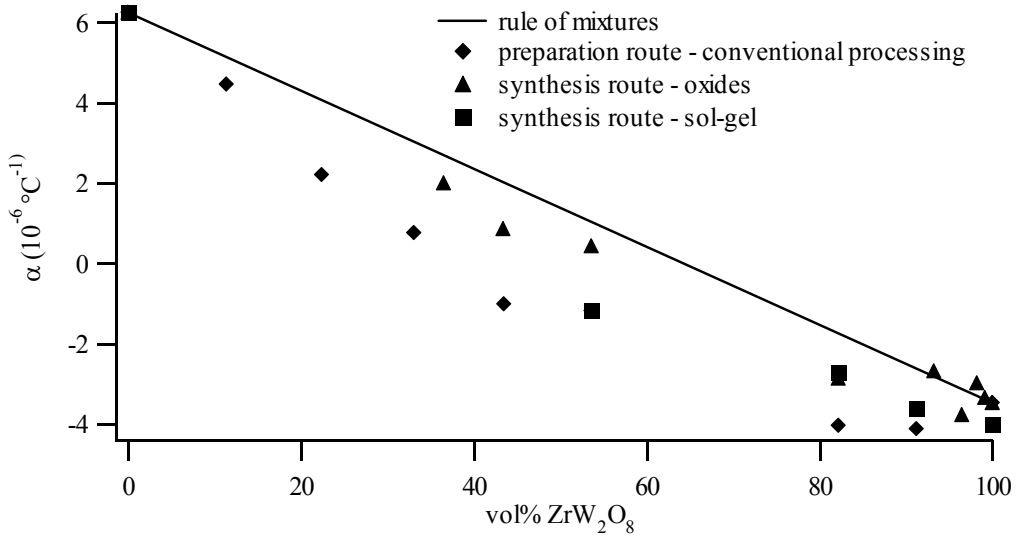

Figure 11: Thermal expansion coefficients for composites prepared by the in situ (by oxides) (▲) conventional method (+) and in situ (sol-gel precursors) (□)

Using the rule of mixtures, the value of the thermal expansion coefficient is predicted to remain negative down to a volume ratio of 64 vol% (at 225 °C). However, we found that volume ratios well below 64 vol% still yielded negative expansion. The experimental data for conventionally prepared composites reveal that zero thermal expansion could be obtained using a 62 vol% ZrO_2 – 38 vol% ZrW_2O_8 composite.

This may have important technological consequences because it shows that a relatively low volume fraction of ZrW_2O_8 is sufficient to compensate effects of thermal expansion in a powderous matrix.

Our results can also help us to predict the composition required to obtain the desired zero thermal expansion. In literature [17], a composite prepared by the conventional method and consisting of 66 w% (63.5 vol%) ZrO_2 and 33 w% (36.5 vol%) ZrW_2O_8 was suggested to result in zero expansion. The change in linear dimensions as a function of temperature for a composite with this composition but prepared using an in situ method with oxides as precursors is given in figure 12. This composites has zero thermal expansion at room temperature. From 160 °C onwards, a slight thermal expansion is noted. This is coincident with the occurrence of the α to β transition and can be explained as follows. The β-phase possesses a lower negative thermal expansion coefficient (-3.4×10^{-6} °C^{-1}) than the α-phase (-10.4×10^{-6} °C^{-1}) and this obviously changes the compensatory effect of the ZrO_2 which exhibits a strongly positive expansion coefficient (9.6×10^{-6} °C^{-1}) which remains constant in the entire temperature region. Looking back at figure 11, the data points collected at 225 °C (β-phase) already suggested a positive thermal expansion coefficient for the chosen composition. An in situ composite with zero thermal expansion starting from 160 °C should contain 55 vol% ZrW_2O_8 and 45 vol% ZrO_2.

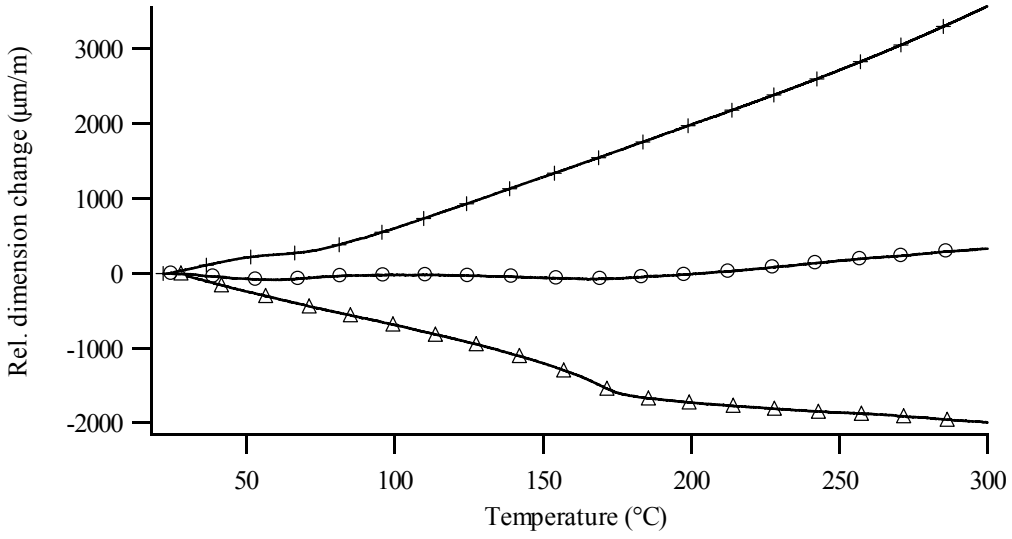

Figure 12: Thermal expansion for ZrO_2 (+), ZrW_2O_8 (Δ) and 36.5 vol% in situ composite (o)

In some cases a synergy effect occurs where the properties of the composites are superior to the combination of the individual characteristics of the isolated components. In order to describe those in a quantitative way, we propose to use a modified form of the linear rule of mixtures. In cases where deviation can be thought as arising from "product properties" or "synergy effects" the following descriptor model is described.

$$X_c = X_m \nu_m + X_d \nu_d + f\left[X_m(1-\nu_m) \times X_d(1-\nu_d)\right] \quad [5]$$

where parameter f represents the weight of the synergy contribution.

As can be seen in figure 13 (a-c), the curve obtained by equation 5 can be fitted to the experimental results by adjusting parameter f. The optimal f value and the average deviation of the experimental results to the fit are mentioned in the graphs. The larger deviation of the rule of mixtures in the conventional prepared composites is translated in a larger f value whereas the in situ composites prepared by oxides show the best fit with a much lower f value. A high f value symbolizes a large deviation of the experimental results to the rule of mixtures and thus a less "ideal" composite material by the influence of the synergy effect.

A possible explanation is already cited above and can be confirmed by the data mentioned in table 7. The particle sizes of the precursor materials used in the in situ synthesis using ZrO_2 and WO_3 are much smaller in comparison with the other materials resulting in a homogeneous end material. Nevertheless the particle sizes of the sol-gel precursors are comparable with those of the conventional preparation route, the benefit of the "in situ" synthesis combining sintering and synthesis results in a "better" composite material (lower f value).

Material	Particle size d_{50} (μm)	Particle size d_{90} (μm)
ZrW_2O_8	12.77	32.46
ZrO_2 (Aldrich)	3.15	6.54
ZrO_2 (milled 24h)	1.06	5.14
WO_3 (milled 24h)	0.62	0.94
sol-gel precursor mixture	11.44	30.25

Table 7: Overview of the particles sizes of the precursor materials

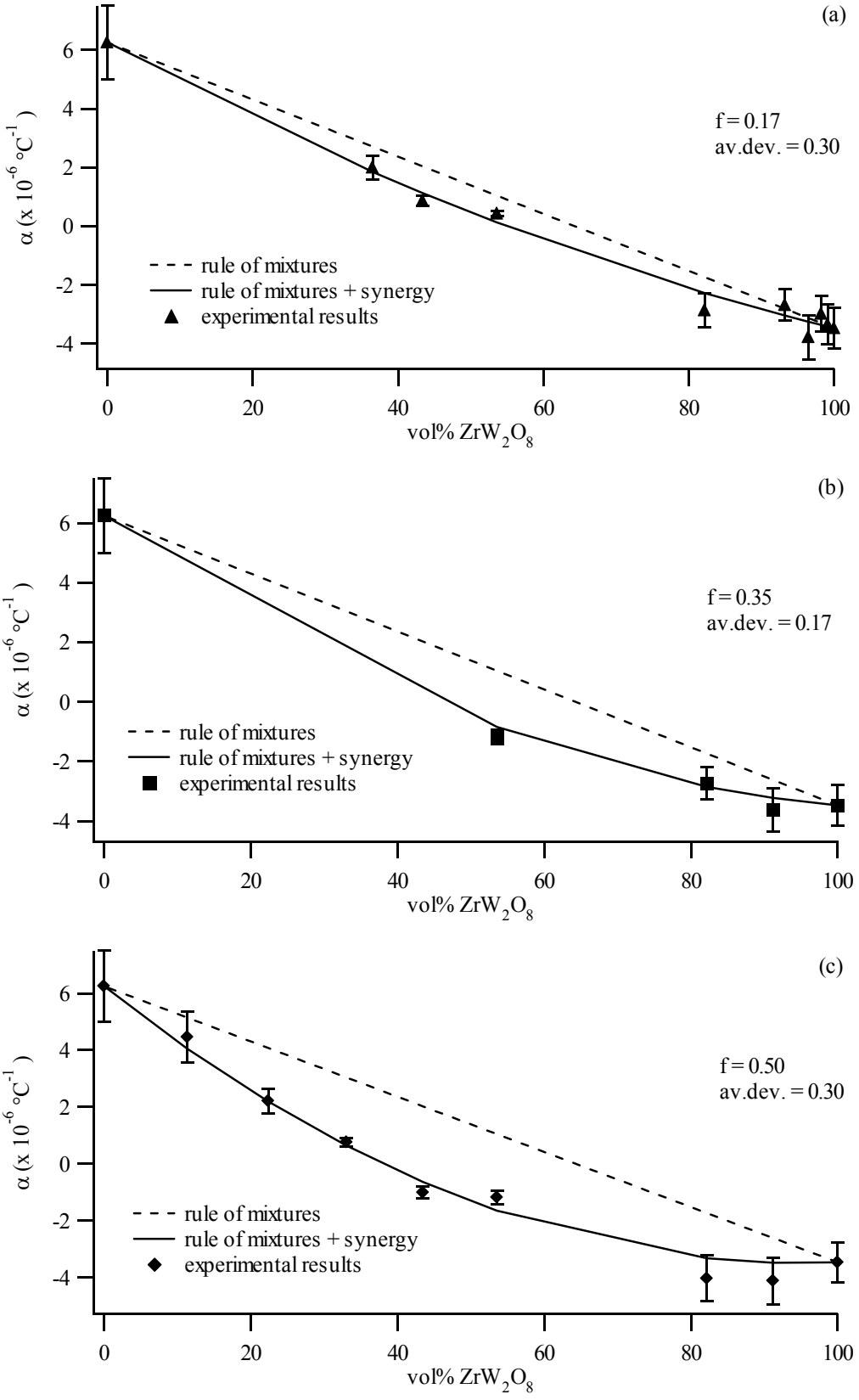

Figure 13: Fitting of the experimental results according to equation 5. (a) "in situ" synthetic route - oxides (b) "in situ" synthetic route – sol-gel (c) "conventional" preparation route

5 Conclusions

Several synthesis and preparation methods for the preparation of ZrO_2 – ZrW_2O_8 composites are described in detail in this chapter. First of all, there is the conventional processing route starting with ZrO_2 and ZrW_2O_8. These composites show very low homogeneity. The ZrO_2 particles are not well distributed resulting in ceramic materials with poor mechanical properties. The synthesis temperature of 1180 °C doesn't allow the composites to sinter completely as the sintering temperature of ZrO_2 lies well above that of ZrW_2O_8.

The second group of synthetic routes uses a mixture of off-stochiometry co-milled ZrO_2 and WO_3 powders. The composites prepared show an improved homogeneity in comparison with the previously mentioned preparation route. The ZrO_2 particles are now well distributed among the ZrW_2O_8 matrix. This has a positive influence on the mechanical properties of the material. A sol-gel method was also used to prepare a homogeneous ZrO_2 – WO_3 powder mixture ideal for the preparation of in situ composites.

By comparison of these methods it can be clearly seen that the porosity affects the mechanical properties in a drastic but predictable way. The lack of well sintered ZrO_2 particles in the composites prohibits the strengthening of the ZrW_2O_8 so that the strength of the prepared bars is exponentially dependent on the total porosity of the composite materials.

The thermal expansion coefficients of the composites do not comply with the linear rule of mixtures: considerably lower volumes of ZrW_2O_8 suffice to compensate for the positive thermal expansion of the ZrO_2 phase than those calculated using this rule. This deviation may be due to the porosity and the changes between mechanical and elastic properties of the individual component used in the composites. This can be illustrated by comparing the conventional method and the in situ method. The deviation of the rule of mixtures is larger in the first synthesis method as this method results in a larger porosity. By modifying the rule of mixtures and including synergy effects, the influence of the synthetic route or processing method can be deduced from the experimental data.

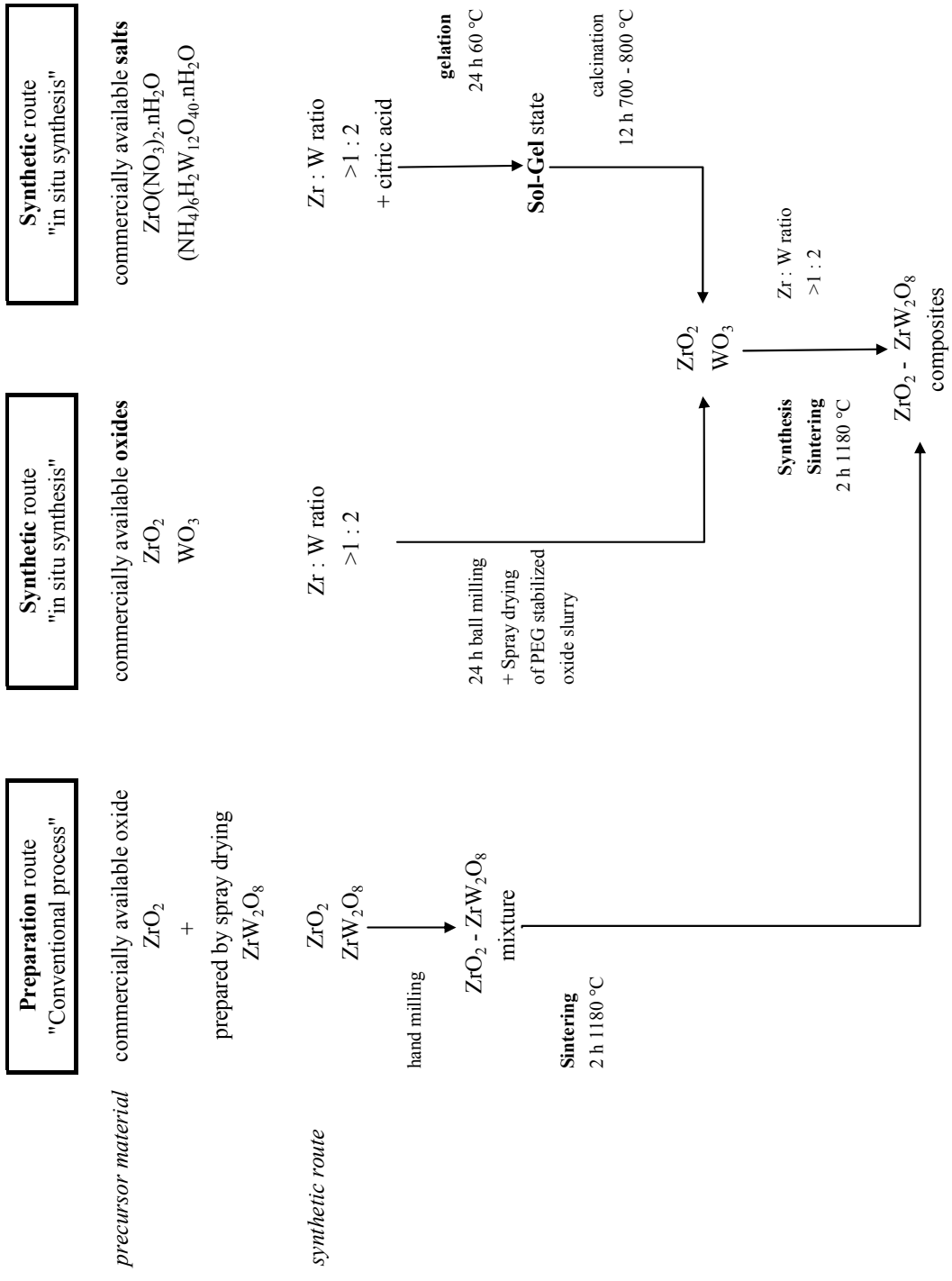

Figure 14: Overview of all preparation and synthetic routes described in this chapter

6 References

1. W.D. Callister, *Materials Science and Engineering: An Introduction*, W. Anderson, Editor. 2000, Wiley & Sons: Danvers. p. 661-664.

2. E. Bruneel, *Supergeleidende composieten op basis van $Bi_{1,5}Pb_{0,5}Sr_2Ca_2Cu_3O_x$*. 2001, Universiteit Gent.

3. Y. Devynck, *Keramische Materialen*. 1996: Universiteit Gent.

4. K.K. Chawla, *Ceramic Matrix Composites*. 1993, London: Chapman and Hall.

5. F.L. Matthews and R.D. Rawlings, *Composite Materials: Engineering and Science*. 1994, London: Chapman & Hall.

6. R.E. Taylor, *Thermal expansion of solids*. 1998, ASM International. p. 1-76.

7. A.W. Sleight, *Negative thermal expansion materials.* Current Opinion in Solid State & Materials Science, 1998. **3**: 128-131.

8. A. Matsumoto, K. Kobayashi, T. Nishio, and K. Ozaki, *Fabrication and thermal expansion of Al-ZrW_2O_8 composites by pulse current sintering process.* Thermec'2003, Pts 1-5, 2003. **426-4**: 2279-2283.

9. H. Holzer and D.C. Dunand, *Phase transformation and thermal expansion of Cu/ZrW_2O_8 metal matrix composites.* Journal of Materials Research, 1999. **14**: 780-789.

10. S. Yilmaz and D.C. Dunand, *Finite-element analysis of thermal expansion and thermal mismatch stresses in a Cu - 60vol% ZrW_2O_8 composite.* Composites Science and Technology, 2004. **64**: 1895-1898.

11. S. Yilmaz, *Phase transformations in thermally cycled Cu/ZrW_2O_8 composites investigated by synchrotron x-ray diffraction.* Journal of Physics-Condensed Matter, 2002. **14**: 365-375.

12. S. Yilmaz, *Thermal mismatch stress development in Cu-ZrW_2O_8 composite investigated by synchrotron X-ray diffraction.* Composites Science and Technology, 2002. **62**: 1835-1839.

13. C. Verdon and D.C. Dunand, *High-temperature reactivity in the ZrW_2O_8-Cu system.* Scripta Materialia, 1997. **36**: 1075-1080.

14. M. Kofteros, S. Rodriguez, V. Tandon, and L.E. Murr, *A preliminary study of thermal expansion compensation in cement by ZrW_2O_8 additions.* Scripta Materialia, 2001. **45**: 369-374.

15. A. Sakamoto, T. Matano, and H. Takeuchi, *Ceramic substrate with negative thermal expansion for athermalization of Fiber Bragg Gratings.* IEICE Transactions on Electronics, 2000. **E83C**: 1441-1446.

16. J.C. Chen, G.C. Huang, C. Hu, and J.P. Weng, *Synthesis of negative-thermal-expansion ZrW_2O_8 substrates.* Scripta Materialia, 2003. **49**: 261-266.

17. E. Niwa, S. Wakamiko, T. Ichikawa, S.R. Wang, T. Hashimoto, K. Takahashi, and Y. Morito, *Preparation of dense ZrO_2/ZrW_2O_8 cosintered ceramics with controlled thermal expansion coefficients.* Journal of the Ceramic Society of Japan, 2004. **112**: 271-275.

Chapter 7

Synthesis and analysis of Zr-substituted $Zr_{1-x}M_xW_2O_8$ materials

ZrW_2O_8 composite materials were described in the previous chapter. Although the use of ZrW_2O_8 lowers the thermal expansion of the composite materials the ever present phase transition represents a drawback. The phase transition temperature (160 °C) separates two domains of slightly different expansion coefficients. A composite of ZrW_2O_8 – ZrO_2 composite with zero thermal expansion over a very large temperature range is therefore impossible to synthesize. Shifting the phase transition temperature is of great practical importance because it allows in principle to exclude a disturbing shift in thermal expansion to outside the range of practical application of the material. In this chapter, we attempt to modulate the phase transition temperature by substituting the Zr^{4+} ions in the octahedra with other suitable M^{4+} ions such as: Ti^{4+}, Sn^{4+} and Ce^{4+}… Extensive analysis of the substituted materials by X-ray analysis, thermomechanical analysis and differential scanning calorimetry is used to understand the mechanisms of the phase transition and the parameters which can influence the phase transition temperature.

This chapter is strongly related to the following article:

"Study of Ti^{4+} substitution in ZrW_2O_8 negative thermal expansion materials"

Klaartje De Buysser, Isabel Van Driessche, Bart Vande Putte, Joseph Schaubroeck, Serge Hoste

Published in Journal of Solid State Chemistry, 180 (2007) 2310-2315

1 Introduction

O^{17} NMR studies have partly revealed the mechanism behind the phase transition. It was confirmed that all oxygen atoms in the structure undergo an exchange even below the phase transition. At the phase transition temperature, adjacent tetrahedra will rotate as a whole in a "ratchet" motion causing mutual exchange between all oxygen sites. This implies breaking of all the Zr – O bounds involved in the Zr – O – W linkages [1]. In that sense, it is clear that substitution of the Zr^{4+} ion within the crystal structure should strongly affect the phase transition temperature. According to conventional knowledge the occurrence of substitutional solid solutions requires that the ions that are replacing each other must be similar in size.[2]

Obviously the charge neutrality of the materials restricts our choice to ions with 4+ valency. Solid solutions were obtained by substituting Zr^{4+} ions (86 pm) [3] by other 4+ valency ions such as Sn^{4+}(83 pm) [4] and Hf^{4+} (85 pm).

The most widely discussed substituted material is HfW_2O_8 [5, 6]. Hafnium tungstate exhibits the same remarkable negative thermal expansion properties as ZrW_2O_8. The α-phase (a = 0.9157 nm at 20 °C) is isostructural with α- ZrW_2O_8 [7]. HfW_2O_8 shows an order-disorder transition at 190 °C. Substitution of the Zr site in ZrW_2O_8 by Sn^{4+} ions induces a decrease in phase transition temperature [4]. In addition to tetravalent substituents, some trivalent ions such as Y^{3+}, Lu^{3+}, Sc^{3+} and In^{3+} were also used to prepare substituted ZrW_2O_8 (O-deficient) materials [8-12]. Again, the phase transition temperature was affected by the substitution as a decrease in phase transition temperature was noticed.

Substitution of the tungsten ion is most widely studied in $ZrMo_2O_8$. Cubic γ-$ZrMo_2O_8$ is isostructural with β-ZrW_2O_8 [13-15]. Recently, it has been shown that it is possible to prepare $ZrW_{2-x}Mo_xO_8$ phases over the entire composition range $0 \leq x \leq 2$ [16-18]. The phase transition temperature shifts to lower values as the amount of Mo present in the material increases. For example, the $\alpha \rightarrow \beta$ phase transition temperature of $ZrMoWO_8$ is reduced by 160 °C compared to the parent compound [19].

2 Synthesis

The $Zr_{1-x}Ti_xW_2O_8$ (x= 0–0.10), $Zr_{1-x}Ce_xW_2O_8$ (x= 0–0.05) and $Zr_{1-x}Sn_xW_2O_8$ (x= 0–0.05) materials were synthesized using a solid state reaction (Chapter 3-§2.3.a) starting from the commercially available oxides ZrO_2, TiO_2 and SnO_2 (Aldrich) and WO_3 was obtained from Acros Organics. CeO_2 was prepared by calcination of $Ce(NO_3)_3.6H_2O$ (Aldrich) in air at 800 °C for 4 h. The amounts of oxides needed are given in table 1. The oxide mixtures were co-milled for 24 h in a tumbler mill filled with zirconia pearls. The powders were put in a horizontally disposed glass container (15 cm^3) and zirconia pearls (Ø = 3.15 mm) are added in a 1:1 mass ratio. These oxide mixtures were pressed at 750 MPa into small bars of 0.3 g (2mm × 2mm × 13mm). The bars were sintered for 15 h in a preheated furnace at 1180 °C, followed by quenching in liquid nitrogen to avoid decomposition into the metal oxide precursors.

$Zr_{1-x}M_xW_2O_8$	mass ZrO_2 (g)	mass WO_3 (g)	mass TiO_2 (g)	mass SnO_2 (g)	mass CeO_2 (g)
ZrW_2O_8	1.050	3.950			
$Zr_{0.99}Ti_{0.01}W_2O_8$	1.040	3.953	0.007		
$Zr_{0.98}Ti_{0.02}W_2O_8$	1.030	3.956	0.014		
$Zr_{0.975}Ti_{0.025}W_2O_8$	1.025	3.958	0.017		
$Zr_{0.97}Ti_{0.03}W_2O_8$	1.021	3.959	0.021		
$Zr_{0.96}Ti_{0.04}W_2O_8$	1.011	3.962	0.273		
$Zr_{0.95}Ti_{0.05}W_2O_8$	1.001	3.965	0.034		
$Zr_{0.975}Sn_{0.025}W_2O_8$	1.022	3.946		0.032	
$Zr_{0.95}Sn_{0.05}W_2O_8$	0.995	3.940		0.064	
$Zr_{0.975}Ce_{0.025}W_2O_8$	1.021	3.942			0.037
$Zr_{0.95}Ce_{0.05}W_2O_8$	0.933	3.934			0.073

Table 1: Preparation scheme for the $Zr_{1-x}M_xW_2O_8$ solid solutions

3 X-ray analysis and thermomechanical properties of the substituted materials

Samples of $Zr_{1-x}Ti_xW_2O_8$ (x= 0–0.10), $Zr_{1-x}Ce_xW_2O_8$ (x=0–0.05) and $Zr_{1-x}Sn_xW_2O_8$ (x=0–0.05) were analyzed by powder X-ray diffraction to determine the solubility limit for substitution. As can be seen in figure 1 for the $Zr_{1-x}Ti_xW_2O_8$ series, no other reflections besides those belonging to ZrW_2O_8 are present expect for the WO_3 reflections at 28.3 and 31.5 2 theta and the TiO_2 (*) reflections in the $Zr_{0.9}Ti_{0.10}W_2O_8$ composition. It is hereby proven that this composition exceeds the limit of the solid solution.

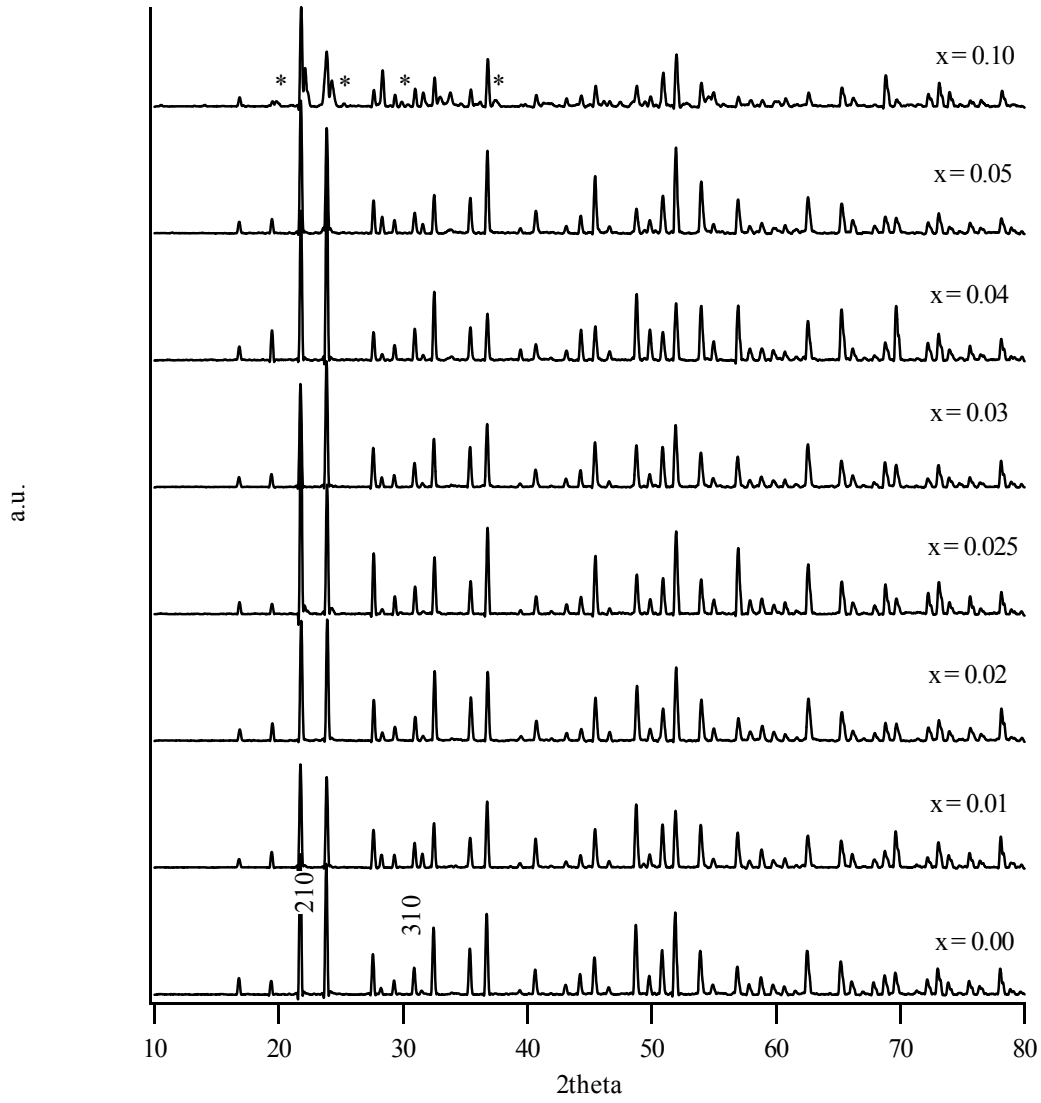

Figure 1: X-ray diffraction patterns of $Zr_{1-x}Ti_xW_2O_8$ (x=0 – 0.) at room temperature (25 °C)

No reflections of impurity phases can be remarked $Zr_{1-x}Sn_xW_2O_8$ series mentioned in figure 2. This is a first indication that a solid solution is formed in this range of composition. De Meyer et al published a solid solid limit of x=0.2 for this type of substitution. For the Ce samples however, a weak reflection at 25.4 2theta can be seen beside the reflections of ZrW_2O_8. This reflection, indicated by an asterisk, is most likely caused by the [-1-21] reflection of CeO_{2-y}.

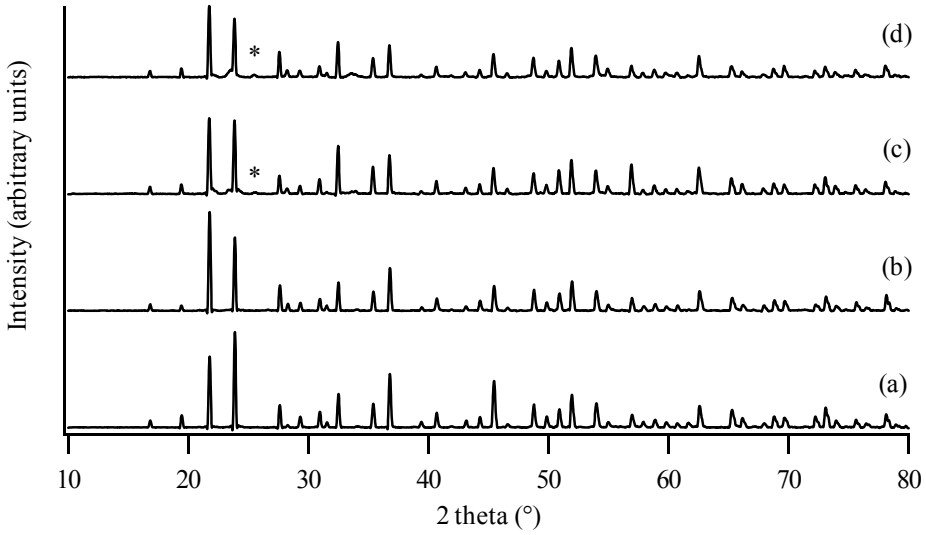

Figure 2: X-ray diffraction patterns of $Zr_{1-x}Sn_xW_2O_8$ (x=0.025 (a); 0.05 (b)) and $Zr_{1-x}Ce_xW_2O_8$ (x=0.025 (c); 0.05 (d)) at room temperature (25 °C)

The change in unit cell parameter caused by substitution of the Zr site with cations with a smaller ionic radius was investigated for all the samples mentioned in figures 1 and 2. The lattice parameters were calculated using 30 reflections between 30 and 80 2theta by a least-square fit after correcting 2θ with Nelson-Riley's method [20]. 6 w% LaB_6 was added to the samples as internal standard.

Figure 3 shows evolution in the cell parameter a for ZrW_2O_8, $Zr_{1-x}Ti_xW_2O_8$ (x = 0.01-0.10), $Zr_{1-x}Ce_xW_2O_8$ (x = 0.025 and 0.05) and $Zr_{1-x}Sn_xW_2O_8$ (x = 0.025 and 0.05) at 298 K. For Ti^{4+} and Sn^{4+}, the relative magnitude of the decrease in unit cell parameter is nicely linked to the relative sizes of the substituting ions versus the size of Zr^{4+}. The linear decrease in unit cell parameter with increasing degree of substitution follows Vegard's law [2, 4]. The $Zr_{0.9}Ti_{0.1}W_2O_8$ material does not obey this law. The cell parameter does not further decrease in comparison with the 5% substituted material which means that the limit for substitution of Ti^{4+} at the Zr^{4+} position is obtained at 5%, which proves the earlier mentioned observations in XRD analysis. The decrease of unit cell parameter in the case of Ti and Sn substitution follows the trend that was already reported for substitution by Hf^{4+} [5]. However, these observations are in contrast with the substitution of Zr^{4+} ion by trivalent ions where a decrease of the unit cell parameter is noticed despite the larger radii. The main reason for this behaviour is the oxygen deficiency caused by the lower valency of the substituting ions [8]. The substitution by Ti^{4+} and Sn^{4+} respects the electroneutrality of the compound without any need for changes in the oxygen content and thus, the smaller ionic radius is directly reflected in a decrease in unit cell parameter.

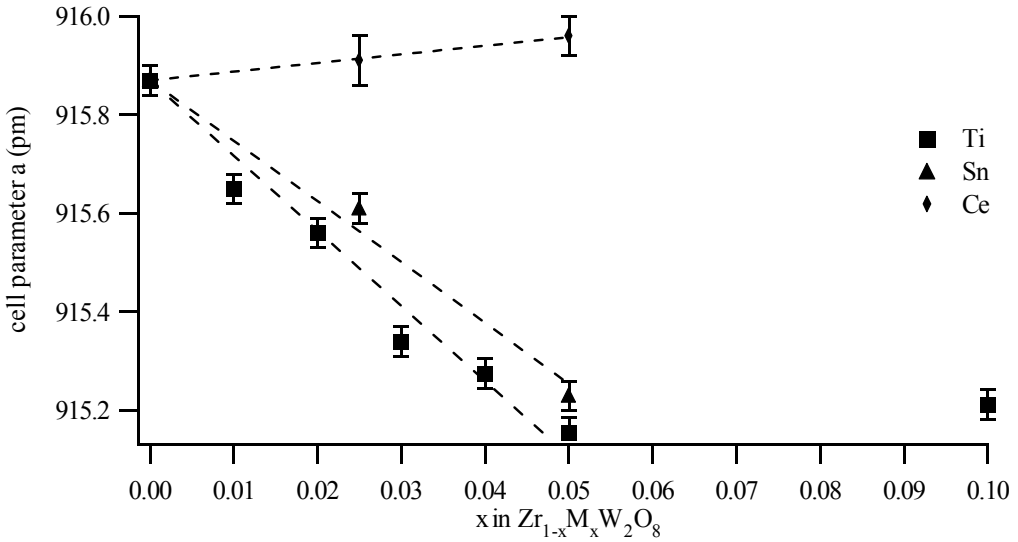

Figure 3: Lattice parameters of ZrW_2O_8 (x=0), $Zr_{1-x}Ti_xW_2O_8$ (x = 0.01-0.10) (▲), $Zr_{1-x}Sn_xW_2O_8$ (x = 0.025 and 0.05) (■) and $Zr_{1-x}Ce_xW_2O_8$ (x = 0.025 and 0.05) (♦) at 298 K. The linearity according to Vegard's Law is indicated by the dotted lines.

Only a small increase of the lattice parameter is detected for Ce^{4+} containing samples. We attribute the lack of substitution to the fact that the ionic radius of Ce^{4+} (101 pm) is too large to fit in the Zr-site even though earlier reports mention the successful substitution of Y^{3+} (104 pm) and Lu^{3+} (100.1 pm). Here again the discrepancy is most likely due to the oxygen deficiency related to the lower valence state of the replacing ions in comparison with Zr^{4+} providing more space to the substitutes [10, 12]. To determine in more detail the percentage of Ce^{4+} substitution, the influence of the Ce-amount on the phase transition temperature was investigated. As can be seen in figure 4 no noticeable shift in phase transition temperature is detected for any of the composites. Sintered mixtures of CeO_2-WO_3-ZrO_2 oxide powders will therefore preferably form a $CeO_2 - ZrW_2O_8$ composite instead of a $Zr_{1-x}Ce_xW_2O_8$ solid solution as already indicated by the X-ray analysis. Those composites are not expected to exhibit a variation in phase transition temperature [21]. As the amount of the positive thermal expansion material CeO_2 increases, the negative thermal expansion decreases.

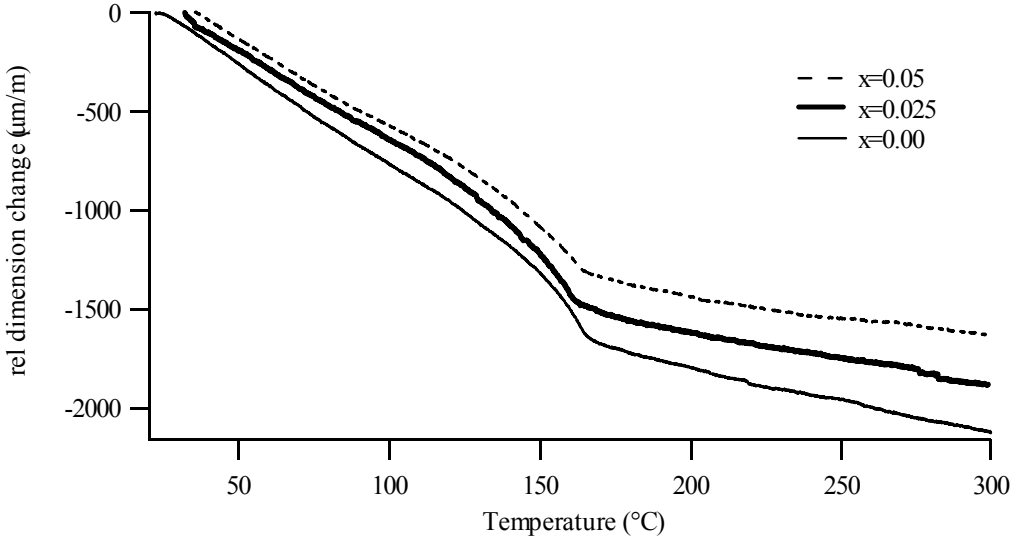

Figure 4: Relative length differences of sintered $Zr_{1-x}Ce_xW_2O_8$ (x = 0.00-0.025-0.05) bars as a function of temperature

Figure 5 shows the thermomechanical analysis of $Zr_{1-x}Ti_xW_2O_8$ (x = 0.00-0.05) samples. The upper curve represents a pure ZrW_2O_8 sample. The phase transition temperatures of ZrW_2O_8, $Zr_{1-x}Ti_xW_2O_8$ (x = 0.01-0.05) and $Zr_{1-x}Sn_xW_2O_8$ (x = 0.025 and 0.05) are gathered in figure 6. The phase transition temperature decreases as the Ti^{4+} substitution degree increases. Translated into the order-disorder theory this means that, with increasing substitution, less thermal energy (reflected in a lower phase transition temperature) is needed to induce the disordering of the WO_4 tetrahedra.

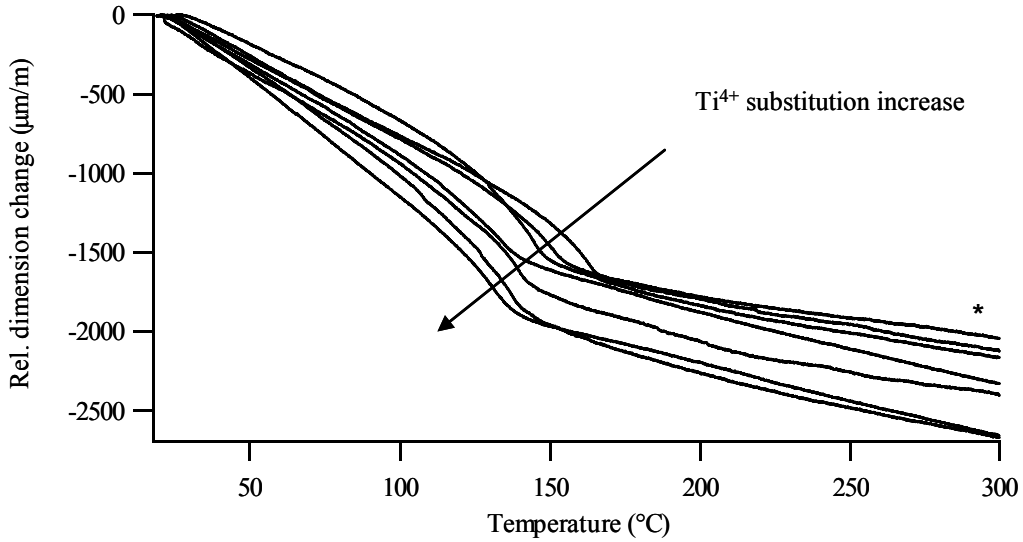

Figure 5: Relative length differences of sintered $Zr_{1-x}Ti_xW_2O_8$ (x = 0.00-0.05) bars as a function of temperature. The upper curve is measured on a pure ZrW_2O_8 bar as indicated by (*)

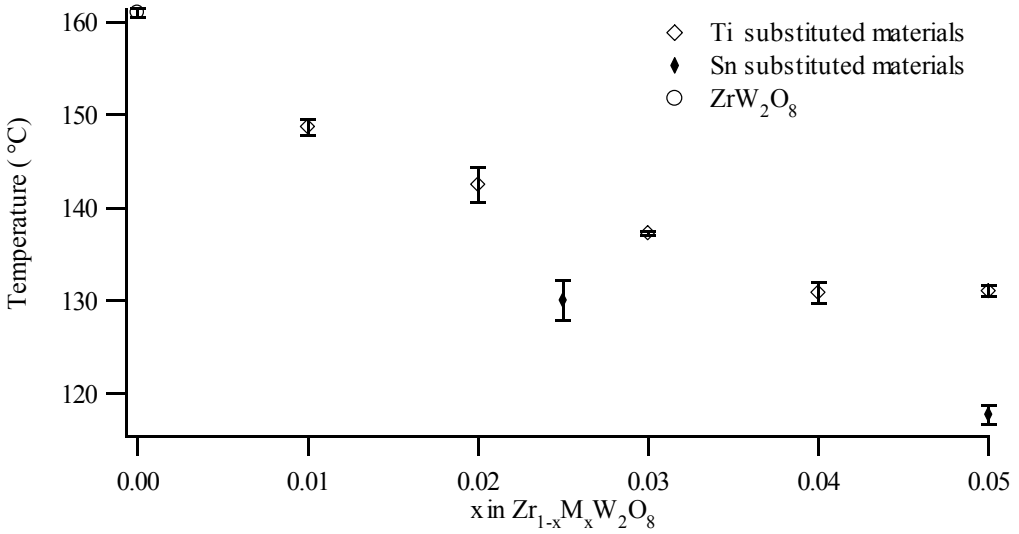

Figure 6: Phase transition temperatures ZrW_2O_8 (x=0)(○), $Zr_{1-x}Ti_xW_2O_8$ (x = 0.01-0.05) (◇) and $Zr_{1-x}Sn_xW_2O_8$ (x = 0.025 and 0.05) (◆)

An even more pronounced decrease in phase transition temperature can be noticed for Sn^{4+} substituted solid solutions. Some authors state that the main reason for the lower phase transition temperature is the presence of a locally disordered state induced by the substituting ion [12]. The disturbance of the periodic order of some WO_4 tetrahedra clusters in the orientationally disordered state in $Zr_{1-x}Ti_xW_2O_8$ can be confirmed by an increase of the FWHM of the [310] reflection. An increase in FWHM of 15% was obtained from $Zr_{1-x}Ti_xW_2O_8$ (x = 0.00-0.05) samples as given in figure 7.

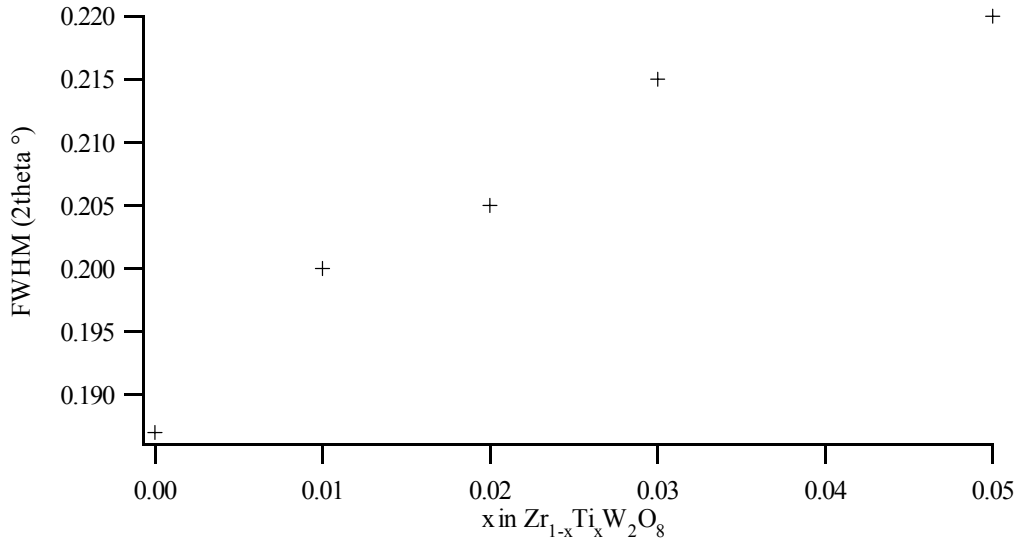

Figure 7: FWHM obtained for the [310] reflection of $Zr_{1-x}Ti_xW_2O_8$ (x=0 – 0.05) solid solutions

The effect of Hf^{4+} substitution mentioned in literature is in contrast with our findings as the phase transition temperature increases with increasing Hf substitution. An explanation for this, as stated in literature [6] is that the phase transition of $Zr_{1-x}Hf_xW_2O_8$ (x = 0-1) solid solutions is dependent on the free lattice volume. The free lattice volume is defined as the unit cell volume minus the sum of the volumes for all ions occupying the unit cell. The increase in the phase transition temperature is considered to be due to hindrance related to the decrease of the free space around the WO_4 tetrahedra. This free lattice volume was calculated for $Zr_{1-x}Ti_xW_2O_8$ (x = 0.00-0.05) and plotted against the phase transition temperature (figure 8). As can be seen in this figure, the phase transition temperature decreases as the lattice free volume decreases which, again, is in contrast with the results mentioned for the Hf^{4+} substitution.

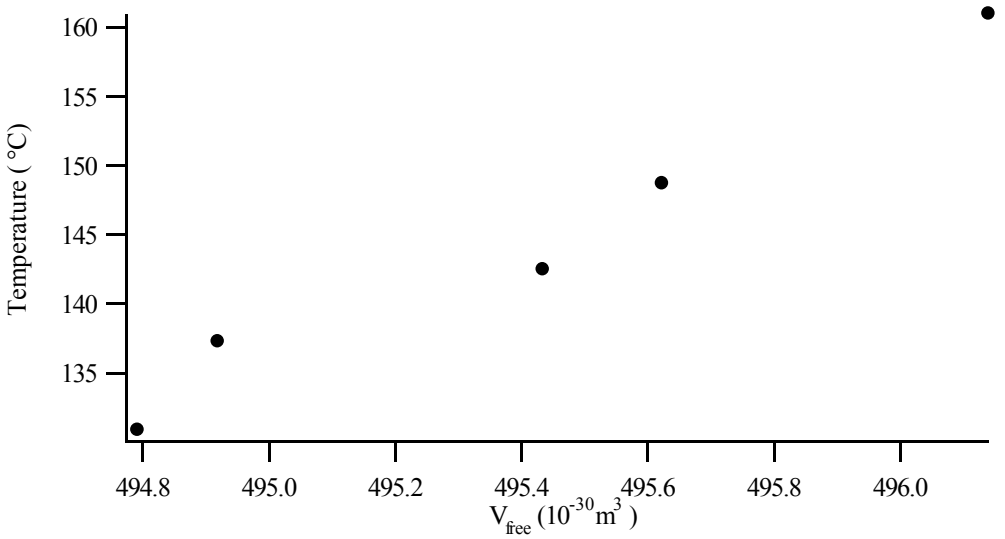

Figure 8: Phase transition temperatures of $Zr_{1-x}Ti_xW_2O_8$ (x = 0.00-0.05) solid solutions versus the calculated lattice free volumes in the unit cell at 25 °C

There is however a parameter which cannot be neglected. The order-disorder transition mechanism, revealed by O^{17} NMR, indicated that during the ratchet motion Zr – O bonds in the Zr – O – W linkages were broken. Substitution of the Zr^{4+} site by another ion may increase or decrease the bond strength. The ionic radii and bond dissociation energy data are assembled in table 1. From this table, it can be seen that the reason for the higher phase transition temperature of Hf substituted ZrW_2O_8 materials must be sought in the higher dissociation energy of the Hf – O bond in comparison with the Zr – O bond. For the Ti^{4+} substitution however, the lower dissociation energy of the Ti – O bond in comparison with the Zr – O bond will compensate the effect of the smaller lattice free volume resulting in an overall decrease of the phase transition temperature as the substitution degree increases. The literature data for Y^{3+} and Lu^{3+}also mention a decrease in phase transition temperature which we can attribute to differences in bond strength. Further confirmation of our proposal can be found in the fact that the decrease of phase transition temperature is larger in the case of $Zr_{1-x}Sn_xW_2O_8$ materials than for $Zr_{1-x}Ti_xW_2O_8$ solid solutions due to the higher dissociation energy of Ti – O in comparison with a Sn – O bond.

$Zr_{1-x}M_xW_2O_8$ with M:	Ionic radius (pm) [3]	M – O bond dissociation energy (kJ/mol) [22]
Zr^{4+}	86	776.1 ± 9.2
Hf^{4+}	85	801.7 ± 13.4
Sn^{4+}	83	531.8 ± 12.6
Ce^{4+}	101	795 ± 8
Ti^{4+}	74.5	672.4 ± 9.2
Y^{3+}	104	719.6 ± 11.3
Lu^{3+}	100.1	678 ± 8

Table 2: Ionic radii and M –O bond dissociation energies of the substituent ions of the $Zr_{1-x}M_xW_2O_8$ materials described in this chapter

4 DSC analysis of the substituted materials

4.1 Experimental set-up

Quantitative information concerning the reaction or transition enthalpy and entropy can be obtained using three different DSC measurements.

- (a) Measurement of two empty aluminum pans: correction for any asymmetry in the heat flow of the system
- (b) Measurement of an empty aluminum pan and a reference material (sapphire) must be performed. This provides a calibration factor that translates the measured heat flow units (mW) into heat capacity units (J/g °C)
- (c) Measurement of the empty aluminum pan and the sample results in the heat flow of the sample (mW)

The measurements were performed under N_2(g) atmosphere (50 mL/min). The thermal procedure was optimized to obtain a maximal signal-noise ratio. The system was allowed to equilibrate at 35°C for 3 min, followed by heating to 200 °C at 20 °C/min. The pans were standard aluminum pans which were non-hermetically closed. The results of these three measurements for a ZrW_2O_8 sample are given in figure 9.

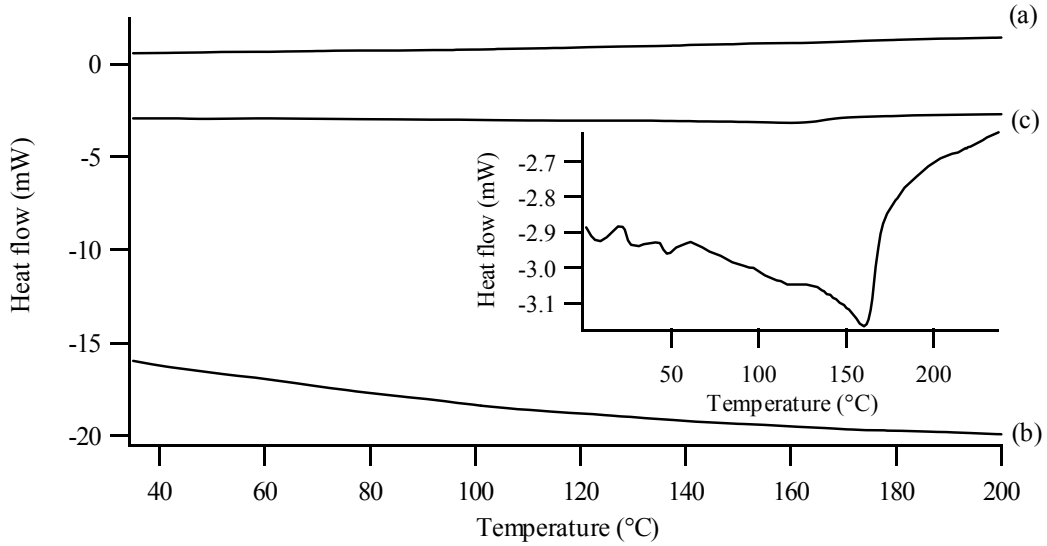

Figure 9: Heat flow measurements of (a) 2 empty pans, (b) empty pan and reference material (sapphire) and (c) empty pan and sample. The insert gives a detail of the measurement of the sample

These data files are combined to calculate the heat capacity of the measured sample using:

$$C_{p,sample}(T)(J/g°C) = \frac{C_{p,sapphire}(T)(J/g°C) \times mass_{sapphire}(mg) \times (q_{sample} - q_0)(mW)}{mass_{sample}(mg) \times (q_{sapphire} - q_0)(mW)} \quad [1]$$

where $C_{p,sample}$ and $C_{p,sapphire}$ are the heat capacities of the sample and reference material, respectively; $mass_{sample}$ and $mass_{sapphire}$ are the weights of the sample and reference material in the aluminum pans. Q_0 is the heat flow during the DSC measurement of two empty pans, whereas $q_{reference}$ and q_{sample} are the results of the DSC measurement of an empty pan with an aluminum pan filled with sapphire and the sample, respectively. The heat capacity of sapphire at various temperatures was calculated using the following expression calculated by the data published by NIST (SRM 720) [23, 24].

$$C_{p,sapphire}(T)(J/g°C) = \sum_{n=0}^{n=3} a_n T^n (°C) \quad [2]$$

with $a_0 = 723.16$; $a_1 = 2.31$, $a_2 = -5.10^{-3}$ and $a_3 = 5.10^{-6}$

Figure 10 shows the results for the heat capacity of the ZrW_2O_8 sample.

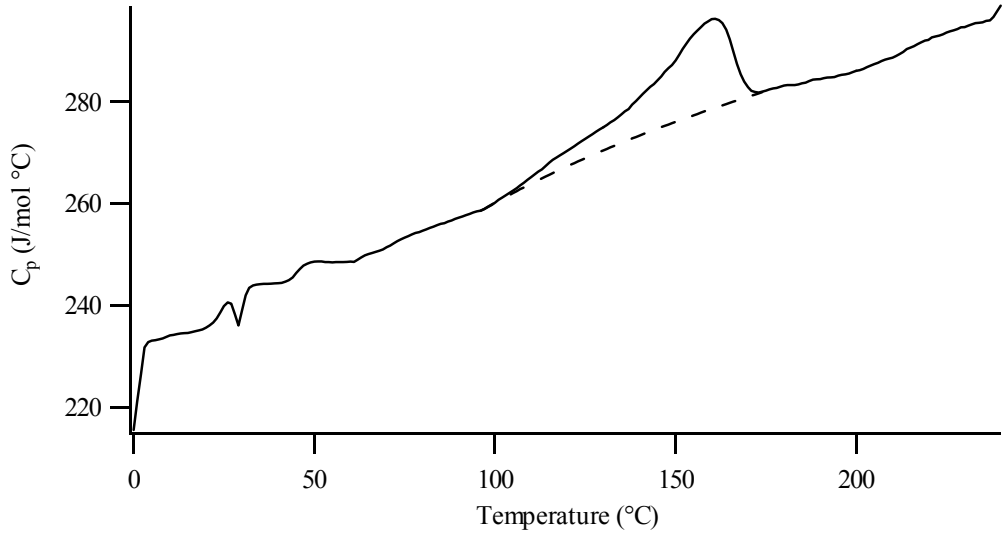

Figure 10: Heat capacity of the ZrW_2O_8 sample

An anomaly in the heat capacity is seen around 160 °C. This temperature corresponds to the phase transition as detected by thermomechanical analysis and X-ray analysis. The shape of the anomaly in the heat capacity indicates that the α to β transition is a λ type transition typical for a second order transition [6-8, 25-29]. This λ shape indicates that the phase transition starts at temperatures considerably lower than the phase transition temperature. This is in strict alignment with the temperature dependence of the order parameter, indicated by the fractional occupancy of the W(1) and W(2) atoms in the two possible tetrahedral orientations along the [1 1 1] diagonal direction determined by neutron powder diffraction [30].

The baseline of the heat capacity was determined by extrapolating the heat capacities in both higher- and lower temperature ranges excluding the phase transition. The excess heat capacity due to the phase transition was obtained by subtracting the baseline and the result is given in figure 11. The lambda shape can be clearly seen and the maximum excess of 17.7 J/mol °C is reached at 160 °C. This maximum is used to extract the phase transition temperature from the DSC measurements.

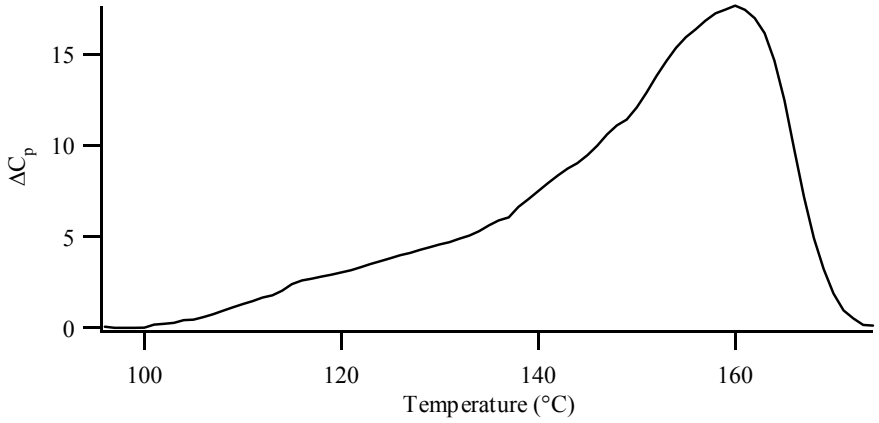

Figure 11: Excess heat capacity of the ZrW_2O_8 sample used for calculation of the transition enthalpy

The transition enthalpies and entropies were estimated from numerical integration of the excess heat capacity according to equation 3 and 4. The excess heat capacity had to be divided by the temperature (in Kelvin) to obtain the right data points for the calculation of the transition entropy as can be seen in figure 12.

$$\Delta H(J/mol) = \int \Delta C_p dT \quad [3]$$

$$\Delta S(J/mol\ K) = \int \frac{\Delta C_p}{T(K)} dT \quad [4]$$

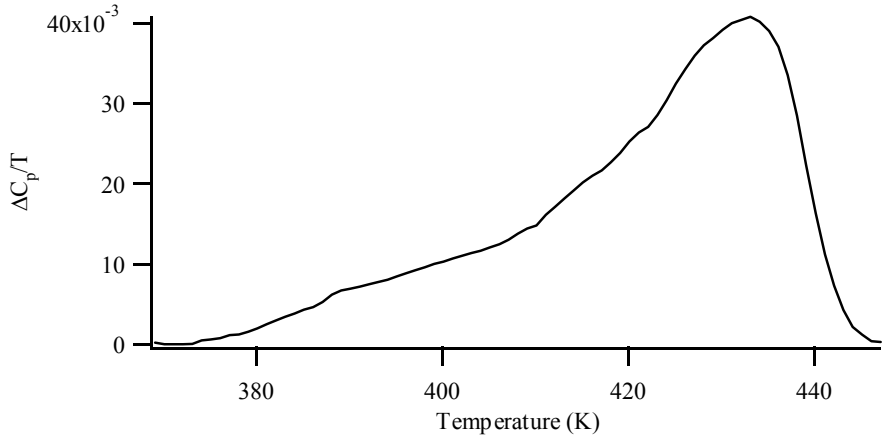

Figure 12: $\Delta C_p/T$ of the ZrW_2O_8 material used for calculation of the transition entropy

These calculations lead to a transition enthalpy of 490.44 J/mol and the transition entropy is 1.16 J/mol K. The magnitudes of ΔH_{tr} and ΔS_{tr} are strongly dependent on the chosen baseline. Although these thermodynamical data have been obtained by other techniques and are generally higher in value (1.56 kJ/mol [29] and 907 J/mol [25]), these measurements represent the first DSC-data available for these materials.

The positive value for the entropy change results from disordering of the orientation of the two WO_4 tetrahedrons lying along the [1 1 1] direction. It is stated by Pryde [31] that the available space for the two WO_4 tetrahedrons in the β phase suggest that only two orientations can be taken into consideration. This would mean that the entropy for the phase transition is expected to be R ln2 (5.8 J/mol K). If the two tetrahedrons could independently take the two possible orientations, the entropy change would shift to R ln4 (11.5 J/mol K). However the value measured by this DSC experiment reveals a lower value for ΔS_{tr} (20 % of R ln2). Other studies by Adiabatic Scanning Calorimetry (4.09 J/K mol [29] and 2.1 J/K mol [25]) also indicated a discrepancy for the theoretical value. As the magnitude of the experimental value lies closer to R ln2 than to R ln4, the order-disorder transition is supposed to be the result of the two WO_4 tetrahedrons along the [1 1 1] with only 2 conformations in a concerted manner.

4.2 Calorimetric data of the substituted materials

DSC measurements were performed for $Zr_{1-x}Ti_xW_2O_8$ (x = 0.01-0.05) and $Zr_{1-x}Sn_xW_2O_8$ (x = 0.025 and 0.05) and were compared with the results of the pure ZrW_2O_8 sample. The same conditions as mentioned above (§4.1) were used for all samples. The DSC measurements are used to confirm the hypothesis (§3) described above. This hypothesis highlights the influence of the metal ion – oxygen bond strength in comparison with the original Zr – O bond. This should be translated into a decrease of transition enthalpy as the substitution degree by Ti^{4+} or Sn^{4+} ions increases.

The phase transition temperature is the first parameter examined. The comparison between the data obtained by TMA (minimum in the thermal expansion coefficient) and DSC (maximum in the excess heat capacity diagram) is made in figure 13. The same tendency can be noticed. The differences between the two analysis techniques are due to differences in the samples (powders (DSC) versus bars (TMA)), differences in heat rate (5 °C/min for TMA versus 20 °C/min for DSC) and differences in gas flow (N_2 (g) during the DSC experiments versus no gas flow during TMA experiments). The gas influences the thermal equilibration whereas a higher heating rate will result in an overshoot of the phase transition temperature. Powder measurements exclude the influence of porosity or cracks present in the bars.

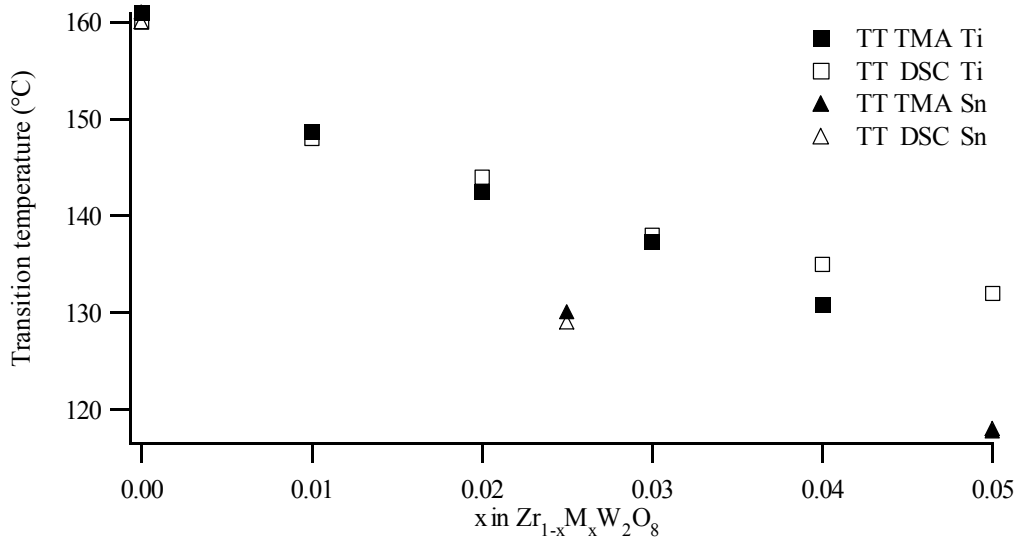

Figure 13: Comparison between T_{tr} obtained by TMA and T_{tr} obtained by DSC

The shift in phase transition temperature can be directly deduced from the heat flow measurements. As the substitution degree by Ti^{4+} or by Sn^{4+} ions increases, a shift to the lower temperature region is seen. This effect is more strongly present in the case of substitution by Sn^{4+} ions which is consisted with the thermomechanical experiments.

The evolution of the phase transition enthalpy with degree of substitution is given in figure 14. A decrease in phase transition enthalpy is noticed as the substitution degree increases. The decrease is more pronounced for the Sn^{4+} substituted materials which can be understood by the lower Sn – O bond strength (versus Ti – O) which facilitates the ratchet motion, breaking of the M – O bonds and lowers the phase transition temperature. The DSC measurements prove that the thermodynamical parameters indeed vary with different substitutional degree. It is clear that our findings support the view of a transition mechanism in which a ratchet motion of tetrahedra is involved. Indeed, the alternatively proposed mechanism only involves breaking of the W – O bond and its thermodynamics would not be affected by substitution at the Zr site.

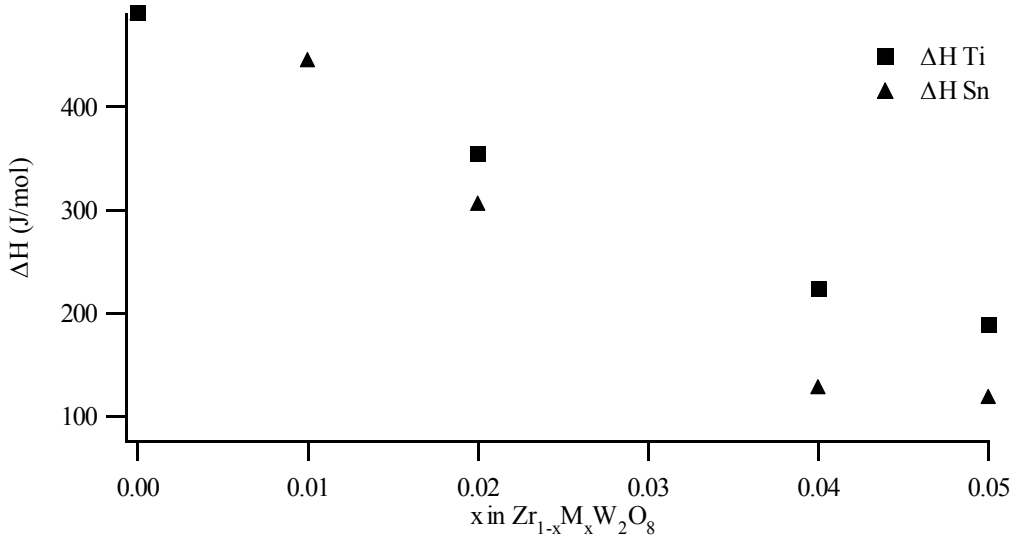

Figure 14: Phase transition enthalpies of substituted $Zr_{1-x}M_xW_2O_8$ materials

The data obtained for the substituted materials were further examined by the use of equation 4 to deduce information concerning the phase transition entropy change. The results are mentioned in figure 15. Again a decrease can be seen as the substitutional degree increases. The effect of substitution by Sn^{4+} ions is again more marked than

that of Ti^{4+} ions. Nakajima [6] found that the entropy value is not affected by Hf substitution because the same order-disorder transition occurs in which the WO_4 tetrahedra along the [1 1 1] direction only have two conformations in a concerted manner. On the other hand, Yamamura [12] stressed the presence of locally disordered regions within the ordered α domain. This should result in a lower entropy increase during the phase transition. As the substitutional degree increases, the disorder in the crystal structure increases and hereby the entropy change after transition decreases.

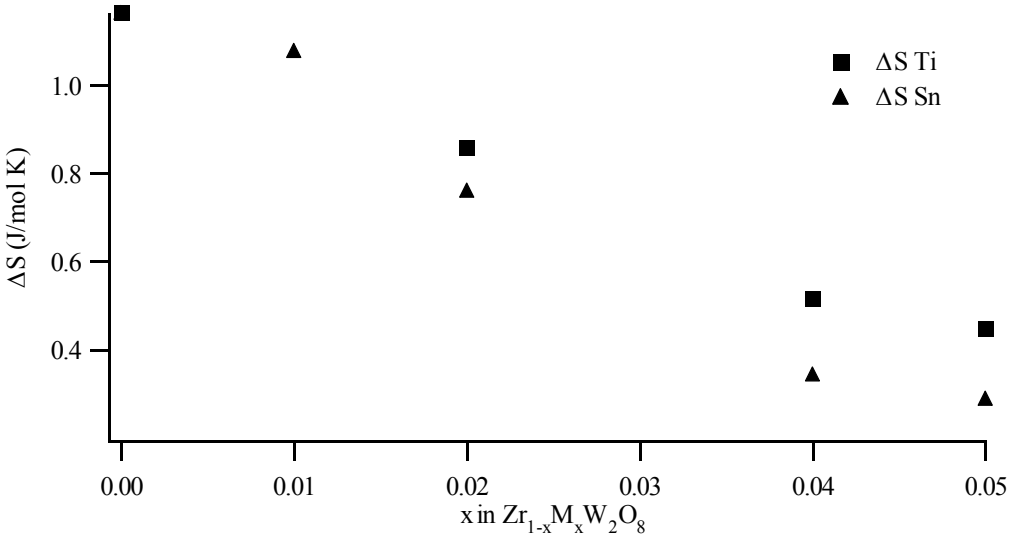

Figure 15: Phase transition entropies of substituted $Zr_{1-x}M_xW_2O_8$ materials

4.3 Pre-treatment of the samples

Some DSC measurements showed two peaks during the first heating cycle. The peak at 133 °C was no longer detected during a second heating cycle as can be seen in figure 16.

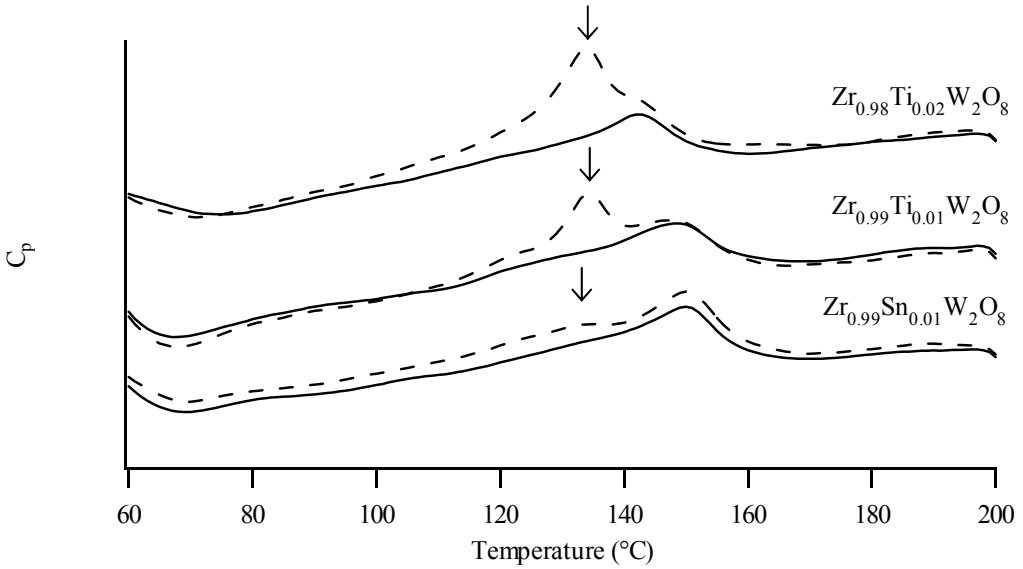

Figure 16: Heat capacity of the substituted materials during first (---) and second (—) heat cycle

This phenomenon is in literature attributed to the loss of water [32]. The authors confirmed this hypothesis by TGA – MS. TGA – DTA on our materials does not indicate the loss of water (figure 17a) nor does IR spectroscopy shows the presence of O – H stretch vibrations (figure 17b). The TGA trace shows a little increase in weight due to drift.

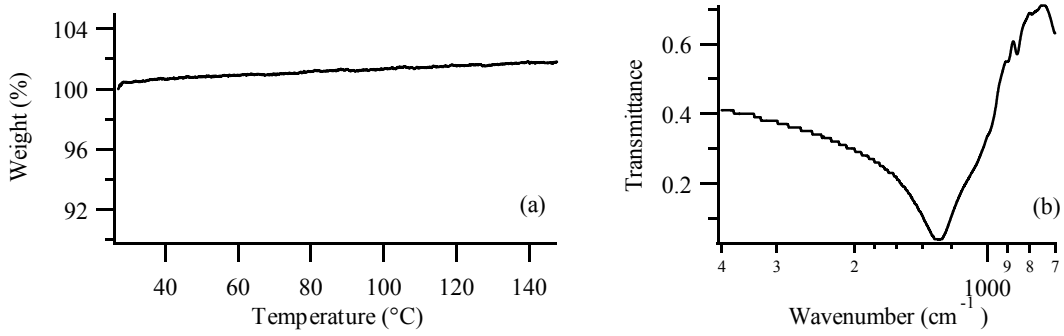

Figure 17: TGA-DTA analysis of ZrW_2O_8 (a) IR spectroscopy of $Zr_{0.97}Ti_{0.03}W_2O_8$ (b)

Heat treatment of materials before they are used is common used to soften steel and other metals[33]. It can be used to relieve stress that has been caused by uneven cooling or other treatment. The materials discussed in this chapter are submitted to extreme cooling from 1180 °C to -200 °C. So it not so unrealistic to think that these materials show internal stresses. Therefore all samples are preheated at 220 °C before the actual recording of the heat flow data, used in the previous mentioned experiments, starts.

Strangely enough these stresses do not affect the crystal structure as the cell parameter a do not change after a preheating treatment. The thermomechanical properties of the material were also examined before and after heating. The cycle given in figure 18 is the result of heating a ZrW_2O_8 bars to 300 °C and cooling down to room temperature for three times. There is no change in phase transition temperature or in thermal expansion behaviour as can be seen in this figure.

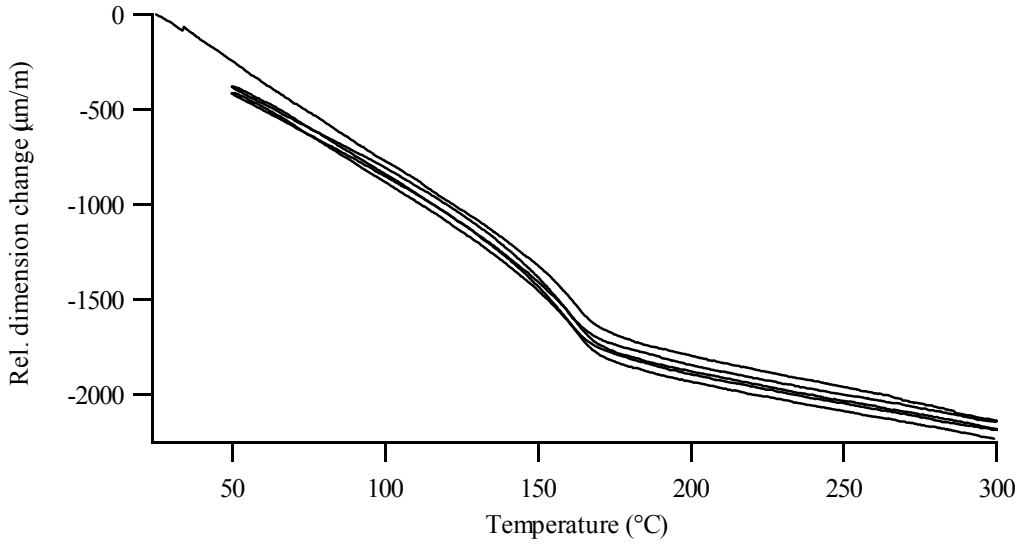

Figure 18: Thermomechanical properties of ZrW_2O_8 during cycle measurement

5 Conclusion

We have shown that Ce^{4+} ions are not able to form $Zr_{1-x}Ce_xW_2O_8$ solid solutions. Consequently, a CeO_2 – ZrW_2O_8 composite was obtained and no noticeable shift in phase transition temperature was noticed in comparison with pure ZrW_2O_8. On the other hand, substitution of Zr^{4+} ions by Ti^{4+} resulted in successful synthesis of $Zr_{1-x}Ti_xW_2O_8$ solid solutions with x= 0.00 – 0.05. A steady decrease in lattice parameters could be identified and was attributed to a smaller ionic radius (74.5 pm) of the substituting metal. The decrease in phase transition temperature noticed in these solid solutions is thought to result from the combination of the presence of a larger disorder state (broadening of the [310] reflection) and a lower bond dissociation energy of the Ti – O bond in comparison with the Zr – O bond which compensates for the decrease in free lattice volume.

Calorimetric analysis of the Ti^{4+} and Sn^{4+} substituted materials revealed that a decrease in reaction enthalpy could be seen. The excess of the heat capacity decreases as the substitution degree increase. This results in a decrease in phase transition temperature. The difference in bond strength between Ti – O and Sn – O is translated to a smaller decrease of the reaction enthalpy in the case of Ti^{4+} substituted materials. A small decrease in reaction entropy is also detected. Substitution can distort the crystal structure of the materials locally. As the phase transition is an order-disorder transition, small distortion of the material before the phase transition will lower the reaction entropy during transition.

6 References

1. M.R. Hampson, P. Hodgkinson, J.S.O. Evans, R.K. Harris, I.J. King, S. Allen, and F. Fayon, *The nature of oxygen exchange in ZrW_2O_8 revealed by two-dimensional solid-state O-17 NMR.* Chemical Communications, 2004: 392-393.

2. A.R. West, *Solid Solutions*, in *Solid state chemistry and its applications*. 1987, Wiley: Chichester. p. 358-374.

3. R.D. Shannon, *Revised Effective Ionic-Radii and Systematic Studies of Interatomic Distances in Halides and Chalcogenides.* Acta Crystallographica Section A, 1976. **32**: 751-767.

4. C. De Meyer, F. Bouree, J.S.O. Evans, K. De Buysser, E. Bruneel, I. Van Driessche, and S. Hoste, *Structure and phase transition of Sn-substituted $Zr_{(1-x)}Sn_xW_2O_8$.* Journal of Materials Chemistry, 2004. **14**: 2988-2994.

5. J.S.O. Evans, T.A. Mary, T. Vogt, M.A. Subramanian, and A.W. Sleight, *Negative thermal expansion in ZrW_2O_8 and HfW_2O_8.* Chemistry of Materials, 1996. **8**: 2809-2823.

6. N. Nakajima, Y. Yamamura, and T. Tsuji, *Phase transition of negative thermal expansion $Zr_{1-x}Hf_xW_2O_8$ solid solutions.* Journal of Thermal Analysis and Calorimetry, 2002. **70**: 337-344.

7. Y. Yamamura, N. Nakajima, and T. Tsuji, *Calorimetric and x-ray diffraction studies of alpha-to-beta structural phase transitions in HfW_2O_8 and ZrW_2O_8.* Physical Review B, 2001. **6418**: art. no.-184109.

8. T. Tsuji, Y. Yamamura, and N. Nakajima, *Thermodynamic properties of negative thermal expansion materials ZrW_2O_8 substituted for Zr site.* Thermochimica Acta, 2004. **416**: 93-98.

9. T. Hashimoto, J. Kuwahara, T. Yoshida, M. Nashimoto, Y. Takahashi, K. Takahashi, and Y. Morito, *Thermal conductivity of negative-thermal-expansion oxide, $Zr_{1-x}Y_xW_2O_8$ (x-0.00, 0.01)-temperature dependence and effect of structural phase transition.* Solid State Communications, 2004. **131**: 217-221.

10. N. Nakajima, Y. Yamamura, and T. Tsuji, *Synthesis and physical properties of negative thermal expansion materials $Zr_{1-x}M_xW_2O_{8-y}$ (M = Sc, In, Y) substituted for Zr(IV) sites by M(III) ions.* Solid State Communications, 2003. **128**: 193-196.

11. Y. Morito, K. Takahashi, S.R. Wang, H. Abe, A. Katoh, and T. Hashimoto, *Press-free preparation method of dense negative-thermal-expansion oxide, $Zr_{1-x}Y_xW_2O_{8-delta}$ (x=0.00-0.02) ceramic using reactive sintering.* Journal of the Ceramic Society of Japan, 2002. **110**: 807-812.

12. Y. Yamamura, M. Kato, and T. Tsuji, *Synthesis and phase transition of negative thermal expansion materials $Zr_{1-x}Lu_xW_2O_{8-y}$.* Thermochimica Acta, 2005. **431**: 24-28.

13. C. Lind, A.P. Wilkinson, C.J. Rawn, and E.A. Payzant, *Preparation of the negative thermal expansion material cubic $ZrMo_2O_8$.* Journal of Materials Chemistry, 2001. **11**: 3354-3359.

14. C. Lind, A.P. Wilkinson, Z.B. Hu, S. Short, and J.D. Jorgensen, *Synthesis and properties of the negative thermal expansion material cubic $ZrMo_2O_8$.* Chemistry of Materials, 1998. **10**: 2335-2337.

15. S. Allen and J.S.O. Evans, *Negative thermal expansion and oxygen disorder in cubic $ZrMo_2O_8$.* Physical Review B, 2003. **68**.

16. C. Closmann, A.W. Sleight, and J.C. Haygarth, *Low-temperature synthesis of ZrW_2O_8 and Mo-substituted ZrW_2O_8.* Journal of Solid State Chemistry, 1998. **139**: 424-426.

17. L. Huang, Q.G. Xiao, H. Ma, G.B. Li, F.H. Liao, C.M. Qi, and X.H. Zhao, *Phase behaviors of the $ZrMo_{2-x}W_xO_8$ (x=0.2-2.0) system and the preparation of an Mo-rich cubic phase.* European Journal of Inorganic Chemistry, 2005: 4521-4526.

18. U. Kameswari, A.W. Sleight, and J.S.O. Evans, *Rapid synthesis of ZrW_2O_8 and related phases, and structure refinement of $ZrWMoO_8$.* International Journal of Inorganic Materials, 2000. **2**: 333-337.

19. J.S.O. Evans, P.A. Hanson, R.M. Ibberson, N. Duan, U. Kameswari, and A.W. Sleight, *Low-temperature oxygen migration and negative thermal expansion in $ZrW_{2-x}Mo_xO_8$.* Journal of the American Chemical Society, 2000. **122**: 8694-8699.

20. J.B. Nelson and D.P. Riley, *An experimental investigation of extrapolation methods in the derivation of accurate unit-cell dimensions of crystals.* Proceedings of the Physical Society, 1945. **57**: 160.

21. K. De Buysser, P. Lommens, C. De Meyer, E. Bruneel, S. Hoste, and I. Van Driessche, *ZrO_2-ZrW_2O_8 composites with tailor-made thermal expansion.* Ceramics-Silikaty, 2004. **48**: 139-144.

22. D.R. Lide, *Handbook of Chemistry and Physics*. 2001, Boca Raton: CRC Press LLC. 9.51-74.

23. D.G. Archer, *Thermodynamic Properties of Synthetic Sapphire (Alpha-Al_2O_3), Standard Reference Material 720 and the Effect of Temperature-Scale Differences on Thermodynamic Properties.* Journal of Physical and Chemical Reference Data, 1993. **22**: 1441-1453.

24. D.C. Ginnings and G.T. Furukawa, *Heat Capacity Standards for the Range 14 to 1200K.* Journal of the American Chemical Society, 1953. **75**: 522-527.

25. Y. Yamamura, N. Nakajima, and T. Tsuji, *Heat capacity anomaly due to the alpha-to-beta structural phase transition in ZrW_2O_8.* Solid State Communications, 2000. **114**: 453-455.

26. R. Stevens, J. Linford, B.F. Woodfield, J. Boerio-Goates, C. Lind, A.P. Wilkinson, and G. Kowach, *Heat capacities, third-law entropies and thermodynamic functions of the negative thermal expansion materials, cubic alpha-ZrW_2O_8 and cubic $ZrMo_2O_8$, from T = (0 to 400) K.* Journal of Chemical Thermodynamics, 2003. **35**: 919-937.

27. A. Hushur, G. Shabbir, J.H. Ko, and S. Kojima, *The phase transitions of ferroelectric $Sr_2Ta_2O_7$ crystals by MDSC, Brillouin and dielectric spectroscopy.* Journal of Physics D-Applied Physics, 2004. **37**: 1127-1131.

28. T. Hashimoto, T. Katsube, and Y. Morito, *Observation of two kinds of phase transitions of ZrW_2O_8 by power-compensated differential scanning calorimetry and high-temperature X-ray diffraction.* Solid State Communications, 2000. **116**: 129-132.

29. Y. Yamamura, T. Tsuji, K. Saito, and M. Sorai, *Heat capacity and order-disorder phase transition in negative thermal expansion compound ZrW_2O_8.* Journal of Chemical Thermodynamics, 2004. **36**: 525-531.

30. J.S.O. Evans, W.I.F. David, and A.W. Sleight, *Structural investigation of the negative-thermal-expansion material ZrW_2O_8.* Acta Crystallographica Section B-Structural Science, 1999. **55**: 333-340.

31. A.K.A. Pryde, K.D. Hammonds, M.T. Dove, V. Heine, J.D. Gale, and M.C. Warren, *Origin of the negative thermal expansion in ZrW_2O_8 and ZrV_2O_7.* Journal of Physics-Condensed Matter, 1996. **8**: 10973-10982.

32. T. Hashimoto and Y. Morito, *Thermal analysis of phase transition in negative-thermal-expansion oxide, ZrW_2O_8 - Detection of trace amount of H_2O and lambda-type transition.* Journal of the Ceramic Society of Japan, 2002. **110**: 823-825.

33. J.F. Shackelford, *Introduction to materials Science for Engineers*. 1988, New York: Macmillan Publishing Company.

Summary and conclusions

The positive thermal expansion of most materials is widely known, nevertheless there are materials which show the opposite behaviour. These "negative thermal expansion" (NTE) materials exhibit shrinkage of the unit cell parameters upon heating which renders them attractive for the development of new high performance materials.

ZrW_2O_8 is the most intensely studied and published representative of the NTE materials. It offers possibilities which are not completely explored yet. Novel synthetic routes were described in this work as well as some applications such as zero expansion composites materials or ZrW_2O_8 solid solutions.

The synthetic routes themselves were described in Chapter 3 and 4. Chapter 3 described the conventional solid state reaction using commercially available ZrO_2 and WO_3 as precursor oxides. The oxide mixture needed to be pre-treated to optimize the homogeneity of the mixtures. Two milling techniques were described: (1) tumbler milling with zirconia pearls and (2) ball milling with agate balls followed by spray-drying of the PEG-stabilized oxide slurry. High temperature treatment of both oxide mixtures resulted in pure ZrW_2O_8 although the morphology of the sintered bars showed some drawbacks. Destruction of PEG lead to pores but even the tumbler milled mixtures without addition of any organic materials resulted in a porous materials. Poor stacking of the powder during pressing is most likely the cause of this porosity.

Milling of the powders is a very energy consuming process. Aqueous solutions of precursor salts containing Zr^{4+} and W^{6+} are an attractive starting point. Two sol-gel routes, one using citric acid and one using EDTA, were suggested. These complexing agents are necessary to maintain the homogeneity of the solutions in a large pH range.

It must be understood that any form of precipitation or coagulation will drastically lower the homogeneity. Both sol-gel routes resulted in pure ZrW_2O_8 with a thermal expansion coefficient close to those obtained by synthesis routes which take strict precautions to avoid any volatilization of WO_3. Fast diffusion and reaction along grain boundaries in homogeneous and small particles improve the negative thermal expansion behaviour of ceramic blocks. Water-based sol-gel systems are a green alternative for the organic sol-gel routes. Further exploration of the sol-gel routes could result in deposition of thin layers of ZrW_2O_8 provided research is performed to tune the heat treatment.

The gels obtained by the citrate gel route with pH values above 6 showed blue colouring after irradiation with sun light. Photoluminescence behaviour of the gels was interpreted on the existence of small, discrete molecular WO_4^{2-} and WO_6^{6-} polyhedra in solution. The presence of WO_4^{2-} tetrahedral species is somewhat unexpected as ammonium metatungstate at pH 7 has the typical Keggin structure with corner and edge share octahedrons. EXAFS studies confirmed the WO_4^{2-} structures in the solutions above pH 6. A shift from octahedral to tetrahedral surrounding of the tungsten atom is suggested by changes noticed in the radial distribution plots. More extensive EXAFS studies could lead towards improved understanding of the chemistry in the precursor solution and the transformation from aqueous solution to the high viscosity gel-state.

The different synthetic routes described above are not only suitable for the synthesis of pure ZrW_2O_8. They can also be used in the preparation of ZrW_2O_8 based composites. In this work ZrO_2 was chosen as a dispersed phase and the synthesis strategies described can be divided into two large classes. The first route used ZrW_2O_8 and ZrO_2. No new phases were formed. These composites showed very low homogeneity as the ZrO_2 particles were not well distributed in the ZrW_2O_8 matrix. This also affects the mechanical properties of the composite materials. The negative thermal expansion can be controlled but the low composite strength is an enormous drawback. An alternative route was a synthetic route using a mixture of off-stochiometric co-milled ZrO_2 and WO_3 powders. ZrW_2O_8 was formed “in situ” and the excess of ZrO_2 was now well dispersed into the ZrW_2O_8 sintered matrix. This

positively influences the mechanical properties of the composites. A third synthetic route used off-stochiometric precursor salts in the sol-gel route as described above.

All composites showed a negative deviation of the rule of mixtures. This deviation is caused by the porosity and the differences between mechanical and elastic properties of the components present in the composites. The comparison between the composites obtained by the conventional preparation route and the "in situ" synthesis methods showed that deviation of the rule of mixtures is more pronounced in the first method due to the higher porosity percentage.

The composition of a zero-thermal expansion composite was predicted using curve fitting to experimental data for different compositions. This composite showed zero thermal expansion but only in a limited range. ZrW_2O_8 undergoes a phase transition together with a change in thermal expansion regime. This phase transition was also noticed in the $ZrO_2 – ZrW_2O_8$ composite material.

It is know from literature that the phase transition temperature of ZrW_2O_8 is affected by substitution of the Zr or W site. A large shift of the α - β transition could increase the temperature range with zero thermal expansion. Ce^{4+} and Ti^{4+} were screened for their potential as substituent for the Zr position in the ZrW_2O_8 crystal structure. Both ions have the same valence state as Zr and the electroneutrality is preserved. Ce^{4+} (101 pm) substitution, most likely due to its large ionic radius in comparison with Zr^{4+} (86 pm). Inserting Ti^{4+} (74.5) in the crystal structure resulted in a stable $Zr_{1-x}Ti_xW_2O_8$ ($0 \leq x \leq 0.05$) solid solution. The cell parameter decreased linearly with increased substitution and the transition temperature shifted to lower values. Comparison with literature results and experiments with $Zr_{1-x}Sn_xW_2O_8$ indicated that the bond energy is an important partner in this process. Lower bond energy results in a lower phase transition temperature. This hypothesis was confirmed by DSC analysis: both reaction enthalpy and reaction entropy decreased as the substitution degree increased. These results also reconfirmed the ratchet motion during the phase transition where Zr – O – W linkages are broken. Information concerning bond energy, valence state and ionic radius could allow suggesting the increase or decrease of the phase transition according to the chosen ion as substituent.

Samenvatting en besluit

Materialen met positieve thermische expansie zijn algemeen gekend. De kristalstructuur van negatieve thermische expansie materialen vertoont een afname van de eenheidcel wanneer deze onderworpen wordt aan een temperatuurstijging waardoor deze materialen aantrekkelijk worden met het oog op de ontwikkeling van hoog-technologische materialen.

ZrW_2O_8 is één van de meest bestudeerde partners van de NTE materialen. Dit materiaal biedt vele mogelijkheden die nog niet volledig geëxploreerd zijn. In dit werk werden enkele vernieuwende syntheseroutes beschreven en werd er aandacht geschonken aan ZrW_2O_8 in solid solutions en thermisch invariante composiet materialen.

De syntheseroutes zelf zijn beschreven in hoofdstuk 3 en 4. Het hoofdstuk 3 beschrijft de conventionele vaste stof reactie waarin ZrO_2 en WO_3 als precursormaterialen worden gebruikt. Dit oxidemengsel moet gehomogeniseerd worden vooraleer men met de thermische behandeling kan beginnen. Twee maalmethodes werden beschreven: (1) samen vermalen van de oxides in de aanwezigheid van zirconia parels en (2) malen met behulp van een balmolen gevolgd door het sproeidrogen van een slurry bestaande uit het fijngemalen poeder in een polyethyleen glycol oplossing. Hoge temperatuursbehandeling van beide oxidemengsels resulteerde in de vorming van puur ZrW_2O_8 maar de morfologie van de gesinterde balkjes was niet optimaal. Ontbinding van PEG leidde tot porievorming maar ook de mengsels zonder organische componenten resulteerden in een poreus materiaal. Dit kan

hoogstwaarschijnlijk verklaard worden door een slechte stapeling van de poederkorreltjes tijdens het persen van de balkjes.

Vermalen van poeders is een energierovend proces. Waterige oplossingen van wolfraam- en zirconiumzouten zijn een aantrekkelijk uitgangspunt. Twee sol-gel routes die gebruik maken ofwel citroenzuur ofwel EDTA werden voorgesteld. De toevoeging van de complexantia was noodzakelijk om de homogeniteit van de oplossingen over een groot pH gebied te vrijwaren. Elke vorm van neerslag of samenklitten moet vermeden worden omdat deze de homogeniteit drastisch verlagen. Beide sol-gel methodes resulteerden in een zuiver zirconiumwolframaat dat gekenmerkt wordt door een thermische expansiecoëfficiënt die dicht in de buurt ligt van deze bekomen door vroeger gepubliceerde synthesemethodes die de sublimatie van WO_3 proberen tegen te gaan. Deze sublimatie zorgt immers voor bijkomende poriën en verstoort de stoëchiometrische verhouding. De homogeniteit en de kleine deeltjesgroottes van de poeders verkregen via de sol-gel methode zorgen voor een snelle diffusie en reactie via de vele deeltjesgrenzen. Water gebaseerde sol-gel methodes bieden ook een "groen" alternatief voor de organische sol-gel routes. Deze sol-gel routes zouden ook geschikt kunnen zijn voor het afzetten van dunne lagen ZrW_2O_8 op een geschikt substraat na verder grondig onderzoek naar het fijnregelen van het thermisch proces.

De gels bekomen door de citraat-gel methode bij een pH boven 6 vertonen een blauwe verkleuring wanneer ze blootgesteld worden aan het zonlicht. Het fotoluminescente gedrag kan toegeschreven worden aan kleine, discrete WO_4^{2-} en WO_6^{6-} polyeders in oplossing. De aanwezigheid van WO_4^{2-} tetraëders is eerder onverwacht aangezien het ammonium metawolframaat gekenmerkt wordt door de Keggin structuur die opgebouwd is uit octaëders. EXAFS analyses bevestigen de aanwezigheid van de WO_4^{2-} species in de waterige oplossingen (pH 6 – 8). De verandering van 6- naar 4-coördinatie rond het centrale wolfraamatoom wordt gesuggereerd door veranderingen waargenomen in de radiale plots. Doorgedreven EXAFS studies zouden een beter inzicht kunnen verschaffen in de chemie heersend in de precursoroplossing en de structurele veranderingen van een waterige oplossing tot een hoog-visceuze gel.

De bovenvermelde synthesemethoden zijn niet alleen geschikt voor de bereiding van zuiver ZrW_2O_8. Ze kunnen daarenboven ook aangewend worden voor de synthese van ZrW_2O_8 composiet materialen. De keuze viel op ZrO_2 als tweede component in het composiet en de bereidings- en/of synthesemethoden kunnen in twee grote groepen ingedeeld worden. De eerste route gebruikt ZrW_2O_8 en ZrO_2 als uitgangsproducten en kan meer een bereidingsmethode benoemd worden aangezien er geen nieuwe fasen worden gevormd. In deze composieten waren de ZrO_2 deeltjes zeer inhomogeen verdeeld. Dit beïnvloedt de mechanische eigenschappen van het composietmateriaal in negatieve zin. De andere methode kan gerangschikt worden als een synthesemethode en gebruikt een niet-stoëchiometrisch mengsel van ZrO_2 en WO_3 oxide poeders. ZrW_2O_8 wordt "in situ" gevormd en hierdoor zijn de ZrO_2 partikels wel mooi verspreid in de ZrW_2O_8 matrix met betere mechanische eigenschappen tot gevolg.

Alle composieten vertoonden een negatieve afwijking van de mengregel. Deze afwijking wordt veroorzaakt door de porositeit en de verschillen in mechanische eigenschappen van de individuele componenten. De vergelijking tussen composieten bereid via de conventionele route en deze gesynthetiseerd met de "in situ" methode toonden aan dat de afwijking van de mengregel opvallender was bij composieten die via de eerste methode "bereid" waren. De samenstelling van een thermisch invariant composiet kon voorspeld worden door een curve te fitten aan de experimentele gegevens bij verschillende samenstellingen. Dit composietmateriaal vertoonde inderdaad geen thermische expansie maar helaas slechts in een beperkt temperatuursgebied. ZrW_2O_8 vertoont een fasetransitie die gepaard gaat met een verschil in expansiegedrag. Deze transitie kon ook waargenomen worden bij de composieten.

Die fasetransitietemperatuur wordt beïnvloed door de substitutie van de zirconium- en wolfraamatomen in het kristalrooster. Een verschuiving van deze temperatuur kan voor bovenvermeld composiet het gebied waarin er geen thermische expansie optreedt verlengen. Ce^{4+} en Ti^{4+} werden onderzocht als potentiële kandidaten om de Zr positie in ZrW_2O_8 in te nemen. Beide ionen hebben dezelfde valentie als Zr zodat de neutraliteit van het kristal bewaard blijft. Ce^{4+} (101 pm) bleek niet geschikt voor substitutie en de relatief grote ionenstraal in vergelijking met Zr^{4+} (86 pm) zou hier

een belangrijke rol in spelen. Substitutie van Zr^{4+} door Ti^{4+} (74.5) resulteerde in een $Zr_{1-x}Ti_xW_2O_8$ ($0 \leq x \leq 0.05$) solid solution. De celparameter daalde lineair in dit gebied en ook de transitietemperatuur ondervond een daling. Het vergelijken van deze waarnemingen met resultaten vermeld in literatuur en experimenten met $Zr_{1-x}Sn_xW_2O_8$ solid solutions toonde aan dat de bindingsterkte (M – O) een belangrijke invloed heeft op de transitie. Een lagere bindingssterkte zal een verlaging van de fasetransitietemperatuur tot gevolg hebben. Deze veronderstelling werd bevestigd door DSC analyse van Ti en Sn gesubstitueerde materialen. Zowel de reactie enthalpie als de entropie daalden bij toenemende substitutiegraad. Deze bevindingen herbevestigden ook het ratelmodel als drijfveer voor de fasetransitie. Bindingssterkte, valentie en ionenstraal zou het hierdoor mogelijk kunnen maken om de verschuiving van de fasetransitietemperatuur te voorspellen.

List of symbols and abbreviations

°C	degree Celsius
Å	Ångström (10^{-10}m)
Ø	Diameter
A	area of a 2D cell
A	cell parameter (x-axis)
B	cell parameter (y-axis)
B	width
BET	Brunauer, Emmet and Teller
C	cell parameter (z-axis)
c_i	contribution of a specific vibrational mode
C	heat capacity
C_P	heat capacity at constant pressure
C_V	heat capacity at constant temperature
CA	Citric Acid
CIT-5	$[Si_{32}O_{60}]$ Californian Institute of Technology
CMC	Ceramic Matrix Composite
D	inter-planar spacing
D	height
d_{50}	50th percentile of the particle size distribution
d_{90}	90th percentile of the particle size distribution
DSC	Differential Scanning Calorimetry
E	modulus of bending
E_0	binding energy of the photo-electron
DUBBLE	Dutch Belgian BeamLine at ESRF

EDTA	Ethylene Diamine Tetraacetic Acid
ESRF	European Synchrotron Radiation Facility
EXAFS	Extended X-ray Absorption Fine Structure
F	load at fracture
f	Weight of the synergy contribution
f(k)	scattering properties
FT	Fourier Transformed
FWHM	Full Width at Half Maximum
g	Gram
GeV	gigaelectron volt (10^9 eV)
h	Hour
h	Miller indices h: x/a
h	Planck's constant: 6.62608 10^{-34} J s
ħ	Reduced Planck's constant: h/2π: 1.05457 10^{-34} J s
HIP	Hot Isostatic Pressing
HT – XRD	High Temperature – X-Ray Diffraction
I	moment of Inertia
I, I_0	Intensity of incident (I_0), transmitted (I)radiation
IR	Infra Red
ITQ-1	$\|H_{2.4}{}^{+}Na_{3.1}{}^{+}\|[Al_{0.41}B_{0.51}Si_{66.5}O_{144}]$ Instituto de Technologia Quimica Valencia
ITQ-3	$[Si_{64}O_{128}]$ Instituto de Technologia Quimica Valencia
k	Miller indices (z/c)
k	wavenumber of the photo-electron
k_B	Boltzmann's constant: 1.38066 10^{-23} J K^{-1}
keV	kilo electron volt (10^3 eV)
kJ	kilo Joule (10^3 J)
L	distance between the supports
L	total orbital momentum
l	Length
l	Miller indices (y/b)
LaTP	$La_{0.33}Ti_2(PO_4)_3$
M	Molarity (mol/L)

m	Mass
mA	Milliampere (10^{-3} A)
mass%	weight percentage
meV	millielectron volt (10^{-3} eV)
MMC	Metal Matrix Composite
mmol	millimol (10^{-3} mol)
MPa	Megapascal (10^{6} Pa)
mW	milliwatt (10^{-3} W)
N	number of neighbouring atoms
n	order of diffraction
nm	nanometer (10^{-9} m)
NASICON	Sodium Super-Ionic conductor
NTP	$NaTi_2(PO_4)_3$
NTE	Negative Thermal Expansion
NWO	Nederlands fonds voor Wetenschappelijk Onderzoek
P	volume fraction porosity
P, p	Pressure
p	momentum
PEG	Polyethylene glycol
pm	picometer (10^{-12} m)
PMC	Polymer Matrix Composite
ppm	parts per million
R	distance to the neighbouring atoms
r	bond length
RE	Rare Earth elements
RT	Room temperature (20 °C)
RUM	Rigid Unit Mode
S	Entropy
S	Spin quantum momentum
S_y	Residual
SEM	Scanning Electron Microscopy
SEM-EDX	Scanning Electron Microscopy (Energy Dispersive analysis of X-rays

SrTP	$Sr_{0.5}Ti_2(PO_4)_3$
SSZ-23	$\|(C_{13}H_{24}N^+)_{4.1}F_{3.3}^-(OH^-)_{0.8}\|[Si_{64}O_{128}]$ Standard oil Synthetic Zeolite
T	Temperature
TT	Transition Temperature
TGA – DTA	Thermo Gravimetric Analysis – Differential Temperature Analysis
TGA – MS	Thermo Gravimetric Analysis – Mass Spectrometry
TMA	Thermal Mechanical Analysis
V	Volume
V%	Volume fraction
W	weight of the observation
w%	weight percentage
XANES	X-ray analysis Near-Edge spectroscopy
XRD	X-Ray Diffraction
Y	observed/calculated intensity

Greek Symbols

α	bonding angle (between y- and z-axis)
α	linear thermal expansion coefficient
B	bonding angle (between x- and z-axis)
β	volume thermal expansion coefficient
Γ	bonding angle (between x- and y-axis)
Γ	Grüneisen parameter
ΔC_P	Excess Heat capacity
ΔD	strain
ΔF	stress
ΔH	Enthalpy
ΔS	Entropy
$\delta(k)$	phase shift
η	geometrical calculable constant
θ	angle between incident or diffracted beam

θ	rotation angle
λ	wavelength of radiation
μm	micrometer (10^{-6} m)
μ	absorption coefficient
ν	vibrational frequency
ν	Volume fraction
ρ	density
σ_f	Flexural Strength
σ^2	Debye-Waller factor: disorder
$\chi(k)$	oscillations as a function of photo-electron wavenumber
χ_T	isothermal compressibility
χ_S	adiabatic compressibility
χ	compressibility

Crystallographic data

Pattern : 00-050-1868 **Radiation =** 1.540598 **Quality :** High

ZrW_2O_8

Zirconium Tungsten Oxide

Lattice : Cubic

S.G. : P213 (198)

a = 9.15510

Z = 4

Mol. weight = 586.92

Volume [CD] = 767.34

Dx = 5.080

Sample preparation: Zr W2 O8 was prepared by heating a mixture of Zr O2 and W O3 in the correct stoichiometric proportion in a sealed platinum tube at 1473 K for 48 hours. Cubic Zr W2 O8 was maintained metastably at ambient conditions by quenching the sample in water.
Color: Colorless
Temperature of data collection: Pattern taken at room temperature.
Data collection flag: Ambient.

Perottoni, C., da Jornada, J., Univ. Federal do Rio Grande do Sul, Porto Alegre, Brazil., Private Communication (1999)

Radiation : CuKa1

Lambda : 1.54056

SS/FOM : F30=1000(0.0002,30)

Filter : Monochromator crystal

d-sp : Calculated spacings

2th	i	h	k	l
13.667	4	0	1	1
16.759	133	1	1	1
19.375	122	0	0	2
21.689	999	0	1	2
23.788	772	1	1	2
27.535	252	0	2	2
29.241	88	1	2	2
30.861	166	0	1	3
32.408	322	1	1	3
33.892	9	2	2	2
35.320	198	0	2	3
36.700	359	1	2	3
39.334	25	0	0	4
40.597	123	0	1	4
41.828	7	0	3	3
43.031	43	1	3	3
44.207	91	0	2	4
45.358	188	1	2	4
46.488	33	2	3	3
48.685	194	2	2	4
49.756	77	0	3	4
50.811	176	0	1	5
51.850	278	1	1	5
53.885	191	0	2	5
54.883	44	1	2	5
56.843	171	0	4	4
57.808	43	1	4	4
58.762	64	0	3	5
59.706	32	1	3	5
60.640	30	0	0	6
61.567	13	0	1	6
62.486	171	1	1	6
65.197	105	0	4	5
66.088	62	1	4	5
66.972	8	3	3	5
67.851	31	2	2	6
68.724	74	0	3	6
69.592	83	1	3	6
71.314	4	4	4	4
72.168	56	2	3	6
73.018	99	0	1	7
73.864	48	1	1	7
74.707	11	0	4	6
75.546	63	0	2	7
76.383	20	1	2	7
78.046	87	2	4	6
78.874	14	2	2	7
79.701	14	0	3	7
80.523	84	1	3	7
82.164	25	0	5	6
82.982	11	1	5	6
84.615	3	0	0	8
85.429	54	0	1	8
86.242	47	1	1	8
87.056	13	3	3	7
87.867	18	0	2	8
88.679	17	1	2	8
89.491	25	3	5	6
91.113	102	0	6	6
91.924	16	0	3	8
92.736	42	0	5	7
93.549	24	1	5	7
94.362	2	2	6	6
95.176	35	2	3	8
95.991	33	2	5	7

Pattern : 00-032-1395 **Radiation =** 1.540598 **Quality :** High

WO_3

Tungsten Oxide

Lattice : Anorthic (triclinic)
S.G. : P-1 (2)

a = 7.30900
b = 7.52200
c = 7.67800
a/b = 0.97168
c/b = 1.02074

alpha = 88.81
beta = 90.92
gamma = 90.93
Z = 8

Mol. weight = 231.85
Volume [CD] = 421.92
Dx = 7.300
Dm = 7.270

General comments: Stable from -40 C to 17 C.
General comments: Single-crystal data used.
Additional pattern: See 20-1323.
Data collection flag: Ambient.

Diehl, R. et al., Acta Crystallogr., Sec. B, volume 34, page 1105 (1978)

Radiation : CuKa
Lambda : 1.54180
SS/FOM : F25= 21(0.0140,87)

Filter : Beta
d-sp : Guinier
Internal standard : NaCl

2th	i	h	k	l
23.144	85	0	0	2
23.643	100	0	2	0
24.367	100	2	0	0
26.490	9	-1	2	0
26.619	13	0	-2	1
26.840	8	-2	0	1
28.383	7	-1	1	2
28.634	13	-1	2	1
28.842	18	1	1	2
28.928	20	-1	-1	2
29.069	8	1	-1	2
33.000	20	0	2	2
33.577	35	-2	0	2
33.677	25	0	-2	2
33.916	25	-2	2	0
34.105	35	2	0	2
34.493	25	2	2	0
35.001	3	-1	2	2
35.388	4	-2	1	2
35.509	4	1	2	2
35.668	7	-2	2	1
35.896	7	1	-2	2
40.705	3	3	-1	1
40.954	17	-2	2	2
41.871	30	2	2	2

Pattern : 00-037-1484 **Radiation =** 1.540598 **Quality :** High

ZrO_2

Zirconium Oxide
Also called: zirconium dioxide, Baddeleyite, syn, zirkite, zirconia

Lattice : Monoclinic
S.G. : P21/a (14)

a = 5.31290
b = 5.21250
c = 5.14710
a/b = 1.01926
c/b = 0.98745

beta = 99.22
Z = 4

Mol. weight = 123.22
Volume [CD] = 140.70
Dx = 5.817
I/Icor = 2.60

Sample source or locality: Sample was obtained from Titanium Alloy Manufacturing Co. (1990) and was heated to 1300° for 48 hours.
Analysis: Spectrographic analysis showed that this sample contained less than 0.01% each of Al, Hf and Mg and between 0.1 and 0.01% each of Fe, Si and Ti.
Structure: The structure of Zr O2 (baddeleyite) was determined by McCullough and Trueblood (1) and confirmed by Smith and Newkirk (2).
Polymorphism: There are a number of polymorphic forms of Zr O2 stable at different temperatures and pressures.
Temperature of data collection: The mean temperature of the data collection was 25.5°.
Additional pattern: To replace 13-307 and 36-420 and validated by calculated pattern 24-1165.
General comments: Pattern reviewed by Holzer, J., McCarthy, G., North Dakota State Univ., Fargo, North Dakota, USA, *ICDD Grant-in-Aid* (1990). Agrees well with experimental and calculated patterns. Additional weak reflections [indicated by brackets] were observed.
Color: Colorless
Additional pattern: See ICSD 18190 (PDF 72-1669); 15983 (PDF 72-597); 26488 (PDF 74-815); See ICSD 60903 (PDF 78-50).
Data collection flag: Ambient.

McMurdie, H., Morris, M., Evans, E., Paretzkin, B., Wong-Ng, W., Hubbard, C., Powder Diffraction, volume 1, page 275 (1986)

CAS Number: 1314-23-4

Radiation : CuKa1
Lambda : 1.54060
SS/FOM : F30=111(0.0073,37)

Filter : Monochromator crystal
d-sp : Diffractometer
Internal standard : Ag FP

2th	i	h	k	l
17.419	3	0	0	1
24.048	14	1	1	0
24.441	10	0	1	1
28.175	100	-1	1	1
31.468	68	1	1	1
34.160	21	2	0	0
34.383	11	0	2	0
35.309	13	0	0	2
35.900	2	-2	0	1
38.396	1	-2	1	0
38.541	4	1	2	0
39.411	1	0	1	2
39.990	1	-2	1	1
40.725	12	-1	1	2
41.150	5	2	0	1
41.374	5	-1	2	1
44.826	7	2	1	1
45.522	6	-2	0	2
48.949	2	-2	1	2
49.266	18	2	2	0
50.116	22	0	2	2
50.559	13	-2	2	1
51.193	5	-1	2	2
54.104	11	0	0	3
54.680	1	2	2	1
55.270	11	1	2	2
55.400	11	3	1	0
55.570	9	-3	1	1
55.883	6	0	3	1
57.168	7	-1	1	3
57.861	4	-1	3	1
58.268	3	-2	2	2
59.775	8	1	3	1
60.055	7	-2	0	3
61.367	5	3	1	1
61.984	5	-3	1	2
62.838	8	1	1	3
64.079	1	3	2	0
64.250	2	2	3	0
64.966	1	0	3	2
65.384	2	-2	3	1
65.700	6	0	2	3
65.884	4	-1	3	2
68.912	1	2	3	1
69.620	1	3	2	1
70.190	1	-3	2	2
71.071	2	-2	2	3
71.300	4	-4	0	1
71.950	1	4	0	0
72.104	1	-2	3	2
72.450	1	0	4	0
72.642	1	3	1	2
73.580	1	-3	1	3
74.682	2	0	0	4
75.046	4	1	4	0
76.410	1	-1	1	4
77.392	1	3	3	0
78.079	1	4	0	1
78.866	1	0	3	3

Pattern : 01-089-4203 **Radiation =** 1.540598 **Quality :** Calculated

TiO_2

Titanium Oxide
Anatase, syn

Lattice : Tetragonal
S.G. : P42/mnm (136)

a = 3.78500
c = 9.51400

Z = 2

Mol. weight = 79.90
Volume [CD] = 136.30
Dx = 1.947
I/Icor = 5.04

ICSD collection code: 044882
Remarks from ICSD/CSD: REM M PDF 21-1272.
Remarks from ICSD/CSD: REM M z(O) in abstract = .2066.
Temperature factor: ITF
Data collection flag: Ambient.

Cromer, T.D., Herrington, K., J. Am. Chem. Soc., volume 77, page 4708 (1955)
Calculated from ICSD using POWD-12++

Radiation : CuKa1
Lambda : 1.54060
SS/FOM : F30=1000(0.0001,38)

Filter : Not specified
d-sp : Calculated spacings

2th	i	h	k	l
18.638	59	0	0	2
25.304	999	1	0	1
33.454	431	1	1	0
36.949	56	1	0	3
37.793	88	0	0	4
38.566	36	1	1	2
44.247	1	1	1	3
48.036	119	2	0	0
51.350	116	1	1	4
51.960	16	2	0	2
53.886	148	1	0	5
55.061	146	2	1	1
58.128	12	0	0	6
62.107	23	2	1	3
62.684	52	2	0	4
68.756	24	1	1	6
70.287	25	2	2	0
73.449	5	2	2	2
74.053	5	1	0	7
75.046	74	2	1	5
76.032	20	3	0	1
78.657	15	2	0	6
78.936	8	1	1	7
80.117	30	3	1	0
80.740	2	0	0	8
82.156	5	3	0	3
82.672	18	2	2	4
83.154	8	3	1	2
83.463	4	2	1	6
86.925	1	3	1	3
89.452	1	2	2	5

Pattern : 00-041-1445 **Radiation =** 1.540598 **Quality :** High

SnO_2

Tin Oxide
Cassiterite, syn
Also called: tin stone, wood tin

Lattice : Tetragonal
S.G. : P42/mnm (136)

a = 4.73820
c = 3.18710

Z = 2

Mol. weight = 150.69
Volume [CD] = 71.55
Dx = 6.994
Dm = 7.020
I/Icor = 1.90

Color: White
Additional pattern: To replace 1-657, 14-567 and 21-1250.
Optical data: B=2.006, Q=2.0972, Sign=+
Additional pattern: See ICSD 39173 (PDF 77-447).
Data collection flag: Ambient.

Welton, J., McCarthy, G., North Dakota State University, Fargo, North Dakota, USA., ICDD Grant-in-Aid (1988)
Powder Diffraction, volume 4, page 156 (1989)

Radiation : CuKa1
Lambda : 1.54060
SS/FOM : F30=105(0.0095,30)

Filter : Monochromator crystal
d-sp : Diffractometer
Internal standard : Si

2th	*i*	*h*	*k*	*l*
26.611	100	1	1	0
33.893	75	1	0	1
37.950	21	2	0	0
38.969	4	1	1	1
42.635	1	2	1	0
51.781	57	2	1	1
54.759	14	2	2	0
57.819	6	0	0	2
61.872	11	3	1	0
62.591	1	2	2	1
64.719	12	1	1	2
65.938	14	3	0	1
69.231	1	3	1	1
71.278	6	2	0	2
71.773	1	3	2	0
74.452	1	2	1	2
78.714	9	3	2	1
81.139	3	4	0	0
83.714	6	2	2	2
84.179	1	4	1	0
87.228	3	3	3	0
89.766	7	3	1	2
90.890	8	4	1	1
93.266	3	4	2	0
93.924	1	3	3	1
95.980	3	1	0	3
98.896	1	3	2	2
99.041	1	1	1	3
100.007	1	4	2	1
108.256	4	4	0	2
108.407	7	2	1	3
111.464	1	4	1	2
111.972	3	5	1	0
114.752	3	3	3	2
115.984	8	5	0	1
118.310	1	2	2	3

Pattern : 00-049-2452 **Radiation =** 1.540598 **Quality :** High

$C_{10}H_{12}N_2O_{18}Zr \cdot 4H_2O$
$/Zr(C_{10}H_{12}N_2O_8) \cdot 4H_2O$

Zirconium edtate tetrahydrate
Also called: zirconium EDTA, zirconium ethylenediaminetetraacetate tetrahydrate

Lattice : Base-centered monoclinic
S.G. : C2/c (15)

a = 11.49500
b = 11.58200
c = 12.17900
a/b = 0.99249
c/b = 1.05155

beta = 102.84
Z = 4

Mol. weight = 611.49
Volume [CD] = 1580.91
Dx = 2.569
I/Icor = 2.30

Sample preparation: Synthesized from a suspension of ethylenediaminetetraacetic acid and a water solution of Zr O Cl2 at 100 C, followed by slow crystallization while cooling and recrystallization from water.
Unit cell: The structure was refined from single-crystal x-ray data: a=11.48(5), b=12.13(5), c=11.58(5), γ=102.0(3), S.G.=`B2/b`, Z=4 [Pozhidaev, A., Porai-Koshits, M., Polynova, T., *Z. Struct. Chim. (Russ.)*, **15** 644 (1974)].
Sample source or locality: The sample was provided by Kuzmina, N., Moscow State Univ., Russia.
Color: White
Temperature of data collection: Pattern taken at 20 C.
General comments: Data collected in transmission mode.
Data collection flag: Ambient.

Mironov, A., Antipov, E., Moscow State Univ., Russia., ICDD Grant-in-Aid (1997)

CAS Number: 51321-09-6

Radiation : CuKa1
Lambda : 1.54060
SS/FOM : F30= 55(0.0121,45)

Filter : Monochromator crystal
d-sp : Diffractometer
External standard : Si

2th	i	h	k	l
12.241	100	-1	1	1
14.216	67	1	1	1
14.901	27	0	0	2
15.283	33	0	2	0
15.787	6	2	0	0
19.189	17	-2	0	2
21.423	3	0	2	2
22.044	1	2	2	0
24.112	2	2	0	2
24.396	9	2	2	1
24.566	6	-3	1	1
25.002	13	-1	3	1
26.026	8	1	3	1
26.341	1	-3	1	2
26.611	33	1	1	3
27.276	3	0	2	3
27.710	1	-1	3	2
28.670	1	2	2	2
28.964	9	-2	2	3
29.614	17	1	3	2
29.998	7	-3	1	3
30.376	2	-1	1	4
30.826	1	0	4	0
31.765	3	0	4	1
31.906	5	4	0	0
32.129	4	-1	3	3
32.979	11	-3	3	1
33.346	14	3	3	0
33.868	1	0	2	4
34.185	1	2	2	3
34.439	2	0	4	2
34.566	3	1	3	3
34.840	8	-4	2	1
*34.840	8	2	4	0
35.410	2	3	3	1
35.552	2	4	2	0
35.751	3	-4	2	2
36.474	1	2	4	1
36.597	3	-2	4	2
37.285	6	2	0	4
37.711	2	-1	1	5
38.264	1	-4	2	3
38.503	4	0	4	3
38.939	1	3	3	2
*38.939	1	-4	0	4
39.742	4	1	5	0
*39.742	4	-2	4	3
40.005	2	-5	1	1
40.502	8	2	2	4
40.824	1	1	5	1
41.003	1	0	2	5
41.305	3	1	1	5
41.579	1	4	2	2
42.062	1	-4	2	4
42.386	6	-5	1	3
43.310	4	1	5	2
43.641	1	3	3	3
43.887	5	-1	3	5
44.140	1	-2	4	4
45.083	2	-1	5	3
45.798	5	-3	5	1
46.371	1	4	2	3
46.968	7	-4	2	5
47.738	5	0	6	1
48.654	2	6	0	0
49.105	1	2	4	4
49.461	3	-2	4	5
50.051	2	4	4	2
50.474	3	-4	4	4
51.331	1	6	2	0
51.711	3	5	1	3
52.329	3	5	3	2
52.753	2	0	6	3
53.388	1	-1	1	7
53.715	1	-2	6	3
54.273	1	4	4	3
54.838	3	-4	4	5
55.217	2	-5	1	6
*55.217	2	2	4	5
55.603	1	3	3	5
*55.603	1	-2	4	6
56.214	1	0	4	6
56.731	1	5	3	3
57.108	3	6	2	2
57.659	1	-7	1	3
57.890	2	-1	7	2
58.298	1	-1	3	7
59.041	1	-6	4	3
59.595	2	-3	3	7
59.978	1	-5	3	6

Scientific work

A1 Publications

C. De Meyer, F. Bouree, J.S.O. Evans, K. De Buysser, E. Bruneel, I. Van Driessche, and S. Hoste, *Structure and phase transition of Sn-substituted $Zr_{(1-x)}Sn_xW_2O_8$.*
Journal of Materials Chemistry, 2004. **14**: 2988-2994.

P. Lommens, C. De Meyer, E. Bruneel, K. De Buysser, I. Van Driessche, and S. Hoste, *Synthesis and thermal expansion of ZrO_2/ZrW_2O_8 composites.*
Journal of the European Ceramic Society, 2005. **25**: 3605-3610.

K. De Buysser, P. Lommens, C. De Meyer, E. Bruneel, S. Hoste, and I. Van Driessche, *ZrO_2-ZrW_2O_8 composites with tailor-made thermal expansion.*
Ceramics-Silikaty, 2004. **48**: 139-144.

K. De Buysser, G. G. Herman, E. Bruneel, S. Hoste and I. Van Driessche, *Determination of the number of unpaired electrons in metal-complexes. A comparison between the Evans'Method and susceptometer results*.
Chemical Physics, 2005. **315**: 286-292.

K. De Buysser, P.F. Smet, B. Schoofs, E. Bruneel, D. Poelman, S. Hoste and I. Van Driessche, *Aqueous sol-gel processing of precursor oxides for ZrW_2O_8 synthesis*
Journal of Sol-gel Science and Technology, 2007. **43**: 347-353

K. De Buysser, I. Van Driessche, B. Vande Putte, J. Schaubroeck, and S. Hoste, *Study of Ti^{4+} substitution in ZrW_2O_8 negative expansion materials*
Journal of Solid State Chemistry, 2007. **180**: 2310-2315

K. De Buysser, I. Van Driessche, B. Vande Putte, P. Vanhee, J. Schaubroeck and S. Hoste, *Study of negative thermal expansion in Ti^{4+} and Sn^{4+} substituted ZrW_2O_8 materials*
Submitted to Inorganic Chemistry

K. De Buysser, I. Van Driessche and S. Hoste, *EDTA assisted sol-gel synthesis of ZrW_2O_8*
Submitted to Journal of Sol-gel Science and Technology

K. De Buysser, I. Van Driessche and S. Hoste, *EXAFS analysis of blue luminescence in polyoxytungstates*
In preparation

C1 International conference proceedings

K. De Buysser, G. G. Herman, E. Bruneel, S. Hoste and I. Van Driessche, *Determination of the number of unpaired electrons in metal-complexes. A comparison between the Evans'Method and susceptometer results*
Measurement Science Review, 2005. **5**: 30-31.

K. De Buysser, S. Hoste en I. Van Driessche, *Synthesis of ZrW_2O_8 ceramics and composites from aqueous precursors*
Advances in Science and Technology, 2006. **45**: 218-222.

International conferences with oral presentation

Solid State Chemistry, Praag, ZrO_2-ZrW_2O_8 composites with tailor made thermal expansion, 13/09/2004

Measurement 2005, Bratislava, Determination of the number of unpaired electrons in metal-complexes, 17/05/2005

CIMTEC 2006, Acireale, Sicilië, Synthesis of ZrW_2O_8 ceramics from Aqueous Sol-Gel precursors, 05/06/2006

ECerS 2007, Berlijn, Duitsland, Thermal expansion, and thermodynamical properties of substituted $Zr_{1-x}M_xW_2O_8$ materials (with M: Ti^{4+} and Sn^{4+}), 19/06/2007

Negative Materials - Fourth International Workshop on Auxetics and Related Systems, Malta, 24-26/09/2007, invited lecture

National meetings with oral presentation

Magnetic Separation in aqueous media, First IMAT workshop, Ugent, 23/05/2002
Vlaams Jongeren Congres, Bepaling van het aantal ongepaarde elektronen in metaal-cyclam complexen, Gent, 16/04/2004

BCerS Meeting, ULB Brussel, ZrO_2-ZrW_2O_8 composites with tailor made thermal expansion, 25/05/2005

Vlaams Jongeren Congres, Synthese van ZrW_2O_8 keramieken op basis van sol-gel precursoren, Leuven, 07/04/2006

National meetings with poster presentation

Doctoraatsymposium Faculteit Wetenschappen, UGent, ZrO_2-ZrW_2O_8 composites with tailor made thermal expansion, 3/05/2005

BCerS meeting, VITO, Mol, Improvement of the mechanical properties of the negative thermal expansion material ZrW_2O_8 by sol-gel synthesis 01/12/2006

Doctoraatsymposium Faculteit Wetenschappen, UGent, Thermal expansion, and thermodynamical properties of substituted $Zr_{1-x}M_xW_2O_8$ materials (with M: Ti^{4+} and Sn^{4+}), 24/04/2007